REVIEW

of the
TRICAL COMMUNICATION LABORATORY

N TELEGRAPH AND TELEPHONE PUBLIC CORPORATION

Former, Reports of the Electrical Communication Laboratory
Nippon Telegraph and Telephone Public Corporation
from Vol.1, No.1, Sept. 1953 to Vol.7, No.12, Dec. 1959

VOLUME 9
NUMBERS 7-8

Published Bimonthly by
ELECTRICAL COMMUNICATION LABORATORY
PON TELEGRAPH AND TELEPHONE PUBLIC CORPORATION
1551, Kitizyôzi, Musasino-si, Tôkyô, Japan

July - August
1961

Review of the Electrical Communication Laboratory

EDITORIAL COMMITTEE

Susumu OKAMURA *Chairman*

Giichi ITO
Hideo KAWASAKI
Yukio NAKAMURA
Tatsuya SHIMBORI
Takuzo SHINDO
Toyotaro SHIRAMATSU
Takakichi UZAWA
Ginsaku YASAKI

Nobukazu NIIZEKI

EDITORIAL STAFF

Takaaki MIWA *Editor*
Tutomu SAITO *Assistant Editor*
Masao HIROSE 〃

The Review of the Electrical Communication Laboratory is published six times a year (bimonthly) by the Electrical Communication Laboratory, Nippon Telegraph and Telephone Public Corporation, 1551, Kitizyôzi, Musasino-si, Tôkyô, Japan. Telephone: Tôkyô (391) 2261 and 2271.

All rights of republication, including translation into foreign languages, are reserved by the Electrical Communication Laboratory, NTT.

Subscriptions are accepted at ¥1,200 per year. Single copy ¥300 each. Foreign postage is ¥400 per year or ¥65 per copy. Remittance should be made in check payable to the Electrical Communication Laboratory and sent to the Director.

Printed by Aoyama Printing Co., Tokyo, Japan

R E V I E W
of the
ELECTRICAL COMMUNICATION LABORATORY

NIPPON TELEGRAPH AND TELEPHONE PUBLIC CORPORATION

Volume 9, Numbers 7-8 July-August, 1961

U.D.C. 546. 28 : 543. 53 : [546. 21+546. 27

Radioactivation Analysis of Oxygen and Boron in Transistor-Grade Silicon*

***Tadashi NOZAKI*†** and ***Junichi SIMADA*†**

Use of the ^{16}O (α, pn) ^{18}F *reaction provided the most accurate and sensitive method yet tried for the analysis of trace quantities of oxygen in transistor-grade silicon, with the determination limit being as low as* 10^{-9} *grams of oxygen. The sample was irradiated with* α*-particles in a cyclotron, and the activity (disintegration-rate) of the* ^{18}F *was measured after chemical separation. It was pointed out, on the other hand, that for an analysis of boron by the* ^{11}B (p, n) ^{11}C *reaction, nitrogen should be determined by another method because of the simultaneous occurence of the* ^{14}N (p, α) ^{11}C *reaction.*

Introduction

Determination of trace quantities of impurities in transistor-grade silicon is very important in the research and production of silicon semiconductor material. Various analytical methods are useful for a variety of impurity elements, but trace quantities of boron, carbon, nitrogen, and oxygen can rarely be determined by either chemical or neutron activation methods.*1 These elements are abundant in nature and it is very probable that they are present in high-purity silicon as impurities. Although neutron-induced nuclear reactions are mainly used for radioactivation analyses, other nuclear reactions using charged particles seem also to be very useful for the determination of small quantities of such elements.

In neutron- and photon-activation analysis the entire sample is activated uniformly. Also,, a standard material containing a known amount of the impurity element is irradiated together with the sample under the same conditions and the impurity content in the sample is calculated with respect to the standard. Since charged particles lose their energy very rapidly in a solid material, the radioisotopes are produced only in limited portions of the sample. Also, the reaction yield of a certain radioisotope is highly dependent on the energy of the incident particle. Therefore, a standard material is useless in such a case, and an absolute method should be adopted. The cross section of the nuclear reaction is accurately measured in advance of

---

* MS received by the Electrical Communication Laboratory on February 25, 1961. Originally published in the *Review of the Electrical Communication Laboratory*, Vol. 9, Nos. 7-8, pp. 403–407, 1961.

† Kobayashi's Research Section.

irradiation with charged particles of different energies. The amount of radioisotope produced is measured absolutely after the sample is irradiated, and the impurity content is calculated from these data. Using the $^{16}O(\alpha, pn)^{18}F$ reaction, the authors have discovered a new method for determining a quantity of oxygen in silicon as small as 1×10^{-3} p.p.m. They have also examined the possibility of the determination of boron in silicon by the use of the $^{11}B(p, n)^{11}C$ reaction.

1. Determination of Oxygen in Silicon

1.1. Survey of Previous Work

Use of the following three reactions has been tried for this purpose(1)~(4); (1) $^{16}O(t, n)^{18}F$, (2) $^{16}O(\gamma, n)^{15}O$, (3) $^{17}O(d, n)^{18}F$. Reaction (1) takes place when an oxygen-containing material in close contact with lithium (or its fluoride) is irradiated by neutrons. Tritium is generated by the reaction $^{6}Li+n \rightarrow t+{}^{4}He$, and has 2.74 MeV energy. Its range is only about 6.4 g/cm^2 in lithium fluoride and 15 mg/cm^2 in copper. Hence the sample should be pulverised and mixed well with the lithium (or lithium fluoride); otherwise only oxygen atoms very near the surface take part in the reaction. Oxygen is readily sorbed on various kinds of surfaces, but the surface contamination is removed only together with a considerable portion of the inner part. Lithium (or its fluoride) always contains a trace of oxygen, and the accuracy and the sensitivity of the determination are inevitably limited.

Use of reaction (2) has a low sensitivity because of the difficulty in separating short lived ^{15}O and because of the abundance of oxygen in air. Reaction (3) is not suitable for radioactivation analysis owing to the limited quantities of ^{17}O.

2. Use of (α, pn) Reaction

The reaction $^{16}O(\alpha, pn)^{18}F$ was adopted by the authors because it appears very probable that this reaction enables more accurate and more sensitive analysis of oxygen than any other nuclear reactions do, so far as the sample has a high melting point and a low vapor pressure.

3. Experimental Process

A silicon plate (30×17×1 mm; 1.2 g) was placed with the aid of spring washer on a

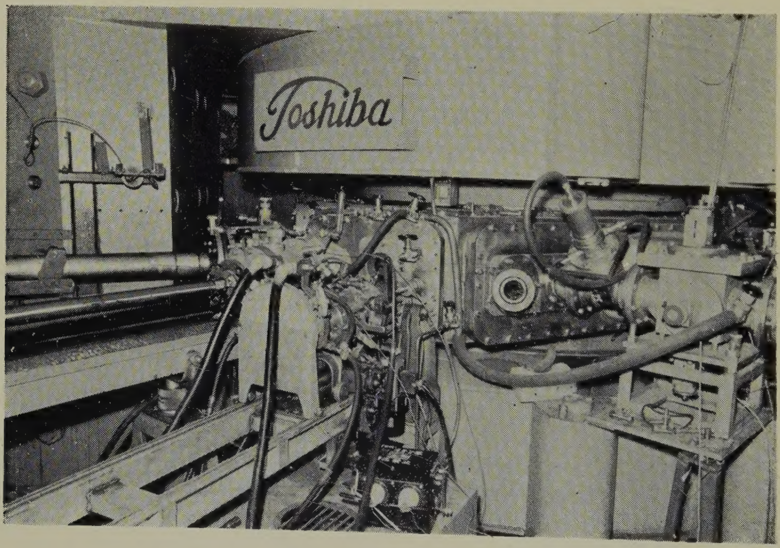

Fig. 1—Cyclotron

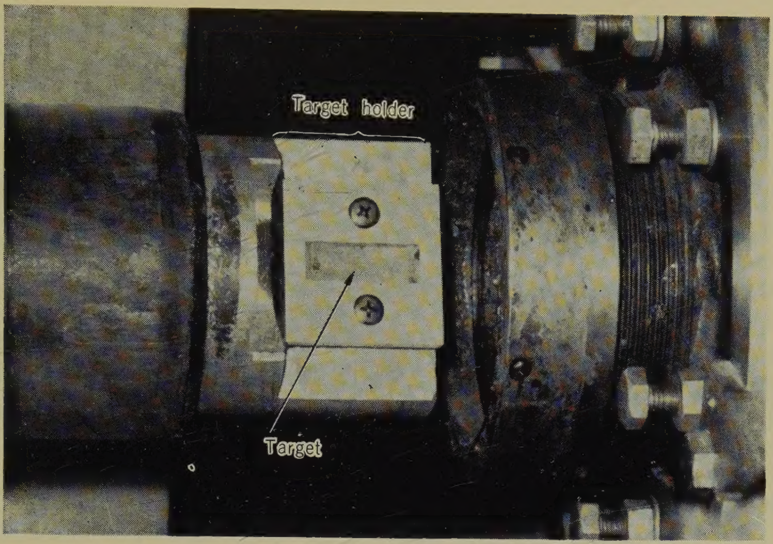

Fig. 2—Target and target holder.

target holder, which was made of aluminum and cooled with running water. The silicon sample was irradiated with α-particles (40 MeV, 7 μA, 15 min.) in a cyclotron (Photo. 1 and 2). (The range of the α-particle in silicon is about 0.8 mm.) Too high a flux or poor contact of the sample with the holder caused slight fusion of the sample.

The activated silicon was carefully treated with hydrofluoric acid containing a small quantity of nitric acid to remove the surface contamination, and pulverised in an iron mortar specially prepared for this purpose. All of the silicon powder was added in small portion into fused potassium hydroxide (25 g) containing sodium fluoride (10 mg) and disodium hydrogen phosphate (10 mg) as the carrier (for fluorine and phosphorus). When the mixture became uniform, sodium nitrate (1 g) was added to oxidize the phosphorus (into the phosphate). This was formed by the reactions ${}^{29}\mathrm{Si}(\alpha, p){}^{32}\mathrm{P}$ and ${}^{30}\mathrm{Si}(\alpha, pn){}^{32}\mathrm{P}$, and serves as an internal monitor for the α-particle flux. The fused cake was then dissolved in sulfuric acid 200 ml) in a distillation flask, and the fluorine was distilled as silicon fluoride at 150~160° C. The distillate was caught in aqueous ammonia, and the fluorine was precipitated as calcium fluoride together with calcium carbonate by adding calcium chloride and sodium carbonate. The precipitate was filtered off and the radioactivity and weight measured. The chemical process required about 2 hours.

Table 1

RADIOISOTOPES OF LIGHT ELEMENTS ($Z<10$) WITH A HALF-LIFE BETEEN 5 MIN. AND 1 YEAR.

Nuclide	Half-life	mode of Decay	β-ray Energy (Mev)	γ-ray Energy (Mev)
${}^{7}_{4}\mathrm{Be}$	53 d	EC α		0. 48
${}^{11}_{6}\mathrm{C}$	20 m	β	0. 968	no
${}^{13}_{7}\mathrm{N}$	10 m	β	1. 2	no
${}^{18}_{9}\mathrm{F}$	112 m	β	0. 649	no

Several devices for the absolute measurement of the radioactivity of ${}^{18}\mathrm{F}$ were used: (1) coincidence detector with two NaI scintillation heads positioned 180° from each other, (2) scintillation detector with a known efficiency (a well-type or a nonwell-type NaI crystal), (3) G-M low background counter with high efficiency.*2) The counting-rate was so high that the use of the first or the second device was preferred (2×10^3 to 2×10^4 c.p.m. for the second device). The counting-rate was measured every hour for 10 hours. The decay curve agreed with that of ^{18}F, and the spectrum consisted only of the annihilation radiation. After measurement of the counting-rate, the amount of fluorine in the precipitate was determined to obtain the yield of the chemical separation, which was about 80%.

4. Results and Discussion

The yield of the reaction $^{16}O(\alpha, pn)^{18}F$ had been determined by two of the authors(5); and it was indicated that when silicon containing 1 p.p.m. of oxygen is irradiated with α-particles of 40 MeV, one atom of ^{18}F is formed for every 2×10^9 α-particles (statistically). Crude silicon contained 4 p.p.m. of oxygen; transistor-grade silicon, which had been purified by floating zone-refining in vacuo, contained 0.3 p.p.m. of oxygen. Such a small amount cannot be detected by infrared absorptiometry. If the sample were kept in a good contact with the holder, irradiation with a higher flux (20 μA) and for a longer period (2 hrs.) should be possible. In such a case, 1×10^{-3} p.p.m. of oxygen would offer a counting-rate, due to the ^{18}F in the separated calcium fluoride, of more than 30 c.p.m. at the initiation of counting when the counting efficiency is 40%. This value is sufficient for a determination of the oxygen.*3) Thus, the sensitivity of this method is much higher than that of any method tried before. With a slight modification of the chemical process, this method can be applied to the determination of oxygen in other materials with a high melting point and a low vapor pressure.

5. Analysis of Boron in Silicon

R. A. Gill(6) reported on the radioactivation analysis of boron in silicon by the use of the $^{11}B(p, n)^{11}C$ reaction. Although his work is quite valuable, the reaction $^{14}N(p, \alpha)^{11}C$ must be taken into account and only the total of the nitrogen and boron can be evaluated, because both reactions give the same nuclide ^{11}C. It is quite probable that a trace of nitrogen, the main constituent of air, is present in silicon. Thus for an accurate determination of boron, either of the following processes must be adopted.

(1) Two pieces of the sample are irradiated with proton beams of different energies. Since the yields for $^{11}B(p, n)^{11}C$ and $^{14}N(p, \alpha)^{11}C$ are dependent on the energy of protons, the amount of ^{11}C produced in each piece is a function of the ^{11}B and ^{14}N content. Whenever the reaction yields are known, both ^{11}B and ^{14}N content are determined individually by solving a pair of simultaneous equations. (2) The content of nitrogen is determined by the use of the $^{14}N(\gamma, n)^{13}N$ reaction. The content of boron is calculated from the amount of ^{11}C formed by one proton bombardment, so far as the excitation function for both reactions are known.

The latter method is preferable, because it would provide better accuracy, and because the determination of the trace of nitrogen is itself important. The determination of nitrogen by the use of a powerful linear accelerator is now being planned.

6. Experimental Process

A silicon plate slightly thicker than that used for the determination of oxygen was bombarded with protons (15 MeV, 10 μA, 5 min.), etched, pulverised, and fused with a mixture of sodium hydroxide (20 g) and sodium nitrate (15 g) containing sodium carbonate (1 g) as the carrier. The fused cake was dissolved in water and sulfuric acid was added until the solution became acid. The carbon dioxide was caught by aqueous ammonia and precipitated as calcium carbonate, which was filtered off, and the radioactivity measured. The yield of the chemical separation was determined after the counting. The separation required about 45 min.; the yield was about 50%. The radiochemical purity of the separated carbonate was satisfactory.

Since the excitation function for the reaction has been measured,(7) the content of boron could be calculated on the assumption that the contribution of nitrogen was negligible (however this assumption is not completely correct).

When silicon containing 5×10^{-3} p.p.m. of boron is irradiated with protons (15 MeV, 10 μA, 5 min.), the activity of ^{11}C in the separated carbonate is about 1×10^3 d.p.m., which is sufficient for an accurate measurement of the nuclide.

Conclusion

A trace quantity of oxygen in transistor-grade silicon was successfully determined by radioactivation analysis utilizing the $^{16}O(\alpha, pn)^{18}F$ reaction. And it was pointed out that for the determination of boron in high-purity silicon by the use of the $^{11}B(p, n)^{11}C$ reaction, nitrogen in the same sample must be determined because of the formation of ^{11}C also by the $^{14}N(p, \alpha)^{11}C$ reaction. Such a radioactivation analysis will surely provide new data that will be very useful for the research and production of transistor-grade silicon and other high-purity materials. Radioactivation analysis using charged particles or photons as the activation source should be further studied for other kinds of trace impurity elements such as carbon and nitrogen, which can be determined neither by the usual chemical methods nor by neutron activation analysis.

Acknowledgement

The authors wish to thank Dr. Akio Kobayashi for his kind encouragement during the course of this work.

---

*1) For a precise determination of a submicroscopic quantity of an impurity element by radioactivation analysis, chemical separation is necessary, unless γ-ray spectroscopy is useful. (In general, γ-ray spectroscopy is a poor tool for a sample activated by charged particles or photons, which usually produce positron emitters.) Hence, a short lived radioisotope —less than 5 minutes—is not useful for the determination of the element. There are only four radioisotopes of light elements (with atomic number less than 10) with a half-life between 5 minutes and 1 year as shown in Table 1.

*2) The first and the second devices measure the annihilation radiation of the positron, while the positron itself is counted by the last. The first gives the highest accuracy for absolute counting, but its counting efficiency is the lowest. The last is indispensable for a very low-level activity, but measurement of the positron is subject to interference by various radiochemical impurities.

*3) By the usual chemical methods, quantitative analysis of 0.1% of oxygen is very difficult. The limit of detection by infrared absorptiometry and by the radioactivation analysis using other reactions are 1 and 0.01 p.p.m. respectively, of oxygen in silicon.

References

(1) Osmond R. H. et al., *Analyt. Chem. Acta.*, **10,** 117, (1954).
(2) Born H. J. et al., *Angew. Chem.*, **21,** 559, (1960).
(3) Beard D. B. et al., *Nucleonics*, **17**, 90, (1959).
(4) Winchester J. W. et al., *J. Geophys. Res.*, **65,** 2533, (1960).
(5) Furukawa M. et al. *J. Phys. Soc. Jap.*, **16,** 129, (1961).
(6) Gill R. A., *A.E.R.E. Report C/R*, 2758, 1958, 50pp. *Analyt. Abstr.* 1959, 2523.
(7) Furukawa M. et al., *J. Phys. Soc. Jap.*, **15,** 2167, (1960).

* * * *

REVIEW OF THE ELECTRICAL COMMUNICATION LABORATORY
VOLUME 9, NUMBERS 7-8, JULY-AUGUST, 1961

U.D.C. 546. 721. 73 : 539. 23 : 539. 1

Observations of Uniaxial Anisotropy in Ferromagnetic Thin Films by Means of Bitter Technique*

Yuzo ODANI and ***Yuzi GOMI***†

Experiments were performed, by means of Bitter technique, on the existence of a uniaxial anisotropy in thin films of Fe, Co, and permalloy; and on its influence on the domain structures. Uniaxial anisotropy, not due to the oblique incidence effect, was observed also in Fe and Co films. In Fe films, uniaxial anisotropy is characterized by the existence of cross-ties; in Co films, by the appearence of zigzag walls; and in permalloy films, by the appearence of slender domains.

I. Introduction

Although ferromagnetic thin films are not fully developed at present, application[1][2] for the memory cores of digital computers is being considered because the switching time is very rapid – namely, a few nanoseconds[3]. The most important and fundamental problems in thin films are the origin of uniaxial anisotropy and its influence on the reversal time[4][5][6][7]. Only problems concerning uniaxial anisotropy are discussed here. At present, these problems are: (1) there may be a different cause of uniaxial anisotropy from that observed in the bulk materials, (2) how the uniaxial anisotropy changes the magnetic domain pattern when the flux is reversed, and (3) why the axis of uniaxial anisotropy varies slightly from point to point in the film plane.

Generally, in thin films, uniaxial anisotropy is induced by evaporation in the presence of a magnetic field[8], and its origin has been proved to be due to (1) short range directional order[9], and (2) angle-of-incidence effects[9]. In thin films, however, there may be a uniaxial anisotropy of still unknown origin. Many experiments have been performed as to its existence, but no definite results have been obtained.

If uniaxial anisotropy of this type exists in thin films, it must also exist in Fe and Co thin films, and it is very interesting to observe the patterns appearing on these thin films. Fuller[10] has experimented on this problem and reported that there was "little anisotropy" in Fe thin films.

Although Fowller et al[11], Fuller[10], and Williams and Sherwood[12] observed the effect of uniaxial anisotropy on the magnetic domain pattern in permalloy films, they did not point out the characteristics appearing when the flux of thin films was reversed. The characteristic is that thin films are always covered with slender domains when whole magnetizations rotate as a single vector quasi-statically and uniformly. This paper reports: (1) in Fe thin films, uniaxial anisotropy does not affect the domain pattern, but the domain walls, and (2) in Co and permalloy thin films, magnetic flux can not rotate quasi-statically in a uniform mode. The experiments were

---

* MS in Japanese received by the Electrical Communication Laboratory, April 25, 1960. Originally published in the *Kenkyû Zituyôka Hôkoku* (*Electrical Communication Laboratory Technical Journal*), N.T.T. Vol. 9. No. 7, pp. 803-815, 1960.

† Magnetic Materials Research Section.

carried out by observing the magnetic domain patterns by means of Bitter technique on miscellaneous specimens made under different conditions.

II. Preparation of Films and Experimental Procedure

The samples used in this investigation were made by evaporating iron, nickel, cobalt, and the alloy of 82 % Ni–18 % Fe on microscope slides. The metal to be evaporated was heated in a helix of tungsten wire.

A pressure of $1\cdot10^{-5}\sim7\times10^{-6}$ mm Hg was maintained during evaporation. Some of the films were deposited on substrates heated to 70°C while others were deposited on substrates heated to 300°C. Some were formed in the presence of a magnetic field of 900 Oe, others in the absence of field. In the next section, the direction along which the magnetic field was applied during evaporation is designated "preferred direction". To prevent oxidization of the samples, they were removed from the vacuum chamber only after they had cooled below 50°C. The field of the earth was compensated by using a Helmholtz coil and the interfering field from the filament current was decreased to about 0.1 Oe by making the loops of the heater circuit as small as possible. The thickness of the films was measured by means of multiple beam interferometry. The errors were within 20 A.

The surface of the substrates was cleaned by the following procedures: First they were cleaned with NaOH, $K_2Cr_2O_7$, and Nitric acid in succession; then dried in successive rinses of distilled water, alcohol, and acetone; and finally heated to 300°C in vacuum and subject to ion bombardment.

The distance between the substrates and filaments was about 30 cm, and a shutter was placed in front of the substrates. The thickness of the films was controlled by varying the length of time the shutter was open. Evaporation speed was about 50 A/sec.

To eliminate the shape effect and to make the conditions similar to those for applications, the samples were formed in 7×16 arrays of circular films about 2.0∼3.0 mm diameter by using an alminium mask. From these spots, two were selected through the observation on the magnetic domains after the ac demagnetization: one, formed by normal incidence; and the other, formed by oblique incidence. On these two spots the following experiments were performed. First, the spots were saturated by applying a magnetic field along a certain direction; then this field was decreased to zero and increased in the reverse direction to the strength which caused the reversed domain to form, and these domains were observed by the Bitter technique. Next, similar experiments were carried out by applying an external field along directions different from that in the above. A uniaxial anisotropy was determined by the changes in the reversed domains and walls according to the directions of the applied magnetic field.

III. Results Obtained

Iron Films

In the iron films (30 A∼1200 A thick) formed on the substrates heated to 70°C in the absence of a magnetic field, the reversing behaviors coincide with those on Fuller's film[10] which was formed on substrates heated to 300°C in a magnetic field of 120 Oe. Results obtained are as follows: (1) reversed domains always point parallel to the direction of the switching field, (2) magnetic walls are 180° Bloch type, (3) the coercive forces are the same in all directions. Therefore, from the standpoint of the domain patterns, uniaxial anisotropy did not seem to exist on these films. Similarly, on the films which were formed on substrates heated to 300°C in the absence of a magnetic field, the reversing behaviors were the same as those in the former case, except that in the latter case the coercive forces were smaller than those in the former by a factor of three and the walls became the cross-tie type. The cross-tie wall was not observed in Fe thin films by Fuller.[10] From these results, it must be concluded that a uniaxial anisotropy does not exist on the films which are formed in the

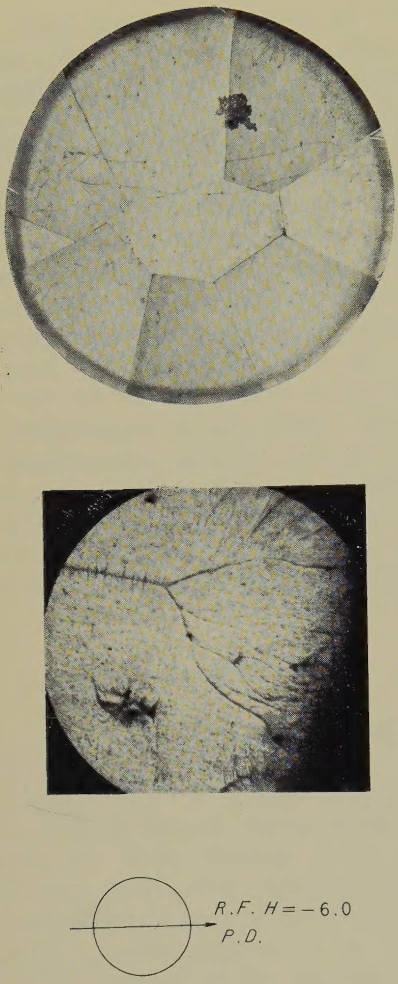

Fig. 1 (a)

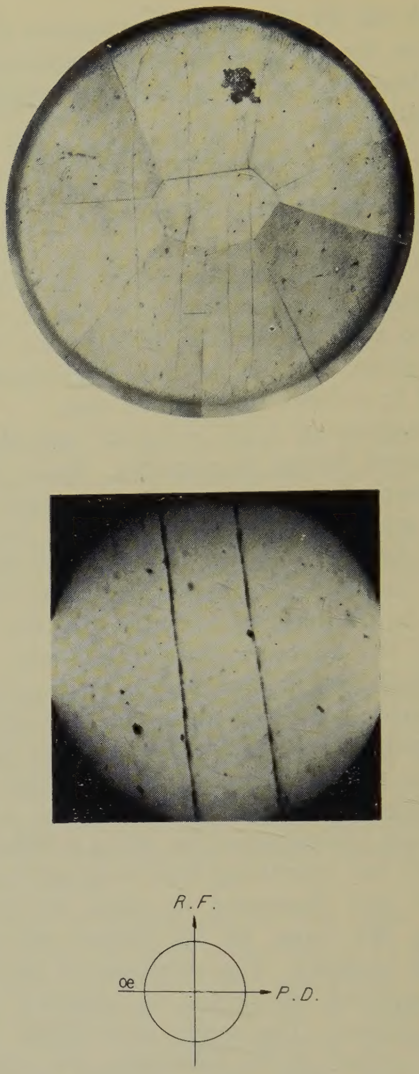

Fig. 1 (b)

Fig. 1—Reversed domains and walls in 510A thick Fe film, evaporated on a 300°C substrate in a magnetic field of 500 Oe. Spot diameter is 2 mm. Figs. 1 (a), (b), and (c) correspond to the cases in which the reversing field of 6 Oe is applied parallel, perpendicular, and at an angle of 60° to the preferred direction, respectively.

absence of a magnetic field by the metal beams which collide with substrates at the normal angle, even if either the thickness of the films or substrate temperature is changed.

On the films formed in the presence of a magnetic field, new phenomena were observed, as illustrated by the following composite photographs. Figs. 1 (a), (b), and (c) show the reversed domains on 510A thick film which was formed on a substrate heated to 300°C in the presence of a magnetic field, and they correspond to the cases obtained by applying a field of 6 Oe parallel, perpendicular, and at a 60° angle, respectively, to the direction in which the magnetic field was

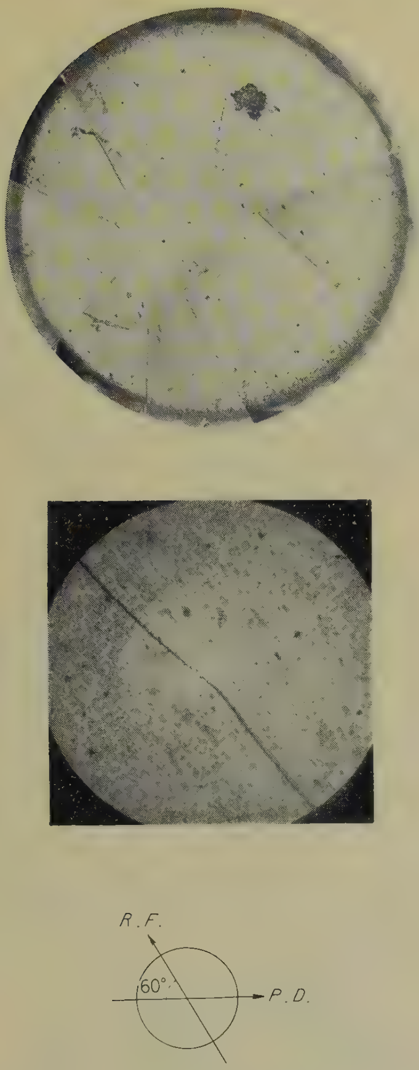

Fig. 1 (c)

applied during evaporation. To clarify the preferred direction of the spot, a mark was made on the cover glass, and this is the black part on the photograph and had no effect on the magnetic film. In all cases, the magnetic walls pointed parallel to the direction of the reversing field, and it is remarkable that the closure domains were found only at the edges of the spot along the reversing field. Therefore, the magnetizations of the spot pointed along the reversing field. However, in Fig. 1 (a) are observed many creases running perpendicularly to the direction of the applied field, and also cross-ties on the magnetic wall. In Fig. 1 (b), there are no cross-ties and creases, and in Fig. 1 (c), few cross-ties and creases. Cross-ties and creases did not appear when the reversing field was applied at an angle greater than 60° to the "preferred direction". The coercive forces were 6.5 Oe, 6.1 Oe, and 6.3 Oe, respectively. The fact shows obviously that a uniaxial anisotropy was induced in iron films which were evaporated in the presence of a magnetic field, and its magnitude was about $3 \cdot 10^3$ erg/cc, which was determined by the measured value of the anisotropy field. It seems due to this uniaxial anisotropy that the walls running parallel to the preferred direction have cross-ties, and those running perpendicular do not. It is concluded that in Fe films weak uniaxial anisotropy is induced by the field deposition, and this weak anisotropy affects neither wall movement nor wall directions, but it affects wall structures. This phenomenon can be explained by a mechanism similar to the buckling model of fine particles or as "inverted films".

Cobalt Films

In Co films, the uniaxial anisotropy resembles that of permalloy films rather than that of iron films. First, the results will be explained for films evaporated at normal incidence, and then for those at oblique incidence.

The experiments were carried out on films which were formed under the following four conditions. The combinations are: substrate temperature of 70°C and 300°C, and magnetic field present and absent during evaporation. On the films formed in the absence of a magnetic field, reversing behavior was the same as that in the iron films. On the films formed on a heated substrate, sometimes cross-tie walls appeared. Next, the case in which the films were evaporated in the presence of a magnetic field, for example, films formed in a field of 500 Oe on a substrate heated to 300°C will be explained. Fig. 2 (a) shows the reversed domains which appeared with a reversing field of about 20 Oe along the preferred direction. When the reversing field is increased to 30 Oe, reversed domains become larger along the direction of the reversing field, as shown in Fig. 2 (b). When the reversing field was applied along the perpendicular to the preferred direction, magnetic patterns were considerably different.

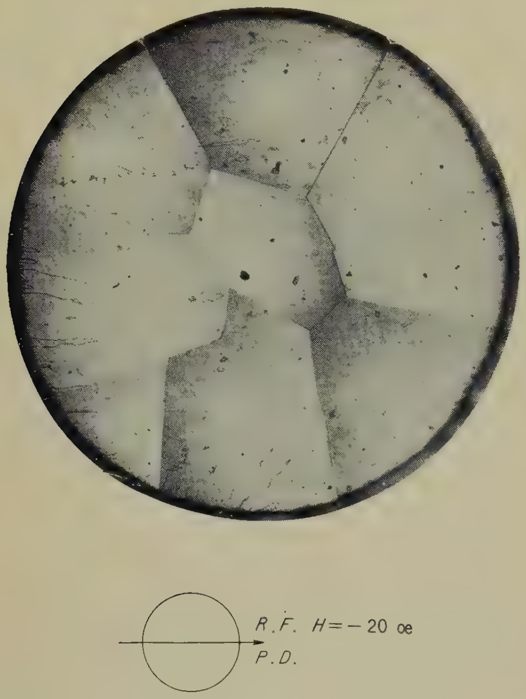

Fig. 2 (**a**)

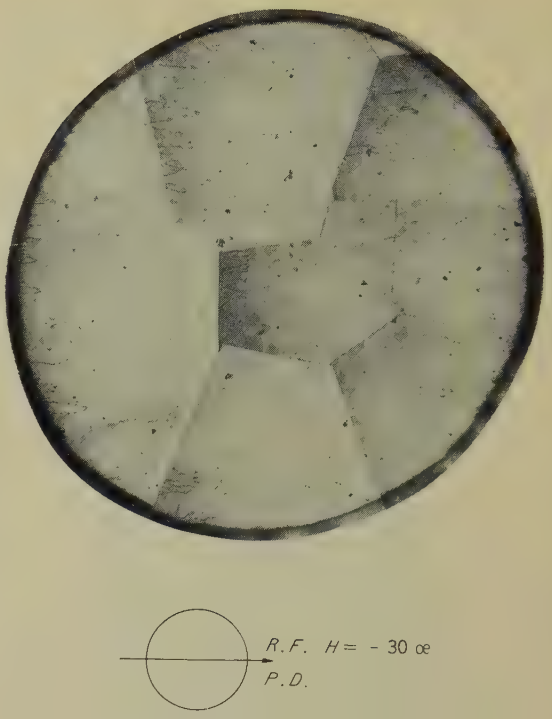

Fig. 2 (**b**)

Fig. 2—Reversed domains on 550 A thick Co film, evaporated on 75°C substrate in a magnetic field of 500 Oe. Spot diameter is 3 mm. In (a) and (b), reversing field is applied parallel to the preferred direction. The strengths are 20 Oe and 30 Oe, respectively. In (c) and (d), reversing field is applied perpendicular to the preferred direction. The strengths are 35 Oe and 40 Oe. In (e), zigzag wall magnified from a part of Fig. 2 (c) is shown. In (f), slender domain magnified from a part of Fig. 2 (d) is shown.

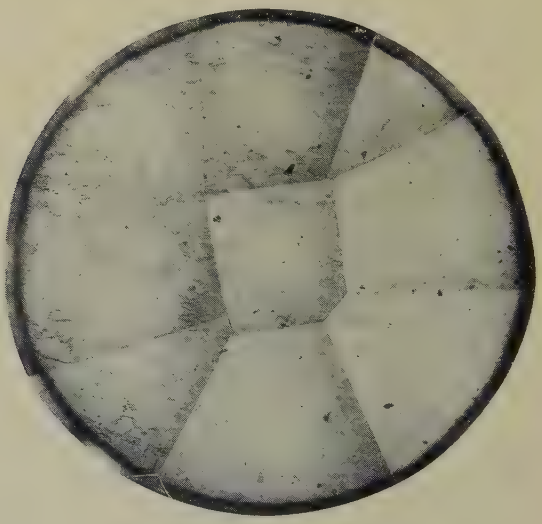

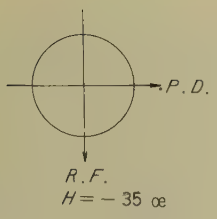

Fig. 2 (c)

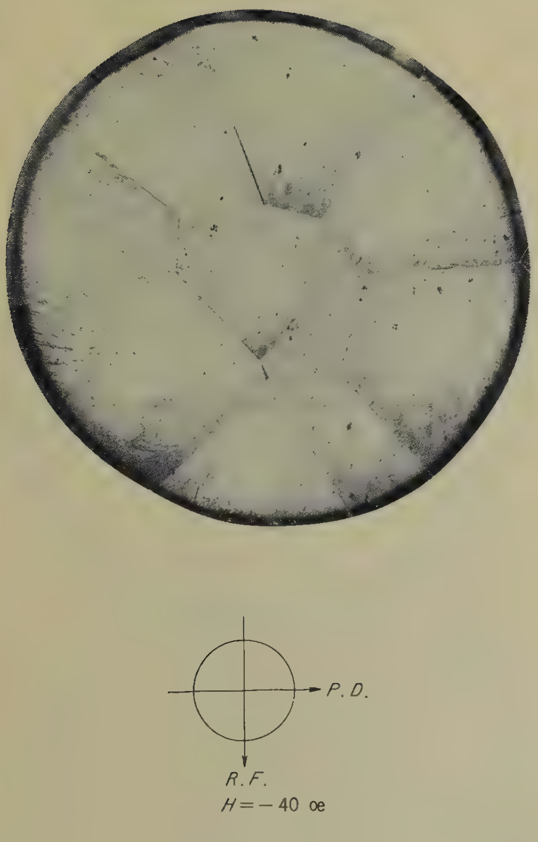

Fig. 2 (d)

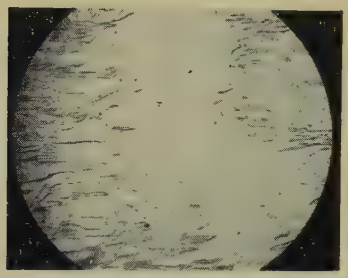

Fig. 2 (e)

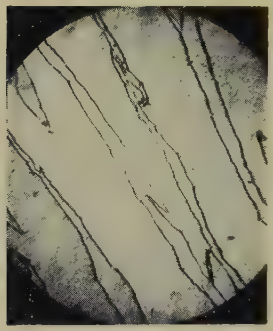

Fig. 2 (f)

Fig. 2 (c) shows the case in which the reversing field is about 35 Oe, perpendicular to the preferred direction. In this case, the domains were separated into white and black ones by the zigzag walls which are magnified in Fig. 2 (e), and the magnetizations pointed along the preferred direction rather than along the reversing field. When the field was increased to 40 Oe, slender domains appeared abruptly in white domains. This state is shown in Fig. 2 (d), and the magnified part in Fig. 2 (f). This reversal mechanism is explained by the rotation of the magnetizations and the growth of slender domains, as shown in Fig. 3. It is due to the variations of uniaxial anisotropy axis in the film plane that the rotations of the magnetizations are divided into a clockwise sense and a counter clockwise sense in Fig. 3 (b). It is not clear why in Fig. 3 (d) the slender domains appear in the white domains.

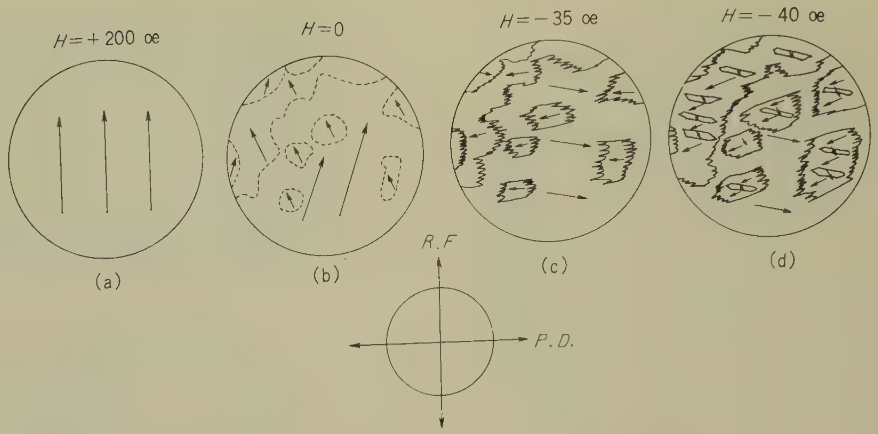

Fig. 3—Magnetization reversal model for Co thin films.

Uniaxial anisotropy induced by the oblique incidence shows a reversing behavior different from that induced by the magnetic field. Fig. 4 (a) shows the pattern which was obtained on the 300 A film formed without a magnetic field on a 300°C substrate by metal beams colliding with the substrate at an oblique incidence. The reversing field was applied along the direction of the uniaxial anisotropy. In this case, until the strength of the reversing field nearly reached the coercive force, reversed domains did not appear. As soon as the field strength reached the coercive force (about 30 Oe), small domains appeared abruptly. With the increase of field strength, the small domains became larger and the unreversed domains became darker. At this stage, when the sense of the magnetic field was reversed, the contrast of the domains was reversed. When the reversing field was applied nearly perpendicular to the direction of the uniaxial anisotropy, new domains appeared after the reversing field reached about 40 Oe, as shown in Fig. 4 (b). The new domains, however, were longer in the direction of the uniaxial anisotropy, which indicates that the direction of the small domains is the same as that of the uniaxial anisotropy. When the strength of the field was 50 Oe, the dark domains almost disappeared, as shown in Fig. 4 (c). This reversing model is nearly the same as that in

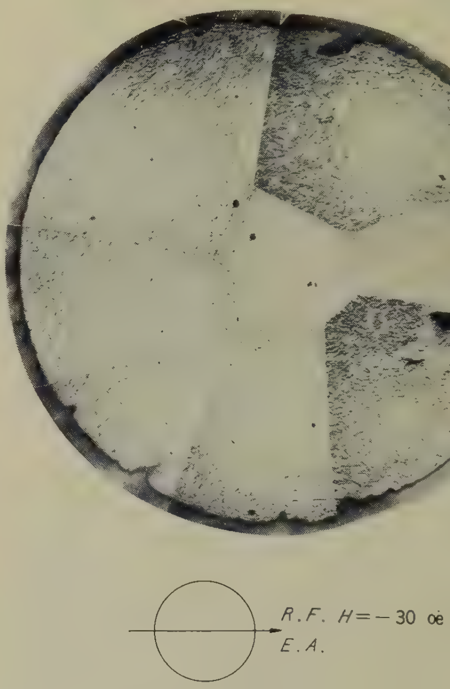

Fig. 4 (**a**)

Fig. 4—Domain patterns on a 300 A Co thin film having uniaxial anisotropy due to angle-of-incidence effect. Spot diameter is 2mm. In (a), a reversing field of 30 Oe is applied along the easy axis. In (b) and (c), a reversing field is applied perpendicular to the easy axis. The field strengths are 40 Oe and 50 Oe, respectively.

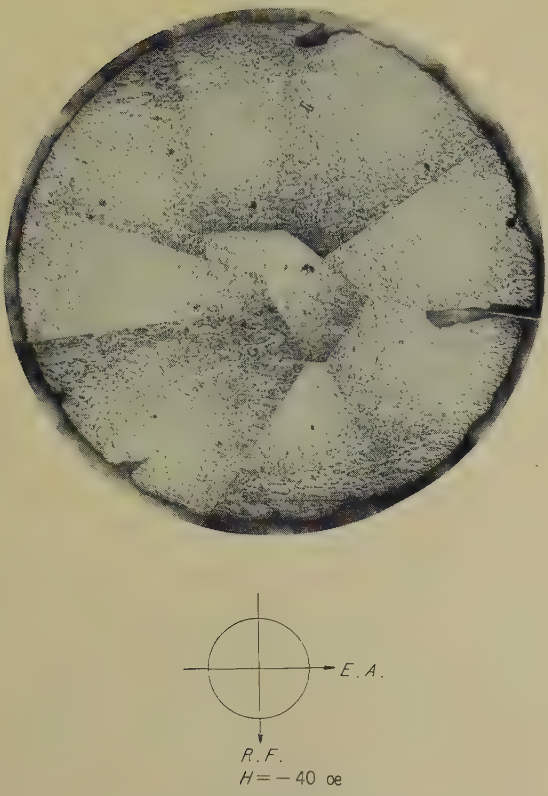

Fig. 4 (b)

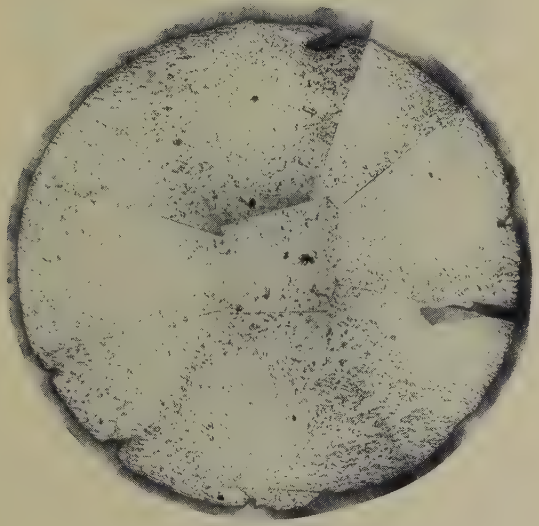

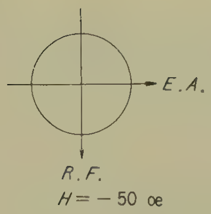

Fig. 4 (c)

Fig. 6, except for the closure domains.

On nickel thin films, the authors could not make out any uniaxial anisotropy, as they could not clearly observe the domain patterns under any evaporating conditions.

Permalloy Films

Fuller[10) reported that the magnetizations could rotate uniformly as a single vector in permalloy thin films. The authors' experiment, however, showed that the magnetizations rotate uniformly to about 120°, but over 120° they cannot rotate in the uniform mode. The same phenomenon was observed in all permalloy films which were evaporated in the presence of a magnetic field. The results will be explained in detail.

Fig. 5 (a) shows the reversed domains on a 540 A film, which appeared when a reversing field of 3.0 Oe was applied along the preferred direction. The film was evaporated on a substrate heated to 70°C in the presence of a magnetic field of 900 Oe. The walls pointed parallel to the preferred direction. With increase of the field strength, the reversing domains grew with the domain walls moving to the perpendicular direction (Fig. 5 (b)).

When the reversing field was applied along the hard direction, many needle domains appeared. This phenomenon will be explained in the near future.

Let us observe the case in which the reversing field is applied along a direction inclined by 5° from the hard direction. After the magnetic field, large enough to saturate the film in that direction, is applied, its strength is gradually decreased. In accordance

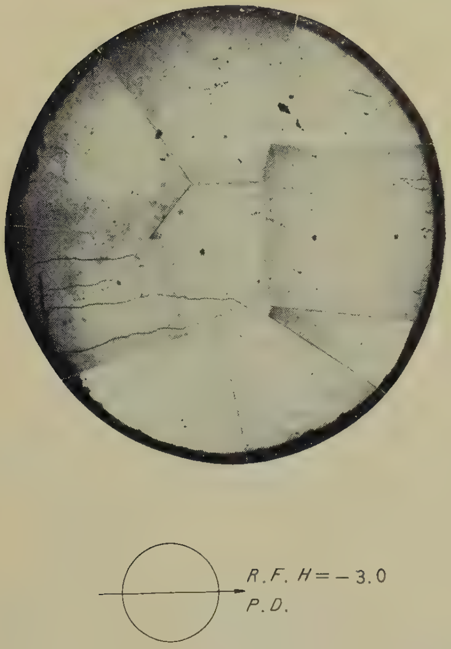

Fig. 5 (a)

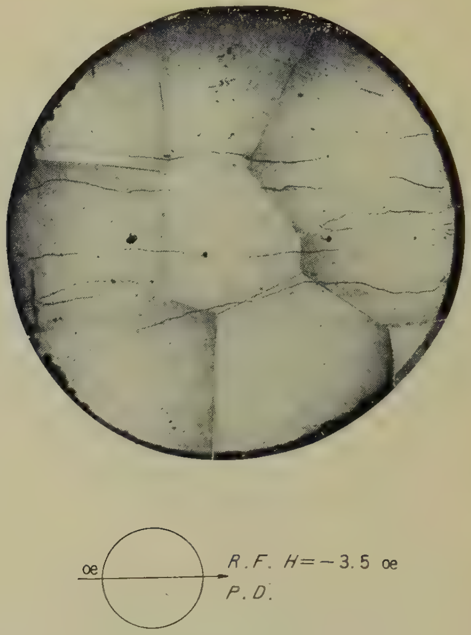

Fig. 5 (b)

Fig. 5—Reversed domains in 540 A permalloy thin film (substrate −75°C; field strength during deposition −900 Oe; diameter −2 mm.) In (a) and (b), reversing field is applied along the preferred direction. Field strengths are 3 Oe and 3.5 Oe. In (c) and (d), reversing field is applied 5° inclined from the hard axis. Field strengths are +6.5 Oe and −6.5 Oe. In (e) the closure domains in (c) are shown. In (f), the slender domains of (d) are shown.

with the decrease of field strength, the magnetization rotates uniformly from the hard direction to the easy direction. When the magnetization rotates about 45° toward the easy axis, closure domains appear at the edge of the spot in both the second and fourth quadrants. Fig. 5 (c) shows the closure domain when the field strength is 6 Oe. When the field strength is decreased further and increased in the reverse direction to about 6 Oe, the dimensions of the closure domains do not change. As soon as the field reaches

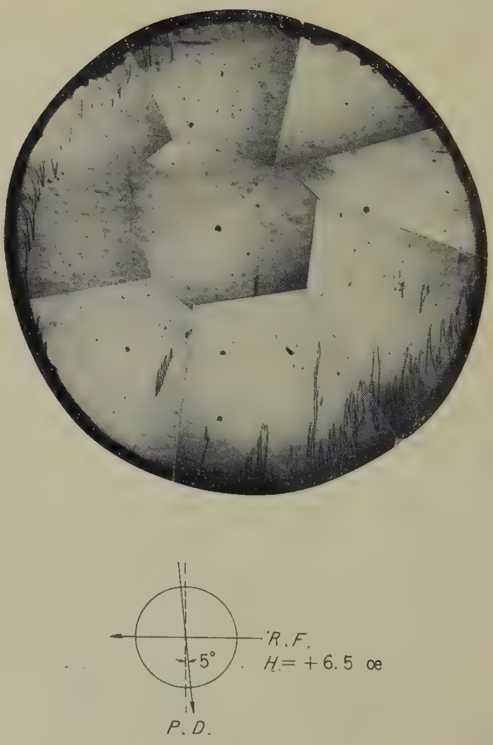

Fig. 5 (c)

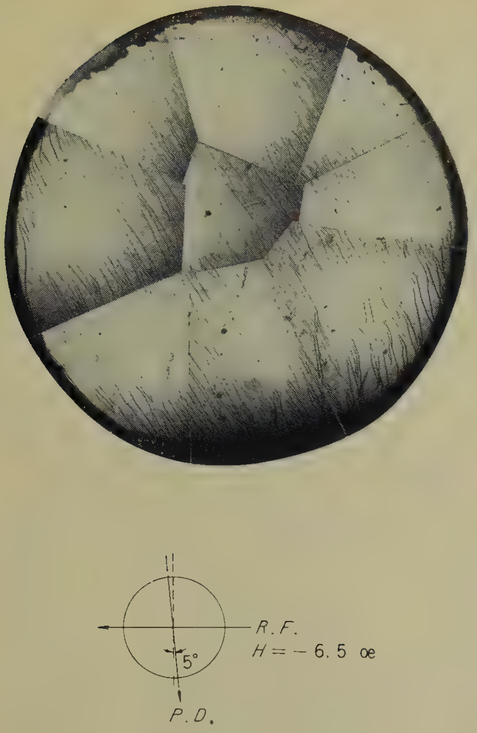

Fig. 5 (d)

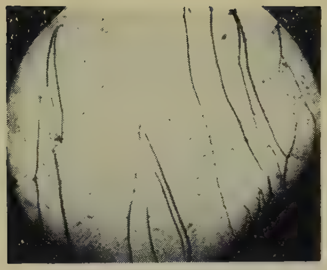

Fig. 5 (e)

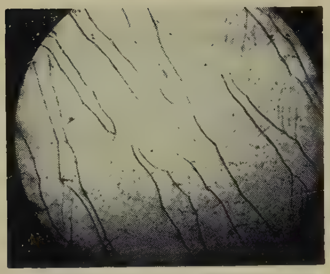

Fig. 5 (f)

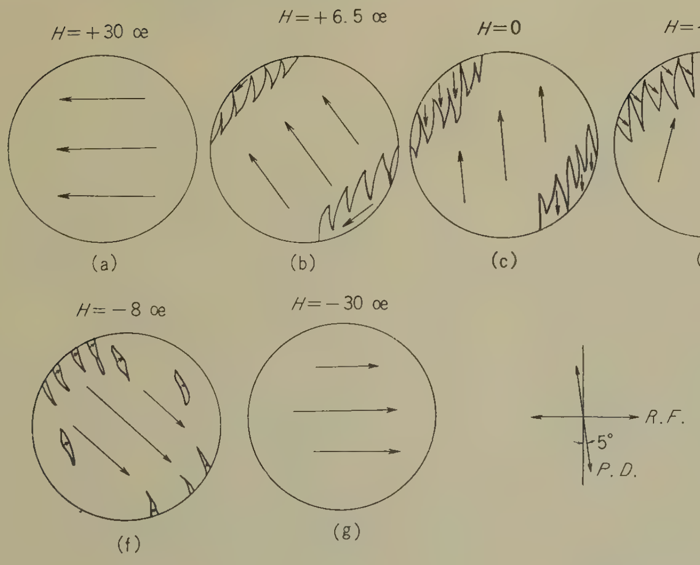

Fig. 6—Reversal model in permalloy thin film having an uniaxial anisotropy.

about 6.5 Oe, many slender domains inclined about 30 degrees from the preferred direction suddenly appear all over the surface (Fig. 6 (d)). When the reversing field is more than 7 Oe, the slender domains disappear. The walls of these slender domains do not have cross-ties, as shown in Fig. 5 (f). This reversal model is shown schematically in Fig. 6. In Fig. 6 (d), the energy of the magnetization which points to the first quadrant is larger than that pointing to the fourth quadrant. And so the magnetizations of the closure domains have lower energy than those of the other parts. Roughly speaking, the coercive force is proportional to the wall energy and the wall energy is proportional to the cos ϕ (where 2ϕ is the angle between the magnetizations of the two domains separated by the wall) and the energy difference between the two domains multiplied by the field applied along the wall; that is, proportional to $HM \cos\phi$. Therefore the coercive force is thought to be independent of the angle between the directions of the two domains. If the field is applied along a direction inclined by the angle φ from the direction of the wall, the force acting on the wall is proportional to $\cos\varphi$. Therefore, until the reversing field is increased to $Hc/\cos\varphi$, the walls can not extend or move, making the angle φ with the applied field. In Fig. 5, this value is about 6 Oe ($Hc = 3.5$ Oe, $\varphi = 60°$). Therefore, until the reversed field reaches 6 Oe, the magnetization of the main parts rotates in the first quadrant, with higher energy than closure domains. As soon as the field reaches 6 Oe, the walls of the closure domains can move, and the closure domains grow over the whole surface as shown in Fig. 5 (d) and Fig. 6 (e), because the closure domains have lower energy. These slender domains grow still further with increasing field, and finally cover the whole surface (Fig. 6 (f)). And then the magnetization rotates in the fourth quadrant to the direction of the applied field.

The authors have observed similar phenomenon on films which were formed on a substrate heated to 300°C in a magnetic field of 900 Oe. Fig. 7 (a) and (b) correspond to Fig. 5 (c) and (d) respectively. The strengths of the field were 1.5 Oe and 3.0 Oe. The phenomenon can be explained by the same mechanism as above.

From the above experiment, it was found that in permalloy films definite uniaxial anisotropy can be induced by evaporation in a magnetic field independent of the temperature of the substrate, and the magnetization can not uniformly rotate quasi-statically.

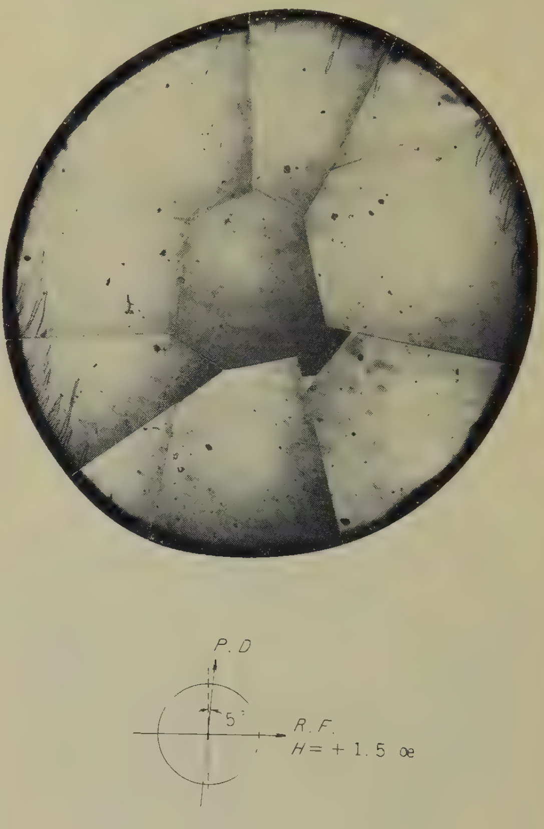

Fig. 7 (a)

Fig. 7—Reversal pattern in 400 A permalloy thin film formed on a 300°C substrate in a magnetic field of 500 Oe. The diameter is 3 mm. In (a) and (b), the field is applied 5° inclined from the hard axis. Field strengths are 1.5 Oe and 3.0 Oe.

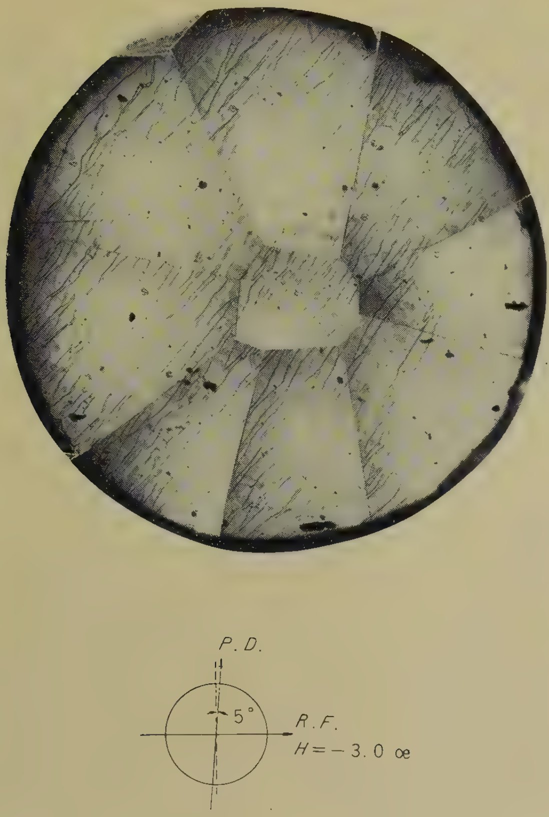

Fig. 7 (b)

4. Conclusions

By observing the domain patterns, it was found that a uniaxial anisotropy is induced also in pure metal films such as Fe and Co by evaporation in a magnetic field. When Fe films have uniaxial anisotropy the walls pointing along the direction of the uniaxial have cross-ties, while the walls perpendicular to it do not have these cross-ties. This phenomenon is interpreted to mean that the wall coercive force is much smaller than the anisotropy field. In Co thin films, the uniaxial anisotropy resembles that of permalloy films. And the oblique incidence effect causes the clear uniaxial anisotropy also in pure metal films, and the domain pattern is very different from usual one.

In permalloy films, uniaxial anisotropy was clearly shown by the domain pattern. It was found that in permalloy films the magnetization could not rotate quasi-statically in the uniform mode from the hard axis to its opposite direction. The reversal mechanism is as follows: first the rotation of a magnetization, then a wall displacement, and finally the rotation of a magnetization.

Acknowledgment

The authors wish to express their hearty gratitude to Mr. T. Sato for his kind assistance in making the magnetic colloids. They also would like to make a grateful acknowledgment to Mr. Y. Schichijo and Mr. M. Sugihara for their helpful advice.

References

(1) J. I. Raffel: Operating Characteristics of a Thin Film Memory, *J. Appl. Phys.*, Suppl to **30**, No. 4, p. 60S, 1959.
(2) E. E. Bittmann: Using Thin Films in High-Speed Memories, *Electronics*, **32**, No. 23, p. 55, 1959.
(3) D. O. Smith: Static and Dynamic Behavier of Thin Permalloy Films, *J. Appl. Phys.*, **29**, No. 3, p. 264, 1958.
(4) C. D. Olson, and A. V. Pohm: Flux Reversal in Thin Films of 82% Ni, 18% Fe, *J. Appl. Phys.*, **29**, No. 3, p. 275, 1958.
(5) R. L. Conger, F. C. Essig: Magnetization Reversal in Thin Films at Low Fields, *J. Appl. Phys.*, **29**, No. 3, p. 855, 1957.
(6) R. L. Conger, F. C. Essig: Resonance and Reversal Phenomena in Ferromagnetic Films, *Phys. Rev.*, **104**, No. 4, p. 915, 1956.
(7) A. L. Hanzel, R. L. Conger: Isolation of Rotational Reversal in Ferromagnetic Films, *J. Appl. Phys.*, **30**, No. 12, p. 1932, 1959.
(8) M. S. Blois, Jr.: Preparation of Thin Magnetic Films and Their Properties, *J. Appl, Phys.*, **26**, No. 8, p. 975, 1955.
(9) D. O. Smith: Anisotropy in Permalloy Films, *J. Appl. Phys.*, Suppl. to **30**, No. 4, p. 264S, 1959.
(10) C. E. Fuller: Domain Patterns and Reversals by Wall Movements of Thin Films of Iron and Nickel-Iron, *J. Phys. et Radium*, **20**, No.

2–3, p. 310, 1959.
(11) C. A. Fowler Jr, E. M. Fryer and J. R. Stevens: Magnetic Domains in Evaporated Thin Films of Nickel-Iron, *Phys. Rev.*, **104,** No. 3, p. 645, 1956.
(12) H. J. Williams and R. C. Sherwood: Magnetic Domain Patterns on Thin Films, *J. Appl. Phys.*, **28,** No. 5, p. 548, 1957.

* * * *

U.D.C. 621. 372. 832. 6. 029. 65

A 48 Gc Center-Excited Type Channel Branching Filter for Circular Electric Waves*

Shin-ichi IIGUCHI,† *Bun-ichi OGUCHI*, and *Kazuo YAMAGUCHI*

A novel center-excited type branching filter has been devised, and its characteristics in the 48 Gc band have been investigated both theoretically and experimentally. This branching filter delivers the circular TE_{01} *wave of each channel from the main circular waveguide to its respective small rectangular guide in a frequency division multi-channel millimeter wave communication system. This filter consists of center-excited type hybrid and frequency rejection filters. The transfer loss of the hybrid is 0.8~1.0 dB over a 2 Gc band at 48 Gc. Two types of rejection filter are considered; a center-excited type rejection filter, and a modified Marcatili-type rejection filter. The three stage characteristics of the former type and the two stage characteristics of the latter type are examined.*

1. Introduction and Principle

It is well known that the circular TE_{01} wave should be used in millimeter wave waveguide transmission for multi-channel communication, for which branching filters are indispensable. There are two methods of securing branching. One method is separation of the channels by branching filters in a rectangular waveguide after the circular TE_{01} wave is transformed to a rectangular TE_{10} wave via a mode transducer; the other is picking out the circular TE_{01} wave of each channel directly from the main circular waveguide and feeding it to the respective rectangular guide. The latter is more desirable if a good branching filter is available.

The center-excited type branching filter may be used in this application. Fig. 1 shows a schematic diagram of this branching filter consisting of a hybrid and two rejection filters. The hybrid is composed of two semicircular waveguide which are separated a metal wedge and have a rectangular guide between them. The two semicircular guides are coupled to the rectangular guide by an array of longitudinal elliptic slots which are located on the common wall separating the narrow sides of the rectangular guide and the bottoms of the semicircular guides, along the center axes of the semicircular guides.

In the semicircular waveguide the only modes which have an axial magnetic field component along the axis are the TE_{0n} modes. Therefore, if the radius of the guide is selected so that the TE_{02} mode is beyond cutoff, the only mode excited by an axial magnetic dipole on the axis in the semicircular waveguide is the TE_{01} mode. The TE_{01} wave incident from the left in Fig. 1 is devided into two semicircular TE_{01} waves without any reflection or disturbance. The two axial magnetic fields of the semicircular TE_{01} waves along the center axes of the two semicircular guides have the same direction, while the

---

* MS in Japanese received by the Electrical Communication Laboratory, Apr. 5, 1960. Originally published in the *Kenkyû Zituyôka Hôkoku* (*Electrical Communication Laboratory Technical Journal*), N.T.T., Vol. 9, No. 5, pp. 565-570, 1960.

† Hyper-frequency Research Section.

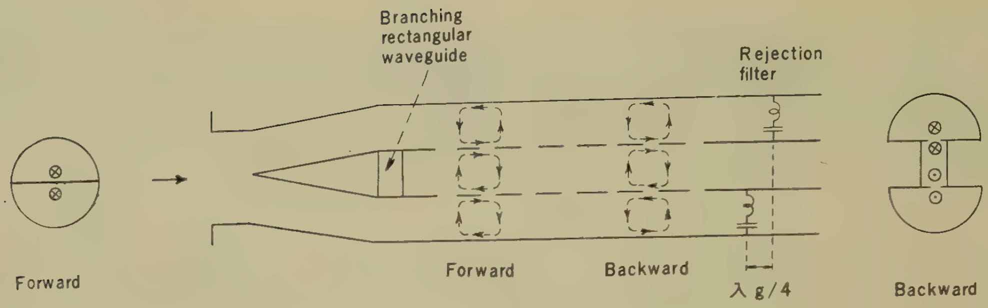

Fig. 1—Schematic diagram of the center-excited type branching filter.

two axial magnetic fields of the rectangular TE$_{10}$ wave along the upper and lower sides of rectangular guide have the opposite direction. Therefore, there is no coupling between the two semicircular TE$_{01}$ modes and the rectangular mode. If the phase of one of the semicircular TE$_{01}$ waves is reversed, the axial magnetic fields of these two semicircular TE$_{01}$ waves excite a TE$_{10}$ wave in the rectangular guide. Therefore, the reflected waves from the two rejection filters located one quarter of a wavelength from each other transfer power into the rectangular guide. In this case, if the modified phase constants, which take the effect of the array of slots into account, of the semicircular guides and rectangular guide are the same and the number of slots are selected properly, it is possible to transfer all of the power reflected from the rejection filters in the semicircular guides into the rectangular guide.

2. Design of the Hybrid

At first several formulas necessary for design will be described. The reflection coefficient and coupling coefficient of one slot, generated by the axial magnetic field on the common guide wall of two waveguides of arbitrarily shaped cross-sections as shown in Fig. 2, are given in the form of the following equations.

The reflection coefficient of one slot in the primary waveguide may be derived from Bethe's theory, and is

$$C_{11}=\frac{\pi}{2\eta\lambda}M_z\ H_{z1}\ H_{z1}. \qquad (1)$$

The reflection coefficient of one slot in the secondary waveguide is

$$C_{22}=\frac{\pi}{2\eta\lambda}M_z\ H_{z2}\ H_{z2}. \qquad (2)$$

The coupling coefficient of one slot between the primary and secondary guides is

$$C_{12}=\frac{\pi}{2\eta\lambda}M_z\ H_{z1}\ H_{z2}, \qquad (3)$$

provided that the thickness of the common wall is assumed to be zero.

In the above equations:

η=intrinsic admittance of free space
λ=wavelength in free space
M_z=main palarization of slot

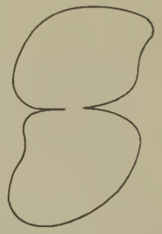

Fig. 2—Coupling of two waveguides of arbitrarily shaped cross-section.

H_{z1}=axial magnetic field at the position of the coupling slot in the primary guide in which unit power is transmitted

H_{z2}=axial magnetic field at the position of the coupling slot in the secondary guide in which unit power is transmitted

Unit power is defined as $\frac{1}{2} R_e \int\int \boldsymbol{Z} \cdot \boldsymbol{E}_t \times \boldsymbol{H}_t^* \, ds = 1$, where $\boldsymbol{E}_t$ and $\boldsymbol{H}_t$ are the transverse electric and magnetic fields in the waveguide. These equations may be used for the design of the center-excited type hybrid.

In the course of applying Eqs. (1), (2), and (3) to the hybrid circuit of Fig. 3, we may divide the rectangular waveguide into two equal guides by the use of a metal plate of zero thickness as shown in Fig. 4, without causing any disturbance to the field configuration in the waveguides. Therefore, it is sufficient to consider the condition of total energy transfer between a half-width rectangular and a semicircular waveguide as shown in Fig. 5.

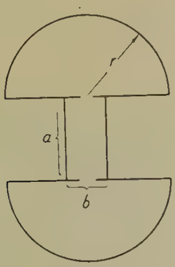

Fig. 3—The cross-section of center-excited type hybrid.

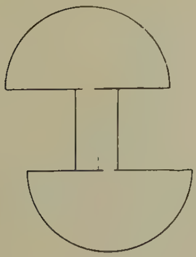

Fig. 4—Equivalent circuit of Fig. 3.

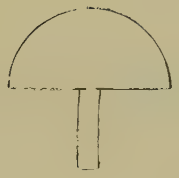

Fig. 5—Half-divided circuit of Fig. 4.

Using Eq. (1), the reflection coefficient of one slot in the half-width rectangular guide is given by

$$C_{11} \simeq C^{\square} = \frac{\pi \lambda_g^{\square}}{a^3 b} M_z, \tag{4}$$

because only the axial magnetic field exists at the center of the slot if there is no slot on the side wall.

Using Eq. (2), the reflection coefficient of one slot in the semicircular guide is given by

$$C_{22} = C^{⌓} = \frac{\chi^2 \lambda_g^{\bigcirc}}{2\pi^2 r^4} \frac{M^z}{[J_0(\chi)]^2} = 4.585 \frac{\lambda_g^{\bigcirc}}{r^4} M_z, \tag{5}$$

if the TE_{01} mode only is transmitted in the guide.

In the above-mentioned equations, $\chi = 3.832$, the first non-zero root of $J_0'(\chi) = 0$.
M_z is main polarization of an elliptic slot, and is approximately given by

$$M_z = \frac{\pi}{3} \frac{l^3}{l_n \frac{4l}{w} - 1} = \frac{(1.047)\, l^3}{(2.303) \log_{10} \frac{4l}{w} - 1}, \tag{6}$$

where $2l$ and $2w$ are the lengths of the major and minor axes, respectively, of the slot. The coupling coefficient between the half-width rectangular and the semicircular waveguide via one slot in a wall of zero thickness is given by

$$C_{12} = \sqrt{C^{\square} C^{⌓}} = 3.795 \frac{\sqrt{\lambda_g^{\square} \lambda_g^{\bigcirc}}}{\sqrt{a^3 b}\; r^2} M_z, \tag{7}$$

An additional insertion loss due to the wall thickness t is

$$\alpha=27.28\sqrt{1-\left(\frac{4l}{\lambda}\right)^2}\ \left(\frac{t}{2l}\right)\ \text{dB}.$$

Thus the coupling coefficient S_{12} containing insertion loss due to the wall thickness is given by

$$S_{12}=C_{12}\cdot\delta, \tag{8}$$

where $20\log_{10}\delta=-\alpha$.

The perturbed phase constants[1)2)] of the half-height rectangular guide and the semi-circular guide are

$$\beta_p{}^{\square}=\beta^{\square}+\frac{C^{\square}}{d},\qquad \beta_p{}^{\circ}=\beta^{\circ}+\frac{C^{\text{⌓}}}{d}.$$

To obtain total energy transfer, it is necessary to satisfy the condition $\beta_p{}^{\square}=\beta_p{}^{\circ}$, from which we get

$$C^{\square}-C^{\text{⌓}}=(\beta^{\circ}-\beta^{\square})\,d. \tag{9}$$

The dimensions of this hybrid with the exception of the number of slots, can be deduced from Eqs. (4)~(9) mentioned above.

To obtain the condition of total energy transfer through an array of n slots of equal size, it is necessary to satisfy the condition

$$n\sin^{-1}S_{12}=\pi/2$$

from which

$$n\,S_{12}\fallingdotseq\pi/2, \tag{10}$$

because the magnitude of S_{12} is small.

Next an example of the design procedure will be described. At first the radius r of the circular guide and the small dimension b of the rectangular guide are determined.

The large dimension a of the rectangular guide and polarization M_z of the slot may be determined after several trial numerical calculations utilizing the experimental data.

Then, the spacing d and number of coupling slots n can be obtained through the following program:

$$\begin{tikzcd}[row sep=tiny] & & d & \\ {} \arrow[r] & C^{\text{⌓}},\,C^{\square} \arrow[ur] \arrow[dr] & & \\ & & C_{12} \arrow[r] & S_{12} \arrow[r] & n. \end{tikzcd}$$

The design values of the dimensions of an experimental model of the hybrid, which has been fabricated by electroforming, will be described. For the first 48 Gc-band model of this hybrid, we used circular waveguide of 13 mm diameter. The small dimension of the rectangular guide used was 2.39 mm; which is identical to the small dimension of the standard rectangular waveguide used in the 50 Gc band.

Then, it is determined that $2r=13.0$ mm, $b=2.39$ mm, $a=5.0$ mm, $2l=2.5$ mm, and $2w=0.8$ mm. By using Eqs. (4)~(10), of the design program, it is found that $d=2.91$ mm and $n=38.8$ when $t=0.4$ mm.

The value of $n=33$ was selected because many experimental results show that a number of slots of about 85 % of the calculated value is suitable for this type of coupler.

3. Measured Results of the Hybrid

3.1. Measurement of Transfer Loss of $\mathrm{TE}_{10}{}^{\square}\rightleftarrows\mathrm{TE}_{10}{}^{\circ}$

Transfer loss between the rectangular TE_{10} and circular TE_{01} modes of the hybrid may be measured in a network of the form of TE_{01} mode transducer. This transducer is formed by short circuiting two semicircular waveguides at one end of the hybrid. The short-circuited positions are one-quarter guide wavelength from each other.

We used Deschamp's method[3)] by which four elements ot the S-matrix of the four terminal network can be obtained.

During the course of the measurements, the network is assumed to be a four-terminal network, even if an unused mode is generated at the transducer, since a TE_{01} mode filter is employed at the output terminal in the circular waveguide in front of the short-circuiting plunger.

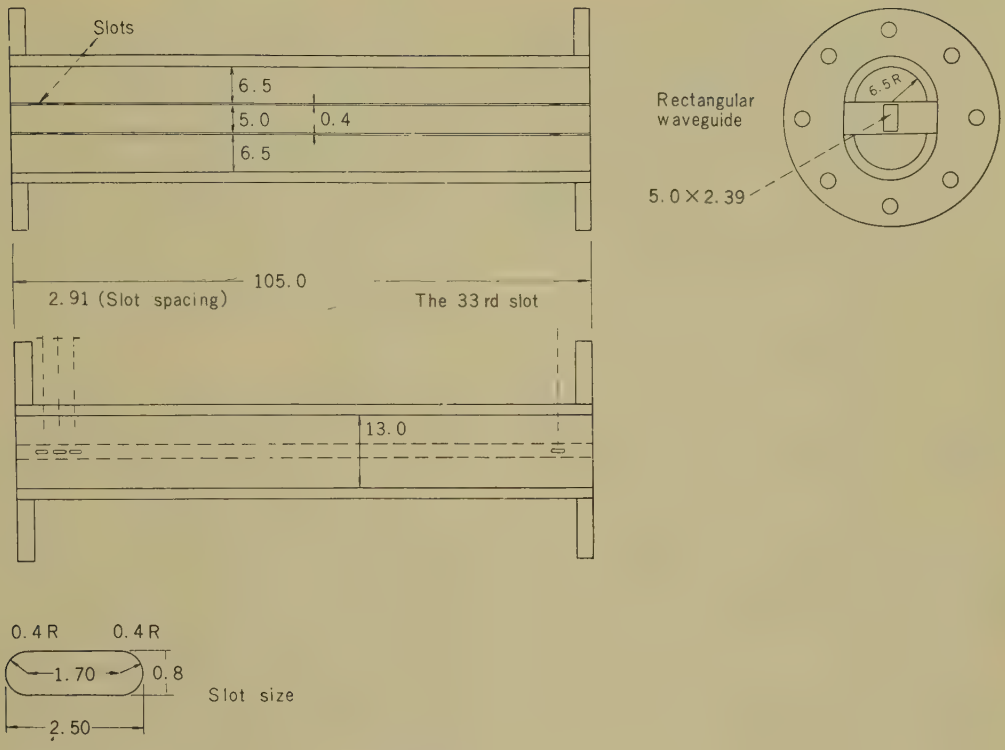

Fig. 6—Construction of the wave coupling.

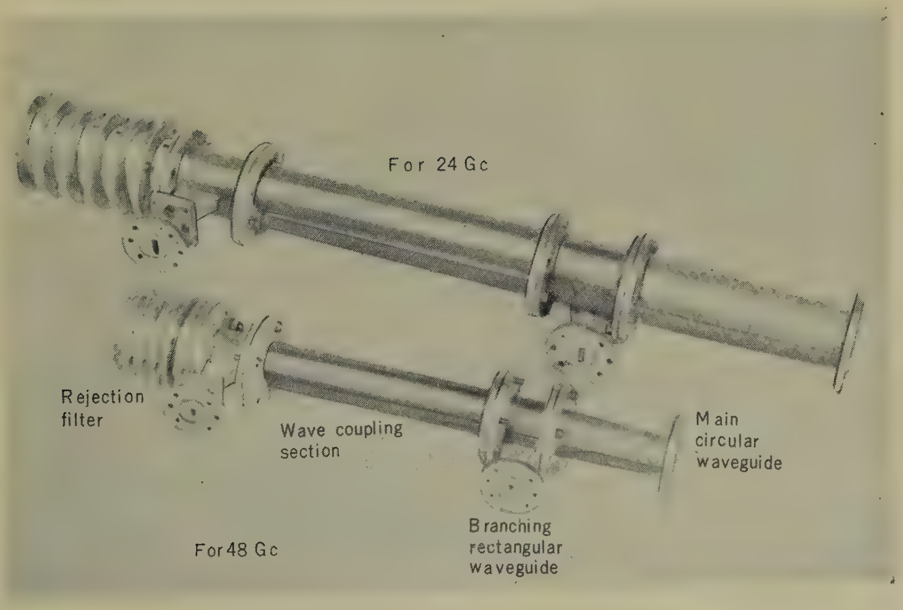

Fig. 7—Photograph of the center-excited type branching filter.

Measured transfer loss is shown in Fig. 8. And V.S.W.R. seen from the branching rectangular waveguide is shown in Fig. 9.

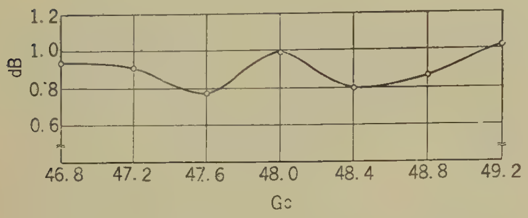

Fig. 8—Transfer loss of $TE_{10}{}^{\square} \rightleftarrows TE_{01}{}^{\circ}$

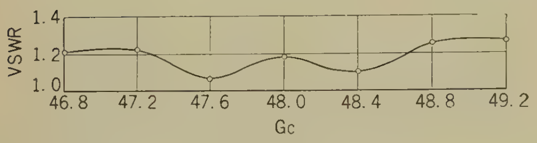

Fig. 9—VSWR seen from the branching rectangular guide.

3.2. Insertion Loss between Two Terminals of the Rectangular Waveguide

The magnitude of the insertion loss, together with transfer loss, are the barometers of the quality of the hybrid. When the magnitude is larger than +15 dB, the design is considered to be satisfactory. Fig. 10 shows the measured insertion loss.

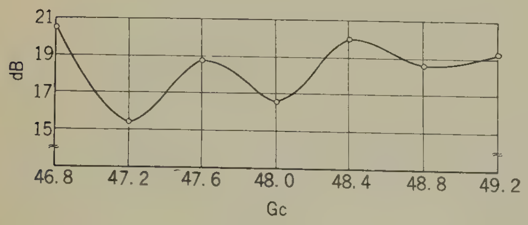

Fig. 10—Insertion loss between two terminals of rectangular guide.

3.3. Unused Modes Generated in the Circular Waveguide

The magnitudes of the unused TE_{11}, TE_{21}, TE_{31}, and TM_{11} modes have been measured by using Miller's coupled wave transducers[1] in the output of circular guide when power is incident from the input of the branching rectangular guide. It is found that the magnitudes of all these modes are smaller than −20 dB.

4. Rejection Filter

4.1. Center Excited Type

This rejection filter consists of a circular TE_{111} cavity which is coupled to the semicircular guide by an elliptic slot located on the center axis of the semicircular guide as shown in Fig. 11. Fig. 11 shows the construction of a three-stage filter of this type. The separation of the adjacent coupling slots is 5/4 λ_g and the loaded Q's of the filter cavities are 60, 40, and 60, respectively. When the size of the coupling slot is 2.8×0.5 mm, the loaded Q is 60, and the loaded Q is 40 when the slot is 2.9×0.5 mm. Fig. 12 shows the measured reflection loss of this three-stage rejection filter.

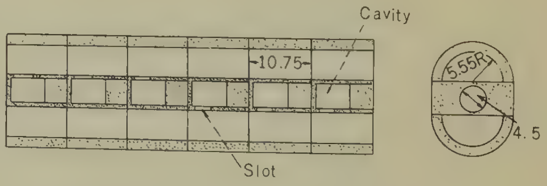

Fig. 11—Three-stage rejection filter of center-excited type.

4.2. Semicircular TE_{02} Cavity Type

Fig. 13 shows a rejection filter of the modified Marcatili type.[4] In the smaller radius region of the filter the TE_{01} wave can propagate while the TE_{02} wave cannot, and in the larger region both the TE_{01} and TE_{02}

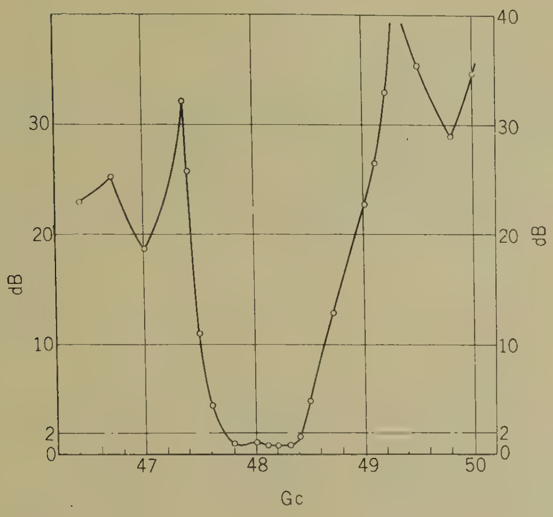

Fig. 12—Reflection loss of rejection filter shown in Fig. 11.

waves can propagate. This larger region becomes the TE_{02} cavity, which reflects the wave at its resonance frequency, if the length of the part properly selected. The incident TE_{01} wave can pass through the region with negligible reflection, if the region is not resonant in the TE_{02} mode.

We have theoretically obtained the condition of total power reflection at the TE_{02} mode resonance through the use of the S-matrix of the region,

$$\phi_{33}-\beta_{02}L=m\pi-|S_{23}|^2\sin(2\phi_{23}-\beta_{01}L-\beta_{02}L)$$

When the TE_{02} wave in the larger region is incident to the smaller region, TE_{01} and TE_{02} waves are reflected from this discontinuity.

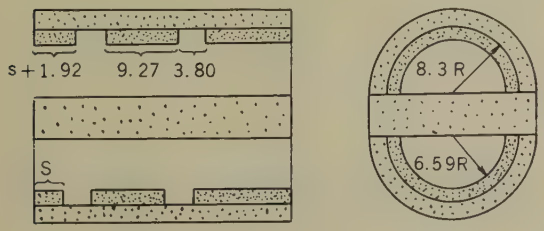

Fig. 13—Two-stage rejection filter of semi-circular TE_{02} cavity type.

ϕ_{23} is the phase angle of the reflected TE_{01} mode and ϕ_{33} is that of the TE_{02} reflected mode. The length of the TE_{02} cavity is L, and m and n are any integers.

Fig. 13 shows the construction of a two-stage of 7/4 λ_g-coupled rejection filter with a loaded Q of 50.

Fig. 14 shows the measured reflection loss of this two-stage rejection filters.

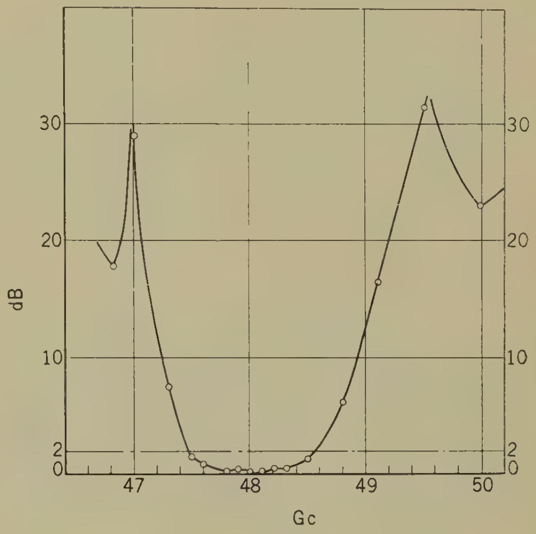

Fig. 14—Reflection loss of rejection filter shown in Fig. 13.

Conclusion

The principles, design, and measured results of a novel center-excited type branching filter for circular TE_{01} waves are described. There are several papers which suggest methods of channel separation for millimeter TE_{01} waves; however, so far the characteristics have not been reported in detail. Our paper proposes a new method of channel separation for millimeter-wave multi-channel communication.

Acknowledgement

The authors are indebted to T. Miwa and N. Kojima of the Laboratory for helpful sug-

gestions relating to this work.

References

(1) S. E. Miller: Coupled Wave Theory and Waveguide Applications, *B.S.T.J.*, **33,** No. 3, p. 661, 1954.

(2) R. W. Dawson: An Experimental Dual Polarization Antenna Feed for Three Radio Relay Bands, *B.S.T.J.*, **36,** No. 2, p. 391, 1957.

(3) G. A. Deschamps: Determination of the Reflection Coefficients and Insertion Loss of a Waveguide Junction, *J. Appl. Phys.*, **24,** (8), p. 1046, 1953, 08.

(4) S. E. Miller: Millimeter Waves in Communication, *Proc. of the Symp. on Millimeter Waves,* (*M.R.I. Symp. Ser.* Vol. 9), p. 25, 1959.

* * * *

REVIEW OF THE ELECTRICAL COMMUNICATION LABORATORY
VOLUME 9, NUMBERS 7-8, JULY-AUGUST, 1961

U.D.C. 621.374.32:621.382.2

The Design of Germanium Diodes used for Junction Capacitance Parametrons*

Yasuhiro HIYAMA†

Diodes used in the junction-capacitance parametron, which is a logical element for ultra-high speed computers, must have very low base resistance and a uniform value of junction capacitance in order to obtain high speed operation and good stability. The important diode parameters and design methods are described in this paper.

Parametron diodes which have a junction capacitance of 94 pF ±15% and a quality factor of 100 ±30%, measured at 20 Mc/s with a bias voltage of 0.5V, have been produced.

Introduction

The junction-capacitance parametron(1) has two advantages in performance. Very high speed operation well into the microwave region and very low power dissipation are possible, because the junction capacitance can be varied with space charge variations in the reverse biased p-n junction, and reversed p-n junctions disipate only little power.

The series resistance in the base region of the parametron diode determines directly the maximum operating frequency. The oscillation voltage of the parametron is controlled by the nonlinear conductance of the junction. Thus the characteristics of the diode affect the performance of the parametron; therefore uniform parameters, especially junction capacitance and quality factor, are necessary for stable logical operation. The deviation of capacitance-voltage sensitivity is not large enough to warrant consideration.

The most dominant parameter that affects the variation of junction capacitance is the diameter of the junction. The variation of quality factor is dependent on the thickness of the semiconductor, which has high resistivity.

It is in the microwave region that the junction capacitance parametron has many advantages for high speed logical operation. However, we designed parametron diodes which have large capacitances and constructed parametrons with lumped constants that operate pumping frequency of 40 Mc/s in order to obtain fundamental quantitative experimental data.

1. Diode Parametron Circuit

Fast rise and decay of parametron oscillation voltage are necessary for high speed operation. The parametron has a tuned circuit, which stores oscillating energy. Therefore in the three-phase pumping system using h-f waves modulated by three-phase rectangular waves, the tuned circuit has damping resistance in order to suppress the oscillations after the pumping signal is interrupted. This resistance causes a delay in oscillation build-up time.

---

* MS in Japanese received by the Electrical Communication Laboratory on 9 May, 1960. Originally published in the *Kenkyû Zituyôka Hôkoku* (*Electrical Communication Laboratory Technical Journal*), N.T.T., Vol. 9, No. 8, pp. 915–928, 1960.

† Electronic Research Section.

In the other pumping system, continuous h-f waves are supplied to parametrons whose bias voltage is modulated by rectangular waves; there is no added damping resistance across the tuned circuits, and the diodes themselves act as the damping resistance when the pumping is interrupted. Hence the quality factor of the tuned circuits is high the build-up time is not influenced by the modulation. But this system has some disadvantages, such as: the modulation power is large, and there are some disturbances from transient effects.

In this paper the former system, the three-phase pumping system by modulated waves; is considered.

1.1. γ and Q

The negative conductance developed across a tuned circuit by parametric excitation is

$$G = -\frac{\gamma}{2}\omega C_0 \tag{1}$$

where γ is the capacitance-voltage sensitivity of the diode and ωC_0 is the susceptance of the junction capacitance at the oscillating frequency. The time required for build-up of A_{cp}(nepers) is

$$\tau_1 = \frac{\dfrac{2A_{cp}}{\omega C_0}}{\left(\dfrac{\gamma}{2} - \dfrac{1}{Q_0}\right)}. \tag{2}$$

A_{cp} is also the coupling attenuation between two parametrons, and Q_0 is the net quality factor of the tuned circuit involving the damping and load resistances. This equation shows that the larger γ and Q_0, the faster the rise time becomes.

The oscillation decay time after pumping is interrupted is described by

$$\tau_2 = \frac{2A_{cp}Q_0}{\omega C_0}. \tag{3}$$

The modulation frequency becomes maximum when $\tau_1 = \tau_2$. The relation between γ and Q_0 which gives the maximum operating frequency can be obtained from (2) and (3):

$$Q_0 = \frac{\gamma}{4}. \tag{4}$$

Furthermore, the quality factor of the reverse-biased junction capacitance has frequency dependence. Therefore, the maximum operating frequency as a parametron is limited to $\gamma/2f_c$, where f_c is the cutoff frequency of the diode capacitance. However, it is not desirable to use a diode having a low quality factor, because quality factor variation will affect the oscillation voltage. Therefore, to obtain uniform for Q_0 for all parametrons, the major part of the loss in the circuit must be alloted to the damping resistance, which generally can be made quite uniform. Therefore, the quality factor of the diode and tuning impedance must have large values.

The capacitance-voltage sensitivity (the rate of parameter excitation) of an alloy junction diode is given theoretically by

$$\gamma = \frac{1}{2} \cdot \frac{V_{2fp}}{(V_{dc} + V_0)} \tag{5}$$

and its maximum value is 0.5 when $V_{2fp} = V_{dc} + V_0$. As the value of γ is mainly determined by the impurity distribution of the p-n junction, its deviation is smaller than that of a ferrite core parametron.

1.2. Base Resistance

The greater part of the loss of a diode capacitor at high frequencies is in the resistance of the base region. The base resistance of an indium alloyed n-type germanium junction can be expressed as

$$R_b = \frac{4\rho_n W'}{\pi D^2} \tag{6}$$

where

ρ_n = resistivity of n-type germanium base material ($\Omega \cdot$cm)

W' = thickness of n-type germanium base

(cm)
D=diameter of junction (cm)

when $D \gg W'$, and the diode is biased in the reverse direction: that is, holes are not injected into the base region and the conductance of the semiconductor is not modulated. The junction capacitance is given by

$$C_d = \frac{\varepsilon}{W_j} \cdot \frac{\pi D^2}{4} = \frac{\pi D^2}{4} \left((V_{dc} + V_0) \cdot 2\mu_n \frac{\rho_n}{\varepsilon} \right)^{-\frac{1}{2}} \tag{7}$$

where

W_j=thickness of junction space charge layer (cm)
ε=dielectric constant of semiconductor material $(=\varepsilon_s \cdot \varepsilon_0)$ (F/cm)
μ_n=mobility of electrons in n-type germanium (cm^2/V·sec).

The quality factor of the diode is

$$\begin{aligned} Q_d &= \frac{1}{\omega C_d R_b} \\ &= \left(\frac{2\mu_n}{\varepsilon} \right)^{\frac{1}{2}} \cdot \frac{(V_{dc} + V_0)^{1/2}}{\omega W' \rho_n^{1/2}}. \end{aligned} \tag{8}$$

From this equation we find that Q_d is depends mainly on the thickness of the n-type germanium and not on the area of the junction.

If the germanium that we use has the following physical constants

$$\mu_n = 3500 \text{ cm}^2/\text{V·sec}$$

$$\varepsilon_s = 16$$

the experession for the quality factor of the diode can be simplified to

$$Q_d = 7.03 \times 10^7 \frac{(V_{dc} + V_0)^{1/2}}{\omega W' \rho_n^{1/2}}, \tag{9}$$

or the cutoff frequency of the diode is

$$f_c = 7.03 \times 10^7 \frac{(V_{dc} + V_0)^{1/2}}{W' \rho_n^{1/2}}. \tag{9'}$$

1.3. Diffusion Admittance

Diffusion admittance, as is well known, arises across a p-n junction with a positive or small negative bias.

$$Y_d = (G_{d0} + jB_{d0})\omega^{1/2} e^{qV/kT}. \tag{10}$$

In the high frequency region the real and imaginary parts of the diffusion admittance are equal in value. Therefore, whenever we attempt to utilize the increase of capacitance-voltage sensitivity that includes diffusion capacitance, the diffusion conductance decreases the quality factor of diode. Accordingly, since we shall not utilize the diffusion capacitance, the reverse bias voltage should be greater than kT/q.

The peak pumping to bias voltage ratio $V_{2fp}/(V_{dc} + V_0)$ that is required to obtain a maximum γ of 0.5 is unity. But it should be smaller than unity for the reason described above. On the other hand, while it seems reasonable to choose a high reverse bias voltage to avoid decrease of Q_d, the power dissipation in the parametron increases. The power dissipation increases with square of the bias voltage as given approximately by

$$P = \omega C_d (V_{dc} + V_0)^2 \left(\frac{1.28}{Q_{d2f}} + \frac{1}{Q_0} \right) \tag{11}$$

where Q_{d2f}=quality factor of diode at pumping frequency $2f$.

Therefore the optimum operating bias voltage of the diode should be selected by the power relations to reduce the dissipation.

1.4. Reverse Breakdown Voltage

The reverse breakdown voltage is not an important parameter, since the peak value of reverse voltage—including d-c bias voltage V_{dc}, pumping voltage V_{2f}, and oscillation voltage V_f—applied to the diode is of the order of $2(V_{dc} + V_0)$, which is generally only several volts.

Therefore the reverse breakdown voltage

V_B may be roughly selected as ten times the bias voltage.

In general, the inner breakdown voltage exceeds the surface breakdown voltage, and both are functions of the resistivity of the germanium. The inner breakdown voltage is given by

$$V_{BI} \approx 83.4\rho_n^{0.61} \text{ (V)} \tag{12}$$

and the surface breakdown voltage by

$$V_{BS} \approx 34.3\rho_n^{0.33} \text{ (V)} \tag{13}$$

which are shown in Fig. 1.(2)

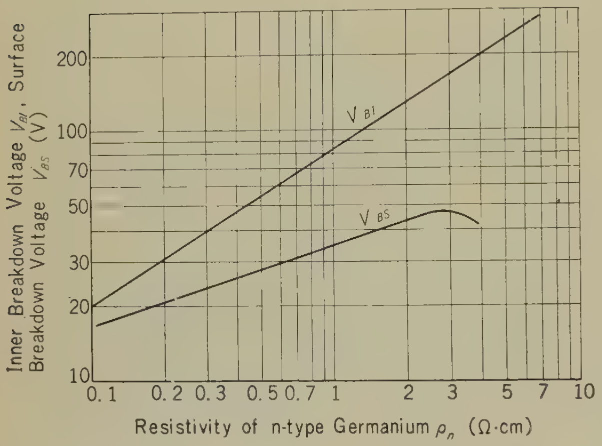

Fig. 1—Breakdown voltage V_{BI} and V_{BS} as functions of resistivity of *n*-type germanium:

The resistivity of the n-type germanium together with the thickness of the base region W' dominates the quality factor as indicated in Eq. (9). The requirements imposed by quality factor and breakdown voltage are contradictory.

1.5. Reverse Current

Reverse current in the parametron diode only affects the power supply d-c bias circuit. This current, which is mostly composed of saturation current, can be expressed as

$$I_s \approx 0.52\rho_n D^{1.1}\cdot W'^{0.55}\cdot 10^{-4} \text{ (A)} \tag{14}$$

where surface recombination velocity of holes $s=300$ cm/sec, diffusion constant of holes in the base region $D_p=44$ cm^2/sec, and intrinsic resistivity of germanium $\rho_i=47$ Ω·cm are employed in this calculation. Supposing that $\rho_n=0.2$ Ω·cm and $W'=100$, the saturation current is 0.1 μA from Eq. (14).

1.6. Impedance of Lead Wires

The impedance of lead wire R and L together with the base resistance of a parametron diode which has large junction capacitance must be taken into consideration. Although the leads must be hermetically sealed to the diode envelope, it is necessary to use heavy, short lead wire of low resistivity material.

1.7. Other Parameters

There are some parameters that are of no importance in parametric use, even though they are important in rectifiers.

(a) The forward resistance is not very important for parametron diodes in which there is no current flow in the forward direction. However, use of low resistance material automatically results in low forward resistance.

(b) Heating the junction increases junction capacitance and reverse current, and decreases breakdown voltage and base resistance. But there is little internal heating of the junction since the diode is operated with small pump power. However, ambient temperature must be kept to constant.

(c) The noise arising from the diode is very low compared to that from the other components such as the ferrite core in the tuning coil.

1.8. Variation of Parameters

In this connection, two parameters, Q_d and C_d, are important. The major part of the variation in C_d is, as obviously indicated in Eq. (7), determined by the diameter of the junction. Variation in Q_d is, as also indicated in Eq. (8), mainly dependent on the thickness of the n-type germanium. The thickness of the germanium wafer of diode can be maintained precisely, but there are considerable variations in the depth of the diffussd indium and soldering material into the n-type germanium wafer.

Careful surface etching and sealing of the junction in a manner similar to the usual rectifier are necessary.

2. Design of Parametron Diodes

These diodes are designed for operation at a pumping frequency of 40 Mc/s, oscillation frequency of 20 Mc/s, and power dissipation of 1 mW.

The junction capacitance must be ten times greater than the stray capacitance C_s in order not to decrease the effective capacitance-voltage sensitivity $\gamma/\{1+(C/C_0)\}$, And also to decrease the resonant impedance to the extent that interference from other elements is negligible, it is desirable to use a large capacitance. However large capacitance causes large power dissipation as shown in Eq. (11). Then taking $\sqrt{2L/C_d}$ as 100, C_d becomes 150 pF.

The reverse bias voltage is given as 0.46 V from Eq. (11); taking $Q_0=15$, $Q_{d2f}=50$, $f=$ Mc/s, and $V_0=0.3$ V.

The resistivity of the n-type germanium is 0.2 Ω·cm for $V_B=20$ V, and the diameter of the junction is 0.73 mm from Eq. (7). This diode is easy to manufacture. Taking the quality factor of the diode as 100 and the lead resistance as 0.1 Ω, the base resistance should be 0.43 Ω and the thickness of n-type germanium wafer $W'=91\ \mu$.

The tolerances of D, W', and ρ_n must be limited. Since the variation of inductance of the trimming coil is ±10%, a tolerance of C_d equivalent to or smaller than this value is desirable. From the relation in Eq. (7)

$$\frac{\Delta C_d}{C_d}=\frac{2\Delta D}{D}+\frac{1}{2}\cdot\frac{\Delta\rho_n}{\rho_n}. \tag{15}$$

If we take $\Delta C_d/C_d \leqslant \pm 10\%$, then $\Delta D/D \leqslant \pm 4\%$ and $\Delta\rho_n/\rho_n \leqslant \pm 4\%$, are necessary. This seems to be a very severe condition. Therefore we shall allow a ±15% veriation of $\Delta C_d/C_d$ and divide the capacitors into three groups that deviate ±5%. Then $\Delta\rho_n/\rho_n=\pm 10\%$ and $\Delta D/D=\pm 5\%$ are possible.

From the relation in Eq. (8)

$$\frac{\Delta Q_d}{Q_d}=\frac{1}{2}\cdot\frac{\Delta\rho_n}{\rho_n}+\frac{\Delta W'}{W'} \tag{16}$$

if we take $\Delta Q_d/Q_d$ as ±30% then $\Delta\rho_n/\rho_n=\pm 10\%$ and $\Delta W'/W'=\pm 25\%$, which is easy to produce.

The simplified design process is shown in Fig. 2. The design proceeds from I, to II, III····; and finally is inspected over again from the viewpoint of the manufacturing technique.

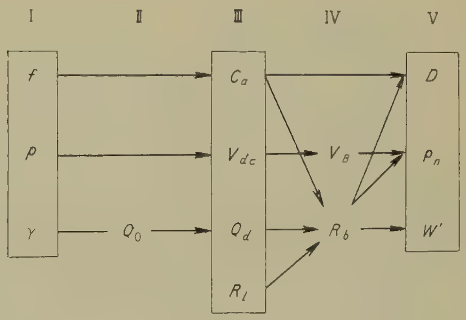

Fig. 2—Simplified design process for parametron diodes.

It is now known, after several pilot production runs, that the specifications should be changed to those listed in Table 1. The reasons are that the deviations of C_d and Q_d are too large and that the smaller C_d makes it easy to satisfy the other conditions.

Table 1

THE SPECIFICATIONS OF PARAMETRON DIODES

Parameter		Value	Tolerance	Measurement condition
Junction capacitance	C_d	betw. 80 & 150 pF	± 15 %	at 0.5 V d-c bias and 20 Mc/s, 10 mV h-f
Quality factor	Q_d	above 40	± 30 %	at 0.5 V d-c bias and 20 Mc/s, 10 mV h-f
Breakdown voltage	V_B	above 15 V	below 20 μA at 15 V	
Reverse current	I_b	below 5 μA		at 10 V d-c
Capacitance-voltage sensitivity	γ	0.5		$V_{2fp}/(V_{dc}+V_0)=1.0$
Lead wire resistance	R_l	0.1 Ω	± 10 %	outside length of wire 5 mm

3. The Characteristics of Manufactured Diodes

The characteristics of the diodes manufactured by three makers—A, B, and C—according to the specifications shown in Table 1, are indicated in Fig. 3 to 5 and Table 2. The A diodes have relatively small I_s but Q_d is also low. In the B diodes Q_d is not decreased in spite of large C_d. The C diodes have high Q_d due probably to smaller C_d and shorter lead wire, because they are sealed in very small glass envelopes (2 mm × 10 mm), while A and B are sealed in larger cans for transistor use. However, this is not certain since the author have no detailed concerning the physical parameters such as D, W', and ρ_n of these diodes.

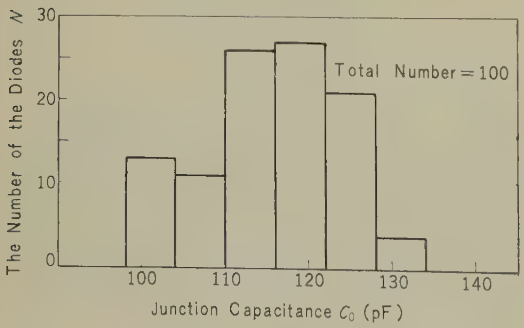

Fig. 3 (a)

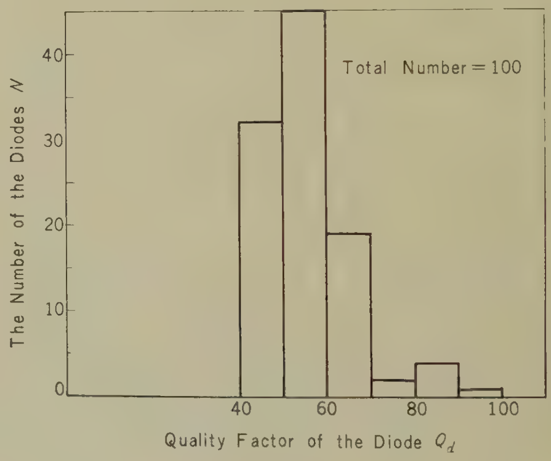

Fig. 3 (b)

Fig. 3—Distribution of junction capacitance and quality factor of A diodes.

The relation between Q_d and C_d for the same production conditions are indicated in Fig. 6.

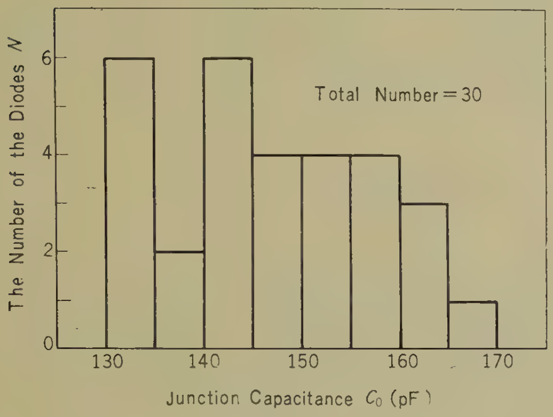

Fig. 4 (**a**)

Fig. 4—Distribution of junction capacitance and quality factor of B diodes.

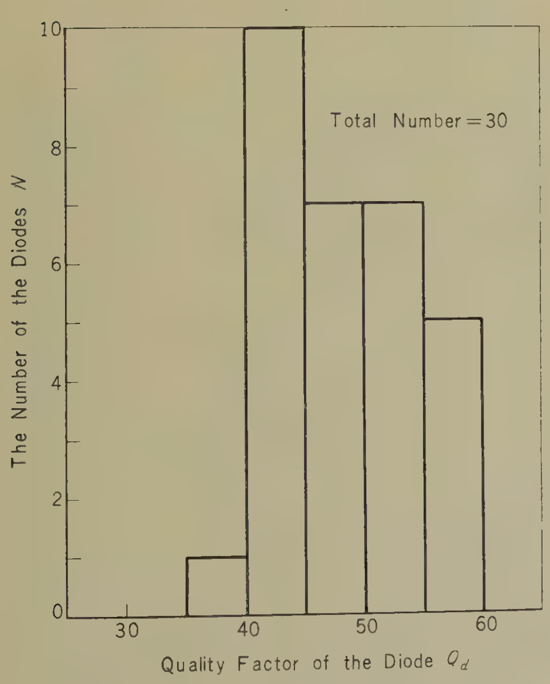

Fig. 4 (**b**)

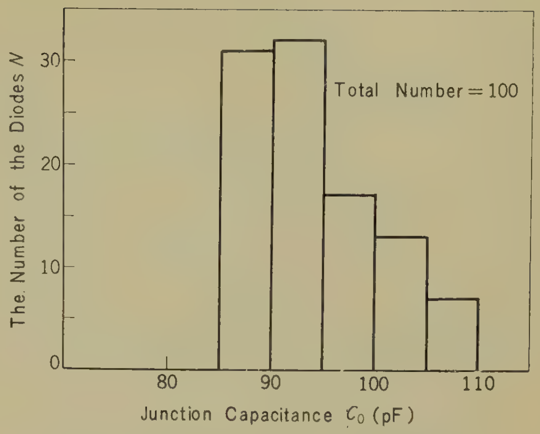

Fig. 5 (**a**)

Fig. 5—Distribution of junction capacitance and quality factor of C diodes.

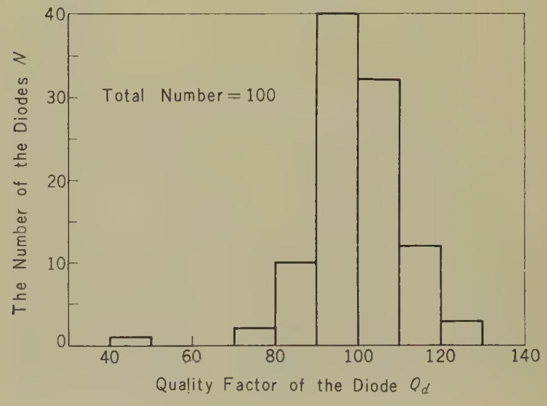

Fig. 5 (**b**)

Table 2

THE RESULT OF MANUFACTURED PARAMETRON DIODES.

Maker	C_d	Q_d	$I_b(-10V)$	$I_b(-20V)$
A	115.4pF	56.1	0.52μA	2.96μA
B	147.7	49.0	2.78	8.28
C	94.2	100.7	2.76	6.18

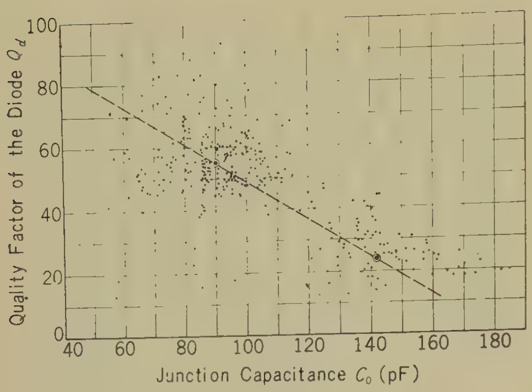

Fig. 6—Relation between junction capacitance and quality factor for the same manufacturing conditions.

Conclusion

It is evident that together with a high cut-off frequency f_c, a high value of capacitance-voltage sensitivity γ is necessary for high speed operation. The value of γ is a function of the impurity distribution in the germanium and can be controlled. High sensitive γ diodes have previously been obtained.(3) However, common alloy junction diodes are more appropriate for mass production at present. A study on the production of diodes with thin bases may be necessary.

From the experience in manufacturing these diodes it has been found that to reduce the deviations of C_d below ±15% would be most difficult by the usual alloy techniques.

Since the C diodes have relatively high values of Q_d, there is still hope that diodes can be produced by the usual alloy techniques.

The author regrets that discussion on the relations between the results and the design parameters was not possible because the details of the manufacturing data was not available.

Acknowledgement

The author wishes to express his sincere thanks to Z. Kiyasu, K. Fushimi, S. Yoshida, R. Shikama, and K. Yamanaka for their useful suggestions and discussions and also to Y. Takeda, T. Asada, H. Yugami, T. Abe, Y. Sawaji, and K. Takahashi for manufacture of the parametron diodes.

References

(1) Z. Kiyasu, K. Hushimi, K. Yamanaka, and K. Kataoka: Parametric Excitation using Barrier-Capacitance of Semiconductor, *J. Inst. Electr. Commun. Eng. Jap.*, Vol. **40**, No. 2, p. 162, 1957.

(2) S. Yoshida and R. Shikama: Crystal Diodes for Speech Path Elements (ECL-1200), *Monthly Rep. Electr. Commun. Labor. NTT. Jap.*, Vol. **11**, No. 1, p. 16, 1958.

(3) M. E. McMahon and G. F. Straube: Voltage-Sensitive Semiconductor Capacitors, *I.R.E. Wescon*, Part. 3, p. 72, 1958.

* * * *

REVIEW OF THE ELECTRICAL COMMUNICATION LABORATORY
VOLUME 9, NUMBERS 7-8, JULY-AUGUST, 1961

U.D.C. 621. 391 : 621. 394] : [621. 391. 883
: 621. 395. 5

Binary Data Transmission on Private Telephone Line*

Toshi MINAMI,† *Hiroshi SUNAGAWA*,†
and *Shun'itsu HAMAO*†

This paper presents theoretical considerations and experimental results on binary data transmission over private telephone lines. Relations between signal distortion (margin) and frequency response of the telephone line, net loss variation, noise, etc. are analyzed. Especially signal distortion caused by relative phase difference between each signal pulse and the subcarrier is examined carefully and a method to eliminate this distortion is given. The results indicate that the speed limit of data transmission over a standard telephone line is about 1750 baud when net loss variation is within ±5 dB and peak S/N is higher than 15 dB.

Introduction

The amount of business communication in various fields of Japanese industry and commerce is increasing enormously in keeping pace with the development of economic activities and the improvement in the standard of living. However, the communication facilities necessary for handling business communications still remain unsatisfactory. For instance, the number of leased telegraph circuits in Japan at the end of 1959 was 2,940; but the demand for leased telegraph circuits by 1966, at the end of the 3rd five-year telegraph and telephone expansion program, is expected to reach at least 30,000, more than ten times the number of existing circuits. But if conventional voice frequency carrier telegraph systems are adopted to construct new business communication facilities, the cost of this program will be so prohibitive that it will not be possible to raise the necessary funds. In addition, it is definitely foreseen that future demands require much improvement in transmission speed and error rate of the circuits; therefore, completion of the program will be impossible from the technical point of view without improving existing telegraph techniques.

Several attempts to develop new techniques have already been made.[1)2)] In this paper an approach to the problem of finding the speed limit of data transmission over private telephone lines by an AM DSB system, and the reliability of the system, is reported.

1. Theoretical Analysis of Data Transmission

1.1. Theoretical Limit of Signaling Speed

Digital data are usually encoded as a series of binary codes and this series of codes are transmitted on an electrical line in the form

---

* MS in Japanese received by the Electrical Communication Laboratory on October 24, 1960. Originally published in the *Kenkyu Zituyôka Hôkoku* (*Electrical Communication Laboratory Technical Journal*), Vol. 10, No. 5, pp. 803–859, 1961.

† Communication Network Section.

of single-current rectangular waves or double-current rectangular waves. Assume that a single-current unit pulse is transmitted on a low-pass transmission system which has a finite bandwidth; then the received pulse is distorted as shown in Fig. 1 (a). But if the amplitude of the received pulse at a sampling point is higher than the threshold level, we can recognize exactly that a unit pulse is sent. Therefore it is more important to detect mark signals as mark and space signals as space than to reproduce the transmitted rectangular waveforms exactly.

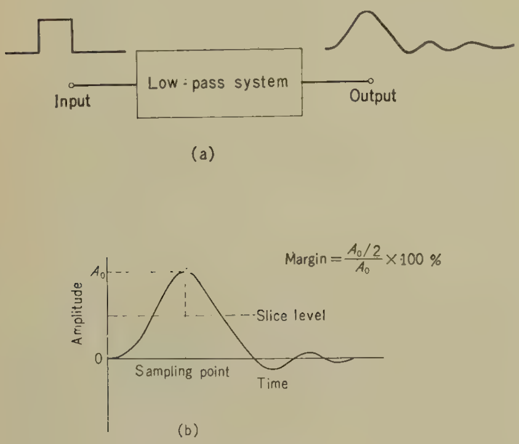

Fig. 1—Input and output waveforms and margin of a low-pass system.

But in an actual system the transmission bandwidth is confined to a small region and the received unit pulse has a long tail. If there are many other pulses before and after the unit pulse, interference will occur at a sampling point from the preceding and succeeding pulses. Now, let the amplitude of the received pulse at a sampling point be A_0, the threshold level be $A_0/2$, interference from the unit pulse just before the particular pulse be α_1, and interference from the nth pulse before the particular pulse be α_n; then the total interference R becomes

$$R = \sum_{\substack{n=-\infty \\ \neq 0}}^{\infty} q_n \alpha_n \tag{1}$$

$$\text{where} \quad \left.\begin{aligned} q_n &= 1 \quad \text{when } n\text{th pulse is present} \\ q_n &= 0 \quad \text{when } n\text{th pulse is not present} \end{aligned}\right\} \tag{2}$$

And the maximum interference in the positive direction $R_{\max}{}^P$ and maximum interference in the negative direction $R_{\max}{}^N$ are

$$\left.\begin{aligned} R_{\max}{}^P &= \sum_{\substack{n=-\infty \\ \neq 0}}^{\infty} \alpha_n{}^P \\ R_{\max}{}^N &= \sum_{\substack{n=-\infty \\ \neq 0}}^{\infty} \alpha_n{}^N \end{aligned}\right\} \tag{3}$$

where

$$\left.\begin{aligned} \alpha_n{}^P &= \alpha_n & \alpha_n &\geq 0 \\ &= 0 & \alpha_n &< 0 \\ \alpha_n{}^N &= 0 & \alpha_u &\geq 0 \\ &= \alpha_n & \alpha_n &< 0 \end{aligned}\right\} \tag{4}$$

Then margin M becomes

$$M = \frac{A_0 + R_{\max}{}^N - R_{\max}{}^P}{2\,A_0} \times 100\,\%$$

$$= \frac{A_0 - \sum\limits_{\substack{n=-\infty \\ \neq 0}}^{\infty} |\alpha_n|}{2\,A_0} \times 100\% \tag{5}$$

When signaling speed is low interference from other pulses is generally small and margin M is nearly 50 %, but the higher the signaling speed becomes the smaller the margin becomes and finally it decreases to 0 %. The signaling speed when the margin becomes zero is the speed limit of the transmission system. Nyquist proved that if the transmission bandwidth is f c/s, it is possible to transmit pulses at an interval of $1/2f$ sec.3) In the case of binary signal transmission, the

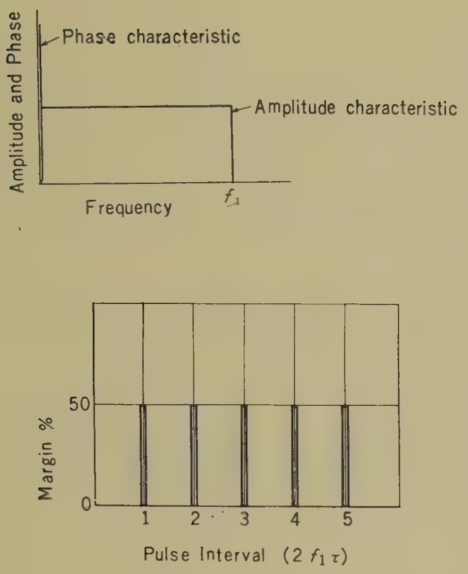

Fig. 2—Frequency and margin characteristics of the ideal low-pass filter.

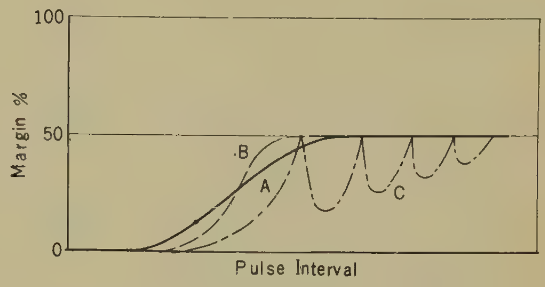

Fig. 3—Margin characteristics.

Nyquist rate can be realized by using a so-called ideal low pass filter[4] (the transmission of the filter is uniform with frequency, and in the passband the phase shift is proportional to frequency). But as shown in Fig. 2, the margin of this filter is zero when the signaling speed differs from $n/2f$ baud; therefore its speed limit is zero in the above described sense.* This means that the so-called ideal filter does not necessarily have an optimum frequency characteristic for binary signal transmission. Then what is the optimum frequency characteristic of a binary signal transmission system?

1.2. Optimum Frequency Characteristic of a Binary Signal Transmission System

When bandwidth f and signaling speed b are given; if $\sum |\alpha_n|$ of a transmission system is smaller than $\sum |\alpha_n|$ of any other system, then it is an optimum binary signal transmission system. But an optimum system at one signaling speed b_1 is not necessarily an optimum system at another signaling speed b_2, as shown in Fig. 3, and it is difficult to select the best characteristic from among the A, B, and C characteristics shown in Fig. 3. Even though signaling speed is fixed, it is very difficult to calculate $\sum |\alpha_n|$ directly from the transmission frequency characteristic.

Therefore instead of calculating $\sum |\alpha_n|$, many approaches to the problem of finding an optimum characteristic have been performed by other methods. Laemmel calculated $\sum |\alpha_n|^2$ of the ideal filter, triangular filter, and cosine filter. The results are shown in Fig. 4, and from these results it is noticed that an optimum characteristic must exist between the rectangular characteristic and the triangular characteristic.[5] Hermann and Schüssler introduced $f_g \times t_g$ as a scale of merit for the appraisal of pulse-shaping networks when q_f and q_t are given, (see Fig. 5), and calculated the position of the zeros and poles of the optimum network transfer function by an analog computer.[6] The tail of the impulse response of this network decreases quickly within $\pm q_t$ but the sum of interference $\sum |\alpha_n|$ is not necessarily minimum compared with $\sum |\alpha_n|$ of any other filter. On the other hand, Chalk derived another optimum pulse shape which minimizes the energy outside a given frequency band.[7]

As described above many studies have been made to find optimum transmission characteristics but this problem has not yet been completely solved. However it may be

---

* See Appendix 1.

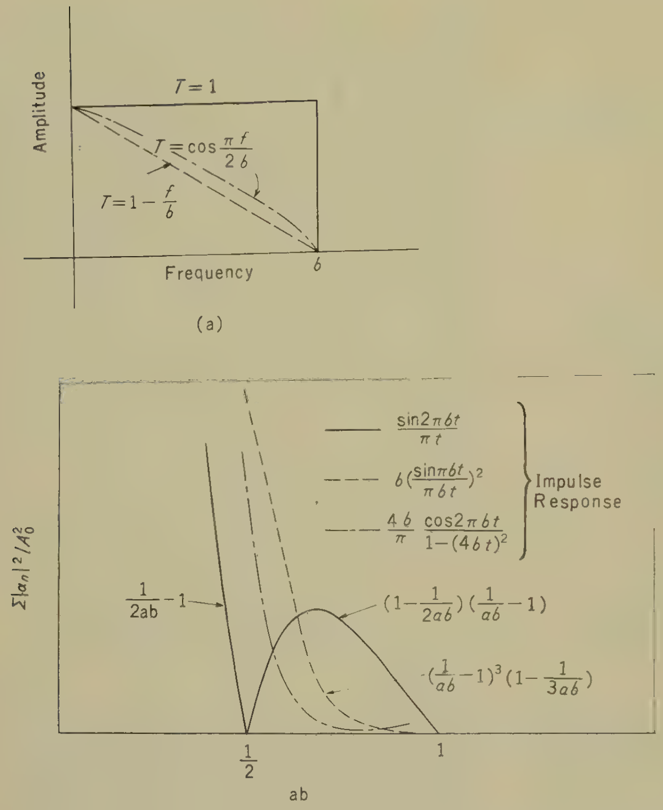

(a)

(b)

Fig. 4—Filter characteristics and total interference.

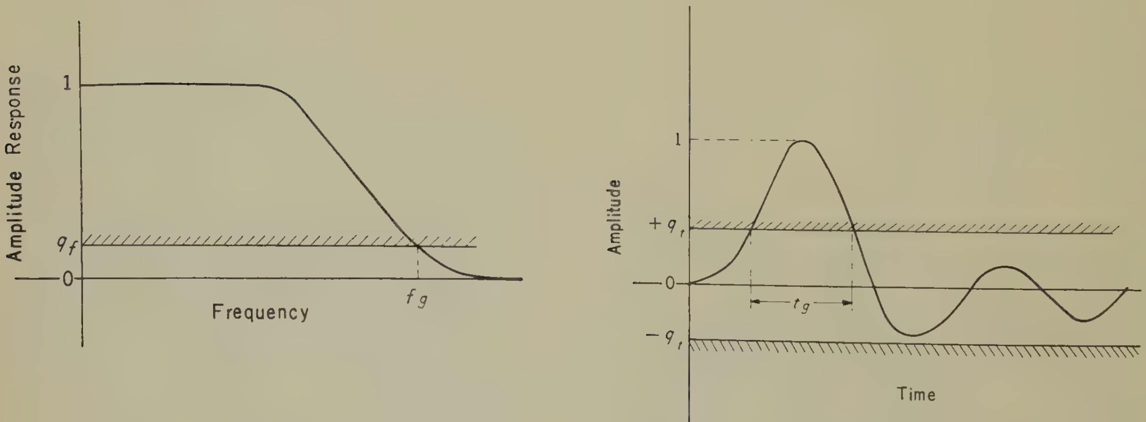

(a)

(b)

Fig. 5—Frequency characteristics of a filter and its impulse response.

true that the phase shift of an optimum transmission system should be proportional to frequency until the attenuation of the system becomes quite high, and the attenuation of the system should increase gradually near the cutoff frequency as a sharp cutoff characteristic is unfavorable for the transmission of a binary signal.

1.3. Binary Data Transmission by an Amplitude Modulation Double Sideband System

1.3.1. Signal Distortion caused by Relative Phase Difference between Subcarrier and Direct Current Signal

In Sections 1.1 and 1.2 the discussions are limited to data transmission through a low pass system; however in actual practice telephone circuits are used to transmit these data. The ordinary telephone circuit in Japan transmits a frequency band of 300 to 3000 c/s; therefore the original direct current signal should be converted to an alternating current signal. In usual carrier telegraphy, the subcarrier frequency is much higher than the signal frequency, but in the case of high speed data transmission on a telephone circuit the signal frequency is close to the subcarrier frequency and the number of cycles of subcarrier contained in a unit signal pulse is very small. For instance, when a 1500 baud signal is transmitted by an AM DSB system with a 1500 c/s subcarrier, only one cycle of subcarrier is included in a unit pulse. Consequently, according to the relative phase difference between the subcarrier and each signal pulse, the modulated current waveforms change as shown in Fig. 6, and signal distortion arises in the detected signal. But it is proved in this paper that this signal distortion can be completely suppressed by letting the original signal pass through an adequate low pass filter before it is fed to the modulator.

Let the original signal be $f(t)$ and the modulated signal be $g(t)$; then

$$g(t)=f(t)\cos(\omega_0 t+\alpha).$$

where ω_0=subcarrier angular frequency
α=relative phase difference between subcarrier and $f(t)$

The frequency spectra of $f(t)$ and $g(t)$ are

$$F(\omega)=\int_{-\infty}^{\infty} f(t)e^{-j\omega t}\,dt, \tag{6}$$

$$G(\omega)=\int_{-\infty}^{\infty} f(t)\cos(\omega_0 t+\alpha)e^{-j\omega t}\,dt$$

$$=\frac{1}{2}[e^{j\alpha}F(\omega-\omega_0)+e^{-j\alpha}F(\omega+\omega_0)]. \tag{7}$$

Let the frequency characteristic of the transmission line be $T(\omega)e^{j\theta(\omega)}$ (in this transmission line the frequency band outside of $\omega_0-\omega_1<\omega<\omega_0+\omega_1$ is considered to have an infinite attenuation); then the waveform $R_0(t)$ after the

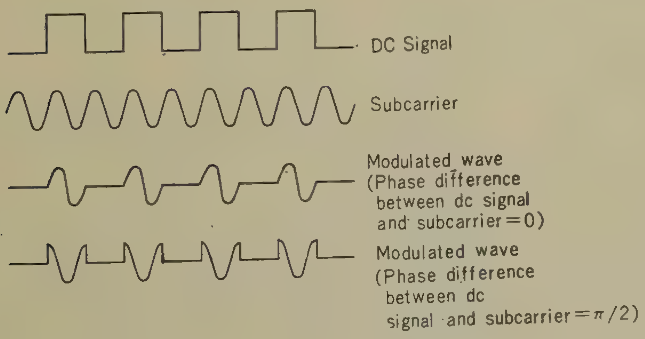
DC Signal
Subcarrier
Modulated wave (Phase difference between dc signal and subcarrier=0)
Modulated wave (Phase difference between dc signal and subcarrier=π/2)

Fig. 6—Effects of phase difference between signal and subcarrier.

modulated wave is sent through this transmission line becomes

$$R_0(t)=\frac{1}{2\pi}\int_{-\infty}^{\infty}G(\omega)T(\omega)e^{j\{\omega t+\theta(\omega)\}}d\omega$$

$$\fallingdotseq\frac{1}{2\pi}\Bigg[\Re\mathrm{e}\int_{-\omega_1}^{\omega_1}F(\omega)e^{j\omega t}T(\omega+\omega_0)e^{j\{\theta(\omega+\omega_0)-\theta(\omega_0)\}}d\omega$$

$$+\Re\mathrm{e}\int_{-\omega_1}^{\omega_1}F(2\omega_0+\omega)e^{j\omega t}T(\omega+\omega_0)e^{j\{\theta(\omega+\omega_0)-\theta(\omega_0)-2\alpha\}}d\omega\Bigg]\cos\{\omega_0t+\theta(\omega_0)+\alpha\}$$

$$-\frac{1}{2\pi}\Bigg[\Im\mathrm{m}\int_{-\omega_1}^{\omega_1}F(\omega)e^{j\omega t}T(\omega+\omega_0)e^{j\{\theta(\omega+\omega_0)-\theta(\omega_0)\}}d\omega$$

$$+\Im\mathrm{m}\int_{-\omega_1}^{\omega_1}F(2\omega_0+\omega)e^{j\omega t}T(\omega+\omega_0)e^{i\{\theta(\omega+\omega_0)-\theta(\omega_0)-2\alpha\}}d\omega\Bigg]\sin\{\omega_0t+\theta(\omega_0)+\alpha\}. \qquad (8)^*$$

where $\Re\mathrm{e}$ designates the real part and $\Im\mathrm{m}$ designates the imaginary part.

In this equation the cosine term and the sine term indicate the in-phase component and the quadrature component respectively. Each term contains an upper and lower sideband component $\left\{F(\omega)T(\omega+\omega_0)\Big|_{-\omega_1}^{\omega_1}\right\}$, and a spurious component $\left\{F(2\omega_0+\omega)\,T(\omega+\omega_0)\Big|_{-\omega_1}^{\omega_1}\right\}$, which is a part of the lower sideband that has been folded at 0 c/s. These relations are illustrated in Fig. 7. From this equation it is easily seen that the relative phase difference α between the signal and subcarrier appears only in the spurious component; therefore if this component is removed prior to the modulation process, the distortion caused by the phase difference can be eliminated. From these considerations the following theorem is derived.

Theorem 1. "In the case of binary data transmission, the signal distortion caused by the relative phase difference between the subcarrier and signal can be eliminated by letting the original signal pass through an adequate low pass filter before it is fed to the modulator, which will suppress the spurious component."

This low pass filter should have uniform amplitude response and linear phase characteristics within the band $0\sim\omega_0$, and sufficient attenuation above $(2\omega_0-\omega_1)$. From this analysis it becomes clear that synchronization between the subcarrier and signal is unnecessary, and the design of the sending circuit

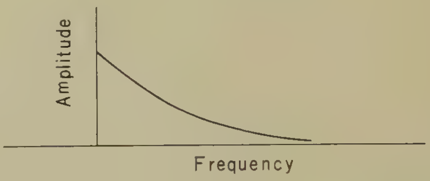

(a) Frequency spectrum of signal

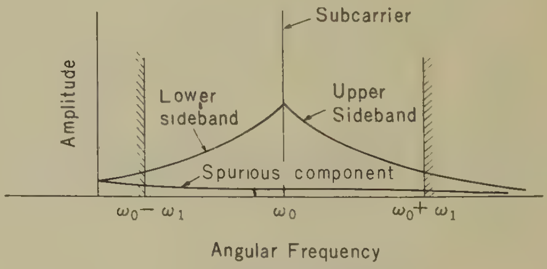

(b) Frequency spectrum of modulated wave

Fig. 7—Schematic description of disturbance by folded component of signal.

---

* See Appendix 2.

is greatly simplified.

1.3.2. Performance of the Modulator

In subsection 1.3.1. the modulated wave is expressed as $f(t)\cos(\omega_0 t+\alpha)$; however in actual practice many unexpected components other than the main component arise in the modulator, and these components interfere greatly with the transmission performance. Especially, when the subcarrier frequency is close to the signal frequency, some of these unexpected components fall in the pass band of the transmission system and it is impossible to eliminate them by any filter, therefore it is necessary to suppress these components by using strictly balanced modulation elements. As described later, a ring modulator is used as the modulating circuit in the ECL experimental system which was designed to investigate binary data transmission performance over telephone lines. An analysis of modulator performance is given below. Now, let us express current i in Fig. 8 (a) as a function of voltages as follows

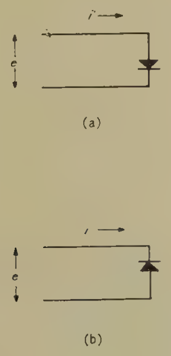

(a)

(b)

Fig. 8—Rectifier circuit.

$$i=\sum_{n=1}^{\infty} C_n e^n \qquad (9)$$

then in Fig. 8 (b)

$$i=-\sum_{n=1}^{\infty} C_n(-e)^n \qquad (10)$$

In Fig. 9 (a) a ring modulator is shown. Here let us assume that the transformers are ideal and the circuit resistances are all zero. If we put

$$\left.\begin{aligned} e_1+e_2&=e \\ e_1-e_2&=\underline{e} \end{aligned}\right\} \qquad (11)$$

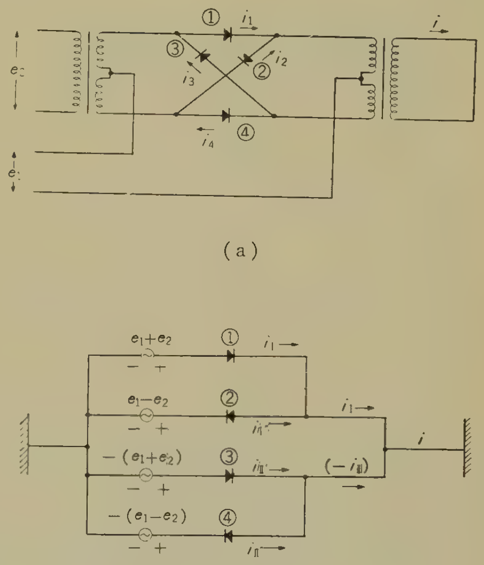

(a)

(b)

Fig. 9—Equivalent circuit of ring modulator.

then Fig. 9 (b) is equivalent to Fig. 9 (a) and we have the following equations

$$\left.\begin{aligned} i&=i_1+i_2+i_3+i_4 \\ i_1&=\sum_1^{\infty} c_{1n}\, e^n \\ i_2&=-\sum_1^{\infty} c_{2n}(-\underline{e})^n \\ i_3&=\sum_1^{\infty} c_{3n}(-e)^n \\ i_4&=-\sum_1^{\infty} c_{4n}\,\underline{e}^n \end{aligned}\right\} \qquad (12)$$

where C_{kn} designates the coefficients of the power series which express the voltage to current characteristic of the kth element. Then i becomes

$$\begin{aligned}
i= & \sum_1^\infty \{c_{1n}e^n-c_{2n}(-e)^n+c_{3n}(-e)^n-c_{4n}e^n\} \\
= & \{(c_{11}+c_{21})-(c_{31}+c_{41})\}e_1+\{(c_{11}+c_{41}) \\
& -(c_{21}+c_{31})\}e_2 \\
& +\{(c_{12}+c_{32})-(c_{22}+c_{42})\}(e_1^2+e_2^2) \\
& +2\{(c_{12}+c_{22}+c_{32}+c_{42}\}e_1e_2 \\
& +\{(c_{13}+c_{23})-(c_{33}+c_{43})\}(e_1^3+3e_1e_2^2) \\
& +\{(c_{13}+c_{43})-(c_{23}+c_{33})\}(e_2^3+3e_1^2e_2) \\
& +\{(c_{14}+c_{34})-(c_{24}+c_{44})\}(e_1^4+e_2^4+6e_1^2e_2^2) \\
& +4\{c_{14}+c_{24}+c_{34}+c_{44})\}(e_1^3e_2+e_1e_2^3) \\
& +\cdots\cdots \qquad (13)
\end{aligned}$$

If all elements have exactly the same voltage to current characteristics, $(C_{1n}=C_{2n}=C_{3n}=C_{4n})$, some terms in equation (13) vanish. The calculated spectra are shown in Fig. 10, where the asterisks designate the spectrum which would not vanish although all elements are completely balanced with each other.

1.3.3. Frequency Response of Transmission Line and Binary Data Transmission Performance

From equation (8) we are able to evaluate the relations between the frequency response of the transmission line and the input-output waveforms, but in the case of binary data transmission, indicial response of the trans

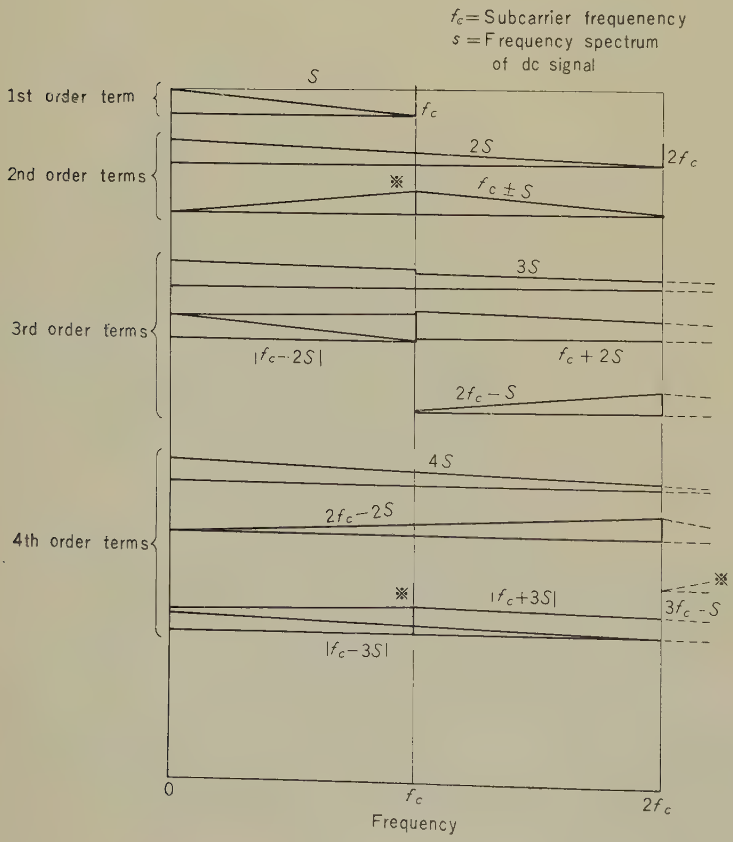

Fig. 10—Frequency spectra of ring modulator output.

mission system is very useful to investigate data-transmission performance of the system. Therefore, the received waveform R_u was calculated for a unit function input current. In this case the amplitude response of the transmission line is divided into a component $T_e(\omega)$ with even symmetry to the subcarrier frequency and a component $T_0(\omega)$ with odd symmetry; similarly the phase characteristics are divided into an odd symmetry component $\theta_0(\omega)$ and an even one $\theta_e(\omega)$, and spurious components are neglected.
The received wave from $R_u(t)$ is

$$R_u(t)=\left[\frac{T(\omega_0)}{2}+\int_0^{\omega_1}\frac{T_e(\omega)\sin\{\omega t+\theta_0(\omega)\}\cos\theta_e(\omega)+T_0(\omega)\cos\{\omega t+\theta_0(\omega)\}\sin\theta_e(\omega)}{\pi\omega}d\omega\right]$$

$$\times\cos\{\omega_0 t+\theta(\omega_0)+\alpha\}$$

$$+\left[\int_0^{\omega_1}\frac{T_0(\omega)\cos\{\omega t+\theta_0(\omega)\}\cos\theta_e(\omega)-T_e(\omega)\sin\{\omega t+\theta_0(\omega)\}\sin\theta_e(\omega)}{\pi\omega}d\omega\right]$$

$$\times\sin\{\omega_0 t\times\theta(\omega_0)+\alpha\}. \qquad (14)^*$$

When the amplitude characteristic has even symmetry to ω_0 and the phase characteristic has odd symmetry to ω_0, $R_u(t)$ becomes

$$R_u(t)=\left[\frac{T(\omega_0)}{2}+\frac{1}{\pi}\int_0^{\omega_1}\frac{T_e(\omega)\sin\{\omega t+\theta_0(\omega)\}}{\omega}d\omega\right]$$

$$\times\cos\{\omega_0 t+\theta(\omega_0)+\alpha\} \qquad (15)$$

From this equation, it is seen that the so-called equivalent low-pass characteristic[8)] is $T_e e^{j\theta_0}$, and the next theorem is obtained.
Theorem 2. "In the case of binary data transmission by an AM DSB system, if interference by spurious components is suppressed sufficiently, and the amplitude characteristic is even symmetrical to subcarrier frequency ω_0 and the phase characteristic is odd symmetrical to ω_0, then a component in quadrature to the subcarrier does not arise at all."

1.4. Noise and Error Rate

A binary data transmission system is a communication system which transmits digital data in the form of a binary signal and if there is noise in the transmission line, some mark signals are changed to space signals and vice versa.[9)] But aside from noise in the transmission line there is interference caused by the tails of the signals preceding and succeeding the particular signal, and if the signaling speed becomes higher and higher the signal distortion increases until it reaches a value which makes communication imposible. Interference caused by preceding and succeeding signals can be calculated from the indicial response,[10)] but the combined effects of circuit noise and interference from preceding and succeeding signals had not yet been examined. An analysis of this problem is shown in the following. Let us rearrange order of the interference $|\alpha_n|$ caused by the preceding and succeeding signals to the sampling point according to their absolute amplitude and designate them a_n, then we get the following series: $|a_1|\geq|a_2|\geq\cdots\cdots\geq|a_n|\geq|a_{n+1}|\geq\cdots\cdots$. If we neglect terms lower than $a_n|$, the number of combinations of interference becomes 2^n from R_1 to R_{2^n}. The envelope of the combined wave of single sinusoidal current and Gaussian noise current falls between Q and $Q+dQ$ with probability[11)]

$$p(Q)dQ=\frac{QdQ}{\varphi_0}\exp\left[-\frac{Q^2+V^2}{2\varphi_0}\right]I_0\left(\frac{QV}{\varphi_0}\right) \qquad (16)^{**}$$

where V is the amplitude of the sinusoidal current
φ_0 is the variance of the Gaussian noise
and I_0 is a modified Bessel function.

---

* See Appendix 3. ** See Appendix 4.

In a binary signal transmission system using AM DSB, the received current at the sampling point may be considered as a sinusoidal wave of amplitude R_i when the signal is a space. Therefore if the slicing level is s, the probability P_{1B} that the space signal is interpereted as mark becomes

$$P_{1B}=\int_S^\infty \frac{1}{2^n}\sum_j \frac{Q}{\varphi_0}\exp\left[-\frac{Q^2+R_j{}^2}{2\varphi_0}\right]I_0\left(\frac{QR_j}{\varphi_0}\right)dQ$$

$$=1-\int_0^S \quad /\!/ \quad dQ$$

$$=1-\frac{1}{2^n}\sum_{j=1}^{2^n}\sum_{m=1}^{\infty}\left(\frac{S}{R_j}\right)^m I_m\left(\frac{SR_j}{\varphi_0}\right)\exp\left(-\frac{S^2+R_j{}^2}{2\varphi_0}\right) \qquad (17)^*$$

And if the amplitude of the mark signal envelope at the sampling point is R_0, the probability P_{2B} that the mark signal is interpereted as space becomes

$$P_{2B}=\frac{1}{2^n}\sum_{j=1}^{2^n}\sum_{m=1}^{\infty}\left(\frac{S}{R_0+R_j}\right)^m I_m\left\{\frac{S(R_0+R_j)}{\varphi_0}\right\}\exp\left\{-\frac{S^2(R_0+R_j)^2}{2\varphi_0}\right\} \qquad (18)$$

From these equations, we can get the following formula as the error probability P_B, where the probability of mark and space are 1/2 respectively.

$$P_B=\frac{1}{2}+\frac{1}{2^{n+1}}\sum_{j=1}^{2^n}\sum_{m=1}^{\infty}\left[\frac{S}{R_0+R_j}I_m\left\{\frac{S(R_0+R_j)}{\varphi_0}\right\}e^{-\frac{s^2+(R_0+Rj)^2}{2\varphi_0}}-\left(\frac{S}{R_j}\right)^m I_m\left(\frac{SR_j}{\varphi_0}\right)e^{-\frac{s^2+Rj^2}{2\rho_0}}\right] \qquad (19)$$

where I_m is a modified Bessel function of the mth order.

But in actual practice the threshold level should be controlled according to the net loss variation of the transmission system in order to compensate for the variation, and the error probability is changed by the net loss variation. In other words, this compensation can be accomplished at the sacrifice of vulnerability to noise, and the analysis of this problem is described in Section 1.5.

1.5. Compensation for Net Loss Variation and Interference Caused by Noise

In an AM system the amplitude of the signal is used as information. Therefore, if the spectra of the net loss variation of the transmission system are the same as the spectra of the transmitted signal, compensation for the net loss variation cannot be accomplished at all. But, since net loss variation is caused by factors which change very slowly, like temperature, and the spectra of the variation are gathered in the low frequency region; therefore, these spectra can be separated from the signal spectra and the variation can be compensated for. For instance, the peak amplitude of the input signal can be obtained by a CR circuit which has a very short charging time constant and very long discharging time constant, and if one-half of the peak amplitude is used as the threshold level, then a communication system which is free from the net loss change is obtained. This compensation system is suitable for closed-circuit operation. But in open-circuit systems the subcarrier wave is not transmitted when communication is suspended; therefore, at the beginning of communication, bias current is zero and we cannot communicate until the bias current increases to its normal value. Furthermore, a system which is capable of compensating for sudden level change has been required recently, therefore in the present ECL experimental system the automatic net loss variation compensation system which consists of delay circuits and the usual threshold circuit has been adopted. The principle of this net loss variation compensation system is as follows:

---

* See Appendix 4.

At first the received wave is delayed 1.5 τ or 2.0τ where τ is the width of a unit pulse and from appropriate points in the delay circuit several outputs are taken; the largest of which is used as the bias current. However, if output current from the midpoint of the delay circuit is used as signal current, the relations between signal and bias becomes as shown in Figs. 11 (a) and 11 (b). It may easily be seen that this system is free from net loss variation. But other than the bias current from the received signal, direct current bias is used to suppress the interference from circuit noise when space signals are transmitted. The value of this direct current bias is determined according to compensating range of the net loss variation. For instance, if we want to compensate ±N dB variation, then one-half of the (normal level–N) dB signal amplitude should be chosen as the value of direct current bias. As the threshold level of the simple slicer is one-half of signal level, this compensation system is liable to error from circuit noise more frequently than a simple slicer when the signal is space. The effective signal to noise ratio is lowered by as much as N dB. The net loss vs. signal distortion characteristic of this system is shown in Fig. 12. The compensation response of this system to net loss variation is very quick and interference by sudden change of net loss can be eliminated within 2 or 3 unit pulses.

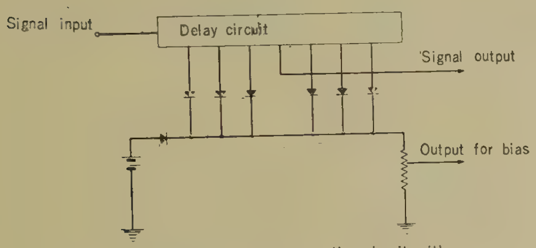

(a) Net loss variation compensating circuit with delay line

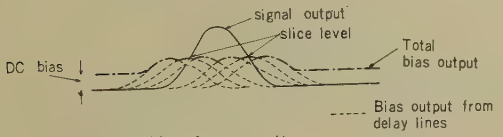

(b) Illustration of compensator

Fig. 11—Net loss variation compensating circuit and its signal waveforms.

1.6. Frequency Response of Carrier Telephone Line in Japan and Limit of Signaling Speed

There are many kinds of carrier telephone systems in Japan and they have different characteristics from each other. Among these characteristics the frequency response of the telephone line and distribution of the noise level are the most important factors relating to data transmission performance. The frequency response of the telephone system

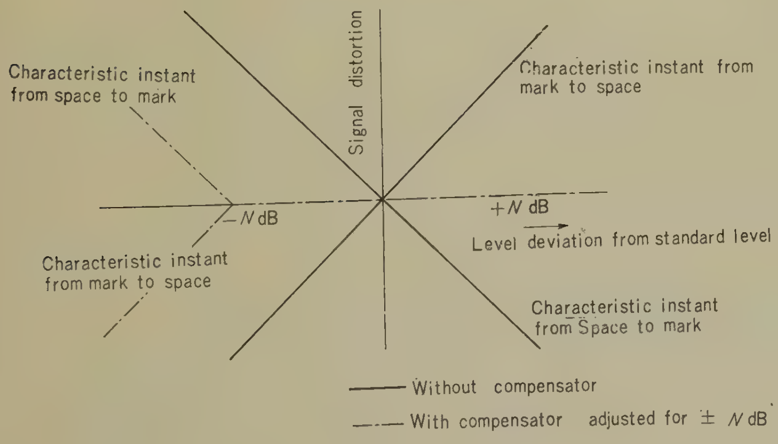

Fig. 12—Illustration of characteristics of net loss variation compensator with delay line.

mainly depends on the frequency characteristics of the channel filter and channel amplifier and does not depend on the type of carrier telephone system. A typical example of the frequency response is shown in Fig. 13. If subcarrier frequency is selected appropriately, the attenuation characteristic and group delay characteristic are both symmetrical to the subcarrier. These characteristics were approximated as a function of frequency in the form of the 8th order polynomials. These approximating formulas were substituted in equation (15) and the integral in (15) was calculated numerically with the M-1 computer, which was developed at the ECL. The results are shown in Figs. 14, 15, and 16. Interferences $|\alpha_n|$ which correspond to various widths of the unit pulse are shown in Table 1. Here sampling point t is given by the following formula

$$t=t_0+\frac{2n+1}{2}\tau \qquad (20)$$

where t_0 is the time of the indicial response across 1/2 of asymptotic value of the response, and τ is the width of the unit pulse. If we substitute these values into equation (4), the relation between the modulation speed and its margin is obtained. These values are also given in Table 1. From these results it is observed that if there is no interference caused by circuit noise the limit of signaling speed is about 3000 baud.

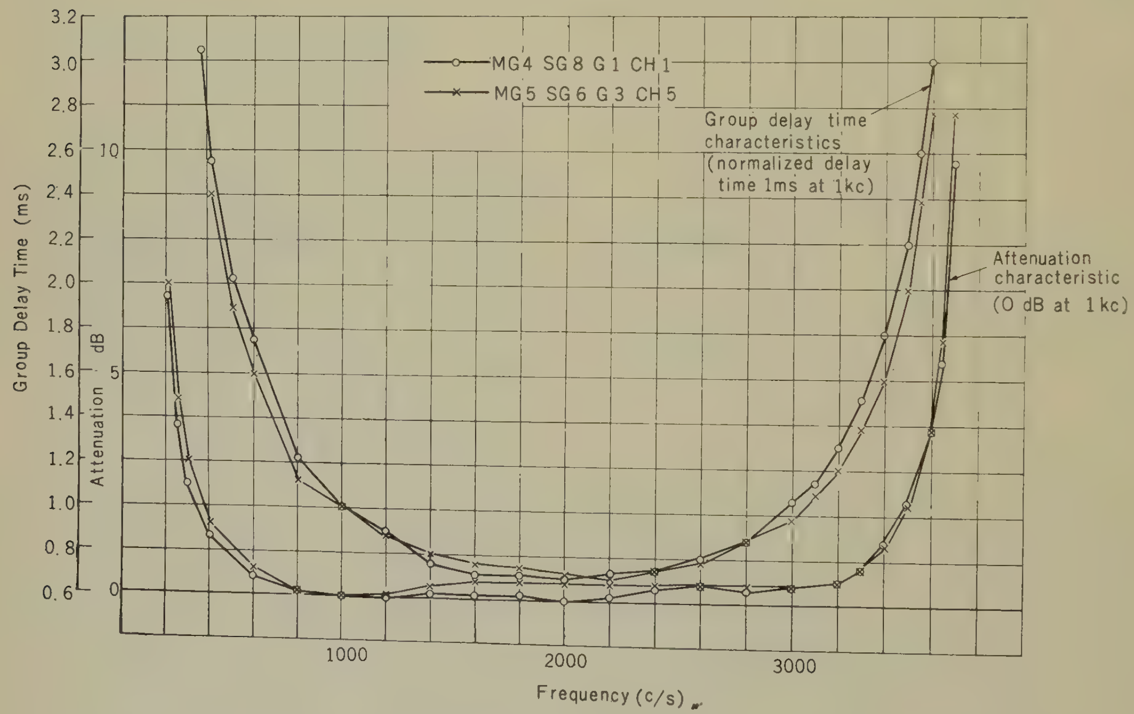

Fig. 13—Frequency characteristics of carrier telephone channels. (12 Mc coaxial transmission system between Takasaki and Kumagaya)

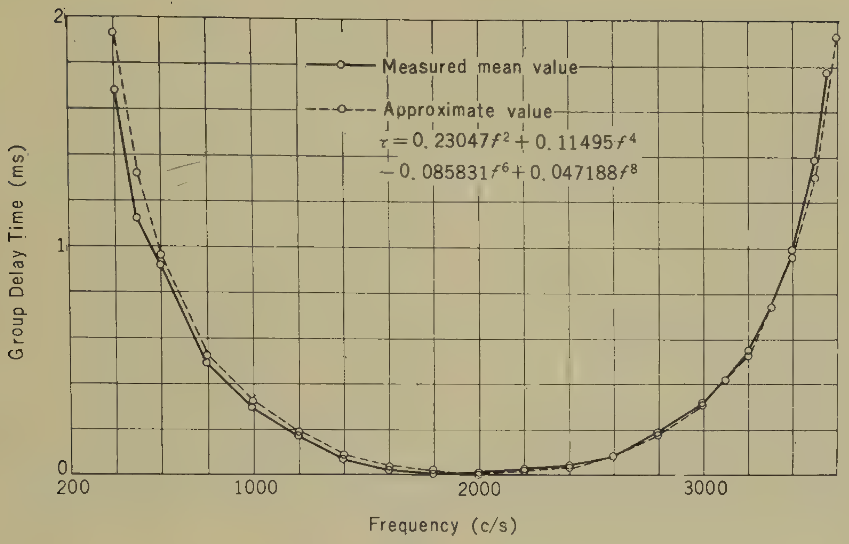

Fig. 14—Group delay time characteristics.

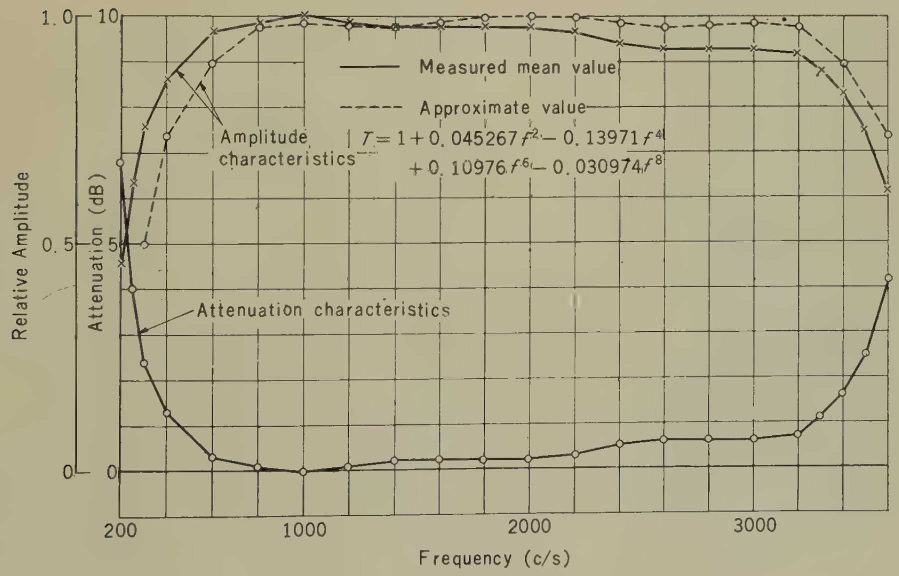

Fig. 15—Transmission characteristics.

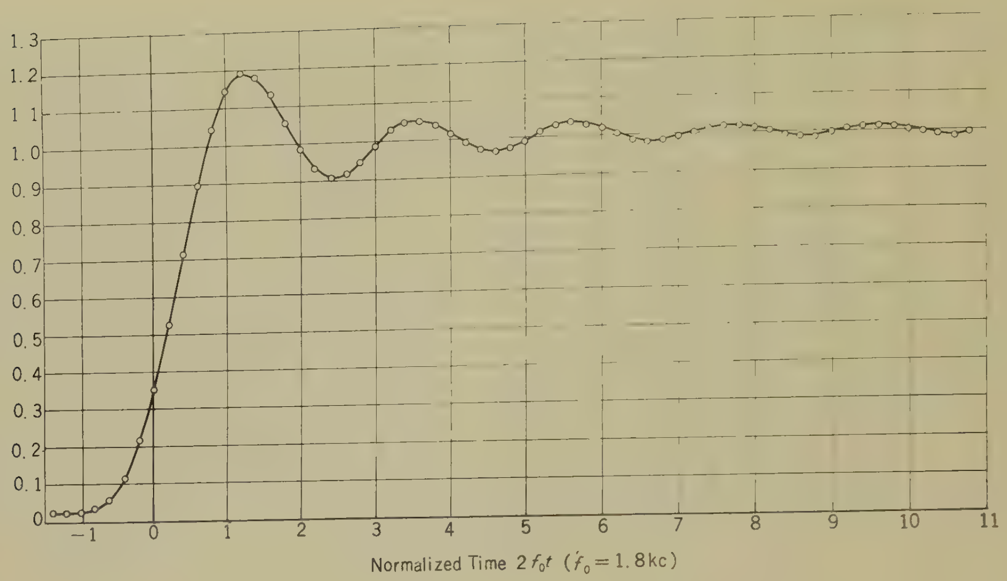

Fig. 16—Unit response of carrier telephone channel. (envelope in AM DSB system)

Table 1

Width of Unit Pulse	1.0	1.2	1.4	1.6	1.8	2.0
Signaling Speed	3600 baud	3000 baud	2560 baud	2250 baud	2000 baud	1800 baud
a_{-1}	0.1417	0.0995	0.0881	0.0644	0.0445	0.0309
a_0	0.8007	0.9245	1.0045	1.0857	1.1220	1.1584
a_1	0.1277	−0.0556	−0.1719	−0.2274	−0.1978	−0.1616
a_2	−0.1621	0.0419	0.1256	0.0735	0.0003	−0.0157
a_3	0.1142	−0.0581	−0.0452	0.0385	0.0153	−0.0065
a_4	−0.0772	0.0636	−0.0157	−0.0112	0.0122	0.0047
a_5	0.0618	−0.0510	0.0305	−0.0208	0.0044	*
a_6	−0.0485	0.0301	−0.0051	−0.0096	*	*
a_7	0.0408	−0.0021	−0.0163	*	*	*
a_8	−0.0334	−0.0113	*	*	*	*
a_9	0.0266	*	*	*	*	*
a_{10}	−0.0219	*	*	*	*	*
$\sum_{i\neq 0} \lvert a_i \rvert$	0.8559	0.4132	0.4984	0.4454	0.2745	0.2194
M	0 (−3 %)	25 %	26 %	32 %	42 %	47 %

2. Experiments on Data Transmission

2.1. Object and Outline of Experiments

In Section 1, theoretical analysis of data transmission by an AM DSB system has been described. In this section experimental analysis will be described. Main purposes of these experiments are

1. to analyze problems of data transmission which could not be solved theoretically
2. to obtain the practical limit of signaling speed experimentally
3. to verify the results of theoretical analysis of data transmission problems.

Moreover, in the theoretical analysis, many conversion processes (for example, the modulation process and detection process) have been assumed to be ideal but in actual practice these processes are not perfectly ideal so that it is necessary to ascertain experimentally that the theoretical results calculated under these simplifying assumptions are correct.

For the purpose of achieving the above object it is necessary to have a standard binary data transmission system with a binary signal generator and signal distortion measuring set. In actual practice it is very difficult to test transmission performance of a part of the system separately. For example, modulator performance can be tested together with demodulator performance; however, it is very hard to determine modulator performance only separated from demodulator performance. But if modulator performance is ideal then the combined performance of modulator and demodulator may be equal to demodulator performance alone. Therefore, if we have an ideal data transmission system we are able to test each part of any transmission system. In this meaning this standard binary data transmission system is very similar to SFERT or ARAEN in the case of speech transmission. The ECL experimental system was designed to satisfy these requirements and signal distortion arising in this apparatus is very small. This system consists of a signal generator, a sending modulator, a sending amplifier, a receiving amplifier, a demodulator, a signal distortion measuring set, etc. The present ECL experimental system was made to test data transmission by an AM DSB system, but if we replace only the modulator and the demodulator with another kind of modulator and demodulator then of course we are able to test the data transmission performance of other kinds of modulation systems.

2.2. Description of the ECL Data Transmission Testing Set (Standard Binary Data Transmission System)

This apparatus was made to test binary data transmission performance through the ordinary telephone line. The front view of the system is shown in Figs. 17 (a) and 17 (b); Fig. 18 is the schematic diagram. At

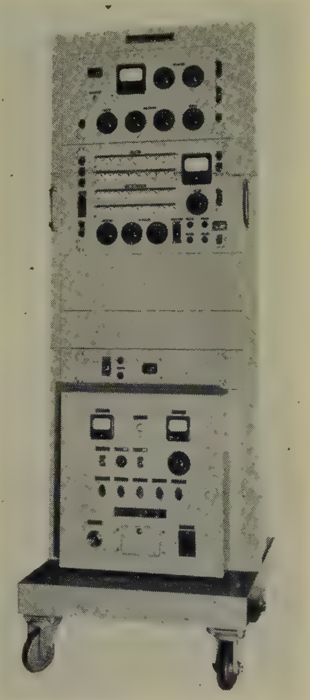

Fig. 17 (a)—Front view of data transmission testing set. (binary code generator and distortion measuring set except cathode ray oscilloscope)

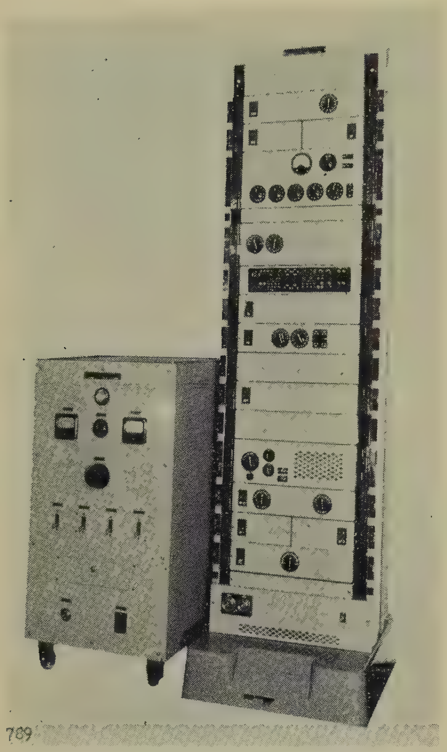

Fig. 17 (b)—Front view of data transmission testing set. (Left: power supply equipment, Right: binary data transmission terminal equipment)

first, let us consider data transmission from station A to station B. As described in Section 1.1 the receiver must sample the received signal at appropriate time points, detect the polarity of the signal, and reproduce the original binary signal series. The process of determining this sampling point is called bit synchronizing. Furthermore a letter signal consists of several bits and the process of selecting the group of a letter signal from a series of binary signals is called letter synchronizing.[12] In general, data transmission performance is expressed by error rate but there are two kinds of error; one kind is errors caused by signal distortion and the other is errors caused by mis-synchronizing. These two kinds of error should be distinguished strictly. We must test the transmission per-

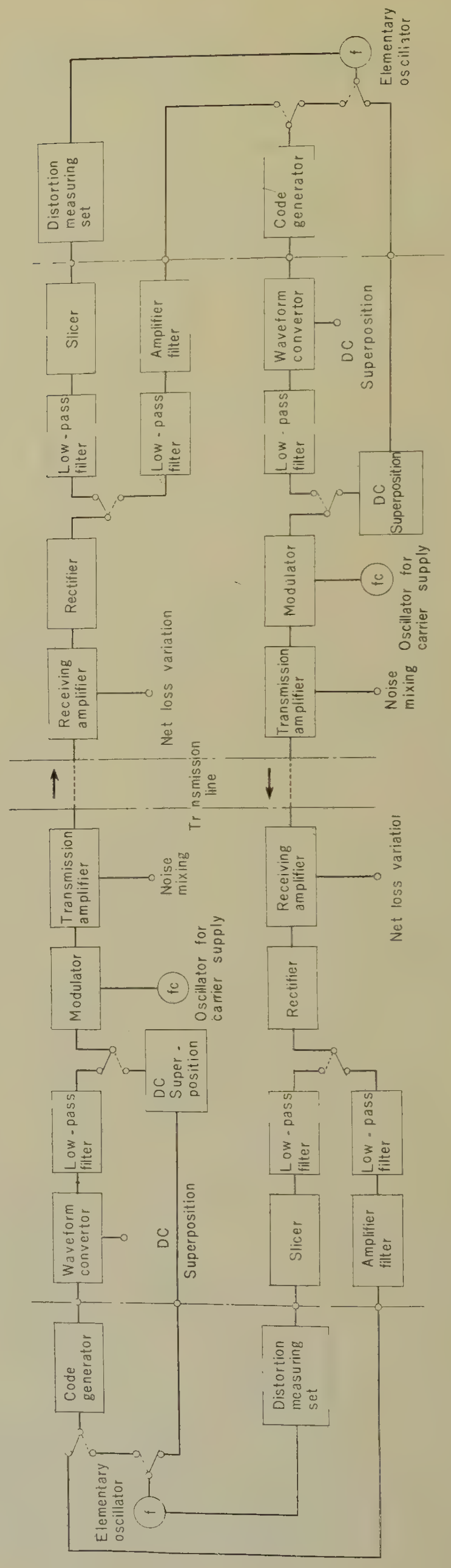

Fig. 18—System diagram of experimental equipment for binary signal transmission test.

formance under perfect synchronizing conditions, otherwise test results will differ according to the synchronizing method. In a loop circuit it is easy to test transmission performance under perfect synchronizing conditions but in the case of point to point communication it is very difficult to synchronize perfectly. In the ECL system standard frequency is sent through the line from B station to A station by the AM SSB system as synchronizing information and this frequency is used in station A for signal generation and in station B for measuring signal distortion. In station A, the received synchronizing signal from station B is led into an amplifier-filter, and interference caused by circuit noise, net loss variation, etc. is removed in this amplifier-filter.

The low-pass filter at the sending station was designed in accordance with the theory described in subsection 1.3.1. and the sending modulator and sending amplifier were designed to prevent the generation of signal distortion in the circuits. In addition, a noise superposing circuit is attached to this sending amplifier and it is used to test effects of circuit noise. The receiving amplifier has a facility to simulate net loss variation in the telephone line (by external drive). The demodulator is a full wave linear rectifier with a low pass filter. In the shaping circuit, a net loss variation compensating circuit, whose compensating region is arbitrarily variable, and a simple slicer are used.

When we use this set as a standard binary data transmission system, it is unnecessary to transmit standard frequency and only the apparatus which is shown in upper half of the schematic diagram is used. In this case, if we replace the transmission line with networks which have various frequency responses then the relations between data transmission performance and frequency characteristic of line are obtained; and, as described before, interference caused by net loss variation and circuit noise can be tested too.

2.2.1. Binary Signal Generator and Signal Distortion Measuring Set

1) Binary signal generator

This apparatus is driven by an f c/s sinusoidal wave and generates an f baud signal with a $2\sim16$ bit pattern. At least a 10 bit pattern will be required as a test signal to examine the characteristic distortion of the transmission system and for reasons of circuit construction a 2^n bit pattern is very convenient; therefore maximum pattern length was selected as 16 bits. Output voltage is ± 10v to a 10kΩ load. In Fig. 19 the schematic diagram and waveforms of each part are shown. At first the f c/s sinusoidal current is amplified, sliced, and then a $2f$ baud 1:1 signal is obtained. This 1:1 signal is led into 4-stages of flip-flop circuits, and the outputs of each stage are passed through a matrix circuit; therefore 16 fundamental signals are obtained and these fundamental signals are used to generate the 16 bits signal pattern. Combinations of 16 bits can be freely selected by push-buttons which are connected to OR-gate circuits.

However, the output signal of the OR-gates has a little distortion caused by the time delay of the flip-flop circuits, and moreover there is a short split between each bit. Therefore this output and the differential pulse of a $2f$ baud 1:1 signal are fed into an AND-gate circuit whose output is used as a test pattern. The distortion of this binary signal generator output is less than 0.1% at 2500 baud. Furthermore, pattern length is freely changeable by resetting the flip-flop circuit at any point. The main specifications of this signal generator are as follows.

Pattern length	from 2 to 16 bits
Signaling speed	1000, 1250, 1500, 1750, 2000, 2250, 2500 baud It is possible to transmit a higher speed signal by external drive.
Output voltage	±10v to 10kΩ load (double current signal)
Combinations of signal pattern	freely changeable by push-button

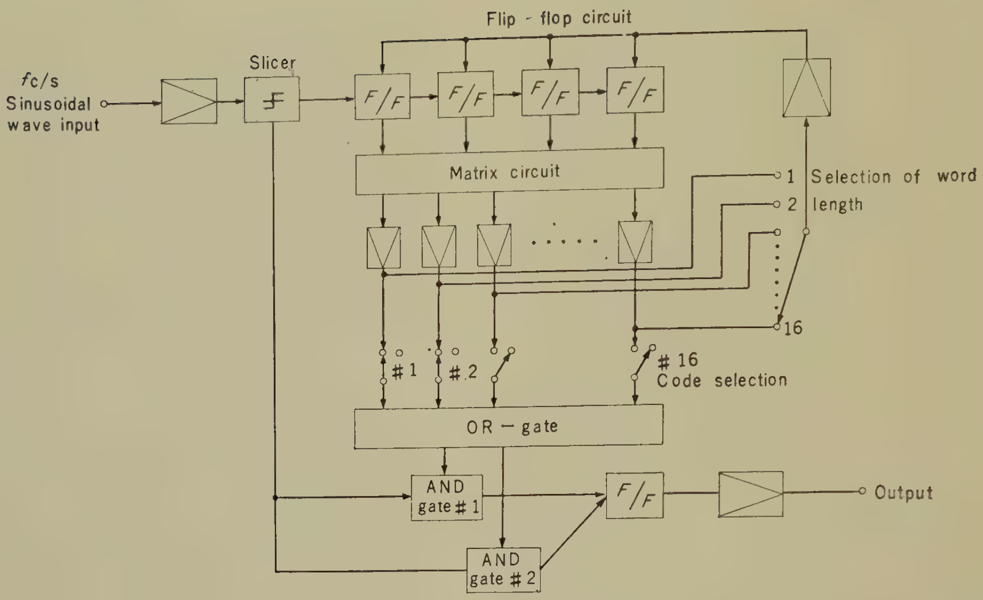

(a) Block diagram

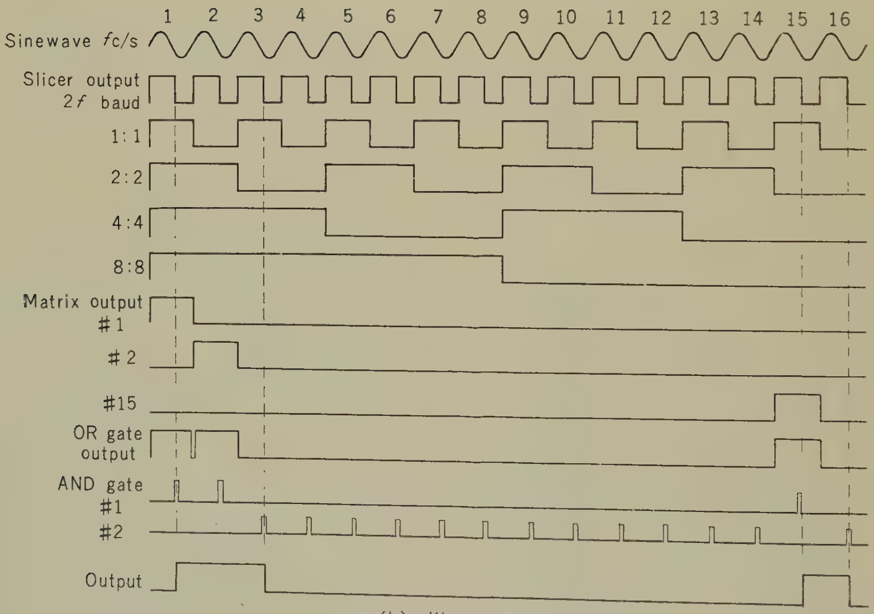

(b) Waveform in Each Part

Fig. 19—Code generator.

2) Signal distortion measuring set

Transmission performance of a binary signal transmission system can be expressed by an error-rate. But beside the error rate, margin and signal distortion are used to designate allowance for error. In this case margin (defined in Section 1.1) expresses vertical allowance for error. In Fig. 20, R is received signal waveform, s is slice level, and the dotted lines represent ideal characteristic times. If the unit pulse length τ, then distortion d may be expressed as

$$d=\frac{\Delta\tau}{\tau}\times 100\,\%.$$

Generally, the error rate of a binary data transmission system is so small that it takes a long time to measure transmission performance by error rate, but signal distortion can be measured in a comparatively short time. If we have data concerning circuit noise and circuit interruption then we are able to estimate the error-rate of the system. In telegraph transmission, signal distortion has been used as a measure to designate transmission performance in various countries. However, in the case of high speed data transmission only error-rate is used as a measure throughout the world, but signal distortion may be more convenient to use than error-rate. And it is easier to make a distortion measuring set than to make a margin measuring set; therefore in the present analysis signal distortion is adopted as a measure to investigate transmission performance.

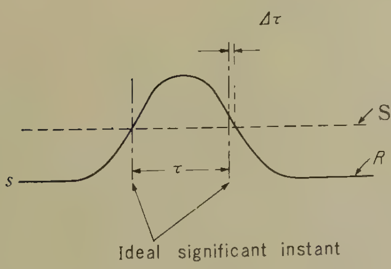

Fig. 20—Received signal and distortion.

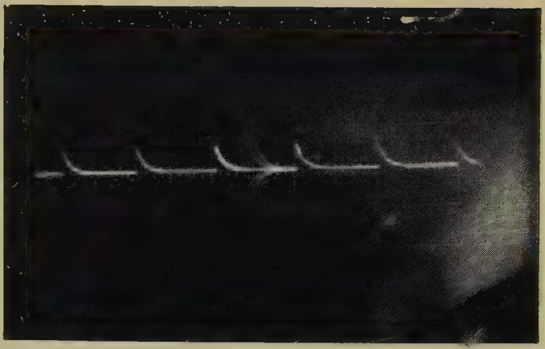

(a) 2 cm 10 %

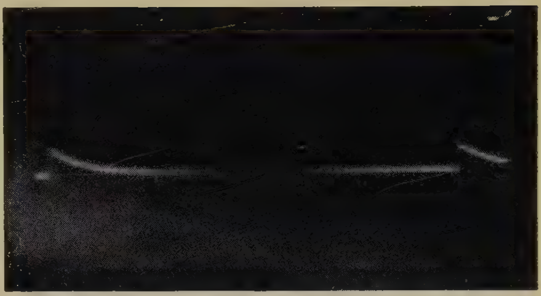

(b) 10 cm 10 %

Fig. 21—Waveforms as seen on distortion measuring set cathode-ray oscilloscope.

The signal distortion measuring set consists of a standard pulse generating circuit and a cathode-ray oscilloscope. Its schematic diagram is shown in Fig. 22. The standard pulse generating circuit is very much like the circuit of the binary signal generator except that a $10f$ c/s oscillator, a 10:1 frequency divider, and a 10 % time-marker pulse generating circuit are added. The most important problem when we make a signal distortion measuring set is how to obtain the standard time. One method is to take the characteristic instant of the sending signal at the sending station as the standard time and to measure the transmission time of this characteristic instant from the sending station to

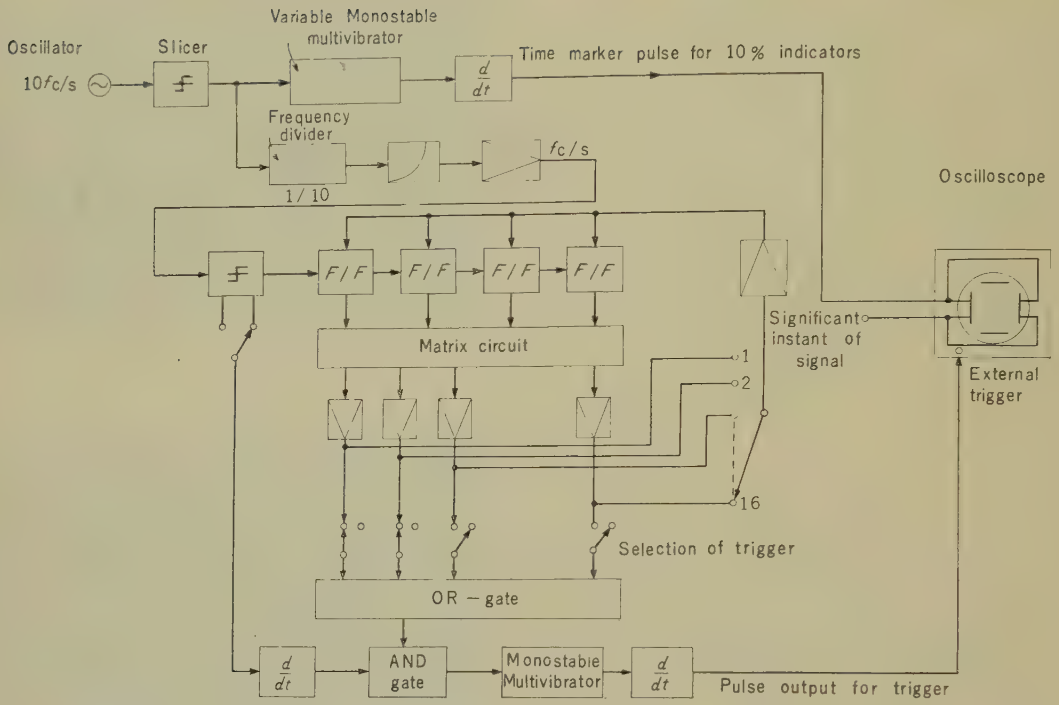

Fig. 22—Distortion Measuring Set.

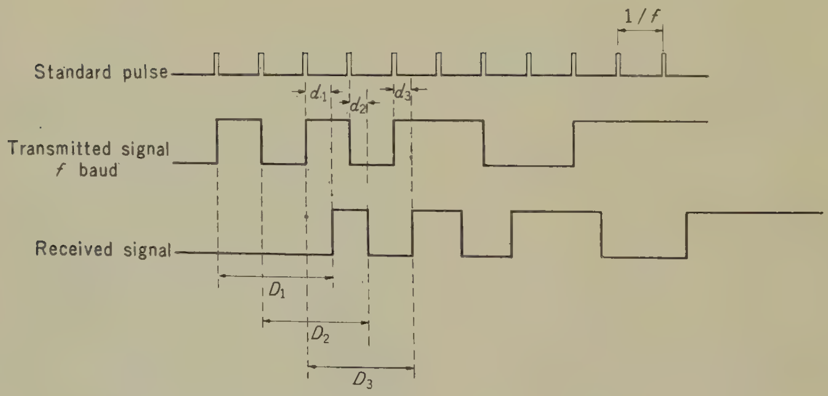

Fig. 23—Principle of measuring isochronous distortion.

receiving station but this method can not be used except for loop-circuit measurement.

However, the absolute transmission delay is not necessarily important and the maximum difference between each transmission delay should be measured; therefore in Fig. 23 we may measure differences between d_i instead of measuring D_i. This means that if we have standard pulses which are arranged in $1/f$ sec intervals, we can measure distortion arising in the transmission line between distant stations. The signal distortion which is measured by this method is called isochronous distortion[13)] and the ECL distortion measuring set is able to measure the distortion of 16 characteristic instants separately or simultaneously. Fig. 21 shows waveforms on the oscilloscope; in which the short pulses are 10% time markers and the long pulses are characteristic instans of the received signal. By an external scale we can measure the distortion with a precision of 0.2%.

2.2.2. Binary Data Transmission System

The outline of the system was already explained in Section 2.1; in this section details of each part will be described.

1) Waveform converter

As the output of the binary signal generator is a double current rectangular wave of ±10v, it must be converted to a single current wave to drive the ring modulator. This waveform converter changes the ±10v signal to a 0 to +4v single current signal. The output level of the ring modulator is exactly proportional to the input single current level, and the output level of the waveform converter is maintained at a constant value by a zener diode irrespective of power source variation, temperature variation, etc. The output impedance is 600Ω ±30Ω irrespective of signal polarity, and direct current can be superposed on the output current. This superposed direct current is used to prevent the output current of low pass filter from becoming negative value and to introduce fortuitous distortion.

2) Sending low-pass filter

This is used to suppress the spurious component as described in subsection 1.3.1. A Tschebyscheff filter and a flat delay filter with a frequency response as shown in Fig. 24 are used. A frequeucy response curve of low pass equivalent of typical telephone line is also shown in Fig. 24.

3) Modulator

A ring modulator is used but the signal current and subcarrier input terminals are interchanged to transmit the direct current component of the binary signal. Gold-bonded germanium diodes are used as modulator elements in order to suppress unwanted spectra. Input and output transformers are carefully balanced to ground. The circuit diagram and overload characteristic are shown in Fig. 25.

4) Sending amplifier

A high-power amplifier is used to test the effect of superposed noise. Second and third harmonic distortion are less than −70 dB and −50 dB respectively when the output level is 30 dbm and superposed noise does not cause overloading.

5) Receiving amplifier

An average gain of 45 dB and an attenuation equalizer are provided in this amplifier. External drive enables this amplifier to simulate slowly changing net loss variation of ±5 dB.

6) Amplifier-rectifier

A linear full wave rectifier is used. Total gain is about 5 dB; output impedance is nearly 600Ω.

7) Receiving low pass filter

A Tschebyscheff filter, flat delay filter, and raised cosine response filter are used to detect the signal component from the output of

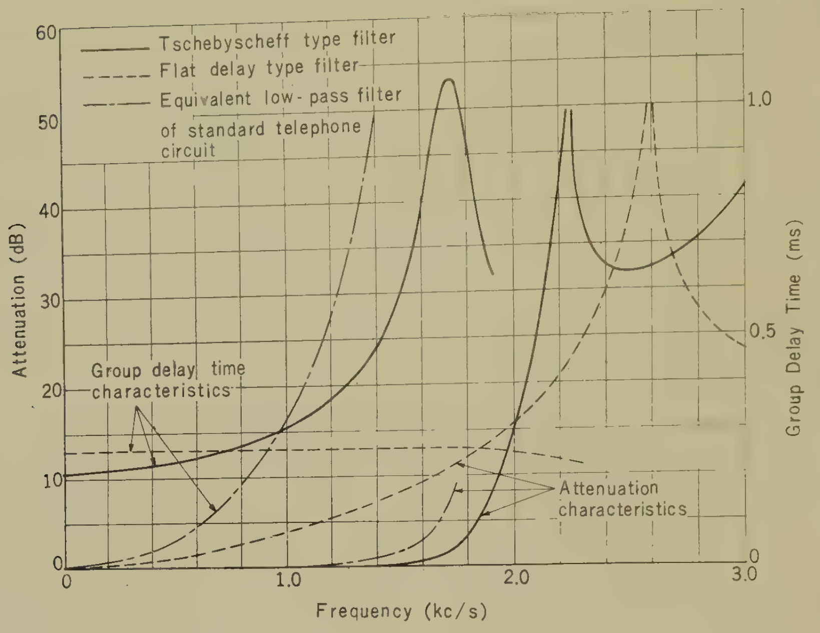

Fig. 24—Frequency characteristics of transmitting filter.

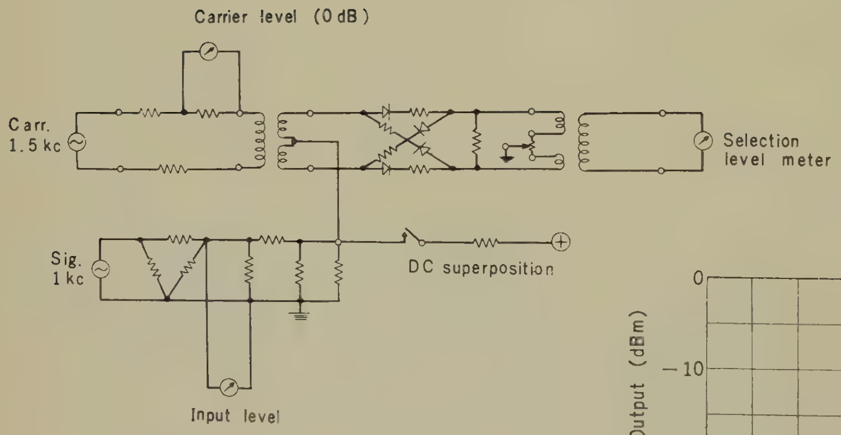

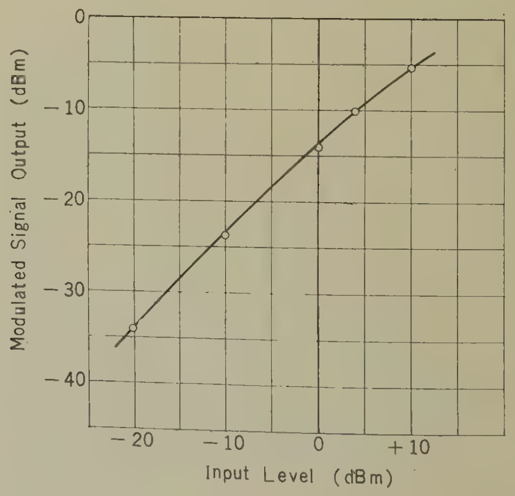

Fig. 25—Overload performance of modulator.

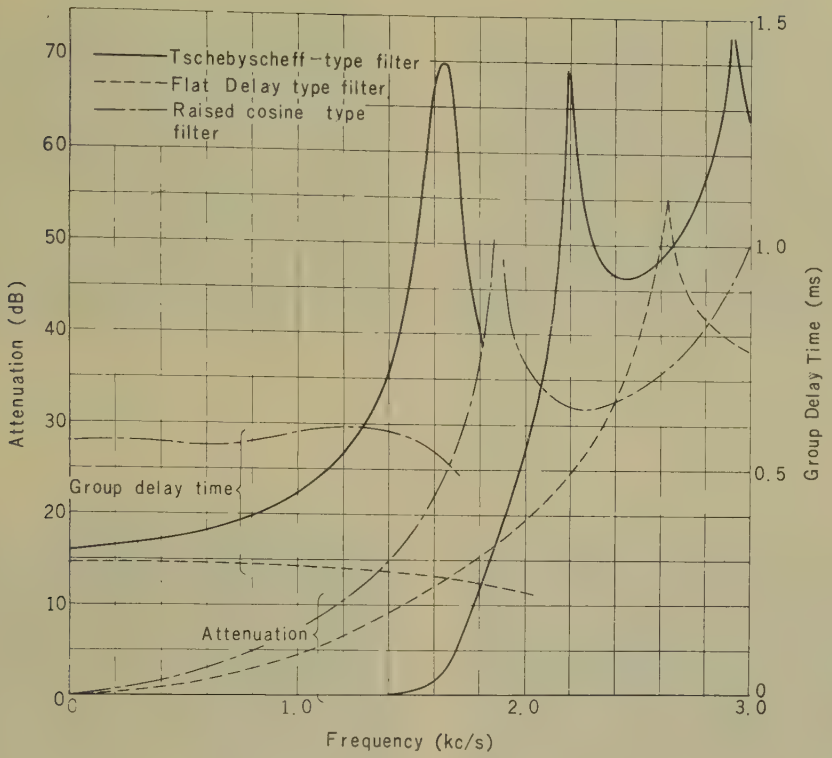

Fig. 26—Frequency characteristics of receiving filters.

the amplifier-rectifier. Their characteristics are shown in Fig. 26.

8) Shaping circuit

The shaping circuit consists of a simple slicer and a net loss variation compensating circuit. Input voltage to the compensating circuit must be about 3v; output is about ±10v to a 10kΩ load. Compensating range is arbitrarily variable.

9) Amplifier-filter

The amplifier filter is used to detect the standard frequency. Its tuning frequency is variable between 1 kc to 2.5 kc according to the signaling speed.

2.3. Experimental Results

When binary signals are transmitted through a telephone channel, the signals are distorted owing to amplitude and phase distortion of the channel; and are disturbed by line noise, net loss variation, etc. The disturbances owing to net loss variation and line noise are dynamic and fluctuate rapidly or slowly with time, while amplitude and phase distortion are static and do not fluctuate with time. Inflences of dynamic disturbances on binary data transmission are different according to the type of net loss variation compensating system. Thus, the experiment was carried out in two steps: One step is the experiment of binary data transmission without noise and net loss variation, and the other is the experiment on net loss variation compensating circuit and influences from noise. Such experimental results will be shown in turn and will be examined carefully.

2.3.1. Binary Data Transmission Performance of Experimental Sets and Telephone Channels

To begin by examining the performance of each part of the set, binary signal waveforms at the outputs of these parts are shown in Fig. 27. In this case, a Tschebyscheff type filter is used as a transmitting filter and a flat delay type filter is used as a receiving filter. Instead of transmission line, variable low pass filters and variable high pass filters are used. The resultant band pass filter transmits frequencies from 150 c/s to 4200 c/s. This test is carried out at signaling speeds of 1000 baud and 2000 baud, with subcarrier frequency is fixed at 1900 c/s.

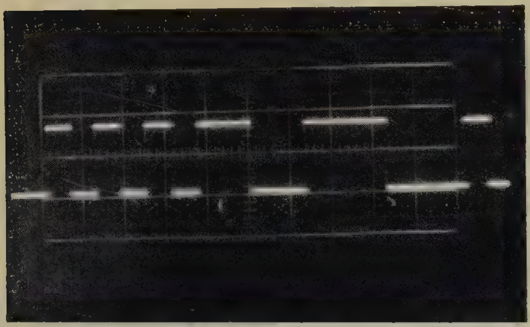

(a) Input signal.

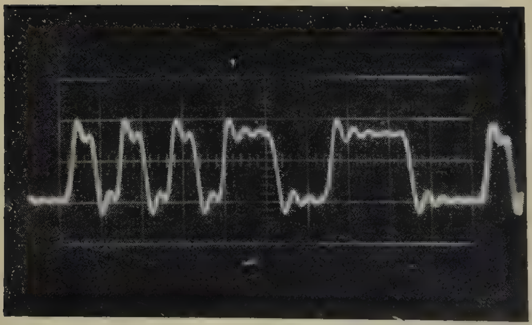

(b) Sending low-pass filter output.
(Tschebyscheff type)

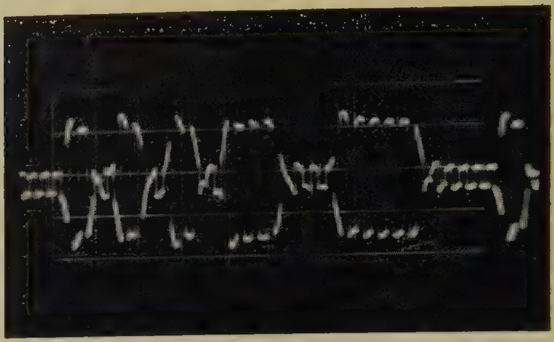

(c) Modulator output.

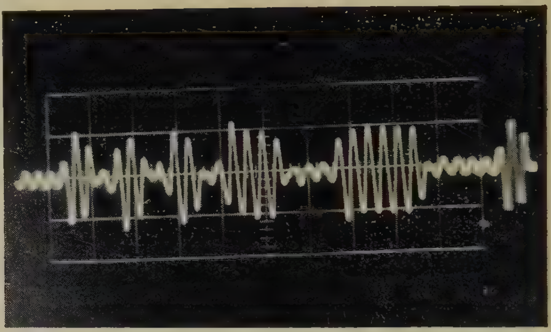

(d) Receiving amplifier input.

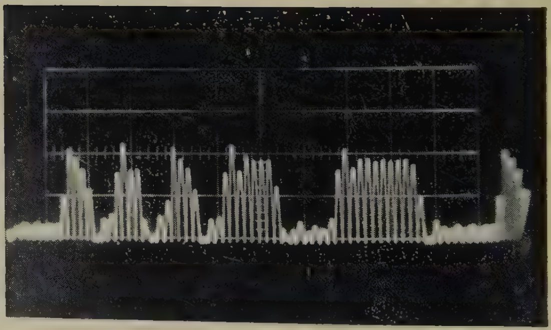

(e) Linear full-wave rectifier output.

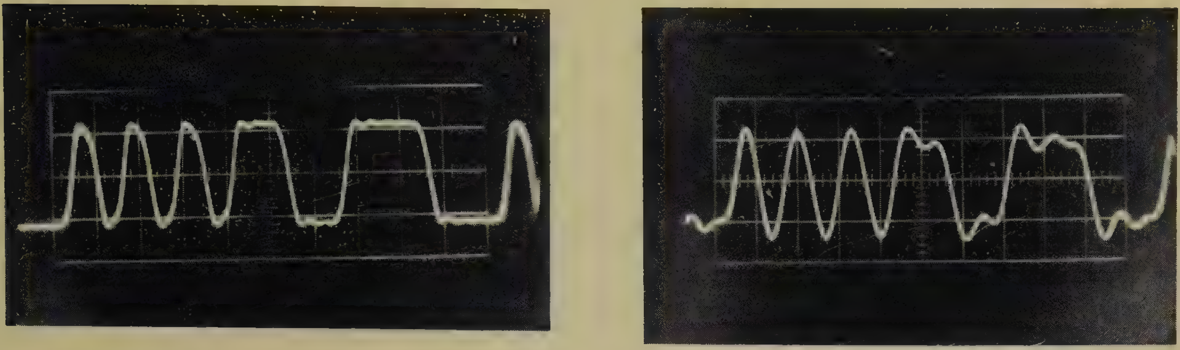

(f) Receiving low-pass filter output. (Flat delay type)

(b) Sending low-pass filter output. (Tschebyscheff type)

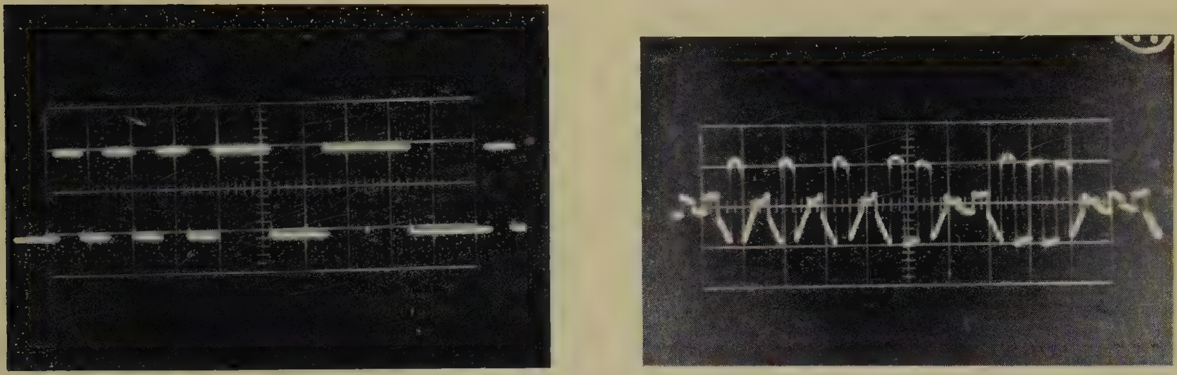

(g) Output signal.

(c) Modulator output.

Fig. 27 (A)—Waveforms of transmitted signal. (signaling speed 1000 baud; subcarrier 1950 c/s)

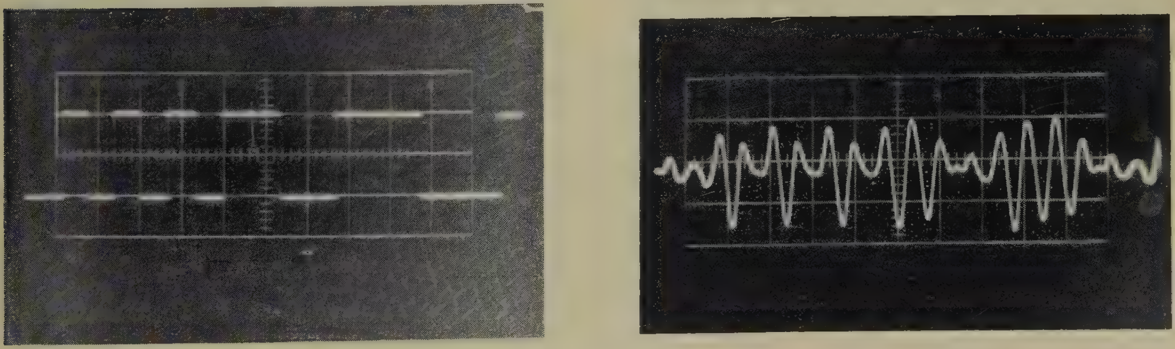

(a) Input signal.

(d) Receiving amplifier input.

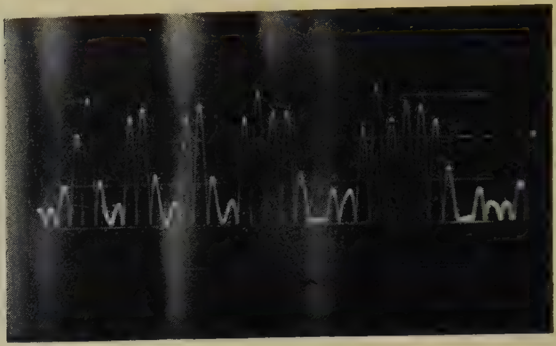

(a) Linear full wave rectifier output. (Relative phase difference between signal and subcarrier=0)

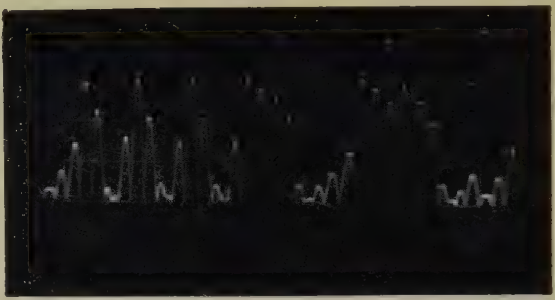

(b) Linear full wave rectifier output. (Relative phase difference between signal and subcarrier=$\pi/2$)

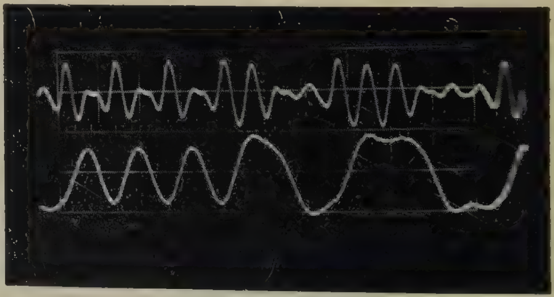

(c) Receiving amplifier input and receiving low-pass filter output. (phase difference=0)

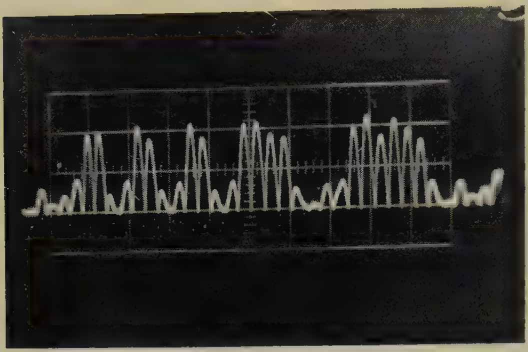

(e) Linear full wave rectifier output.

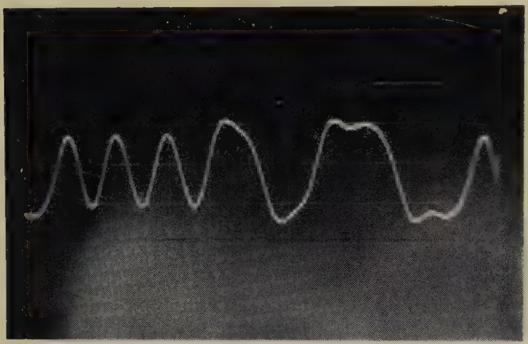

(f) Receiving low pass filter output. (Flat delay type)

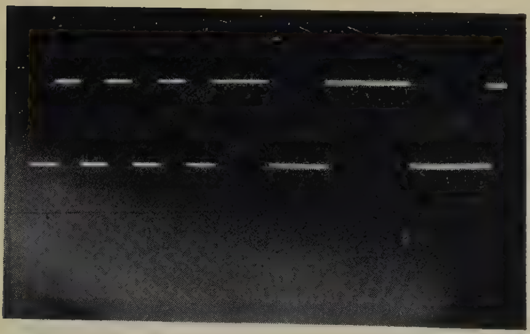

(g) Output signal.

Fig. 27 (B)—Waveforms of transmitted signal. (Signaling speed 2000 baud; subcarrier 1950 c/s)

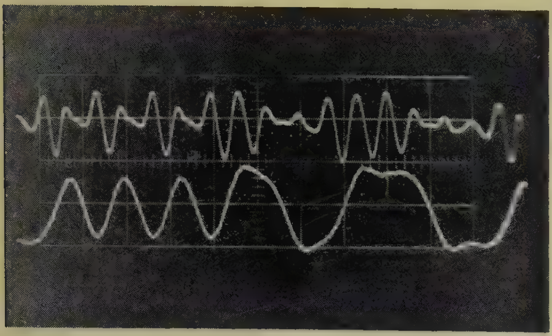

(d) Receiving amplifier input and receiving low-pass filter output. (phase difference $=\pi/2$)

Fig. 28—Effects of relative phase difference between signal and subcarrier. (signaling 2000 baud; subcarrier 2000 c/s)

Next, Fig. 28 illustrates waveforms at the outputs of transmission line, full wave rectifier, and receiving low pass filter when relative phase differences between binary signal and subcarrier are 0 and $\pi/2$, where signaling speed is 2000 baud and subcarrier frequency is 2000 c/s. As seen in the figure, the signal waveforms at the output of the receiving filter scarcely differ from one another, and the degree of fortuitous distortion caused by such phase difference does not reach 1%. This demonstrates the conclusion which is described in subsection 1.3.1.

Now, as described in subsection 2.2.1, signal distortion is adopted as an index to show binary data transmission performance in the ECL experimental system. All data following will be represented by (isochronous) distortion. Furthermore, it is noted that in the following experiments only "1010101100111000" and its inverse are used as code patterns. These code patterns would be expected to generate a larger characteristic distortion than any other combination of codes.

Fig. 29 shows the distortion characteristics when the transmitting filter is directly connected in tandem with the receiving filter. As the image impedance of the flat delay filter is 600 Ω pure resistance, direct connection causes no inconvenience.

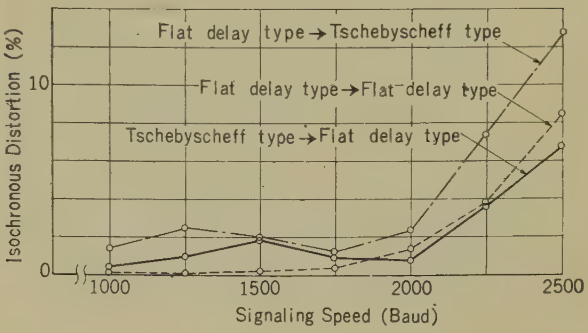

Fig. 29—Distortion performance of some filter combinations.

The transmission performance including the modulation and demodulation process is shown in Fig. 30. In this case, as the transmitting amplifier is directly connected with the receiving amplifier, performance is not influenced by transmission line characteristics, but the degree of signal distortion is increased as compared with the distortion of the direct current system (Fig. 29) by useless frepuency components produced in the modulator due to the unbalance of the modulation elements and insufficient suppression of spurious components. According to this result the distortion increases only 1% at 2000 baud and

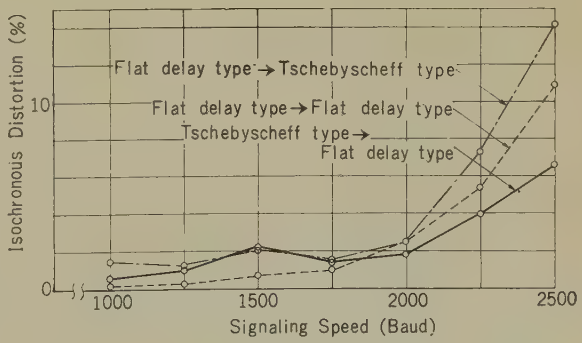

Fig. 30—Total distortion performance of experimental set.

2% at 2500 baud. Finally as an example of binary data transmission performance through a telephone channel, signal distortion characteristics are shown in Fig. 31. In this case the 12Mc coaxial cable carrier system, which is now being tested for reliability, was used. The difference of distortion characteristics between Figs. 30 and 31 is considered as reduction of performance owing to the limitations of the frequency band by the telephone channel used, but the amounts of the reduction are different according to filter combinations. The fact that distortion with the Tschebyscheff type and flat delay type filter combination is worse than distortion with the two flat delay type filter combination is caused by phase distortion of the Tschebyscheff type filter, and quadrature components owing to the asymmetry of line attenuation characteristics about the subcarrier frequency of 2 kc/s. When a flat delay filter is used at the sending station, the asymmetry of the line characteristics may be corrected by the narrow band characteristics of the transmitting flat delay filter (see Fig. 32). From the results mentioned above, it seems that the filter combination of two flat delay types is the best from the standpoint of distortion characteristics but in practice we must choose the combinations from considerations of other points such as vulnerability to noise and net loss variation.

2.3.2. Binary Data Transmission Performance of Net Loss Variation Compensating Circuit

(1) Net loss variation compensation characteristic

Figs. 33 (a), (b) are signal distortion characteristics to input signal level when a band pass filter, whose characteristic is shown in Fig. 34, is used as the transmission line. A compensating range of ± 3 dB is chosen; if the input signal level decreases below −3 dB, its distortion increases suddenly. Theoretically, at input signal levels over −3 dB, the curves should be parallel to the axis of abscissas, but the curves have small positive and negative slopes. This comes from the fact that, if input signal level increases, current in the diodes (see Fig. 11) increases and decrease of diode resistance makes the

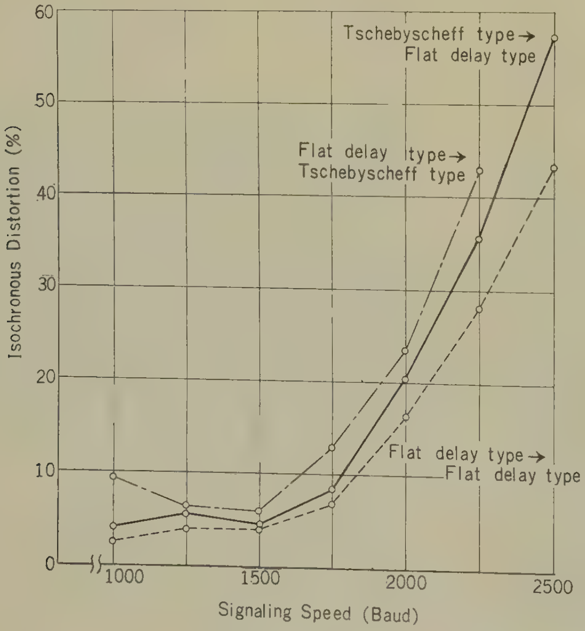

Fig. 31—Distortion performances when used over telephone channel.

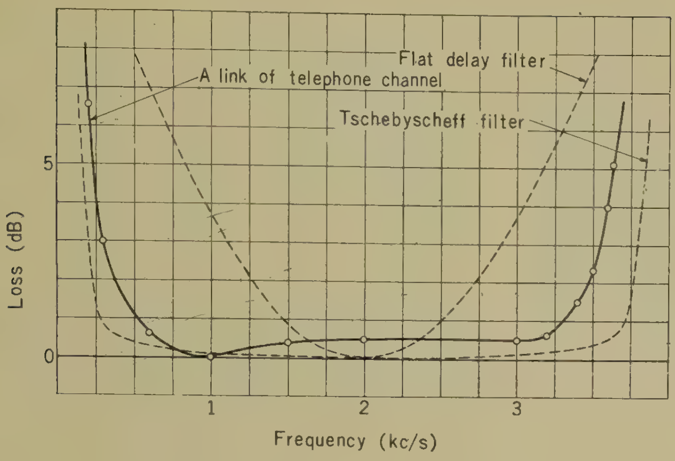

Fig. 32—Equivalent bandpass characteristics of transmitting filters.

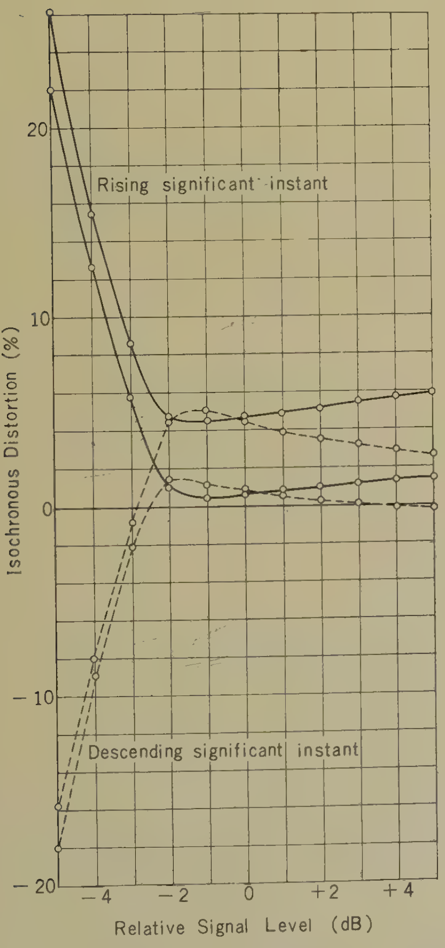

Fig. 33 (a)—Level compensating performance of slicer with delay line at 1500 baud. (Tschebyscheff filter as transmitting filter and flat delay filter as receiving filter).

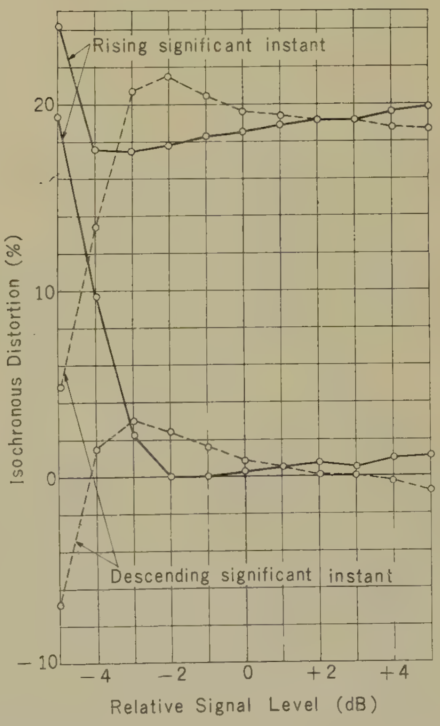

Fig. 33 (b)—Level compensation performance of slicer with delay line at 2000 baud. (Filter combination is same as Fig. 33. (a)).

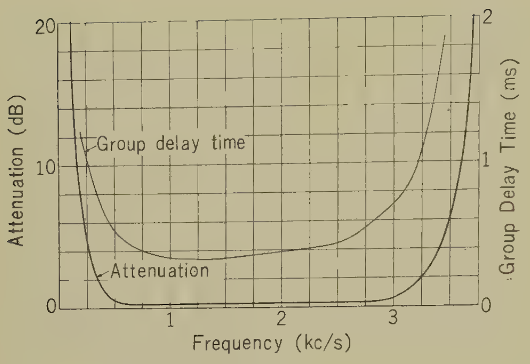

Fig. 34—Frequency characteristics of transmission channel.

AC bias higher than the design value.

At standard input signal level, this level compensating slicer has more distortion than a simple slicer because at higher modulation speeds different code combinations have different peak voltages and AC bias differs in each case. These phenomena are explained in Fig. 35.

Figs. 36 and 37 show distortion performance of this compensator when it is adjusted for ± 3 dB net loss variation. Fig. 36 is the performance when modulator and demodulator are connected directly and Fig. 37 is the performance when the transmission line is replaced by a voice-frequency band-pass filter.

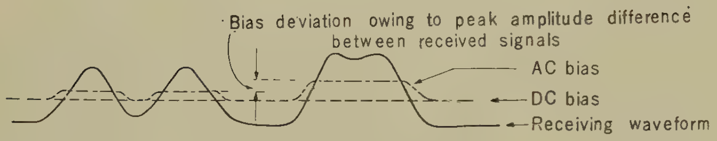
Bias deviation owing to peak amplitude difference between received signals
AC bias
DC bias
Receiving waveform

Fig. 35—Characteristic distortion caused by compensating level variations.

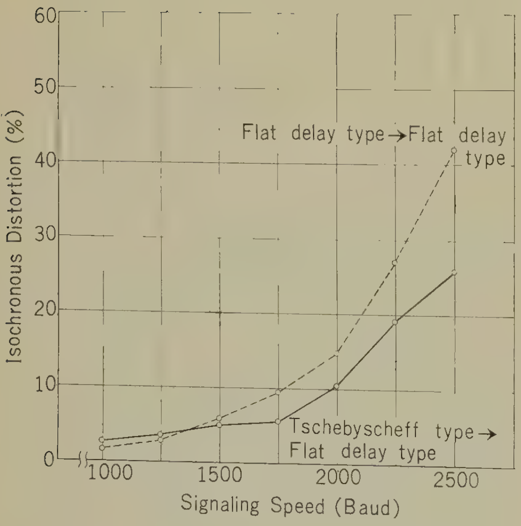

Fig. 36—Distortion performance of level compensating slicer adjusted at ± 3 dB level deviation. (without transmission line).

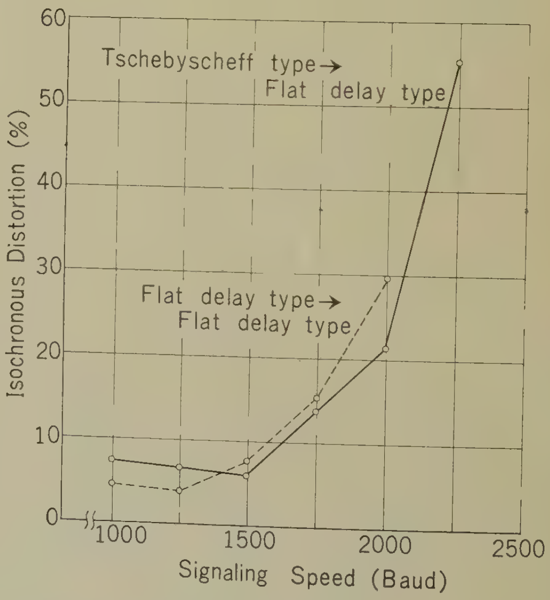

Fig. 37—Distortion performance of level compensating slicer and standard band-pass filter.

(2) Vulnerability to noise

Generally speaking, the degree of fortuitous distortion caused by noise is inversely proportional to the build-up and fall time of the received binary signal, and there is a large correlation between build-up and fall time and signaling speed. Therefore, the build-up times of indicial response were measured for various filter combinations. The results are tabulated in Table 2.

Next, Figs. 38 and 39 show distortion performance when a single sinusoidal wave is superposed on the transmitted signal as noise, where the transmission line was a band-pass filter which transmitted the frequency band from 0.15∼4.2 kc/s. The attenuation distortion and phase distortion of this filter in the band corresponding to a telephone channel are negligible but higher harmonics of the modulated wave are suppressed sufficiently.

Table 2

BUILD UP TIME OF THE INDICIAL RESPONSE

Combination of Filters	Build up time
Tschebyscheff type→Flat delay type	440 μs
Flat delay type →Flat delay type	520 μs
Flat delay type →Tschebyscheff type	450 μs

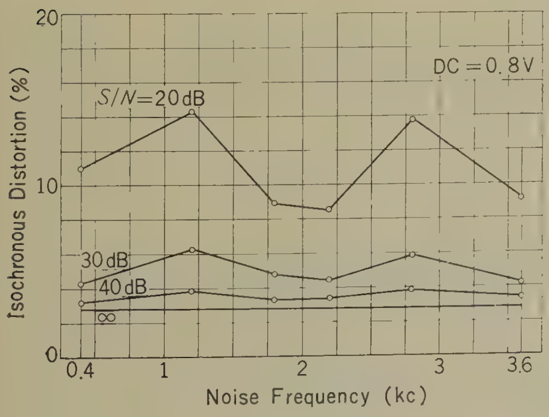

Fig. 38—Noise performance of level compensating slicer (1000 baud).

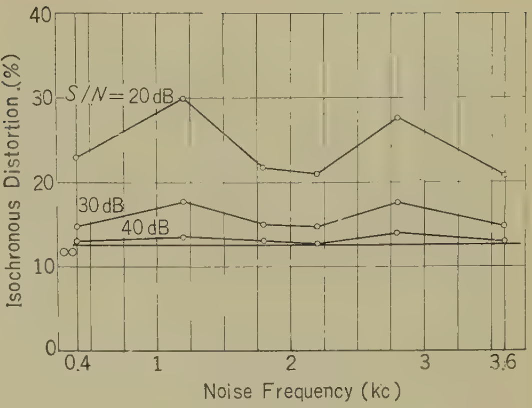

Fig. 39—Noise performance of level compensating slicer (2000 baud).

2.3.3. Review of Special Problems

In the preceding subsections, experimental results are described and remarks on them are made, but other than these remarks there are many other problems to be discussed. In this subsection, these special problems will be reviewed.

1) Distortion and margin

In order to simplify the discussion, let us consider distortion and margin of the trapezoidal waves which are shown in Fig. 40. Assume that the build-up time of the wave is τ seconds, then it is possible to transmit these trapezoidal waves without decreasing margin until $1/\tau$ baud. With greater increase of signaling speed, however, the margin decreases in inverse proportion to the speed, reaching zero at $2/\tau$ baud, and binary communication ultimately becomes impossible. However it must be noted that distortion of the trapezoidal waves remains at zero per cent. In consequence, it is probable that the

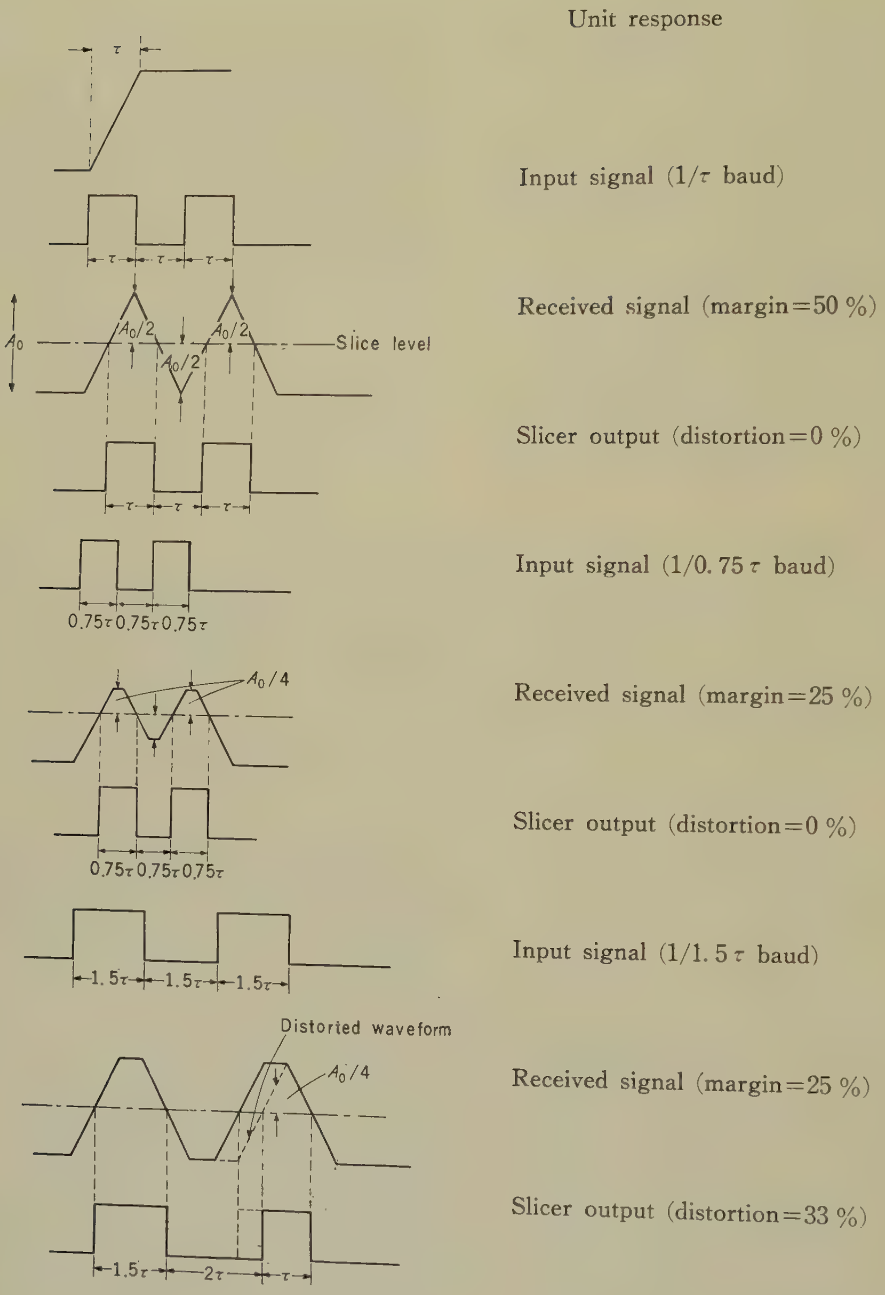
Unit response
τ
Input signal (1/τ baud)
τ τ τ
Received signal (margin=50 %)
A0
A0/2
A0/2
A0/2
Slice level
Slicer output (distortion=0 %)
τ τ τ
Input signal (1/0. 75 τ baud)
0.75τ 0.75τ 0.75τ
Received signal (margin=25 %)
A0/4
Slicer output (distortion=0 %)
0.75τ 0.75τ 0.75τ
Input signal (1/1. 5 τ baud)
1. 5τ 1.5τ 1.5τ
Distorted waveform
A0/4
Received signal (margin=25 %)
Slicer output (distortion=33 %)
1.5τ 2τ τ

Fig. 40—Relation between distortion and margin.

margin is near 0% in spite of little distortion. The above consideration indicates that the quality of a binary data transmission system cannot be expressed by distortion characteristics only. But in order to measure the margin of a signal we must specify sampling times and measure differences of sampled voltages from standard voltage. This is quite difficult. On the other hand, as described in the subsection 2.2.1, distortion characteristics can be obtained comparatively easily by measurement of the displacement of significant instants from the standard time. Therefore, for the purpose of judging actual quality of binary data transmission, it may be best to test distortion performance of the transmission system against noise, net loss variation, and many other interferences at various signaling speeds and to estimate error rate under several conditions. Now, as an indication of the signaling speed where margin reduction begins, reversals of build-up time ($1/\tau$'s) and the corresponding signaling speeds are calculated and shown in Table 3 for various filter combinations. These values accurately correspond to the results which are obtained from Fig. 27 (B.f). That is to say, the amplitude of the 1:1 signal is smaller than the amplitudes of 2:2 or 3:3 signals, and the margin of the 1:1 signal is smaller than that of a 2:2 or 3:3 signal too. This amplitude reduction of the signal is most striking for filter combinations of flat delay type, and its margin characteristic is worst even though its distortion performance is comparatively good.

Table 3

SIGNALING SPEED WHEN MARGIN REDUCTIONS BEGIN TO APPEAR

Combination of Filters	$1/\tau$
Tschebyscheff type→Flat delay type	2270 baud
Flat delay type →Flat delay type	1920 baud
Flat delay type →Tschebyscheff type	2220 baud

2) Specification of frequency characteristics of transmitting and receiving filters

As described in Section 1.2 indicial response of the equivalent low pass filter of a binary data transmission system should have a short build-up time and rapidly decreasing transient response. If the amplitude characteristic and group delay time of the transmission line are symmetric about the subcarrier frequency, this equivalent low pass filter can be synthesized from the transmitting low pass filter, transmission-line equivalent low pass filter, and receiving low pass filter. This relation is shown in Fig. 41. Therefore, to some extent, there is freedom in choice of transmitting and receiving filter characteristics even though the over-all frequency characteristic is fixed. Since noise and net loss variation generally occur in a transmission line, cutting off part of the signal energy in the

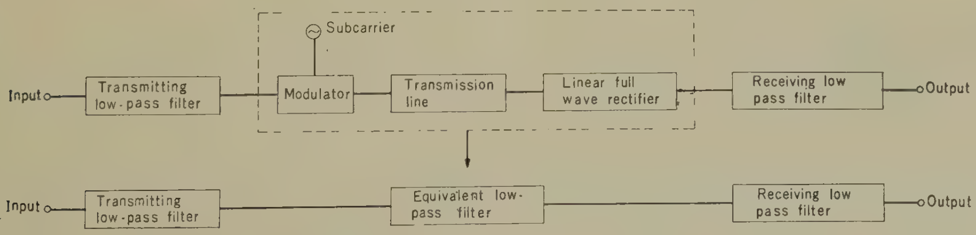
Subcarrier
Input
Transmitting low-pass filter
Modulator
Transmission line
Linear full wave rectifier
Receiving low pass filter
Output
Input
Transmitting low-pass filter
Equivalent low-pass filter
Receiving low pass filter
Output

Fig. 41—AM DSB communication system and its equivalent loss-pass system.

transmitting filter results in a reduction of the equivalent S/N of the system. However, in the receiving filter signal energy and noise are attenuated simultaneously and, roughly speaking, S/N remains constant. Accordingly, the frequency response of the transmitting filter should be uniform in the pass band and the frequency response of the receiving filter should be chosen so as to make the indicial response of the system the desired waveform. From the experimental results, a Tschebyscheff filter and flat delay filter combination is the best of the three filter combinations. This confirms the above discussion. Phase characteristics of the Tschebyscheff filter are not so good, but as compared with the phase characteristic of the usual telephone channel, it is rather good and its influence is small at 2000 baud (see Fig. 24).

3) D.C. component superposed on original signal

If the indicial response of the transmitting low pass filter has overshoot, the output signal from the filter can become negative when the transmitted signal pattern has special combinations and overmodulation occurs. The detected envelope of the overmodulated wave is not a replica of the original signal owing to unnecessary higher harmonics in the rectified signal of the overmodulated wave. To remove such harmonics, positive d.c. voltage which is not smaller than the absolute value of the maximum negative transient response may be superposed on the output from the transmitting filter (see Fig. 42). Moreover, this superposed d.c. voltage has the effect of reducing interference by the quadrature component. The received signal when quadrature components exist is expressed by formula (14) and its envelop is $\sqrt{P_u^2+Q_u^2}$.

If $P_u \gg Q_u$, then

$$\sqrt{P_u^2+Q_u^2} \doteqdot P_u\left(1+\frac{1}{2}\frac{Q_u^2}{P_u^2}+\cdots\cdots\right) \qquad (24)$$

and the disturbance from Q_u is negligible, but it increases suddenly as Q_u increases. When a d.c. component is superposed on the original signal, the envelope of the received signal becomes

$$\sqrt{(P_u+D)^2+Q^2} \doteqdot (P_u+D)\left\{1+\frac{1}{2}\frac{Q_u^2}{(P_u+D)^2}+\cdots\cdots\right\} \qquad (25)$$

and disturbance from Q_u may be reduced.

To increase the d.c. voltage as keeping power of the modulated wave constant is to

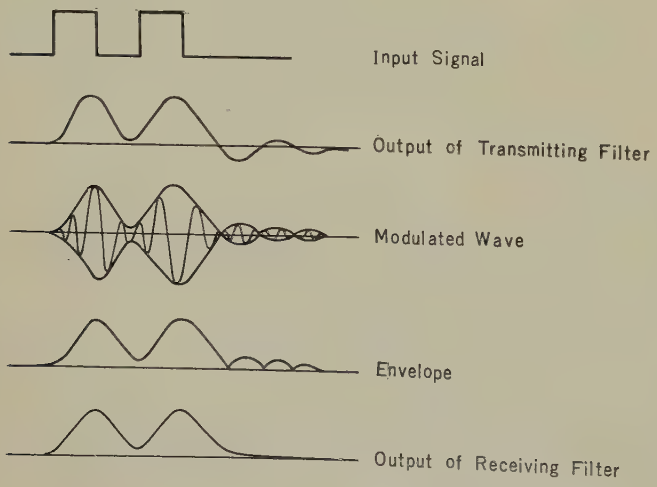

Fig. 42—Effects of Overmodulation.

decrease signal power relatively and then the vulnerabilities to noise and net loss variation of transmission line will be increased. Accordingly, the value of the dc voltage must be determined from consideration of its merits and demerits. From the experimental results, the best distortion performance is obtained when a Tschebyscheff filter is used as the transmitting filter and the value of the dc voltage is as much as 20% of the signal amplitude. When a flat delay filter is used instead of a Tschebyscheff filter the performance without superposed dc voltage is better because there are no overshoots in the indicial response of the filter.

4) Influence of noise

In this paragraph some striking points which are observed in Fig. 38 and Fig. 39, will be examined. In the first place noise disturbance depends on the noise frequency. This is caused by the level compensator with delay line, that is, if the slice level of this compensator is set at one-half of signal peak amplitude, single frequency noise, whose period is equal to the width of a unit pulse, enhances the signal level near the signal peak and decreases the signal level near the characteristic instant and the largest distortion occur.

If $f(t)\cos\omega_c t$ is received wave and $k\cos\omega_n t$ is noise, then

$$\begin{aligned} & f(t)\cos\omega_c t+k\cos\omega_n t \\ & \quad =\{f(t)+k\cos(\omega_c-\omega_n)t\}\cos\omega_c t \\ & \quad +\{k\sin(\omega_c-\omega_n)t\}\sin\omega_c t \qquad (26) \end{aligned}$$

and for $f(t)\gg k$

$$\begin{aligned} & \sqrt{\{f(t)+k\cos(\omega_c-\omega_n)t\}^2+\{k\sin(\omega_c-\omega_n)t\}^2} \\ & \quad \doteqdot f(t)+k\cos(\omega_c-\omega_n)t=f(t)+k\cos\omega_a t. \qquad (27) \end{aligned}$$

Thus, the noise influence on distortion is symmetric about the subcarrier frequency. Therefore, there are two frequencies which generate maximum distortion, and both are determined by build-up time of the received signal as well as by the characteristics of the receiving filter. In the second place the fact that the disturbance by noise decreases as noise frequency increases comes from higher attenuation of higher frequency noise by the receiving low-pass filter.

In the third place, the noise level at which errors begin to occur is about −13 dB below signal level regardless of the signaling speed, 1000 baud and 2000 baud, where level variations of ±3 dB are compensated. Generally speaking, in a simple dc binary data transmission system, a minimum tolerable S/N is 6 dB, if the slice level is set at one-half of mark signal amplitude. In an AM DSB binary data transmission system, the amplitude of the receiving filter output is $2/\pi$ of the peak amplitude of the subcarrier which is being transmitted continuously, while the peak amplitude of the low frequency noise is not changed because higher harmonics of the full wave rectified noise are little attenuated by the filter. This fact results in a margin (S/N) reduction of as much as $20\log 2/\pi=3.9$ dB. As described in Section 1.5, there is a reduction of noise margin by as much as N dB owing to level compensation of ±N dB, and the tolerable S/N becomes (6+3.9+N) dB. The experimental results roughly verify the above assertions.

Besides, if the carrier frequencies of carrier telephone systems at the transmitting and receiving offices are unsynchronized with one another, the frequency of the subcarrier will be changed. However influence on the performance of a binary data transmission system are scarcely observed.

3. The Problems in Binary Data Transmission through Telephone Channels and Transmission Quality

As a rule, data processing systems are divided into two categories; "real time data processing systems" such as seat reservation systems, and "delayed time data processing systems" such as systems for processing inventories. In the former case, electrical communication systems must be utilized as the

Table 4

BINARY DATA TRANSMISSION PERFORMANCE OVER JAPANESE STANDARD TELEPHONE CIRCUIT

	One voice link				Two voice links			
Deviation of group delay time (1000 ～ 3000 c/s)	less than 0.3 ms				less than 0.6 ms			
Netloss variation	less than ± 3 dB				less than ± 5 dB			
Signaling speed	1500 baud		2000 baud		1500 baud		2000 baud	
Isochronous distortion	6 %		16 %		6 %		22 %	
Transmission level	− 6 dBmo	−12 dBmo	− 6 dBmo	−12 dBmo	− 6 dBmo	−12 dBmo	− 6 dBmo	−12 dBmo
Maximum tolerable instantaneous noise level	−19 dBmo	−25 dBmo	−19 dBmo	−25 dBmo	−21 dBmo	−27 dBmo	−21 dBmo	−27 dBmo

data transmission means because the data must be transmitted whenever needed, while in the latter case vehicles and airplanes may be used to transmit data because some delay is permissible. Therefore the most favorable transmission system can be chosen from considerations of speed, reliability, cost, etc. In this section, binary data transmission systems are examined not from the standpoint of economy but signaling speed and reliability.

Telephone channels were originally developed for speech transmission, and are not suitable for data transmission, but binary data transmission systems must be designed keeping in mind the telephone channel characteristics. Moreover, in a binary data transmission system, the output level of the transmitted signal must be evaluated to prevent the binary data transmission channel from interfering with the neighboring telephone channels. In the design of the present carrier telephone system, −15 dBm has been adopted as a conventional value to represent the mean absolute power level (at a zero relative level point) of the speech plus signaling currents, etc.[14] Putting the probabilities of occurence of mark and space codes as 1/2, the mean power of the transmitted binary signal pattern is 3 dB smaller than the mean power of the continuous subcarrier. If the mean power of the continuous subcarrier is set to −12 dBm then the average power of the signal pattern becomes −15 dBm and this value corresponds to speech level, therefore it is unnecessary to decrease the subcarrier level to a value smaller than −12dBm. Considering that the peak factor of binary signal is small compared with that of speech current, the mean power of a binary signal may be increased a little. Therefore, Working Party 43 of CCITT on data transmission recommends the value of −6 dBm as the mean power of the continuous subcarrier.[15] In this section data transmission quality at a sending level of −6 dBm and −12 dBm will be examined.

Of the many characteristics of a telephone line, (1) frequency characteristics, (2) net loss variation, (3) noise, and (4) interruption are the main factors which effect the transmission quality. As described in Section 6.1, the frequency characteristics of a telephone channel are determined roughly by channel filters and channel amplifiers regardless of type of carrier system. Therefore the transmission qualities are examined using the characteristics shown in Fig. 13 as representative. For net loss variation of the line, the values of ±3 dB and ±5 dB are adopted. To estimate the noise disturbance of a binary signal transmission, the data of frequency distribution of instant noise amplitudes is more useful than the data of its mean power, but having no such data, only maximum tolerable noise level will be indicated.

When data is transmitted through rented telephone channels which have little impulsive noise compared with switched telephone channels, AM DSB system would be the best system because of its simplicity and reasonable cost. This binary data transmission system may be designed by considering the frequency characteristics and net loss variations characteristics of the transmission line.

The transmission quality estimated from this study under the conditions described above are shown in Table 4.

Conclusions

In Section 1, it is proved that the signal distortion owing to the relative phase difference between each signal pulse and subcarrier can be completely suppressed by letting the signal pass through an adequate low pass filter before it is fed to the modulator and by eliminating the spurious frequency spectra arising in the modulator. From this analysis it became clear that synchronization between subcarrier and signal is unnecessary and design of the sending circuit is simplified. The indicial response of the standard telephone circuit in Japan was calculated with the M-1 computer, which was developed in the ECL, and from that result the relation between modulation speed and its margin is obtained. This value of margin serves as a reference for the design of data transmission sets.

In Section 2, experimental results are described. Among them, the analysis of interference from line noise and net loss variation in the case of binary data transmission by an AM DSB system is very useful to know the application limit of the AM system and to fix the output level of the modulated signal.

In this paper, the performance of data transmission through private telephone lines is studied and some useful results are obtained but there remains some problems to be studied such as interruption of the transmission line, noise level distribution, etc. The problem of interruption is being studied and the results will be published soon but the investigations of interruption must be continued hereafter because the frequency of interruptions vary with time according to the increase of the number of telephone channels, with types of transmission system, etc.

Furthermore it is necessary to investigate the quality of data transmission through switched telephone channels. In this case frequency modulation or phase modulation systems may be more useful than amplitude modulation systems.

Appendix 1.

Let the cutoff frequency of an ideal low-pass filter be f c/s and impulse response of the filter be $I(t)$; then

$$I(t)=\frac{\sin 2\pi f_1 t}{2\pi f_1 t}. \tag{1.1}$$

As $I(t)$ becomes zero when $2f_1 t=\pm n\pi$; $t=\pm 1/2f, \pm 2/2f, \pm 3/2f, \cdots\cdots$, a series of pulses which are sent with the interval of $1/2f$ do not interfere with each other. But if the pulse interval changes from the above mentioned value, the sum of intervals from preceding and succeeding pulses at a sampling point will increase to a value which is higher than the threshold level even though the deviation of the interval is very small. The following discussion is an explanation of this fact.

Now let
$$\left.\begin{aligned} &f(x)=(\sin x)/x \qquad x>0 \\ &f(0)=1 \end{aligned}\right\} \tag{1.2}$$

$$\alpha>0,\ \beta\geqq 0.$$

Then let us prove that $\sum_{n=0}^{\infty} |f\{(n\alpha+\beta)\pi\}|$ diverges except when α and β are both integers.

1) α=integer, $\beta \neq$ integer

$$\sum_{n=0}^{\infty} |f\{(n\alpha+\beta)\pi\}| = \sum_{n=0}^{\infty} \frac{|\sin \beta\pi|}{(n\alpha+\beta)\pi}$$

$$= \frac{|\sin \beta\pi|}{\alpha\pi} \sum_{n=0}^{\infty} \frac{1}{n+\frac{\beta}{\alpha}} > \frac{|\sin \beta\pi|}{\alpha} \sum_{n=0}^{\infty} \frac{1}{n}$$

$$= +\infty \tag{1.3}$$

where $N>\beta/\alpha$.

2) When α is a rational number

We take positive integers p, q such that $(p, q)=1$, and put $\alpha=p/q$; then no two of the integers $0p$, $1p$, ……, $(q-1)p$ are congruent modulo q. For, if there were two integers k_1 and k_2, such that $k_1 p \equiv k_2 p \pmod{q}$; from $q|(k_1-k_2)p$ and $(p, q)=1$ it follows $q|(k_1-k_2)$. Therefore $\{0p, 1p, \cdots\cdots, (q-1)p\}$ is merely a relabelling of $\{0, 1, q-1\} \pmod{q}$. Next we define $\{x\}$ to be the absolute value of the difference between x and its nearest integer. And let γ be the minimum value among $\{\beta\}, \{\beta+1/q\}, \cdots\cdots, \{\beta+(q-1)/q\}$ except zero. Then the minimum value among $\{\beta\}, \{\beta+p/q\}, \cdots\cdots, \{\beta+(q-1)p/q\}$ except zero is also γ and furthermore $(q-1)$ numbers among them are not less than γ.

$$\therefore \sum_{n=0}^{\infty} |f\{(n\alpha+\beta)\pi\}| = \sum_{r=0}^{\infty} \sum_{s=0}^{q-1} \left| f\left[\left\{\left(rq+s\right)\frac{p}{q}+\beta\right\}\pi\right]\right.$$

$$- \sum_{r=0}^{\infty} \sum_{s=0}^{q-1} \frac{\left|\sin\left(\frac{sp}{q}+\beta\right)\pi\right|}{\left(rp+\frac{sp}{q}+\beta\right)\pi} \geqq \sum_{r=0}^{\infty} \left(q-1\right) \frac{\sin \gamma\pi}{\left(rp+\frac{q-1}{q}p+\beta\right)\pi}$$

$$\geqq \frac{q-1}{p\pi} \sin \gamma\pi \sum_{r=0}^{\infty} \frac{1}{r+1+\beta-\frac{1}{q}} \geqq \frac{q-1}{p\pi} \sin \gamma\pi \sum_{r=N}^{\infty} \frac{1}{r} = +\infty \tag{1.4}$$

where $N>1+\beta-1/q$.

The above discussion does not include the case when α is an irrational number, but perhaps $\sum_{n=0}^{\infty} f\{(n\alpha+\beta)\pi\}|$ will diverge in this case too. Fig. 2 (b) is the result of this discussion.

Appendix 2.

Let $R_0(t)$ be the output waveform of a transmission line when the input is $g(t)$; then

$$
\begin{aligned}
R_0(t) &= \frac{1}{2\pi}\int_{-\infty}^{\infty} G(\omega)\ T(\omega)\ e^{j\{\omega t+\theta(\omega)\}}\ d\omega \\
&= \frac{1}{4\pi}\int_{-\omega_0-\omega_1}^{-\omega_0+\omega_1}+\int_{\omega_0-\omega_1}^{\omega_0+\omega_1} F(\omega-\omega_0)\ T(\omega)\ e^{j\{\omega t+\theta(\omega)\}}\ e^{j\alpha}\ d\omega \\
&\quad + \frac{1}{4\pi}\int_{-\omega_0-\omega_1}^{-\omega_0+\omega_1}+\int_{\omega_0-\omega_1}^{\omega_0+\omega_1} F(\omega+\omega_0)\ T(\omega)\ e^{j\{\omega t+\theta(\omega)\}}\ e^{-j\alpha}\ d\omega \\
&= \frac{\cos\alpha}{2\pi}\ \Re\mathfrak{e}\int_{\omega_0-\omega_1}^{\omega_0+\omega_1}\Big\{F(\omega+\omega_0)+F(\omega-\omega_0)\Big\}\ T(\omega)\ e^{j\{\omega t+\theta(\omega)\}}\ d\omega \\
&\quad + \frac{\sin\alpha}{2\pi}\ \Im\mathfrak{m}\int_{\omega_0-\omega_1}^{\omega_0+\omega_1}\Big\{F(\omega+\omega_0)-F(\omega-\omega_0)\Big\}\ T(\omega)\ e^{j\{\omega t+\theta(\omega)\}}\ d\omega \\
&= \frac{\cos\alpha}{2\pi}\cos\Big\{\omega_0 t+\theta(\omega_0)\Big\}\Re\mathfrak{e}\int_{-\omega_1}^{\omega_1}\Big\{F(2\omega_0+\omega)+F(\omega)\Big\}\ T(+\omega_0)\ e^{j\{\omega t+\theta(\omega+\omega_0)-\theta(\omega_0)\}}\ d\omega \\
&\quad - \frac{\cos\alpha}{2\pi}\sin\Big\{\omega_0 t+\theta(\omega_0)\Big\}\Im\mathfrak{m}\int_{-\omega_1}^{\omega_1}\Big\{F(2\omega_0+\omega)+F(\omega)\Big\}\ T(\omega+\omega_0)\ e^{j\{\omega t+\theta(\omega+\omega_0)-\theta(\omega_0)\}}\ d\omega \\
&\quad + \frac{\sin\alpha}{2\pi}\cos\Big\{\omega_0 t+\theta(\omega_0)\Big\}\Im\mathfrak{m}\int_{-\omega_1}^{\omega_1}\Big\{F(2\omega_0+\omega)-F(\omega)\Big\}\ T(\omega+\omega_0)\ e^{j\{\omega t+\theta(\omega+\omega_0)-\theta(\omega_0)\}}\ d\omega \\
&\quad + \frac{\sin\alpha}{2\pi}\sin\Big\{\omega_0 t+\theta(\omega_0)\Big\}\Re\mathfrak{e}\int_{-\omega_1}^{\omega_1}\Big\{F(2\omega_0+\omega)-F(\omega)\Big\}\ T(\omega+\omega_0)\ e^{j\{\omega t+\theta(\omega+\omega_0)-\theta(\omega_0)\}}\ d\omega \\
&= \frac{1}{2\pi}\Big[\Re\mathfrak{e}\int_{-\omega_1}^{\omega_1} F(\omega)\ T(\omega+\omega_0)\ e^{j\{\omega t+\theta(\omega+\omega_0)-\theta(\omega_0)\}}\ d\omega \\
&\quad + \Re\mathfrak{e}\int_{-\omega_1}^{\omega_1} F(2\omega_0+\omega)\ T(\omega+\omega_0)\ e^{j\{\omega t+\theta(\omega+\omega_0)-\theta(\omega_0)-2a\}}\ d\omega\Big] \\
&\quad \times \cos\ \{\omega_0 t+\theta(\omega_0)+\alpha\} \\
&\quad - \frac{1}{2\pi}\Big[\Im\mathfrak{m}\int_{-\omega_1}^{\omega_1} F(\omega)\ T(\omega+\omega_0)\ e^{j\{\omega t+\theta(\omega+\omega_0)-\theta(\omega_0)\}}\ d\omega \\
&\quad + \Im\mathfrak{m}\int_{-\omega_1}^{\omega_1} F(2\omega_0+\omega)\ T(\omega+\omega_0)\ e^{j\{\omega t+\theta(\omega+\omega_0)-\theta(\omega_0)-2\alpha\}}\ d\omega\Big] \\
&\quad \times \sin\ \{\omega_0 t+\theta(\omega_0)+\alpha\}. \qquad (2.1)
\end{aligned}
$$

Appendix 3.

Let us assume that the input signal $f(t)$ is equal to the following value.

$$\left.\begin{array}{ll} f(t)=0 & t<0 \\ f(t)=e^{-\gamma t} & t>0 \end{array}\right\} \tag{3.1}$$

where γ is a positive real number and sufficiently small.
The frequency spectrum of $f(t)$ becomes

$$F(\omega)=\int_0^{\infty} e^{-(\gamma+j\omega)t}\,dt=\frac{1}{\gamma+j\omega}. \tag{3.2}$$

Let the integral of the first term in equation (2.1) be I_1

$$\begin{aligned} I_1&=\frac{1}{2\pi}\mathfrak{Re}\int_{-\omega_1}^{\omega_1} F(\omega)\,T(\omega+\omega_0)\,e^{j\omega t}\,e^{j\{\theta(\omega+\omega_0)-\theta(\omega_0)\}}\,d\omega \\ &=\frac{1}{2\pi}\mathfrak{Re}\int_{-\omega_1}^{\omega_1}\frac{T(\omega+\omega_0)\cos\{\omega t+\theta(\omega+\omega_0)-\theta(\omega_0)\}}{\gamma+i\omega}\,d\omega \\ &+\frac{1}{2\pi}\mathfrak{Re}\int_{-\omega_1}^{\omega_1}\frac{T(\omega+\omega_0)\,j\sin\{\omega t+\theta(\omega+\omega_0)-\theta(\omega_0)\}}{\gamma+j\omega}\,d\omega. \end{aligned} \tag{3.3}$$

If we put $\gamma\to 0$ then the input signal becomes a unit function and

$$\begin{aligned} \lim_{\gamma\to 0} I_1=\lim_{\rho\to 0}\Bigg[&\mathfrak{Je}\,\frac{1}{2\pi j}\int_{-\omega_1}^{-\rho}\int_{\rho}^{\omega_1}\frac{T(\omega+\omega_0)\cos\{\omega t+\theta(\omega+\omega_0)-\theta(\omega_0)\}}{\omega}\,d\omega \\ &+\mathfrak{Re}\,\frac{1}{2\pi j}\int_{-\rho}^{\rho}\frac{T(\omega+\omega_0)\cos\{\omega t+\theta(\omega+\omega_0)-\theta(\omega_0)\}}{\omega}\,d\omega \\ &+\mathfrak{Re}\,\frac{1}{2\pi}\int_{-\omega_1}^{\omega_1}\frac{T(\omega+\omega_0)\sin\{\omega t+\theta(\omega+\omega_0)-\theta(\omega_0)\}}{\omega}\,d\omega. \end{aligned} \tag{3.4}$$

As the integral of the first term in the above equation becomes real, equation (3.4) becomes

$$\begin{aligned} \lim_{\gamma\to 0} I_1&=\lim_{\rho\to 0}\mathfrak{Re}\,\frac{1}{2\pi j}\int_{-\rho}^{\rho}\frac{T(\omega_0)}{\omega}\,d\omega \\ &+\frac{1}{2\pi}\int_{-\omega_1}^{\omega_1}\frac{T(\omega+\omega_0)\sin\{\omega t+\theta(\omega+\omega_0)-\theta(\omega_0)\}}{\omega}\,d\omega. \end{aligned} \tag{3.5}$$

If we take the path of integration as shown in Fig. 43 and put

$${}_{-\rho}^{\rho}\left[\omega=\rho\,e^{j\rho}\right]_{\pi}^{2\pi} \tag{3.6}$$

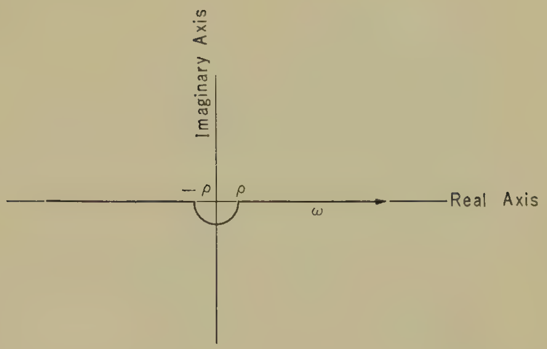

Fig. 43—Intergration path.

then

$$\lim_{\gamma\to 0} I_1 = \frac{T(\omega_0)}{2} + \frac{1}{2\pi}\int_{-\omega_1}^{\omega_1} \frac{T(\omega+\omega_0)\sin\{\omega t+\theta(\omega+\omega_0)-\theta(\omega_0)\}}{\omega}\,d\omega. \tag{3.7}$$

And let the integral of the third term in equation (2.1) be I_2; then

$$\lim_{\gamma\to 0} I_2 = -\lim_{\rho\to 0} \mathfrak{Im}\left[\left[\int_{-\omega_1}^{-\rho} + \int_{-\rho}^{\rho} + \int_{\rho}^{\omega_1}\right] \frac{T(\omega+\omega_0)}{2\pi j\omega} e^{j\{\omega t+\theta(\omega+\omega_0)-\theta(\omega_0)\}}\,d\omega\right]. \tag{3.8}$$

But as the integral $\int_{-\rho}^{\rho}$ becomes real, equation (3.8) becomes

$$\lim_{\gamma\to 0} I_2 = \lim_{\rho\to 0}\left[\left[\int_{-\omega_1}^{-\rho} + \int_{\rho}^{\omega_1}\right] \frac{T(\omega+\omega_0)}{2\pi\omega} \cos\left\{\omega t+\theta(\omega+\omega_0)-\theta(\omega_0)\right\} d\omega\right]. \tag{3.9}$$

There are following relations between $T, T_e, T_0, \theta, \theta_e$ and θ_0

$$\left.\begin{aligned} T(\omega_0+\omega) &= T_e(\omega)+T_0(\omega) \\ T(\omega_0-\omega) &= T_e(\omega)-T_0(\omega) \\ \theta(\omega_0+\omega)-\theta(\omega_0) &= \theta_0(\omega)+\theta_e(\omega) \\ \theta(\omega_0-\omega)-\theta(\omega_0) &= -\theta_0(\omega)+\theta_e(\omega) \end{aligned}\right\}. \tag{3.10}$$

Therefore,

$$\begin{aligned} &\int_{-\omega_1}^{-\rho} \frac{T(\omega+\omega_0)\cos\{\omega t+(\omega+\omega_0)-\theta(\omega_0)}{\omega}\,d\omega \\ &= -\int_{\rho}^{\omega_1} \frac{T(\omega_0-\omega)\cos[\omega t-\{\theta(\omega_0-\omega)-\theta(\omega_0)\}]}{\omega}\,d\omega \\ &= -\int_{\rho}^{\omega_1} \frac{\{T_e(\omega)-T_0(\omega)\}\cos\{\omega t+\theta_0(\omega)-\theta_e(\omega)\}}{\omega}\,d\omega \\ &= -\int_{\rho}^{\omega_1} \frac{T_e(\omega)[\cos\{\omega t+\theta_e(\omega)\}\cos\theta_0(\omega)+\sin\{\omega t+\theta_e(\omega)\}\sin\theta_0(\omega)]}{\omega}\,d\omega \\ &\quad+\int_{\rho}^{\omega_1} \frac{T_0(\omega)[\cos\{\omega t+\theta_e(\omega)\}\cos\theta_0(\omega)+\sin\{\omega t+\theta_e(\omega)\}\sin\theta_0(\omega)]}{\omega}\,d\omega. \end{aligned} \tag{3.11}$$

In the same way, the following equation is obtained.

$$\begin{aligned}
&\int_{\rho}^{\omega_1} \frac{T(\omega+\omega_0)\cos\{\omega t+\theta(\omega+\omega_0)-\theta(\omega_0)\}}{\omega}\,d\omega \\
=&\int_{\rho}^{\omega_1} \frac{T_e(\omega)[\cos\{\omega t+\theta_e(\omega)\cos\theta_0(\omega)-\sin\{\omega t+\theta_e(\omega)\}\sin\theta_0(\omega)]}{\omega}\,d\omega \\
+&\int_{\rho}^{\omega_1} \frac{T_0(\omega)[\cos\{\omega t+\theta_e(\omega)\}\cos\theta_0(\omega)-\sin\{\omega t+\theta_0(\omega)\}\sin\theta_0(\omega)]}{\omega}\,d\omega.
\end{aligned} \tag{3.12}$$

Here, T_e, θ_e, T_0 and θ_0 can be expanded as follows

$$\left.\begin{aligned}
T_e&=k_0+k_2\omega_2+k_4\omega^4+ \cdots\cdots\cdots\cdots\cdots \\
T_0&=k_1\omega+k_3\omega^3+k_5\omega^5+ \cdots\cdots\cdots\cdots \\
\theta_0&=K_1\omega+K_3\omega^3+K_5\omega^5+ \cdots\cdots\cdots\cdots \\
\theta_e&=K_0+K_2\omega^2+K_4\omega^4+ \cdots\cdots\cdots\cdots\cdots
\end{aligned}\right\} \tag{3.13}$$

and

$$\left.\begin{aligned}
&\frac{T_0(\omega)\cos\{\omega t+\theta_0(\omega))\cos\theta_e(\omega)}{\omega} \to k_1 \\
&\frac{T_e(\omega)\sin(\omega t+\theta_0(\omega))\sin\theta_e(\omega)}{\omega} \to k_0K_1K_0
\end{aligned}\right\} \quad \rho\to 0.$$

Therefore the lower limit of the integration range, ρ, can be replaced by 0 and $R_u(t)$ becomes

$$\begin{aligned}
R_u(t)=&\left[\frac{T(\omega_0)}{2}+\frac{1}{\pi}\int_0^{\omega_1}\frac{T_e\sin(\omega t+\theta_0(\omega))\cos\theta_e(\omega)+T_0\cos(\omega t+\theta_0(\omega))\sin\theta_e(\omega)}{\omega}\,d\omega\right] \\
&\times\cos(\omega_0 t+\theta(\omega_0)+\alpha) \\
&+\left[\frac{1}{\pi}\int_0^{\omega_1}\frac{T_0\cos(\omega t+\theta_0(\omega))\cos\theta_e(\omega)-T_e\sin(\omega t+\theta_0(\omega))\sin\theta_e(\omega)}{\omega}\,d\omega\right] \\
&\times\sin(\omega_0 t+\theta(\omega_0)+\alpha).
\end{aligned} \tag{3.14}$$

Appendix 4.

Gaussian noise I_N can be expressed as

$$I_N=\sum_{n=1}^{M} C_n\cos(\omega_n t-\varphi_n) \tag{4.1}$$

where φ_n is phase angle and uniformly distributed in the region $(0, 2\pi)$ and C_n is constant when the noise is white. Now let the envelope of combined wave I of single sinusoidal wave plus Gaussian noise be $Q(t)$; then

$$\left.\begin{aligned}
&I=I_N+V\cos pt \\
&Q^2(t)=(V+I_c)^2+I_s^2
\end{aligned}\right\} \tag{4.2}$$

where

$$\left.\begin{aligned} I_c &= \sum C_n \cos[(\omega_n-p)t-\varphi_n] \\ I_s &= \sum C_n \sin[(\omega_n-p)t-\varphi_n] \\ I_N &= I_c \cos pt - I_s \sin pt \end{aligned}\right\}. \quad (4.3)$$

Since I_c and I_s are distributed normally about zero with the variance φ_0, the probability density of $x=V+I_c$ and $y=I_s$ are respectively

$$(2\pi\varphi_0)^{-1/2}\cdot \exp\left\{-\frac{(x-V^2)}{2\varphi_0}\right\}$$

and $$(2\pi\varphi_0)^{-1/2}\cdot \exp\left\{-\frac{y^2}{2\varphi_0}\right\}.$$

Here, we put $x=Q\cos\theta$, $y=Q\sin\theta$; then the probability that the point (x,y) falls between Q and $Q+dQ$ becomes

$$\frac{QdQ}{2\pi\varphi_0}\int_0^{2\pi}\exp\left[-\frac{1}{2\varphi_0}(Q^2+V^2-2QV\cos\theta)\right]d\theta$$

$$=\frac{QdQ}{\varphi_0}\exp\left[-\frac{Q^2+V^2}{2\varphi_0}\right]I_0\left(\frac{QV}{\varphi_0}\right). \quad (4.6)$$

Here if we define

$$v=\frac{Q}{\varphi_0{}^{1/2}} \quad dv=\frac{dQ}{\varphi_0{}^{1/2}} \quad a=\frac{V}{\varphi_0{}^{1/2}} \quad (4.7)$$

then

$$p(v)=v\exp\left[-\frac{v^2+a^2}{2}\right]I_0(av). \quad (4.8)$$

Next if we use the formula

$$\frac{d}{du}\left[u^n I^n(au)/a\right]=u^n I_{n-1}(au) \quad (4.9)$$

then following equation is obtained

$$\int_0^v p(u)du=\int_0^v u\, I_0(au)\exp\left[-\frac{u^2+a^2}{2}\right]du$$

$$=\exp\left[-\frac{v^2+a^2}{2}\right]\cdot\frac{v\, I_1(av)}{a}$$

$$+\int_0^v\frac{u^2}{a}\, I_1(au)\cdot\exp\left[-\frac{u^2+a^2}{2}\right]du$$

$$=\exp\left[-\frac{v^2+a^2}{2}\right]\frac{v\, I_1(av)}{a}$$

$$+\exp\left[-\frac{v^2+a^2}{2}\right]\left(\frac{v}{a}\right)^2 I_2(av)$$

$$+\int_0^v\frac{u^3}{a^2}\, I_2(au)\exp\left[-\frac{u^2+a^2}{2}\right]du$$

$$=\cdots\cdots\cdots=\exp\left[-\frac{v^2+a^2}{a}\right]\sum_{n=1}^{\infty}\left(\frac{v}{a}\right)^n I_n(av).$$

$$(4.10)$$

From this equation, equation (17) can be obtained easily.

Appendix 5.

Let us assume that the amplitude characteristic and group delay characteristic are both symmetrical to the subcarrier frequency and approximate its low-pass equivalant characteristic by a function of frequency f (kc/s). At first let τ be as follows

$$\tau=B_2f^2+B_4f^4+B_6f^6+B_8f^8. \quad (5.1)$$

When bandwidth is $2f_0$,

$$\tau=f_0{}^2B_2\left(\frac{f}{f_0}\right)^2+f_0{}^4B_4\left(\frac{f}{f_0}\right)^4$$

$$+f_0{}^6B_6\left(\frac{f}{f_0{}^6}\right)+f_0{}^8B_8\left(\frac{f}{f_0}\right)^8$$

$$=f_0{}^2B_2F^2+f_0{}^4B_4F^4+f_0{}^6B_6F^3+f_0{}^8B_8F^8. \quad (5.2)$$

Let τ be τ_1 τ_2 τ_3 and τ_4 when $F=1/4, 2/4, 3/4, 4/4$; then the B's become

$$\left.\begin{aligned} B_2&=\left(\frac{2}{f_0}\right)^2\Big[2^2\tau_1-3\tau_2+\frac{2^2}{3}\tau_3 \\ &\quad -\frac{1}{2^2}\tau_4\Big] \\ B_4&=\left(\frac{4}{f_0}\right)^4\Big[\frac{-13}{3}\tau_1+\frac{19}{2^2}\tau_2 \end{aligned}\right.$$

$$\left.\begin{aligned}&-\frac{7}{3}\tau_3+\frac{11}{2^3\cdot 3}\tau_4\Big]\\ B_6&=\left(\frac{6}{f_0}\right)^6\left[\frac{3}{2}\tau_1-2\tau_2+\frac{7}{2\cdot 3}\tau_3\right.\\ &\left.-\frac{1}{2^2}\tau_4\right]\\ B_8&=\left(\frac{8}{f_0}\right)^8\left[\frac{-1}{2\cdot 3}\tau_1+\frac{1}{2^2}\tau_2\right.\\ &\left.-\frac{1}{2\cdot 3}\tau^3+\frac{1}{2^3\cdot 3}\tau_4\right]\end{aligned}\right\}. \qquad (5.3)$$

Therefore if we know $\tau_1 \sim \tau_4$, an approximating formula is easily obtained by equation (5.1) and (5.3). Phase characteristic θ is obtained by the next formula.

$$\theta\,(\text{in radian})=\int\tau\,(\text{in sec})\,d\omega=\int 2\pi\tau\,df\,(\text{in c/s})$$

$$=\int 2\pi\tau(\text{in ms})\,df\,(\text{in kc/s}). \qquad (5.4)$$

In the case of amplitude characteristic T, $T-1$ is approximated by the same equation form.

$$T-1=A_2f^2+A_4f^4+A_6f^6+A_8f^8. \qquad (5.5)$$

The values of the A's are exactly the same as the B's in equation (5.3). Approximating formulas to the characteristics which are shown in Fig. 13 are as follows. These curves are shown in Figs. 14 and 15.

Group delay characteristics

$$\tau=0.23047f^2+0.11495f^4-0.085831f^6$$
$$+0.047188f^8. \qquad (5.6)$$

Amplitude characteristic T

$$T=1+0.45267f^2+0.13971f^4+0.10976f^6$$
$$-0.030974f^8. \qquad (5.7)$$

Appendix 6.

The group delay time of a telephone line at the frequency of the band edge is higher than the delay time in the middle of the frequency band. This comes from the fact that a telephone line is designed to have a uniform amplitude characteristic and the poles of the transfer function of the telephone line exist near the band edge. Therefore when we transmit a binary signal through a telephone line, it is desirable to use a low pass filter whose group delay characteristic is a complement of the characteristic of the telephone line. The group delay characteristic of the filter described below does not fulfill this requirement but it has flat delay characteristic and furthermore it is very easy to realize the actual circuit of the transfer function.

Let the transfer function be $W(p)$ and its partial transfer function be $W_n(p)$, that is

$$W(p)=W_1(p)\,W_2(p)\cdots\cdots\cdots W_N(p). \qquad (6.1)$$

Now let us think of the $W_n(p)$ which has the following characteristic

$$W_n(p)=\frac{1}{1+Z_n(p)} \qquad (6.2)$$

where $Z_n(p)$ is the passive driving point immittance function. At first, put $Z_r(p)=T_rp$ (T_r is positive real number).

In this case

$$\left.\begin{aligned}&W_r(p)=1/(1+T_rp)\\ &|W_r(i\omega)|^{-2}=1+T_r^2\omega^2\\ &\alpha_r=-\mathfrak{Im}\log W(i\omega)=\tan^{-1}T_r\omega\\ &\tau_r=\frac{d\alpha_r}{d\omega}=T_r\cdot|W_r(i\omega)|^2\end{aligned}\right\} \qquad (6.3)$$

where τ_r is group delay and α_r is phase characteristic. In the above equation τ_r is proportional to $|W_r|^2$, this means that the group delay characteristic is flat in the region where the attenuation characteristic is flat and the group delay decreases when attenuation increases. And next let us put $W(p) = W_M{}^M(p)$, then

$$\left.\begin{aligned} &|W_M(i\omega)|^{-2}=1+T_M{}^2\omega^2 \\ &|W(i\omega)|^{-2}=(1+T_M{}^2\omega^2)^M \\ &\alpha=M\tan^{-1}T_M\omega \\ &\tau=M\cdot T_M\cdot|W_M(i\omega)|^2 \end{aligned}\right\}. \qquad (6.4)$$

When M is large; attenuation increases quickly at the band edge. If there is a requirement that working attenuation $\beta=-\Re\log W(i\omega)$ must be greater than β_1 in the region $\omega \geq \omega_1$, then T_M is easily obtained from the following equations.

$$|W(i\omega_1)|^{-2}=(1+T_M{}^2\omega_1{}^2)^M=e^{2\beta_1} \qquad (6.5)$$

$$T_M=\sqrt{e^{2\beta_1/M}-1}. \qquad (6.6)$$

In Fig. 44, the β and τ characteristics are shown with the parameter M when $\beta_1=3\,\text{dB}$.

And next let us consider the following function

$$Z_n(p)=\frac{2R_n p}{p^2+\omega_{0n}{}^2}. \qquad (6.7)$$

In this case

$$\left.\begin{aligned} &|W_n(i\omega)|^2=\frac{\left\{1-\left(\dfrac{\omega}{\omega_{0n}}\right)^2\right\}^2}{1+\left\{\left(\dfrac{2R_n}{\omega_{0n}}\right)^2-2\right\}\left(\dfrac{\omega}{\omega_{0n}}\right)^2+\left(\dfrac{\omega}{\omega_{0n}}\right)^4} \\ &\alpha_n=\tan^{-1}\frac{2R_n\omega}{\omega_{0n}{}^2-\omega^2} \\ &\tau_n=\frac{2R_n}{\omega_{0n}{}^2}\,\frac{1+\left(\dfrac{\omega}{\omega_{0n}}\right)^2}{1+\left\{\left(\dfrac{2R_n}{\omega_{0n}}\right)^2-2\right\}\left(\dfrac{\omega}{\omega_{0n}}\right)^2+\left(\dfrac{\omega}{\omega_{0n}}\right)^4} \end{aligned}\right\} \qquad (6.8)$$

τ_n is not proportional to $|W_n(i\omega)|$. To prevent τ_n from increasing, let us put R_n as follows

$$\left(\frac{2R_n}{\omega_{0n}}\right)^2-2=1 \qquad (6.9)$$

$$R_n=\sqrt{3}\ \omega_{0n}/2. \qquad (6.10)$$

Then

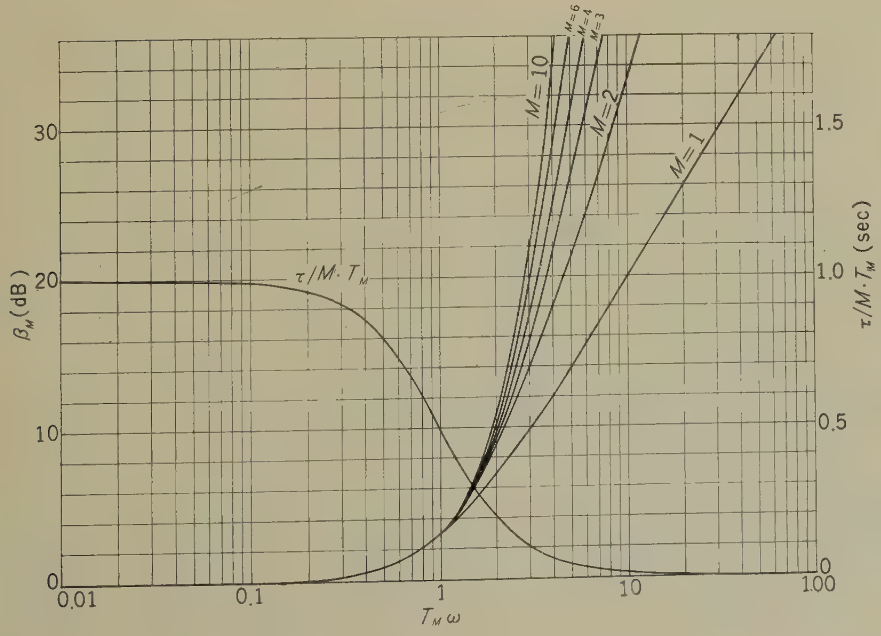

Fig. 44—Frequency characteristics of filter parts.

$$\left.\begin{aligned} W(p) &= \frac{p^2+\omega_{0n}{}^2}{p^2+\sqrt{3}\,\omega_{0n}p+\omega_{0n}{}^2} \\ |W_n(i\omega)|^2 &= \frac{\left\{1-\left(\frac{\omega}{\omega_{0n}}\right)^2\right\}}{1+\left(\frac{\omega}{\omega_{0n}}\right)^2+\left(\frac{\omega}{\omega_{0n}}\right)^4} \\ &= \left\{1+\frac{3}{\left(\frac{\omega}{\omega_{0n}}-\frac{\omega}{\omega_{0n}}\right)^2}\right\}^{-1} \\ \tau_n &= \frac{\sqrt{3}}{\omega_{0n}}\,\frac{1+\left(\frac{\omega}{\omega_{0n}}\right)^2}{1+\left(\frac{\omega}{\omega_{0n}}\right)^2+\left(\frac{\omega}{\omega_{0n}}\right)^4} \end{aligned}\right\}. \quad (6.11)$$

The zeros, $\pm i\omega_{0n}$, of W_n are decided according to the requirement of attenuation, and $W(p)$ is obtained as follows

$$W(p)=\prod_{n=1}^{N} W_n(p) \qquad (6.12)$$

where $2N$ is the number of zeros. In Fig 45, τ_n and β_n are shown.

Let the working attenuation defined by equations (6.6) and (6.11) be β_M and β_n, then

$$\left.\begin{aligned} \beta_M &= \frac{M}{2}\log\left\{1+(T_M\omega)^2\right\} \\ \beta_n &= \frac{1}{2}\log\left\{1+\frac{3}{\left(\frac{\omega}{\omega_{0n}}-\frac{\omega_{0n}}{\omega}\right)^2}\right\} \end{aligned}\right\} \quad (6.13)$$

In equation (6.13), changes of T_M and ω_{0n} correspond to the parallel transition of the β_M and β_n characteristic curve to logarithmic frequency (see Figs. 44 and 45). Therefore if the attenuation characteristic is given, the desired filter can be easily synthesized by adding some characteristic curves like in the case of a Zobel filter. From these procedure M, T_M, and zeros, ω_{0n}, are easily obtained and the transfer function becomes

$$W(p)=W_M{}^M(p)\cdot\prod_{1}^{N} W_n(p). \qquad (6.14)$$

Since the denominator of the above equation is a Hurwitz polynomial and the numerator is lower order polynomial, its physical realizability is assured. Furthermore if we realize the above transfer function by a lattice circuit with iterative impedance of constant resistance or by a bridged-T circuit with image im-

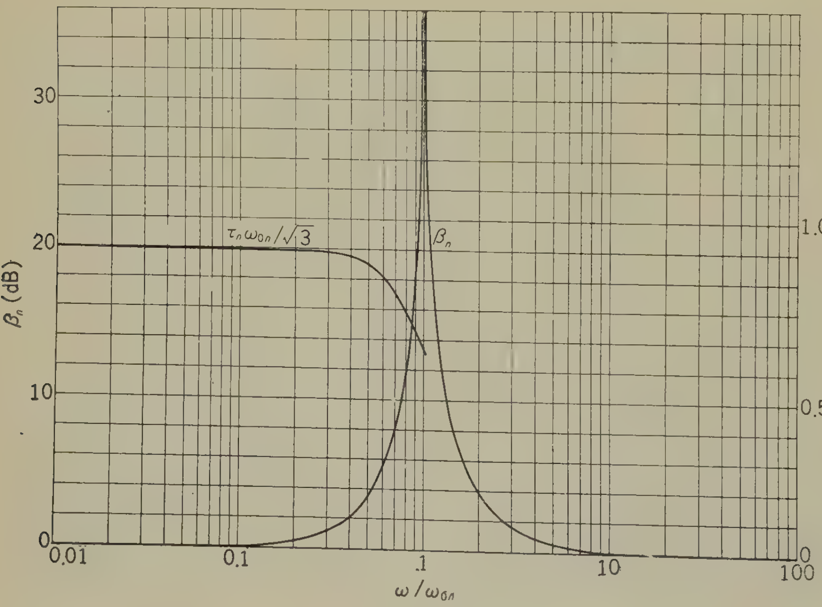

Fig. 45—Frequency characteristics of filter parts.

$$W(p)=W_M{}^M(p)\cdot\prod_1^N W_n(P)$$

$$=\frac{1}{(1+T_MP)^M}\prod_1^N\frac{1}{1+\frac{\sqrt{3}\,\omega_{on}p}{p^2+\omega_{on}^2}}$$

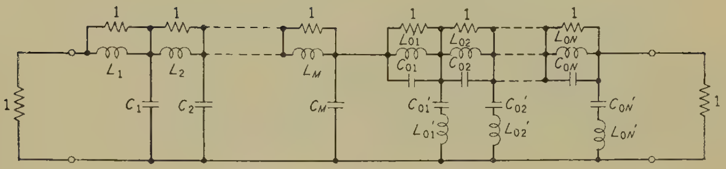

Fig. 46—Example of flat delay filter.

$L_1=L_2=\ldots\ldots\ldots=L_M=T_M$ $\qquad$ $L_{0n}=C_{0n}'=\sqrt{3}/\omega_{0n}$

$C_1=C_2=\ldots\ldots\ldots=C_M=T_M$ $\qquad$ $C_{0n}=L_{0n}'1/(\sqrt{3}\,\omega_{0n})$

pedance with constant resistance, we can realize the partial transfer function separately and calculation becomes very easy. An example is shown in Fig. 46.

Next let us consider the impulse response of this filter. As indicated in equation (6.3) the Pole of $W(p)$ is at $-T_M{}^{-1}$ and is a m-ple pole. Accordingly, its impulse response $I(t)$ becomes

$$I(t)=\frac{t^{M-1}\cdot e^{-1/T_M}}{T_M{}^M(M-1)\,!}. \qquad (6.15)$$

Since $I(t)$ is not smaller than zero when t is positive, there is no overshoot regardless of M. Impulse response of $W_n(p)$ has no meaning itself, therefore let us consider the position of the pole. The position is shown in Fig. 47 and the absolute value of the real part is greater than that of the imaginary part, and attenuation of transient response is very quick.

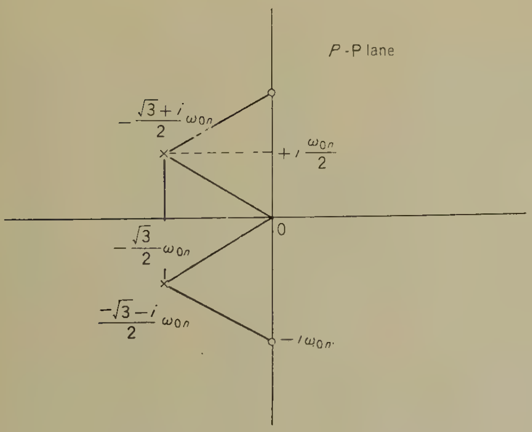
P-Plane
$-\frac{\sqrt{3}+j}{2}\omega_{0n}$
$+j\frac{\omega_{0n}}{2}$
0
$-\frac{\sqrt{3}}{2}\omega_{0n}$
$\frac{-\sqrt{3}-j}{2}\omega_{0n}$
$-j\omega_{0n}$

Fig. 47—Positions of zero and poles of filter parts.

References

(1) Matsuzaki, T.; Kato, M.; and Watanabe, K., Study of error correcting system, *Techn. J., Electr. Commun. Labor. NTT.*, 8(6) pp. 858-863, 1959.

(2) Kameda, O., Toyosawa, H. and Shimizu, T., Transmission of pulse codes through telephone channel, *Tech. Jour., Electr. Commun. Labor. NTT.*, 8(8), pp. 1138-1163, 1959.

(3) Nyquist, H.: Certain topics affecting telegraph speed, *B.S.T.J.*, 3(4), pp. 324-346, 1924.

(4) Sunde, E. D.: Theoretical fundamentals of pulse transmission, Part 1, *B.S.T.J.*, **33**(3), pp. 721-788, 1954.

(5) Laemmel, A. E.: Proceedings of the symposium on modern network synthesis, *Interscience Publishers*, New York, London, p. 211, 1955.

(6) Hermann, O. and Schüssler, W., Zur Auswahl von Filtern mit günstigem Einschwingverhalten, *A.E.Ü.*, **14**(4), pp. 183-189, 1960.

(7) Chalk, J. H. H.: The optimum pulse-shape for pulse communication, *Proc. of I.E.E.* Pt. III, **97**(5), pp. 88-92, 1950.

(8) Aigrain, P. A., Teare, B. R. and William, E. M., Generalized theory of the band-pass low-pass analogy, *Proc. I.R.E.*, **37**(10), pp. 1152-1155, 1949.

(9) Hoshiko, S., Minami, T. and Omori, T., Influence of noise in binary data transmission, *Techn. J., Electr. Commun. Labor. NTT.*, **8**(6), pp. 793-799, 1959.

(10) Hoshiko, S. Minami, T. and Omori, T., Error rate and distortion performance in binary data transmission, *J. Inst. Electr. Commun. Eng. Jap.*, **43**(2), pp. 146-153, 1960.

(11) Rice, S. O., Mathematical analysis of random noise, *B.S.T.J.*, **24**(1), pp. 46-156, 1945.

(12) Minami, T., Group synchronization in binary data transmission, *Techn. J., Electr. Commun. Labor. NTT.*, **9**(4), pp. 425-429, 1960.

(13) I.T.U. List of difinitions of essential telecommunication terms, *I.T.U.*, Geneva, p. 226, 1957.

(14) C.C.I.F.: XVIII th Plenary Assembly Vol. III bis (Line transmission, Maintenance), *I.T.U.*, Geneva, p. 53, 1958.

(15) Working party 43, Report on the meeting of working party 43 on data transmission, GT 43-No. 20, *C.C.I.T.T.*

* * * *

REVIEW OF THE ELECTRICAL COMMUNICATION LABORATORY
VOLUME 9, NUMBERS 7-8, JULY-AUGUST, 1961

U.D.C. 547.962:548.55:537.226

Growth and Electrical Properties of Ferroelectric Glycine Sulfate Single Crystals*

Hiroo TOYODA,† *Yoichi TANAKA*,† and *Wataru SHIOKAWA*†

The crystal growth, distribution of dislocation lines, electrical conductivity and dielectric constant of ferroelectric glycine sulfate are investigated. The effects of crystal imperfection on these properties are particularly interesting.

Addition of Cr^{+3}, Sn^{+2}, and OH^- to the mother solution brings about some appreciable changes in the crystal habit. Most of the dislocation lines rise from the pores near the seed crystal and the distribution of lines seems to be related to the domain structure. The d.c. conduction of the crystal obeys Ohm's law; the resistivity along the b axis is 2×10^{14} ohm-cm at room temperature. The resistivity shows a temperature dependence of exp ($\Delta E/kT$), where ΔE is 1.5 ev in the ferroelectric phase and 0.7 ev in the paraelectric phase. Irradiation with X-rays decreases the resistivity by one order of magnitude and causes a slight increase of ΔE in the paraelectric phase. The dielectric constant of a normal crystal below the Curie point increases with signal amplitude and shows a low frequency dispersion. Impurity addition and irradiation diminish or remove these dependencies and cause some added anomalies between 52 and 56° C. Heavy irradiation lowers the peak value at the Curie point. The crystal imperfections affect the ferroelectric properties through the increase of short-range-order.

1. Introduction

The authors have reported in a previous paper1) that the polarization reversal of a triglycine sulfate (hereafter abbreviated as TGS) crystal is affected by irradiation and by impurity ions. It is an interesting problem to clarify the effects of the crystal imperfections on the other electric properties.

The changes of the properties of ferroelectric substances due to crystal imperfections depend on the crystal symmetry and bonding. For example, the effects of irradiation of $BaTiO_3$2) differ from the effects observed in TGS or rochelle salt.4) TGS has a marked crystal anisotropy and is a typical molecular crystal suitable for the study of the effects of imperfections.

In order to change the crystal habit, impurities are frequently added to the mother solution.5) The experiments with Pb^{+2} in alkali halide and Sn^{+4} in ADP crystals are typical examples. TGS grows with the highest rate along the *b* axis in the usual manner. It is necessary to be able to vary the growing rate depending on the ultimate use of the crystal, and for this purpose the effects of more than ten kinds of impurity ions have been examined.

There have been few reports on the conductivity of molecular crystals except for the case of the π electron network. The study

---

* MS received by the Electrical Communication Laboratory on October 15, 1961. Originally published in the *Kenkyû Zituyôka Hôkoku* (*Electrical Communication Laboratory Technical Journal*), N.T.T., Vol. 10, No. 6, pp. 1181–1195, April 1961.

† Ferroelectric Materials Research Section.

of ferroelectric polarization reversal necessitates information on conductivity. It is interesting that the d.c. conductivity of TGS crystals shows a clear dependence on temperature, a peculiar feature at the Curie point, and is affected by crystal imperfections.

Some precautions are required to obtain the change of dielectric constant with frequency and temperature, as the polarization has a non-linear dependence on the measuring field. The main part of the non-linearity originates from the partial reversal of spontaneous polarization, and it is important to know how the dielectric constant behaves when the introduction of imperfections suppresses the reversal.

2. Crystal Growth

All the crystals were grown by a slow-cooling method. The additional impurity ions examined in the growing experiments near 40°C are Na^+, K^+, NH_4^+, Mg^{+2}, Mn^{+2}, Co^{+2}, Ni^{+2}, Cu^{+2}, Zn^{+2}, Cd^{+2}, Sn^{+2}, Al^{+3}, Cr^{+3}, Fe^{+3}, Ti^{+4}, Sn^{+4}, OH^-, Cl^-, and NO_3^-. The impurity concentrations were from 0.032 to 0.5 mole per cent for Cr^{+3}, 0.2 and 0.5 mole per cent for Sn^{+2}, and up to 10 mole per cent for the others.

Of these ions, Cr^{+3}, Sn^{+2}, and OH^- appreciably change the crystal habit. The addition of Cr^{+3} enlarges the faces belonging to the $[10\bar{1}]$ zone and gives a light purple coloration. Fig. 1 shows the changes of habit with increasing concentration. The Sn^{+2} ions lower the growing rate along the *a* axis (Fig. 2). The OH^- ions have a similar effect, though less considerable. The crystal habit also depends on the growing temperature and cooling rate (Fig. 3).

It is thought that the Cr ion is apt to adhere to the $(12\bar{1})$ face, and the Sn ion to the (100) face. The light purple color of a crystal containing Cr fades gradually with the lapse of time after it is taken out of the mother solution. The domain structure of the impurity-doped crystals is quite different from that of the normal crystal and composed

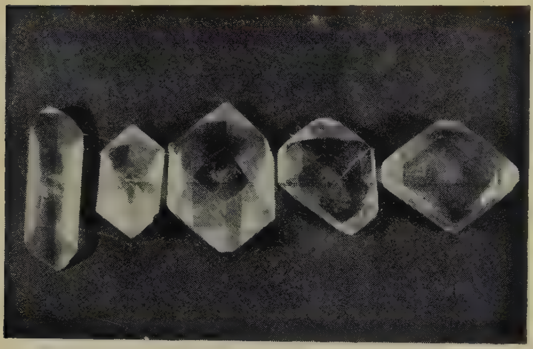

(a)

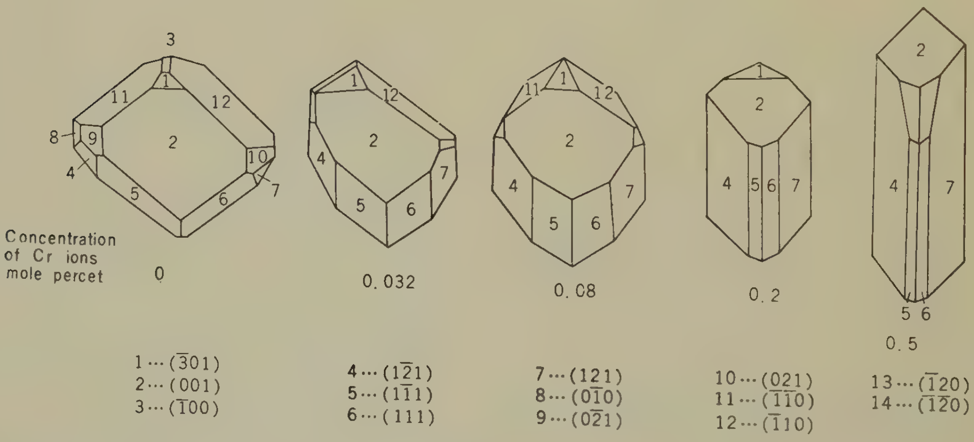

(b)

Fig. 1—The Change of Crystal Habit due to Cr Ions. (*b* axis holizontal.)

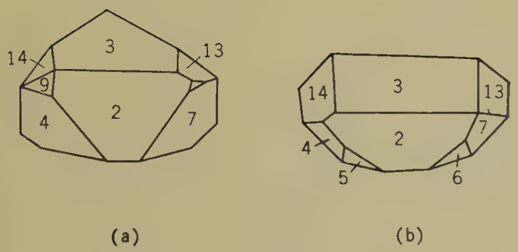

Fig. 2—The Change of Crystal Habit due to Sn Ions.
Impurity concentrations are 0.2 mole percent in (a) and 0.5 mole percent in (b).

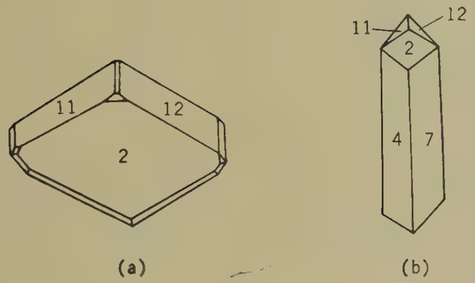

Fig. 3—Crystals Grown in Paraelectric Phase (55°C)
(a) Normal crystal.
(b) Crystal grown in an aqulous solution containing 0.5 mole percent Cr.

of rectilinear domain boundaries.1) The distribution of impurity ions seems to be not uniform, as the polarization reversal characteristics vary from place to place in the crystal.

3. Crystal Dislocation

Crystal dislocation is expected to have some interesting effects on the ferroelectric properties. The etch pits on the (001), (110), and (010) faces of a TGS crystal7) have some peculiar features corresponding to the dislocation line, and the distribution density of the pits closely relates to the seed crystal and seems to bear some relations to the domain structure.

The pits on the (001) face represent the linear imperfections which lie in the (010); namely, the cleavage plane, and are most dense near the site, shown as D in Fig. 4, where the [102] axis passing through the seed crystal cuts the (010) face. On the {110} faces, the pit density is high only near the site B, where the ⟨110⟩ axes passing through the seed crystal cut the faces. On a cleavage face, the pits should concentrate in a fan-shaped region shown as E in Fig. 4, bounded by the lines connecting the seed with the [110] edges, and observation assures that this is really the case. A poling experiment has shown that the fan-shaped region contains a number of domains which are difficult to be reversed[1], and sharp and linear domain bound-

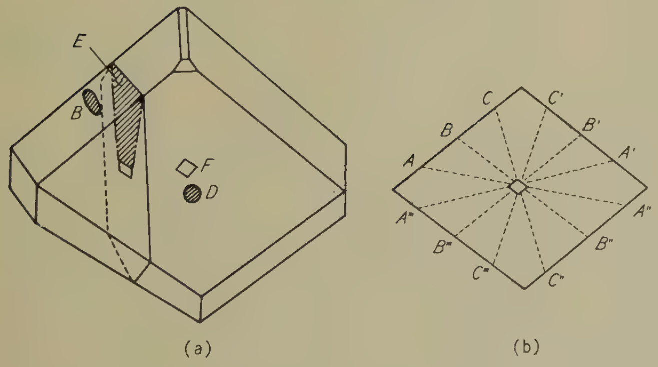

Fig. 4—The Distribution of Etch Pits.
(a) F; seed crystal.
The pits are most dense at B, D, and E.
(b) is a schematic projection along the [001] axis. The pit densities at A, B, and C are similar to those of A″, B″, and C″, respectively.

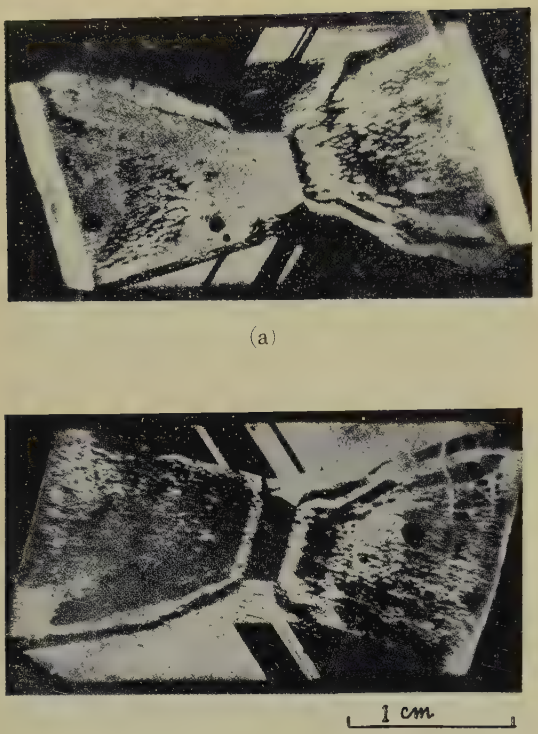
(a)

(b)

Fig. 5—Pictures of Ferroelectric Domains.
The pictures show two faces of a 0.2 cm thick cleaved plate etched with methyl alcohol. The dark area corresponds to the positive end of polarization and the white area to the negative end.

aries with index (201) are frequently observed (Fig. 5). These results suggest a probable effect of dislocation on the domain construction.

4. D.C. Conduction

4.1. Specimens and Method

D.C. conduction was measured along the *a*, *b*, and *c* axes of normal and irradiated crystals and also for crystals grown from aqueous solution containing 0.2 mole per cent of Cr^{+3} and Fe^{+3}. The 0.05 cm thick gold-evaporated crystals are irradiated 4.5 cm from a source of 35 kv X-rays, and the neutron dosage is 3×10^{16} nvt.

When a d.c. voltage is applied to the crystal, both charging and conduction currents flow in the external circuit. The former current decays exponentially but a part of the latter current accumulates, forming a space charge which reduces the field in the crystal to some degree. The conduction current is given by

$$I=(V_0-V_s)/R=V_0/R',$$

where V_0 and V_s are the applied and the reversed voltage due to the space charge, and R and R' are true and apparent resistances, respectively.

4.2. Estimation of Space Charge

The current attains a constant value in about ten minutes (Fig. 6), and when the applied voltage is removed and the circuit is shorted, a discharge current flows in the opposite direction. Assuming that the discharge time constant for the static capacity is much smaller than that for the space charge, and that the space charge accumulates

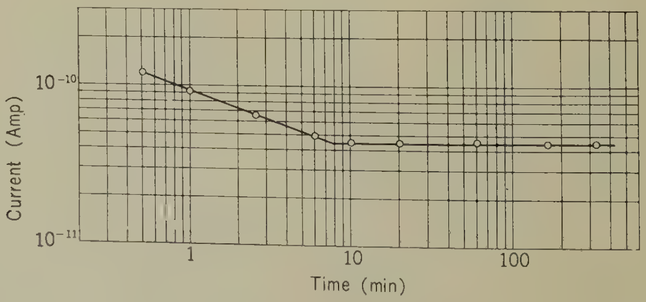

Fig. 6—The current change with time after the application of d.c. voltage.

just below the surfaces, the value of V_s along the b axis was calculated. The value of V_s is proportional to V_0; the result showing agreement with Ohm's law, and it amounts to about six per cent of the applied voltage when saturated and shows little temperature dependence. The space-charge discharging current decays approximately as t^{-1} throughout the test temperature range between 25 and 80°C. The resistivities hereafter are corrected for the space charge field.

4.3. Resistivity

The resistivity along the b axis is 2×10^{14} ohm-cm at room temperature and decreases with temperature as $\exp(\Delta E/kT)$. As shown in Fig. 7, the curve of $\log \rho$ vs $1/T$ exhibits a clear kink at the Curie point. The activation energy is 1.5 ev in the low temperature phase and 0.7 ev in the high temperature phase, respectively. The temperature dependence of the conduction along the other two axes are similar, and the resistivity along the c axis only is smaller by one order of magnitude.

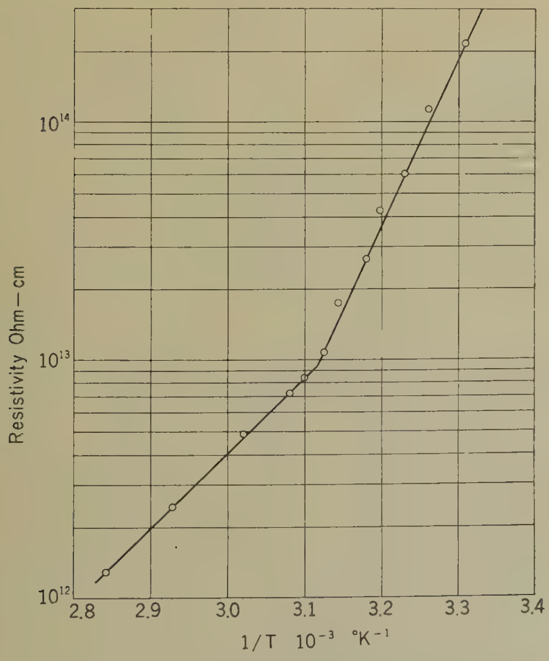

Fig. 7—Temperature dependence of resistivity along the b axis.

Irradiation by X-rays brings about a decrease of resistivity, the effect being particularly considerable along the c axis. As represented in Table I, fifteen minutes irradiation suffices to decrease the resistivity at room temperature and further irradiation merely causes an increase of activation energy above the Curie point.

The activation energy along the b axis may be arranged in the following order:

virginal ferro. phase $\approx$ irradiated ferro. phase $>$ irradiated para. phase $>$ virginal para. phase.

The addition of impurities does not affect the resistivity at room temperature, but increases the activation energy in a manner similar to irradiation. In a polarization reversal experiment$^{1)}$, the biasing field due to irradiation or impurity addition tends to be annealed by heating above the Curie point, but this is not the case for resistivity and the temperature dependence does not vary in heating and cooling runs.

5. Dielectric Constant

The specimens and treatment were the same as in the previous section, but were limited to the direction along the b axis. The test frequency varied from 30 c/s to 5 Mc/s.

5.1. Field Dependence

The polarization of ferroelectrics has a non-linear relation to the applied field and accordingly, the dielectric constant varies with the test signal amplitude. The main contribution to the non-linearity may originate from the reversal of spontaneous polarization. Figs. 8 and 9 show the field dependencies of dielectric constant for various temperatures and frequencies. There seems to exist a definite threshold field, E_T, where the non-linearity starts. The lower the signal frequency and the higher the temperature, the smaller the threshold field becomes. At room temperature E_T is about 2 V/cm for 120 c/s.

Irradiation diminishes the field dependence

Table I

RESISTIVITY OF TGS CRYSTALS

Axis	Treatment	Resistivity (Ω cm)		Activation Energy (eV)	
		27° C	48° C	Ferro. Phase	Para. Phase
b	Normal	1.5×10^{14}	8.5×10^{12}	1.5	0.7
//	X-ray 15 mins.	1.9×10^{13}	6.5×10^{11}	1.35	0.73
//	X-ray 1 hr.	2×10^{13}	6.5×10^{11}	1.39	0.84
//	X-ray 4 hrs.	2.1×10^{13}	6.0×10^{11}	1.52	0.92
//	Neutron	1.8×10^{13}	6.2×10^{11}	1.58	0.9
//	Fe^{+3}	3×10^{14}	1×10^{13}	1.47	0.9
//	Cr^{+3}	3.5×10^{14}	7×10^{12}	1.68	0.9
//	Cr^{+3} X-ray 4 hrs.	3.5×10^{13}	8×10^{11}	1.6	0.9
c	Normal	2.7×10^{13}	1.2×10^{12}	1.3	0.75
//	X-ray 15 mins.	7×10^{11}	1.4×10^{10}	1.9	0.6
//	X-ray 1 hr.	8.5×10^{11}	1.5×10^{10}	1.86	0.67
//	X-ray 4 hrs.	7×10^{11}	2.5×10^{10}	1.65	0.71
//	Fe^{+3}	1.3×10^{12}	3.1×10^{10}	1.65	0.6
//	Fe^{+3} X-ray 1 hr.	8.5×10^{11}	1.6×10^{10}	1.84	0.68

of the dielectric constant. For example, five minutes irradiation of X-ray augments E_T of 120 c/s up to 8 V/cm and fifteen minutes irradiation raises it to over 30 V/cm. The dielectric loss angle of virgin crystal also increases with the signal amplitude, and the introduction of crystal imperfections not only lessen its field dependence, but also lower the absolute value measured with a small signal.

5.2. Frequency Dependence

To obtain the frequency dependence of the dielectric constant, a sufficiently small signal is used lest the apparent dispersion according to the field dependence should disturb the measurement. For a virgin crystal, the dielectric constant shows marked dispersion below 1 kc/s and above 100 kc/s at room temperature. The dielectric loss angle takes a minimum of 0.04 at 10 kc/s (Fig. 10). Irradi-

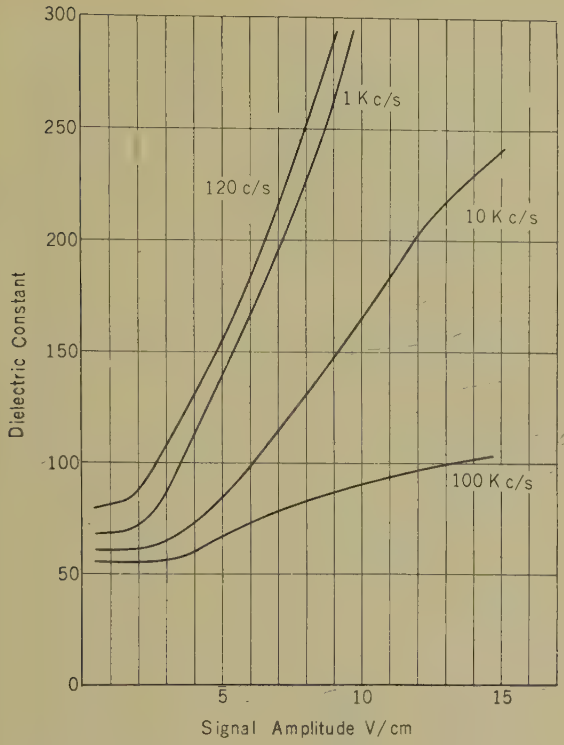

Fig. 8—Field dependence of dielectric constant of normal crystal at 28° C.

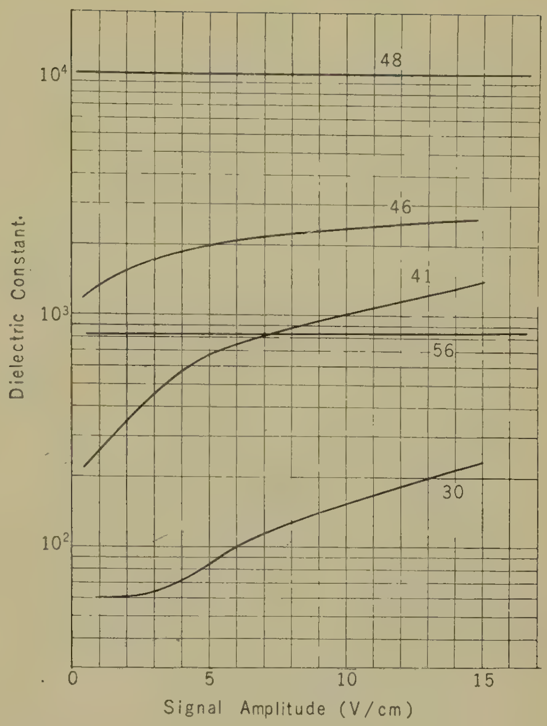

Fig. 9—Field dependence of dielectric constant normal crystal; 10 kc/s; Numerals are test temperatures in °C.

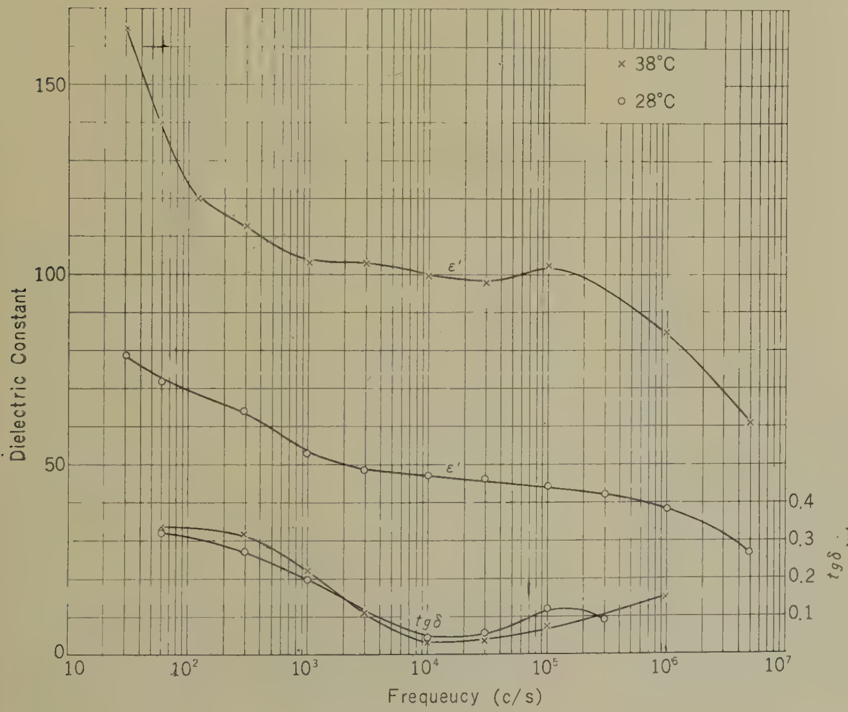

Fig. 10—Frequency dependence of dielectric properties (normal crystal): ×38°C; ○28°C

ation and impurity addition remove the low frequency dispersion, but have little effect on the dispersion above 100 kc/s.

5.3. Temperature Dependence

The temperature dependence of the dielectric constant is measured at 10 kc/s, where the dispersion is not marked. Fig. 11 shows the change of virgin crystal. The dielectric constant reaches a peak of 2×10^4 at the Curie point. X-ray irradiation does not give any marked effect on the room temperature constant, but lowers the peak value, which becomes 2×10^3 after four hours irradiation. X-ray irradiation up to four hours does not change the Curie point, but neutron irradiation lowers it about 2°C (Figs. 12 to 16).

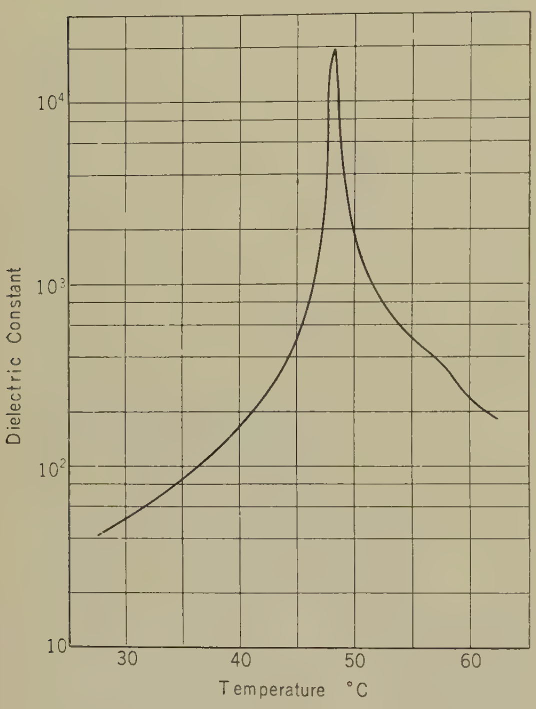

Fig. 11—Dielectric constant of normal crystal. (10 kc/s)

The addition of Cr^{+3} and Fe^{+3} does not affect the Curie point nor the peak value. In

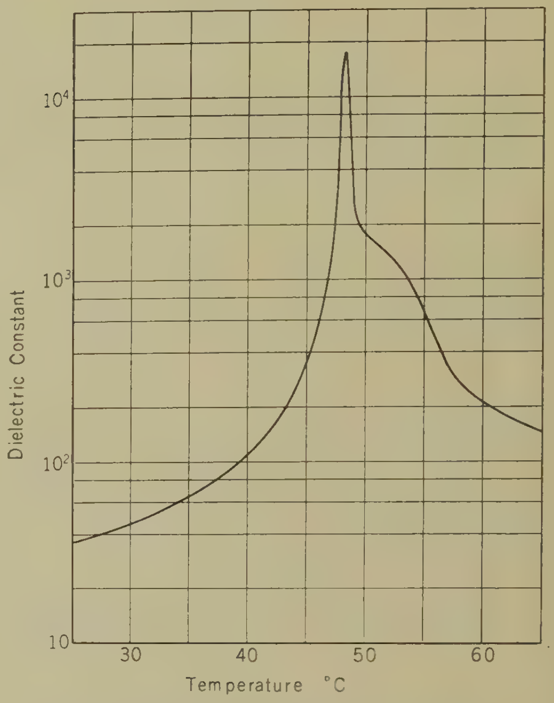

Fig. 12—Dielectric constant of crystal irradiated for 5 minutes. (10 kc/s)

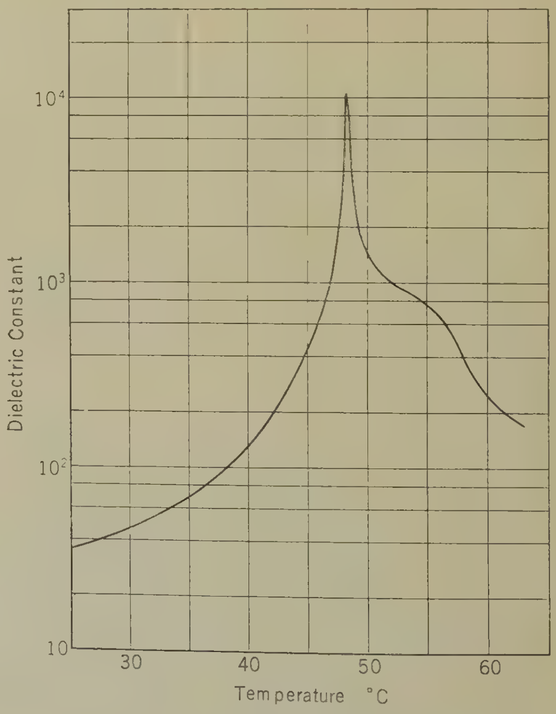

Fig. 13—Dielectric constant of crystal irradiated for 15 minutes. (10 kc/s)

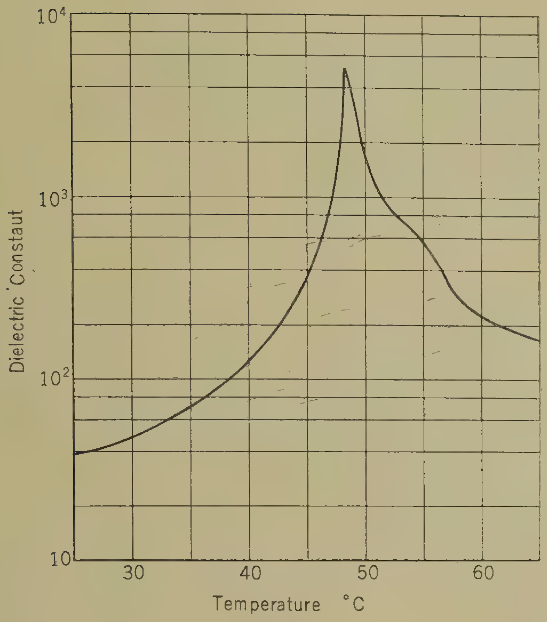

Fig. 14—Dielectric constant of crystal irradiated for 1 hour. (10 kc/s)

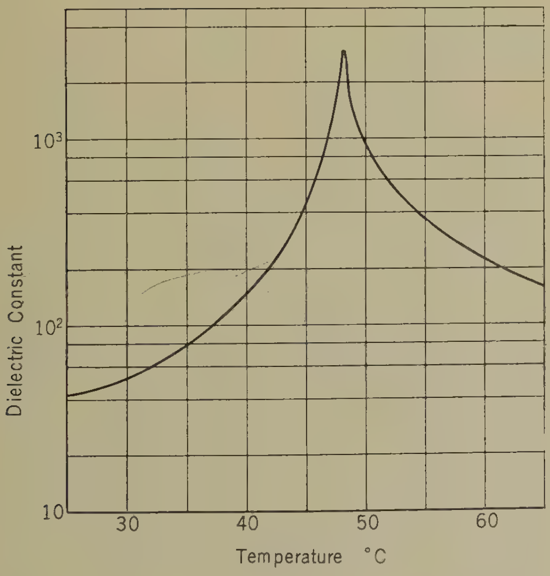

Fig. 15—Dielectric constant of crystal irradiated for 4 hours. (10 kc/s)

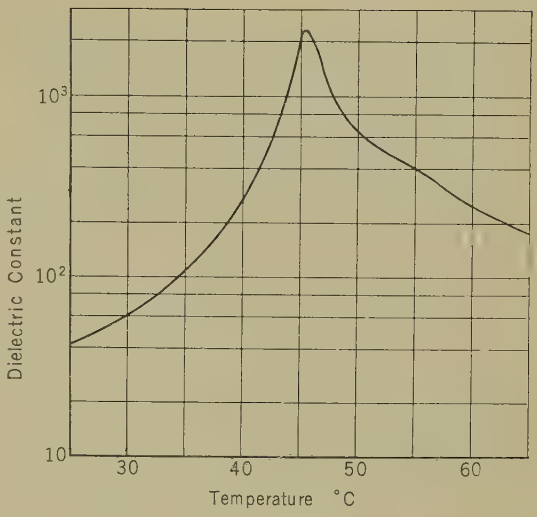

Fig. 16—Dielectric constant of crystal irradiated with neutrons. (10 kc/s)

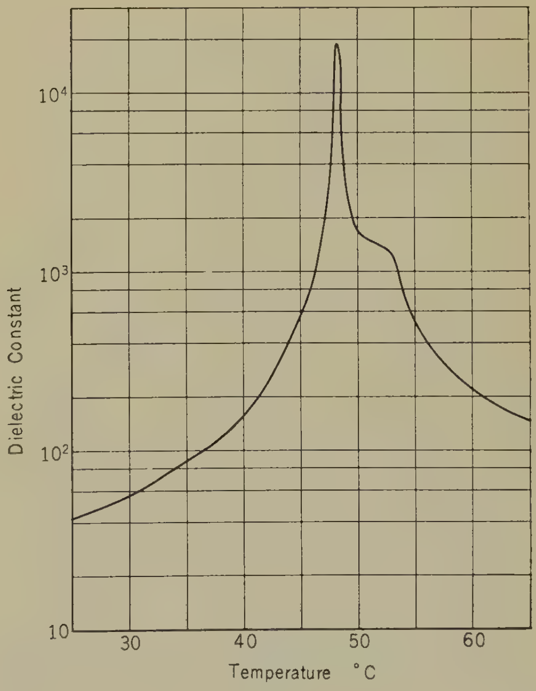

Fig. 17—Dielectric constant of crystal containing Cr ions. (10 kc/s)

these crystals and weakly irradiated crystals, marked added anomalies appear between 52 and 56°C (Fig. 17). These anomalies become less considerable for heavy irradiation, but it is unknown whether they are really lost or driven away to a higher temperature range.

The dielectric constant above the Curie point is known to obey the Curie-Weiss formula,

$$\varepsilon' = 2\pi / A(T - T_C).$$

As TGS crystal undergoes a second order transition of the order-disorder type,[8] T_C is nearly equal to the transition temperature. As seen in Fig. 18, the inversely proportional relation also holds below the Curie point.

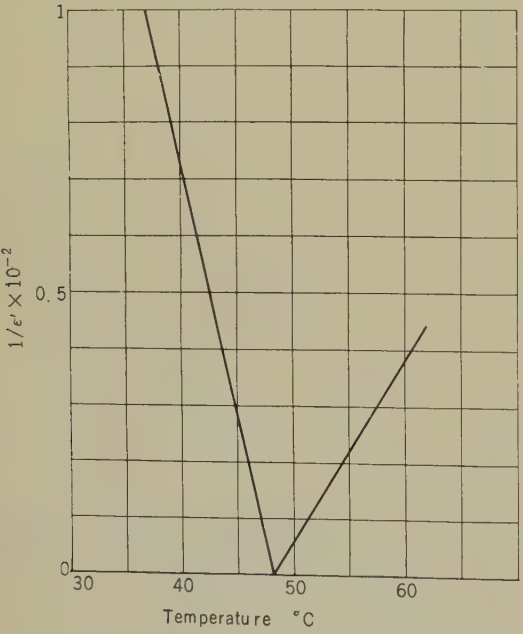

Fig. 18—Normal crystal. (10 kc/s)

Although Devonshire's theory[9] predicts that the ratio of the slopes of the two curves should be equal to −2, the observed value is −3. A similar discrepancy has been found by Triebwasser,[10] and Hoshino et al.[11] In heavily irradiated crystals, the lines of ferroelectric phase show a kink below which the slopes are common for all crystals. The slopes of the curves just above the Curie point have a nearly common value regardless of added anomalies and can be represented by $A = 1.9 \sim 2.2 \times 10^{-3}/°C$.

6. Discussion

It has not yet been determined whether the carriers of electric conduction are electrons or ions. TGS crystals are composed of glycinium and sulfate ions, and zwitter ions of glycine[8]; and can not be considered as an intrinsic molecular crystal, but these ions are not conceived to move in the crystal. The carriers should be electrons or protons or hydroxyl ions. From the saturation characteristic as shown in Fig. 6, and so far as the current after saturation is concerned, the majority carriers seem to be electrons.

At the Curie point, long-range-order in the TGS crystal vanishes, while short-range-order remains over 80°C. Since the temperature coefficient of electronic conduction in a ordered state exceeds, in general, that of a disordered state, a kink observed at the Curie point in the case of TGS may have a relation to the ordering.

The coercive field of a ferroelectric substance is defined from the hysteresis loop, as a field where the average polarization vanishes. The field does not, therefore, mean a minimum field strength required for the partial reversal of polarization, but depends on the value of dE/dt of the test signal.[12] Although E_T defined in the previous section is much smaller than the coercive field, it is doubtful whether a field lower than E_T would not reverse the polarization, because the dielectric constant measured by the smaller signal exhibits a dispersion below 1 kc/s in the virgin crystal, and the dispersion is removed by the irradiation. The generation of a biasing field due to irradiation lessens the field dependence and may remove the apparent dispersion.

The decrease of peak value due to irradiation can not be attributed to the absence of field dependence, because the peak value does not depend on the test signal field nor the frequency (up to 1 Mc/s). Irradiation causes an increase of short-range-order, which lessens, in general, the dielectric constant near the transition temperature. The change of short-range-order due to irradiation is larger in the paraelectric phase than in the ferroelectric phase and corresponds to the change of the activation energy of conductivity.

Though there have been many reports of irradiation effects on ferroelectric properties, the mechanism is not yet under-stood. In ferroelectric molecular crystals, such as rochelle salt and TGS, even X-ray irradiation of smaller energy than that required to knock on the atoms gives some appreciable effects. Irradiation affects the electronic configuration, primarily ionizing the bonds between the ions and secondarily causing their rearrangement. An increase of short-range-order results around the imperfection introduced. A similar mechanism is conceived to occur with the addition of impurity ions.

The pile irradiation has a possibility to knock on the atoms or ions, but the reason why the Curie point shifts to a lower temperature is not yet understood. Tanaka and his co-workers reported a similar shift caused by γ-rays.[13)]

7. Conclusion

The addition of impurity ions to the mother solution of growing TGS crystal not only changes the crystal habit, but also influences the domain structure, polarization reversal, electric conductivity, and dielectric constant. The impurity effect resembles that of irradiation with a small dosage and these effects may be treated en bloc as phenomena due to crystal imperfections. The study of the effect of imperfections is important to know the structure-sensitivity of ferroelectrics and worthwhile to explain some paradoxes among the experimental results so far reported. In a crystal, such as TGS, which undergoes an order-disorder transition, the introduction of imperfections affects the ferroelectric properties through the increase of local order.

The d.c. conduction of TGS obeys Ohm's law, if the space charge field is taken into account and the resistivity varies with temperature as exp $(\Delta E/kT)$, where ΔE is smaller in the paraelectric phase. Irradiation decreases the resistivity and brings about a slight increase of ΔE in the paraelectric phase. The current seems to be transported by electrons.

The field dependence and low frequency dispersion of the dielectric constant of a normal crystal are lessened or removed by the introduction of crystal imperfections, or in other words, by the restriction of polarization reversal. The lowering of the peak value at the Curie point due to irradiation is considered as caused by an increase of local ordering.

The authors are grateful to Dr. H. Hirabayashi and the other members of the Ferroelectric Research Division for their helpful suggestions and cooperation.

References

(1) H. Toyoda and Y. Tanaka: Growth and Domain Structure of and Irradiation Effect on Ferroelectric Glycine Sulfate Single Crystals, *J. Appl. Phys. Japan*, **29**, (1960), 521.
(2) I. Lefkowitz: Radiation-Induced Changes in the Ferroelectric Properties of Some Barium Titanate-type Materials, *J. Phys. Chem. Solids*, **10**, (1959), 169.
(3) A. G. Chynoweth: Radiation Damage Effect in Ferroelectric Triglycine Sulfate, *Phys. Rev.*, **113**, (1959), 159.
(4) K. Okada: Some Properties of X-ray Damaged Rochelle Salt, *J. Phys. Soc. Japan*, **15**, (1960), 363.
(5) H. E. Buckley: Crystal Growth, p. 339, John Wiley & Sons, New York, 1951.
(6) J. J. Kobb: Habit Modification of Ammonium Dihydrogen Phosphate Crystals during Growth from Solution, *J. Am. Chem. Soc.* **67**, (1945), 894.
(7) H. Toyoda: Dislocations in Ferroelectric Glycine Sulfate Single Crystals, *J. Phys. Soc. Japan*, **15**, (1960), 1539.
(8) S. Hoshino, Y. Okaya, and R. Pepinsky: Crystal Structure of the Ferroelectric Phase of (Glycine)$_3$ H_2SO_4, *Phys. Rev.*, **115**, (1959), 323.
(9) A. F. Devonshire: Theory of Ferroelectrics, *Advances in Phys.*, **3**, (1954), 86.

(10) S. Triebwasser: Study of the Second-Order Ferroelectric Transition in Tri-Glycine Sulfate, *I.B.M. J. Res. Dev.*, **2**, (1958), 212.
(11) S. Hoshino, T. Mitsui, F. Jona, and R. Pepinsky: Dielectric and Thermal Study of Tri-Glycine Sulfate and Tri-Glycine Fluoberyllate, *Phys. Rev.*, **107**, (1957), 1255.
(12) H. Shibata, H. Toyoda, and S. Waku: Ferroelectric Polarization Reversal by Linear Fields to be published in this Reports.
(13) K. Toyoda, A. Kawabata, and T. Tanaka: The Effects of γ-Ray Irradiation on the Properties of Triglycine Sulfate Crystals, *Read in the 13th Annual Meeting of Physical Society of Japan*, 1960, October.

* * * *

REVIEW OF THE ELECTRICAL COMMUNICATION LABORATORY
VOLUME 9, NUMBERS 7-8, JULY-AUGUST, 1961

U.D.C. 537.533.3:621.385.65.001.2

A Study of M-type Tube Electron Guns*

Tomoyuki UNOTORO†

Electron orbits in M-type tube guns have been investigated. New types of simple designs with good characteristics, i.e. a plane electrode gun, a cylindrical electrode gun and also convergent guns of the immersed type, have been obtained.

The experimental results have proved the utilities of these new designs.

1. Introduction

The M-type traveling wave tube, a so-called crossed-field tube, is a microwave tube in which the beam travels perpendicular to crossed static electric and magnetic fields. Its basic structure is shown schematically in Fig. 1.

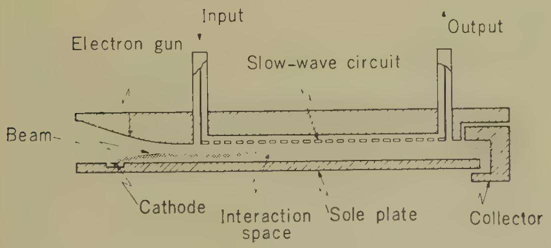

Fig. 1—Structure of M-type traveling wave tube.

This figure shows the cross section of the tube cut through the middle. The electrons, after being emitted from the cathode, travel in the form of planar beam through the interaction space along the flat slow-wave circuit at a velocity nearly equal to that of the circuit waves. For this purpose, positive voltage is applied to the upper electrode, and a uniform magnetic field whose direction is perpendicular to the plane of the paper is also applied. Thus, the vertical force on the electrons due to the static electric field is balanced by the vertical Lorentz force due to the static magnetic field against eletrons travelling horizontally, and the electrons can be kept in horizontal motion.

The special features of this type of tube are its high efficiency and large output. The mechanism of energy transfer is the same as that in the magnetron. Namely, the potential energy of the electrons is changed into high-frequency energy. Thus, high efficiency like that of the magnetron is realized in this tube.

As mentioned above, in the M-type tube, the static magnetic field must be transverse to the beam and the electron beam must be planar. Accordingly, the geometry of the electron gun, its electron accelerating system, is quite different from that of the commonly used O-type traveling wave tube.

In the M-type traveling wave tube, two types of electron gun have been widely used: one is a short gun in which the cycloid orbit of the electrons is curved on the way, and the other a long gun in which a hyperbolic electrode is used.1)

---

* MS in Japanese received by the Electrical Communication Laboratory, on October 28, 1960. Originally published in the *Kenkyû Zituyôka Hôkoku* (*Electrical Communication Laboratory Technical Journal*), N.T.T., Vol. 10, No. 5, pp. 731–770, 1961.

† Electronic Components Research Section.

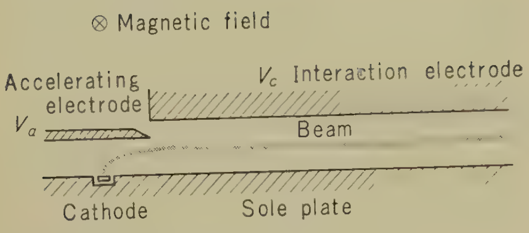

Fig. 2—M-type short gun.

As shown in Fig. 2, the short gun injects the electrons emitted from the cathode horizontally into the interaction space by doubling the electric field when the electron has traveled for half the period of the cycloidal orbit. In this type of gun, there is only one set of d-c electric and magnetic fields which gives ideal conditions. Therefore the potential of the interaction electrode cannot be changed without changing the voltage of the accelerating electrode. This causes much inconvenience in a backward wave tube whose beam voltage must be widely varied. This type of gun, however, is sometimes best, because of its simple construction and short length. Further description will not be made because it has been in use so long and has been studied so closely.

The long gun in which a hyperbolic electrode is used is schematically shown in Fig. 3. As shown, a high-potential hyperbolic cross-section accelerating electrode, which constitutes the accelerating system which is the gun, faces the cathode. The electron is accelerated by the gradually increasing electric field, and then is injected into the interaction space.[1)]

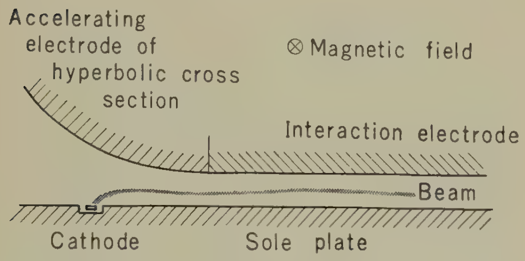

Fig. 3—M-type long gun (Hyperbolic electrode gun).

In this electron gun, it is needless to readjust electrode voltages even when beam voltage is changed. In the backward wave tube, it is advantageous because beam voltage can be changed; therefore, it has come to be used more widely with the development of M-type tubes. In fact, however, the manufacture of this gun is not easy, because the hyperbolic cross-section electrode cannot easily be made by machine.

The only reason why a hyperbolic cross section was chosen as the curved surface is that the analytical solution of the electron orbit is made easier by the use of this particular form.

Therefore, it would be very advantageous to be able to use a simpler electrode shape without decreasing the effectiveness of the gun. But up to now no research has been conducted to determine whether use of simpler electrode shapes is feasible because an analytic solution of the equation of electron motion is not possible.

In addition, the essential features of the M-type traveling tube are displayed to the fullest when the output is large. Therefore, a large electron beam is required. In the usual traveling wave tube types, a convergent electron gun is used; the electron beam emitted from the wide cathode surface is converged so that the electron current density may be increased. The existence of a magnetic field, however, makes the design of an electron gun very difficult. In the M-type tube, the existence of the transverse magnetic field is essential; therefore an immersed-type convergent electron gun could not be designed.

But thanks to the electronic computer, it has recently become possible to solve numerically the differential equation whose analytic solution is impossible. The auther conducted research on M-type electron guns with the help of the electronic computer, and obtained interesting solutions of the above-mentioned problems.

At first, the electron orbit of a gun with a simple planar accelerating electrode, instead of the difficult-to-manufacture hyperbolic electrode, was studied. It was found that the electron orbit is nearly the same as that with the hyperbolic electrode. Also a method of designing the plane electrode has been developed. Now it can be said that the hyperbolic gun is no longer necessary.[2)]

Then, the electron orbit was examined by using a circular cylinder as an accelerating electrode. It was found that when the diameter of cylindrical electrode becomes small enough the shape of electron orbit is changed so as to make possible the rippleless injection of electrons into the interaction space. Therefore, by improving this type, a short gun for which no extra accelerating electrode voltage is necessary was thought to be obtainable.[2)]

Another study was made using the computer on the possibility of the realization of immersed-type convergent guns. It was clarified that this type of gun could be obtained if even quite simple cylindrical electrodes were applied to it. This type is very convenient for practical use because it has only to be immersed in the same uniform magnetic field as the interaction space.[3)]

Test tubes were made following these computed results, and experiments were made on them.[4)] According to them, it was found that the simple plane gun also gave very good beam transmission and that a convergent gun with perveance of 10×10^{-6} was obtained even in the test tubes.

2. Hyperbolic Electrode Gun

This type of electron gun has been in common use since its use for the M-type traveling wave tube was proposed in France, and the equation of orbit has already been obtained.[1)]

In general, when an electron is in motion in the plane determined by x and z, and the static magnetic field $-B_y$ is vertical to these planes, the equations of motion of an electron are as follows:

$$\frac{d^2x}{dt^2}=-\left(\frac{-e}{m}\right)\left[E_x-B_y\frac{dz}{dt}\right] \qquad (1)$$

$$\frac{d^2z}{dt^2}=-\left(\frac{-e}{m}\right)\left[E_z+B_y\frac{dz}{dt}\right] \qquad (2)$$

where

E_x : Static electric field in x direction
E_z : Static electric field in z direction
B_y : Static magnetic field in y direction
e : Electron charge (negative value)
m : Electron mass.

As shown by these differential equations, so long as the value of (electric field)/(magnetic field)^2 is kept constant, the shape of the orbit does not change. When the dimensions are multipled by L, the magnetic field multiplied by M, and the voltage multiplied by L^2M^2; the size of the orbit becomes L times as large. That is to say, the shape of the orbit is invariable, as a result of uniform enlargement. This is known as the scaling law.

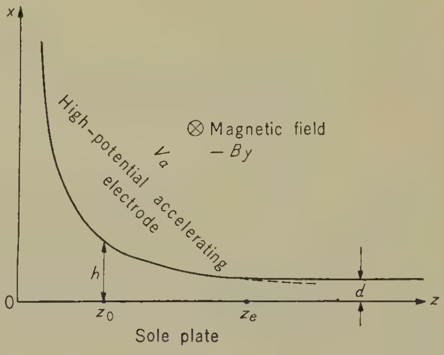

Fig. 4—Hyperbolic electrode gun.

If the hyperbolic shape in Fig. 4 is applied to the high potential electrode, and if the shape can be represented by

$$kx'z'=V_a \qquad (3)$$

where

V_a : Accelerating electrode voltage
k : Shape constant of hyperbolic electrode

then the electron orbit in this system is shown approximately by

$$z=z_0[\exp(c/B)t-(C/B^2)\sin Bt] \qquad (4)$$

$$x=z_0(C/B^2)[\cosh(C/B)t-\cos Bt] \qquad (5)$$

where

z_0 : Initial position of electron
$c=\eta k$
$B=\eta B_y$ (cyclotron frequency)
$\eta=(-e/m)$.

From these equations, so long as $z_0 \doteqdot 0$, the electron orbit proves always to have ripple with the period of cyclotron motion superposed on it.

Suppose that two parallel plane electrodes are placed at a distance of d from each other, the potential difference V_0 is given, and the magnetic field B_y is in existence; then the electron which has started from the low potential electrode at the initial velocity of 0 travels along a cycloid orbit. The cycloid radius R_c is obtained from:

$$R_c=\frac{\eta V_0}{d}\frac{1}{(\eta B_y)^2}=\frac{\eta V_0}{d}\frac{1}{B^2} \qquad \text{or}$$

$$R_c=\frac{1}{\eta}\frac{(\text{electric field strength})}{(\text{magnetic field strength})^2}. \qquad (6)$$

On the other hand, as mentioned above, the ripple R_p of the electron orbit in this hyperbolic gun is given by the coefficient of Eq. (5). If the height of the accelerating electrode from the cathode position z_0 is h, as shown in Fig. 4, then the R_p is transformed as follows because $kz_0=V_a/h$:

$$R_p=z_0\frac{C}{B}=\frac{\eta V_a}{h}\frac{1}{B^2}. \qquad (7)$$

Through comparison between Eqs. (6) and (7), the ripple R_p in the gun proves to be the same as that of the cycloid orbit between parallel plate electrodes at the same potential separated by the gap h.[5)] In other words, this gun is good in that the electron beam is injected into the interaction space caused in a narrow gap and that the amplitude of beam ripple caused at that time is kept as small as the electron orbit between parallel electrodes at the great distance of h from each other shown by Eq. (7).

In addition, the electric field strength due to the hyperbolic electrode at the point z_0 becomes

$$E_{x0}=-V_a/h. \qquad (8)$$

From Eqs. (6) and (7), therefore, the ripple of electron orbit in this accelerating system proves to become equal to the cyclotron radius given by the electric field at the starting point of the electron. So it has been ascertained that the shape of the orbit is decided at the starting point of the electron.

Fig. 6 shows a computed example of an electron orbit in the electrode system whose constants are given in Fig. 5.

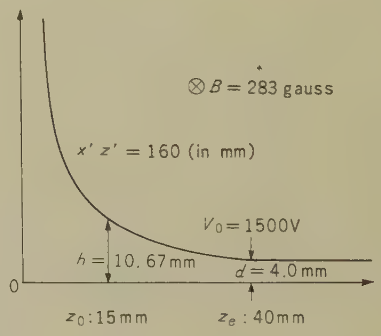

Fig. 5—Dimensions of hyperbolic electrode gun for computation of electron orbit.

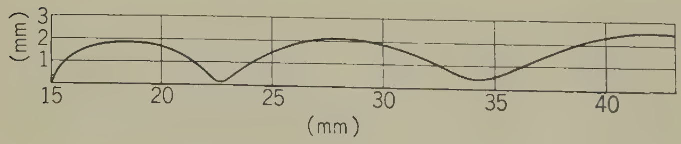

Fig. 6—Computed electron orbit of hyperbolic electrode gun.

3. Plane Electrode Gun

First, the electron orbit in a plane electrode system, which is the simplest electrode to manufacture, is investigated.

The equations of motion of an electron in this system, in polar coordinates, are as follows:

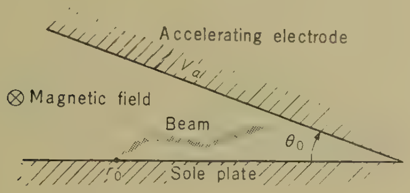

Fig. 7—Plane electrode gun.

$$\frac{d^2r}{dt^2}-r\left(\frac{d\theta}{dt}\right)^2=-Br\frac{d\theta}{dt} \tag{9}$$

$$r\frac{d^2\theta}{dt^2}+2\frac{dr}{dt}\frac{d\theta}{dt}=B\frac{dr}{dt}+\frac{D}{r} \tag{10}$$

where

$B=\eta B_y$ (perpendicular magnetic field)

$D=\eta k'$ (electric field).

With an electronic computer, such differential equations can be solved numerically with ease. In Chart 1, some computation results are shown.[2)] In this case, polar coordinates were used for the equations of electron motion, and computations was carried out in it. But considering the convenience in plotting the orbit, the results of computation were transformed into cartesian coordinates, and are shown together with the results in polar coordinates.

Considering the convenience for the comparison with the computation result of an electron orbit in the hyperbolic gun which is shown in Fig. 6, the transformation was made on the assumption that the cathode was situated at the distance of 15 mm. At the same time, the velocities of the electron were obtained.

Fig. 8 shows the results of the computation of electron orbits which were carried out, for various values of the angle θ between the

Chart 1

COMPUTER OUTPUT OF SOLUTION OF ELECTRON ORBIT IN A PLANE ELECTRODE GUN.

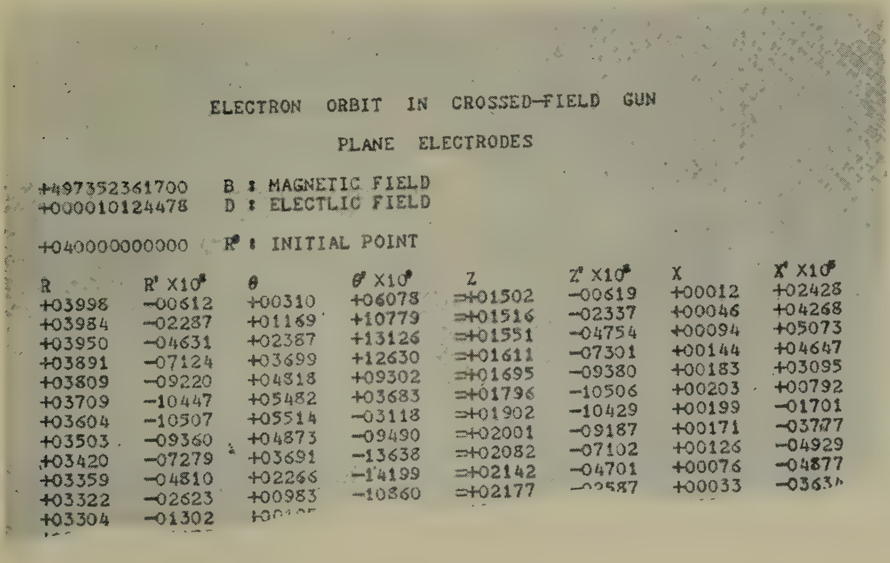

```
               ELECTRON  ORBIT  IN  CROSSED-FIELD  GUN

                         PLANE  ELECTRODES

+497352361700   B : MAGNETIC FIELD
+000010124478   D : ELECTLIC FIELD

+040000000000   R : INITIAL POINT

R         R' X10    θ         θ' X10    Z          Z' X10    X         X' X10
                                                                       +02428
+03998    -00612    +00310    +06078    =+01502    -00619    +00012    +04268
+03984    -02287    +01169    +10779    =+01516    -02337    +00046    +05073
+03950    -04631    +02387    +13126    =+01551    -04754    +00094    +04647
+03891    -07124    +03699    +12630    =+01611    -07301    +00144    +03095
+03809    -09220    +04318    +09302    =+01695    -09380    +00183    +00792
+03709    -10447    +05482    +03683    =+01796    -10506    +00203    -01701
+03604    -10507    +05514    -03118    =+01902    -10429    +00199    -03777
+03503    -09360    +04873    -09490    =+02001    -09187    +00171    -04929
+03420    -07279    +03691    -13638    =+02082    -07102    +00126    -04877
+03359    -04810    +02266    -14199    =+02142    -04701    +00076    -0363
+03322    -02623    +00983    -10860    =+02177    -02587    +00033
+03304    -01302
```

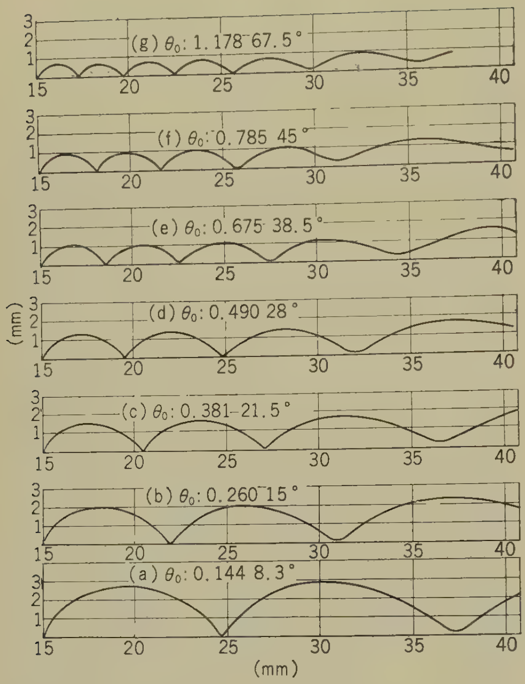

Fig. 8—Computed electron orbits in plane electrode guns.

two electrodes, i.e. accelerating electrode and sole electrode.[2] In all cases, it was assumed that the accelerating electrode voltage V_0 and the magnetic field B_y were 1,500 V and 283 gauss respectively as in the case of hyperbolic electrode shown in Figs. 5 and 6. The distance from the cathode to the entrance of the interaction space of the 4 mm gap was 25 mm. Fig. 9 illustrates the electrode structure whose $\theta_0=15°$ corresponds to that of the hyperbolic accelerating electrode shown in Fig. 5.

For this plane structure, as seen in Fig. 9, at the cathode and the entrance point, *c* and *d* respectively, the vertical distances *h* and *d* from the sole plate to the accelerating electrode are equal to those of the hyperbolic. As a result of comparison between the shapes of these electron orbits, it is found that the orbit in the plane electrode gun closely resembles the orbit in the hyperbolic electrode gun.

Therefore, it can be concluded that even

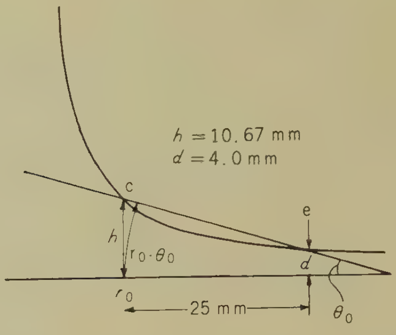

Fig. 9—Dimensions of a plane electrode gun equivalent to a hyperbolic electrode gun.

if the hyperbolic electrode is replaced by the plane electrode, the performance of the gun is not degraded.

For further clarification of the property of electron orbits, researches were made to find common rules among superposed ripples, on the basis of the orbits shown in Fig. 8. First, the amplitudes of ripples of these orbits were numerically evaluated, and are shown in Chart 2 together with the parameters of the electrodes. In the chart, θ means the angle between the electrodes as shown in Fig. 9; $r_0\theta_0$ means the product of the angle and the initial value r_0, which shows the length of arc which passes the cathode to be cut by the two electrodes. On the other hand, the electric field E_θ between the planes is given by

$$E_\theta=-\frac{1}{r}\frac{\partial\varphi}{\partial\theta}. \tag{11}$$

Accordingly, the strength of electric field at the position of the cathode becomes

$$E_\theta=-\frac{V_a}{r_0\theta_0}. \tag{12}$$

The strength of electric field at the position of electrode was calculated, from Eq. (12) and the results are shown in Chart 2.

In order to examine the relation between the amplitude of the ripples obtained here

Chart 2

RIPPLE AMPLITUDES IN PLANE ELECTRODE GUNS AND ELECTRIC FIELD STRENGTHS AT CATHODE.

θ_0	0.144 8.3°	0.260 15°	0.381 21.5°	0.490 28°	0.675 38.5°	0.785 45°	1.178 67.5°
Ripple mm	2.80	2.05	1.62	1.33	1.05	0.95	0.68
$r_0\,\theta_0$	7.58	10.40	13.32	15.93	20.25	22.77	31.40
Electric field strength at cathode $V_a/r_0\,\theta_0$	$\times 10^5$ 1.978	1.443	1.127	0.942	0.741	0.659	0.478

and the strength of electric field, both values are plotted in Fig. 10. As shown, the points expressing these values are arranged in a straight line. By using Eq. (6), the cycloid radius of electron motion when a uniform field, which is the same as the electric field on the cathode, exists between the parallel planes was drawn as seen here. It was found that the ripple of these plane electrode guns corresponds completely to the cycloid radius as shown by the straight line in this figure.[2)]

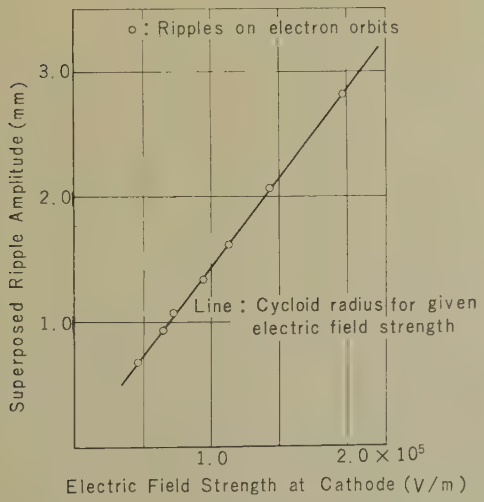

Fig. 10—Ripple amplitude v.s. electric field strength at cathode in plane electrode gun.

It has already been clarified by Eq. (7), for hyperbolic electrode guns, that the ripple of the beam becomes equal to the cyclotron radius given by the electric field on the cathode surface. From Fig. 10, the important conclusion that in the plane electrode guns, as well as in hyperbolic electrode guns, the ripple of the electron orbit becomes equal to the cyclotron radius determined by the electric field on the cathode, i.e. the starting point of electron is obtained.

Thus, as for hyperbolic guns, distinct design data were obtained for the plane electrode guns. If the allowable ripple amplitude is given, the electric field strength on the cathode is fixed by this relation, and the design of plane accelerating electrode is completely determined. The electron orbit of the plane electrode gun has proved not inferior to that of the hyperbolic electrode gun. From now, the easy-to-manufacture plane electrode gun can be used without hesitation.

4. Cylindrical Electrode Gun

The cylinder is the surface which is the easiest to be made by machine. Subsequently, investigations were made on the electron orbit of guns in which a cylindrical high-potential electrode is used.

In Fig. 11, if the center of the electrode

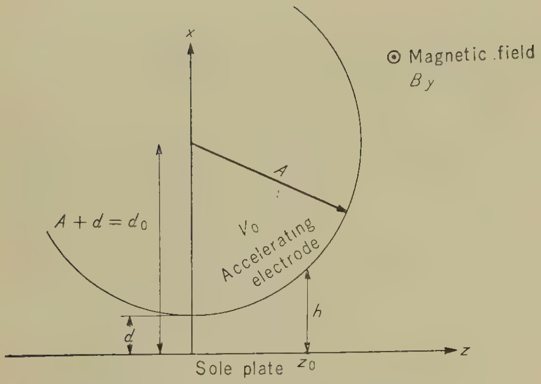

Fig. 11—Cylindrical electrode gun.

with radius A is at the distance of $d_0(=A+d)$ from the sole plate, and the voltage is V_a; then the potential distribution is given by

$$\varphi=\frac{V_a}{2\cosh^{-1}\left(\dfrac{d_0}{A}\right)}\ln\left[\frac{(x+a)^2+z^2}{(x-a)^2+z^2}\right] \tag{13}$$

where $a=\sqrt{d_0^2-A^2}$.

If E_x and E_z obtained from this equation are substituted into Eqs (1) and (2), then the equations of electron motion for this cylindrical electrode system become as follows:

$$\frac{d^2x}{dt^2}=-\eta\left[-\frac{2a\,V_a}{\cosh^{-1}\left(\dfrac{d_0}{A}\right)}\cdot\frac{(z^2-x^2+a^2)}{\{(x+a)^2+z^2\}\{(x-a)^2+z^2\}}-B_y\frac{dz}{dt}\right] \tag{14}$$

$$\frac{d^2z}{dt^2}=-\eta\left[\frac{2a\,V_a}{\cosh^{-1}\left(\dfrac{d_0}{A}\right)}\cdot\frac{2xz}{\{(x+a)^2+z^2\}\{(x-a)^2+z^2\}}+B_y\frac{dx}{dt}\right]. \tag{15}$$

Electron orbits obtained by electronic computer are shown in Fig. 12.[2] In this case, V_a and B_y are 1500 V and 283 gauss respectively (the same as above) and d is 4 mm (also the same as before). Only the electrode radius A is changed; the cathode z_0 is put at the point 25 mm to the right of the origin; if the interaction space is connected to the left at the origin, the distance between this entrance point and the cathode becomes equal to those in the two types mentioned before. The values on the abscissa of the graph of electron orbit are chosen to coincide with those of the two previous types. When $A=50$ mm, the height from the cathode to the accelerating electrode equals h in the previous example of the hyperbolic electrode (See Fig. 4.). Like curve of $A=50$ in Fig. 12, the orbit obtained here closely resembles the orbit due to the hyperbolic electrode in Fig. 6.

Reduction of the accelerating electrode radius A means either the enlargement of the angle θ of the plane electrode gun or increase of the distance between the cathode and the entrance point of the hyperbolic electrode gun; therefore this results in a decrease of the electric field strength on the cathode. But as shown by the illustration of the orbit obtained by calculation; when the radius A is small, the superposed ripple amplitude does gradually decrease, in contradistinction to the two previous examples. In this case, therefore, it is not so easy to examine the relationship between the ripple and the electric field strength on the cathode as in the previous cases.

To inquire into the nature of this gun, the first maximum ripples were taken up, and comparison was made between the ripple when a 50 mm radius cylindrical electrode was used, and the ripple when a plane electrode with an angle θ of 15° was used. It was found that in both cases, the height to the accelerating electrode at the cathode position was the same but that the ripple amplitude was 2.06 mm in the case of plane electrode gun, and 2.10 mm in the case of the cylindrical electrode gun.

Therefore, it is not always profitable to re-

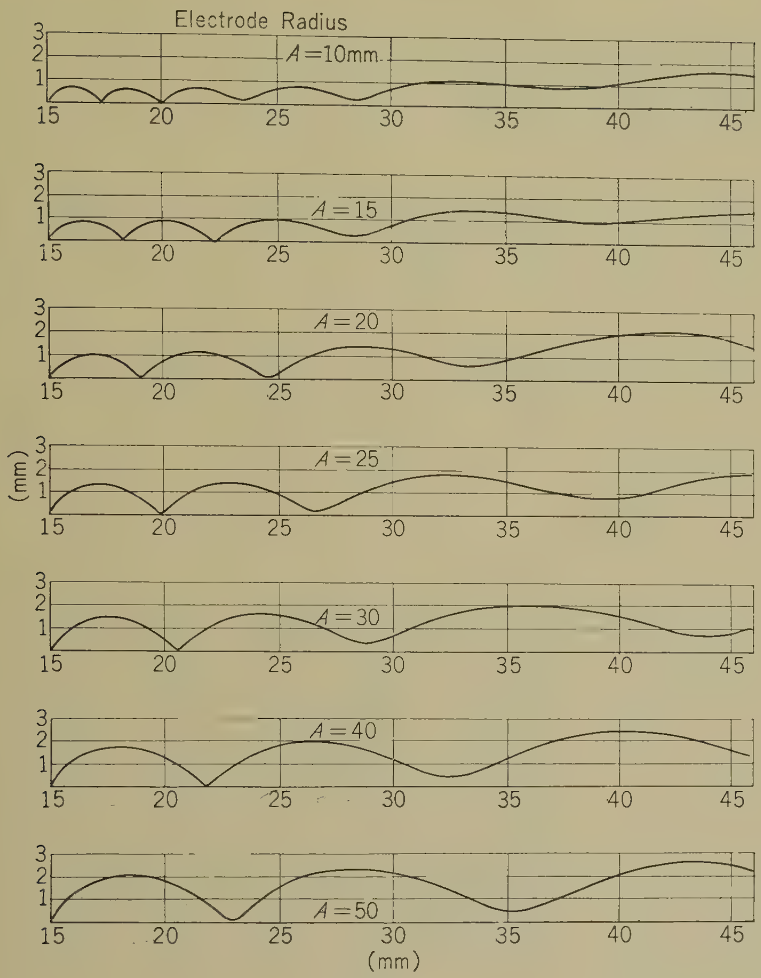

Cathode at 15 mm, Center of electrode at 40 mm.

Fig. 12—Computed electron orbits in cylindrical electrode guns.

place the plane by the cylinder.

As seen by Fig. 12, reduction of the accelerating electrode radius results in a location where the ripple of the electron orbit is very small. By using this part, perfect rippleless injection of electron beam into the interaction space may become possible. On the other hand, if the radius of accelerating electrode is reduced, the electric field strength on the cathode surface drops remarkably. Therefore, the radiated electron beam decreases markedly. This fact shows that it is disadvantageous for practical use if left as is. To improve the perveance as an electron gun by the increasing electron emission, the electric field on the cathode surface should be intensified by putting another accelerating electrode near the cathode.

From Fig. 12, it is found possible to obtain a short gun like that in Fig. 2 by placing a cylindrical accelerating electrode of small radius near the cathode. However, according to the examinations by electronic computer, it was clarified that the velocity did not agree in general with the condition of horizontal injection; therefore, realization of short guns is impossible without modification.

However, further investigation showed that it would become feasible if the sole plane, common with the cathode surface, was made not flat, but cylindrical. The electron orbit between the eccentric cylinders can be obtained by computation if the constants of Eqs. (14) and (15) are changed. For example, a short gun with a single accelerating voltage, constructed as shown in Fig. 13, was found to be obtainable.[2)]

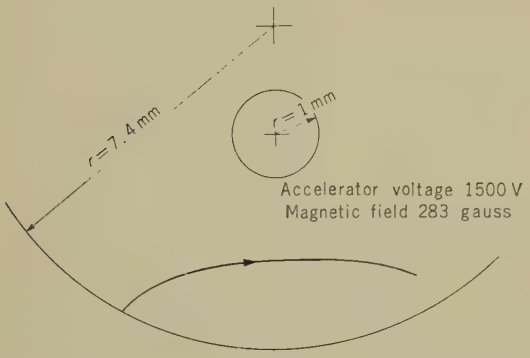

Fig. 13—Electron orbit in an eccentric cylinder short gun.

5. Ripple of Electron Orbit between Parallel Electrodes

In general, when an electron starts at an arbitrary velocity of (u_0, v_0) from the point P between the parallel eletrodes as shown in Fig. 14, and the coordinates of point P are (o, p); then the orbit traced is given by

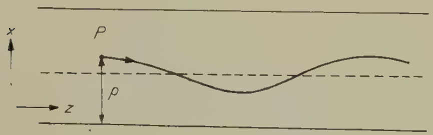

Fig. 14—Rippled electron orbit between parallel plate electrodes.

$$z=\bar{U}_0 t+\left(\frac{u_0-\bar{U}_0}{B}\right)\sin Bt+\frac{v_0}{B}(1-\cos Bt) \tag{16}$$

$$x=\left(p-\frac{u_0-\bar{U}_0}{B}\right)+\left(\frac{u_0-\bar{U}_0}{B}\right)\cos Bt+\frac{v_0}{B}\sin Bt \tag{17}$$

where $\bar{U}_0$ shows the velocity at which the electron travels along a linear orbit in this space, namely

$$\bar{U}_0=E/B.$$

The vertical ripple amplitude R_r in this case is obtained from Eq. (17) as follows:[5)]

$$R_r=\frac{1}{B}\sqrt{(u_0-\bar{U}_0)^2+v_0^2}\,. \tag{18}$$

As described in the previous sections, the electron orbits of the plane electrode gun and the cylindrical electrode gun have already been calculated on an electronic computer. However, the problem still left unsolved is the problem of the ripple in the interaction space.

Now let us compare typical examples of ripples with one another by using the interaction space orbit Eqs. (16) and (17). The dimensions of the electrodes considered are as follows:

Electrode in hyperbolic electrode gun; as shown in Fig. 5.
″ in plane electrode gun; included angle of 15°
″ in cylindrical electrode gun; radius of 50 mm

In these examples, when the distance between the cathode and the injection point is 25 mm as mentioned above, all the heights from the cathode to the accelerating electrode are equal. The electron orbit for each of these electron guns was obtained by electronic computer; under the assumptions that the accelerating electrode voltage was constant at 1,500 V, and the magnetic field B_y was variously 283 gauss, 258 gauss and 231 gauss. The results are shown in Fig. 15. These three values of magnetic field correspond to the three potentials of an electron beam which should travel along a horizontal linear

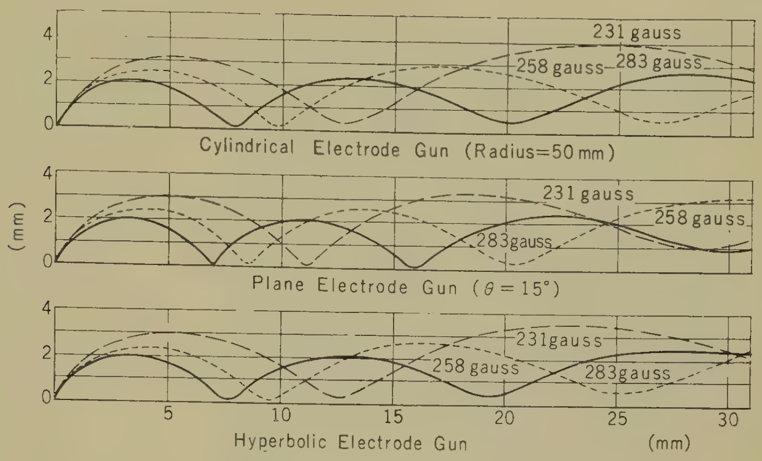

Fig. 15—Electron orbits in three different guns.

Chart 3

RIPPLES AND CENTERS OF ELECTRON ORBITS IN INTERACTION SPACE.

Accelerating system	283 gauss		258 gauss		231 gauss	
	Ripple	Center	Ripple	Center	Ripple	Center
Hyperbolic electrode gun	1. 03	1. 53	1. 16	1. 82	1. 42	2. 22
Plane electrode gun	0. 90	1. 43	1. 40	1. 85	1. 33	2. 17
Cylindrical electrode gun	1. 06	1. 58	1. 15	1. 78	1. 62	2. 38
R_p of eq. (7)	1. 00		1. 20		1. 50	

Veltage 1500 V. Gap of interaction space 4 mm. Values in mm.

orbit, in the interaction spaces of a 4 mm gap: namely, 500 V, 600 V, 750 V. From the electron position and its velocity at the injection point (the point 25 mm on the abscissa) obtained by electronic computer, the ripple amplitude and the height of the center of electron beam were calculated through Eqs. (16) and (17). The results are shown in Chart 3.$^{2)}$ For the sake of comparison, R_p given by Eq. (7), i.e. the ripple of electron orbit in the hyperbolic electrode gun, is also shown. According to this chart, little difference, either advantageous or disadvantageous, exists between the states of the beams of these three accelerating systems when the magnetic fields are changed. In conclusion, from the view-point of stability, neither plane electrode guns nor cylindrical electrode guns are inferior to hyperbolic electrode guns.

6. Convergent Gun

Beam convergence of the electron guns described thus far was not considered in their expositions. That is, when based on cross sections, consideration has been made on the assumption that electron is emitted from one point and that the beam has no thickness. In fact, the cathode has width and the beam has thickness, but no steps were taken to converge the beam by making it as thin as possible. In this section, an electron gun in which the electron beam emitted from the cathode is positively converged is treated.

To construct a convergent gun, the orbit of the electron beam emitted from a large-area cathode must be given the tendency to converge into a point or a line.

Unfortunately however, in a M-type tube with a transverse static magnetic field, analysis of the electron orbit is much more difficult than in the case of a tube with no magnetic field. This is because a force perpendicular to the traveling direction of electron exists in response to the electron velocity. No immersed-type convergent gun whose electron gun part exists in a uniform magnetic field has yet been reported.

To obtain the M-type convergent gun, let us begin by considering a magnetron whose cathode surface, illustrated in Fig. 16, is on the inner side of the outer cylinder. We will consider a magnetron whose inner cylinder is the anode, unlike the magnetron commonly used whose cathode is situated inside of its anode cylinder. In this case, one of the conditions of the above-shown convergent gun, i.e. a broad cathode area, is satisfied.

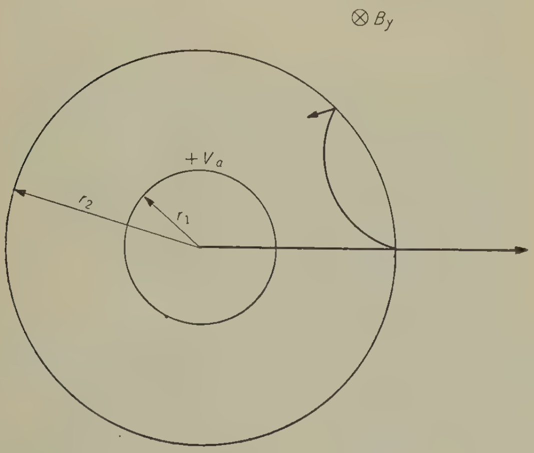

Fig. 16—Outer cathode magnetron.

But it remains to be shown that the orbit of the emitted electrons can be converged. In an outer-cathode type magnetron like this, if the space charge is neglected, the electron orbit is represented by the following equations:

$$\frac{d^2r}{dt^2}-r\left(\frac{d\theta}{dt}\right)^2-\frac{(-e)}{m}B_y r\frac{d\theta}{dt}+\frac{(-e)}{m}\cdot\frac{V_a}{\ln\left(\frac{r_2}{r_1}\right)}\cdot\frac{1}{r}=0 \qquad (19)$$

$$r\frac{d^2\theta}{dt^2}+2\frac{dr}{dt}\cdot\frac{d\theta}{dt}+\frac{(-e)}{m}B_y\frac{dr}{dt}=0 \qquad (20)$$

where

V_a : Anode voltage
B_y : Transverse magnetic field
r_1, r_2: Radii of inner and outer cylinders respectively.

The analytical solution of these differential equations is impossible. In the case of a strong magnetic field, it was only supposed that a curve similar to a hypocycloid would be drawn.

Therefore this electron orbit was calculated on an electronic computer, fixing the potential difference between inner and outer electrodes, and changing the magnetic field little by little. As a result, it was clarified, as shown in Fig. 17, that with its approach to the center the electron orbit deviated more and more from the hypocycloid, sank at the perihelion, and run along a coaxial circle.[3]

Convergent guns can be produced by using this characteristic. For instance, if it is constructed as shown by the cross section in Fig. 18, electrons emitted from the wide cathode surface are converged within a certain range as illustrated in the figure. In this way, a convergent electron gun can be made. But as shown in Fig. 18, this coaxial cylinder structure results in a convergence characteristic with some degree of aberration. Practically, it is necessary to make the aberration as small as possible. As is well known, the period of cyclotron motion of an electron

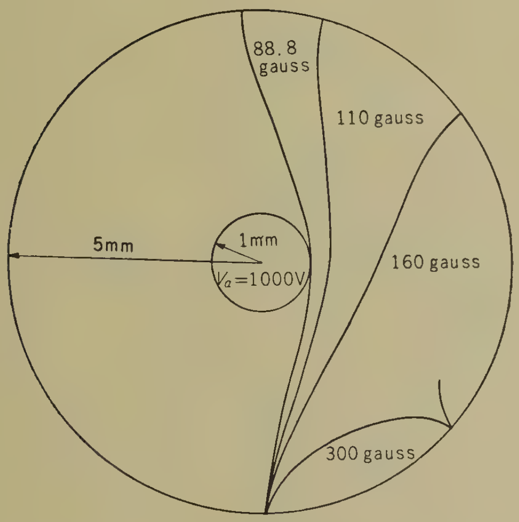

Fig. 17—Computed electron orbits in outer cathode magnetron.

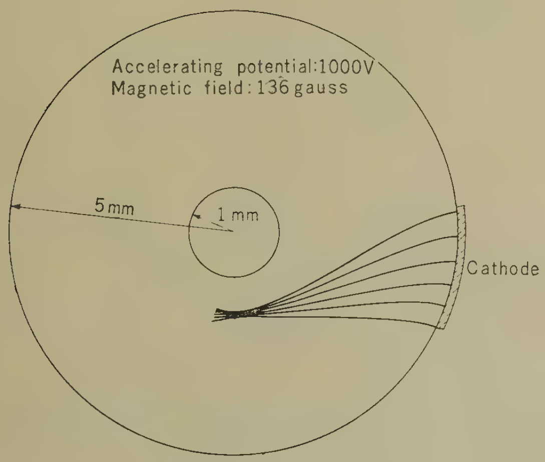

Fig. 18—Coaxial convergent gun.

in the crossed electric and magnetic fields becomes longer with the increase of the electric field strength, if the magnetic field is kept constant. Let us observe Fig. 18, keeping in mind this fact. Then the following supposition is possible for the improvement of the convergence characteristic. At a place far from the focus on the cathode surface, the electric field must be intensified, and at a place near the focus the electric field must be weakened so that the aberration of electron orbit near the focus may be reduced. The simplest way to put it into shape is to move the center of the high potential electrode or the accelerating electrode. For such an eccentric coaxial electrode arrangement, the electron motion equations are similar in shape to Eqs. (14) and (15), and different from (19) and (20). These also can be solved with the help of the electronic computer. Speaking in more detail, the constants of Eqs. (14) and (15) are changed in such a way that the equipotential lines may correspond to the positions of the inner and outer cylindrical electrodes; the initial value is given so that the electron may start from the inner surface of the outer cylinder; then the electronic computer is operated. The electron orbits were numerically obtained, moving the accelerating electrode center little by little, and the results are shown in Fig. 19.[3] As seen in this figure, excellent convergent orbits prove to be obtainable as expected, if the accelerating electrode center is moved properly.

Fig. 19 shows the orbits calculated on the assumption that the electrons were emitted from a fairly large region on the curved cathode surface. As described later, this whole surface can not always be used, but in practice, the electron emission surface must be put in an appropriate range. When this emission surface is small, and aberration is allowed to some extent, the eccentricity of the accelerating electrode is not so precise, as seen from Fig. 19. Furthermore, in this case, focal length is adjusted by eccentricity.

Even the convergent electron gun obtained in this manner is not satisfactory if the characteristic is too critical against changes of voltage and magnetic field. To examine this, change of shape of the orbits against voltage was obtained and is shown in Fig. 20. For this examination, the dimensions of example (e), with the smallest aberration, in Fig. 19 was chosen, and three different voltages were used. It was ascertained that the convergent character is not changed by volt-

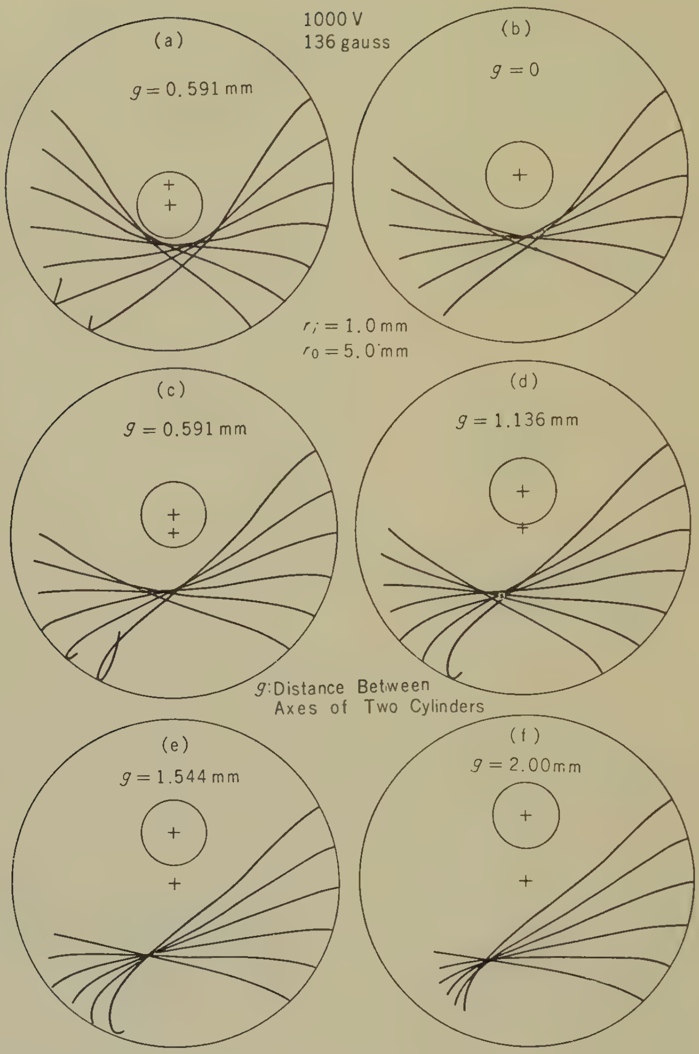

Fig. 19—Electron orbits in eccentric cylindrical electrode systems.

age variation, and that its stability is satisfactory.

The calculation above was applied only to a few sorts of examples. But these calculation results are applicable even for various combinations of voltage, magnetic field, and dimensions, if the scaling law is used. Thus they are applicable fairly widely to the design of tubes. Besides, against any sort of combination, the design can be made easily, if only the program of electronic computer is prepared.

7. Effect of Space Charge

In the examination above, the effect of space charge was not taken into account. In this section, space charge will be investigated to obtain some design data.

In the case of the M-type electron beam, a planar beam is used. Therefore, it becomes a two-dimensional problem. If the boundary of a planar beam travels inward at the point where $z=0$ as shown in Fig. 21, then without a magnetic field, this beam boundary

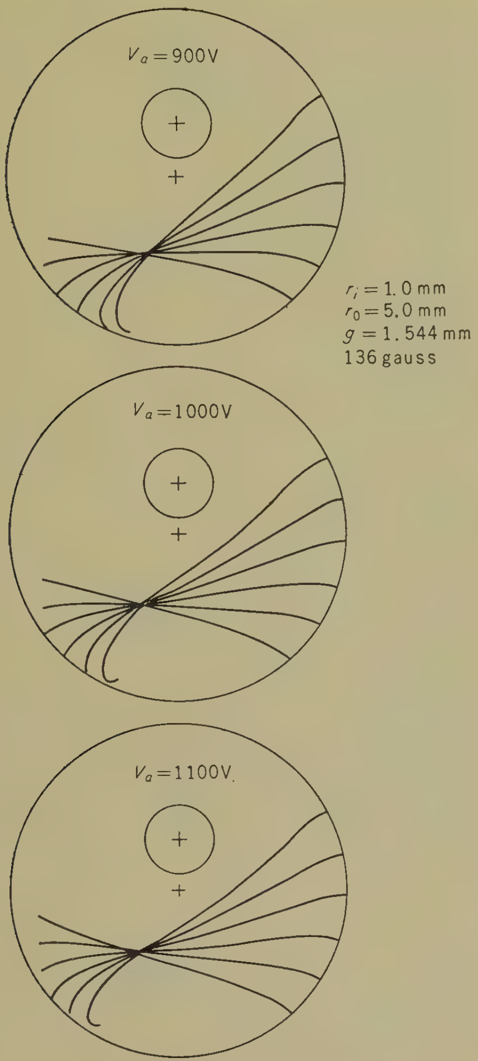

Fig. 20—Electron orbits of different anode voltages in an eccentric convergent gun.

forms the following quadratic curve because of the diverging effect of space charge.[6]

$$\frac{x}{x_0}-1=\left(\frac{z}{x_0}\right)^2\cdot\frac{I}{V_0^{3/2}}\cdot\frac{x_0}{8\varepsilon\sqrt{2\eta}}+\frac{z}{x_0}x_0' \quad (21)$$

where

I : Total current per unit width
V_0 : Potential of electron beam
η : $|e/m|$
ε : Dielectric constant of space
x_0' : dx/dz on the initial slope of beam boundary line, where $z=0$.

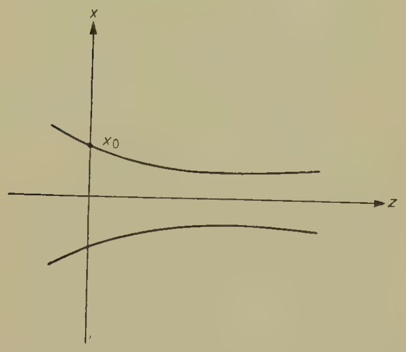

Fig. 21—Sheet beam path with space charge effect.

From Eq. (21), when the initial slope x_0' is

$$x_0'|_0=-\sqrt{\frac{I}{V_0^{3/2}}\cdot\frac{x_0}{2\varepsilon\sqrt{2\eta}}} \quad (22)$$

the thickness proves to become zero. When the initial slope becomes large, the boundary lines cross each other. In this case if the focus point z_f' is obtained, the first beam focus z_f changes as

$$z_f'=z_f\left(1+\frac{x_0}{x_0'^2}H\right), \quad (23)$$

thus it moves far away.[3] In Eq. (23), H shows the constant by space charge and is related to the perviance $P=I/V^{3/2}$, and the next relation is formed:

$$H=P\frac{1}{8\varepsilon\sqrt{2\eta}}=2.378\times10^4 P \quad (24)$$

Subsequently, practical values will be considered. For example, when beam voltage $=1{,}000$ V, the initial height of the beam boundary $z_0=1$ mm, and the initial slope$=$ 30°; the following percentage displacement of focal length is obtained:

0.71 % (when current per width 10 mm= 31.6 mA)
7.1 % (when current per width 10 mm= 316 mA).

As seen from this, the displacement of focus is not very large in the case of practical values. So the displacement can be considered to have little effect upon actual design.

8. Design of Convergent Gun

The converging orbits of the electron beam treated above were calculated for the electric field constructed with two cylinders. If left as it is, the outer cylinder is closed and prevents electron from being injected into the interaction space. In case of injection, not only the geometrical combination of electron orbits and potential distribution is necssary but also the electron velocity must satisfy the conditions of a linear orbit in the interaction space.

To satisfy these conditions, an electrode structure which gives the necessary distribution of the potential must be obtained. For this purpose, the resistive carbon paper method is recommendable. As a result of examination of various electrode structures, the structure shown in Fig. 22 which satisfies the conditions was obtained. In Fig. 22, the dotted lines show the potential distribution when the outer cylinder is completely closed. Like this, in the converging part of electron beam, the potential distribution shows complete correspondence to the distribution in the case of a completely closed outer cylinder. The electron velocity at the focus position becomes 1.0×10^7m/sec. (potential: 283 V), and so for a magnetic field of 136 gauss, the electric field must be 1.36×10^5, from the condition of horizontal linear orbit in the interaction space, i.e. from $E_x=u_0B_y$. As the gap of the interaction space is 2 mm, a suitable potential difference between the upper and lower electrodes of the space is 273 V. As it can be seen, the condition is satisfied with the electrode structure and the arrangement of electrode voltages in Fig. 22.

As shown in Fig. 22, the convergent gun of this structure needs three different electrode voltages, among which the accelerating electrode voltage must have a higher potential than the other two. It seems not to be convenient in practical use that such a special

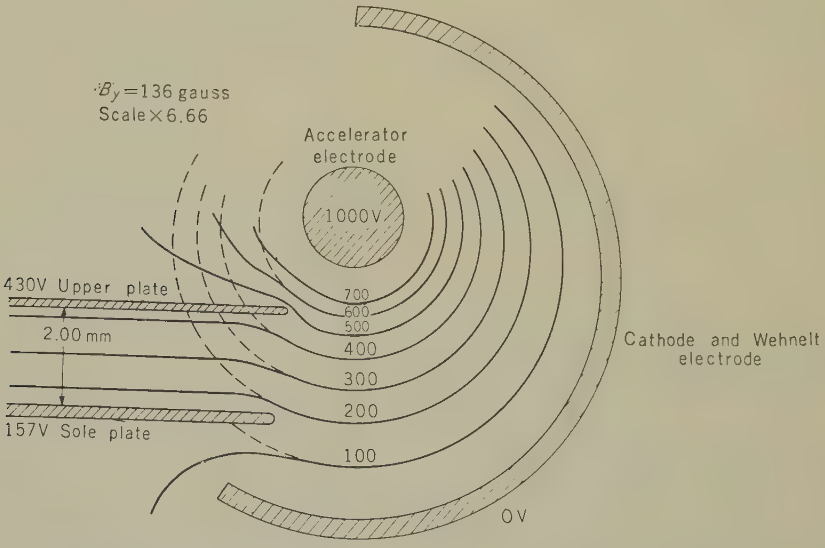

Fig. 22—Design example of M-type convergent gun with electric potential distribution. (Separated accelerator type).

high potential needless on the other electrodes must be supplied.

Now another examination will be tried on the calculated electron orbit. As an example of a system with good convergence characteristics, that in Fig. 23 is shown. This was chosen the one in Fig. 19 (e) to which equipotential lines were given afterwards. By observing the electron orbits in this figure, it is found that no electrons pass through the space of very high potential. If we limit the orbits in a certain range, it is possible to spare those electrons that pass through the region of potential higher than 400 V. Therefore, if a cylindrical high-potential electrode of the same in shape as the 400 V equipotential circle is inserted, and 400V applied, then the potential distribution of the accelerating space is not changed. Then it becomes possible to constrain the electrons in the same converging orbit as shown in Fig. 23, even at a lower accelerator voltage. With this consideration, and with no change of potential distribution, the simplest structure of electrodes and voltages was searched for by the resistive carbon paper method as before. As a result, the design shown in Fig. 24 was obtained.[4]

In this figure, at the electron beam focus, the potential is 263 V and the electron velocity is 9.6×10^5m/sec. Therefore the condition of linear orbit between parallel electrodes with a separation of 2 mm, i.e. $E_x = B_y u_0$, is satisfied with the potential difference of about 270 V. Therefore, by this design, without special accelerating electrode voltage, a converging system is obtainable at an electrode voltage equal to the interaction circuit voltage. Thus, it seems convenient in practical use. As shown in the figure, the accelerating electrode is obtained only by planing a part of the cylinder, without using any special curved surface, and so its fabrication is also very simple without any more difficulties than in the case of the electrode structure shown in Fig. 22.

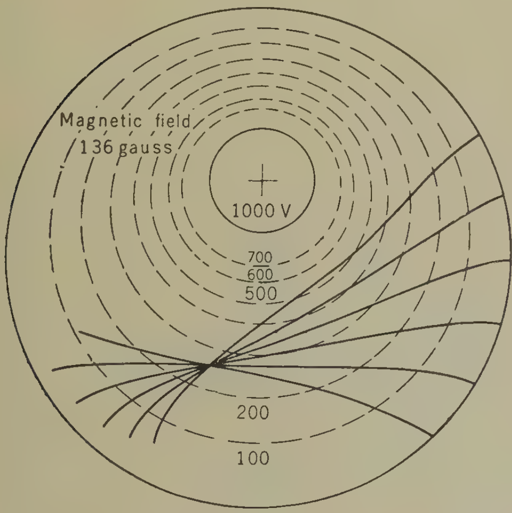

Fig. 23—Electron orbits and equipotential lines in covergent system.

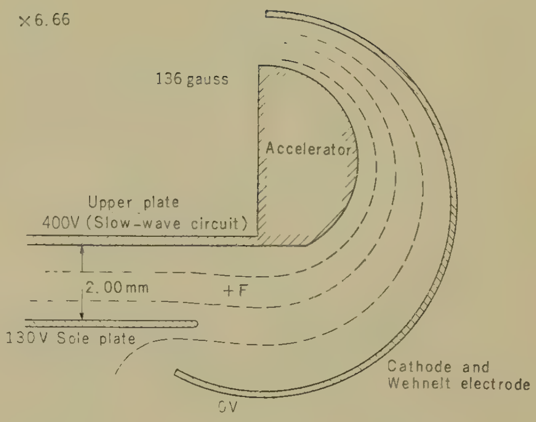

Fig. 24—Improved design of M-type convergent gun. (Equipotential accelerator type).

In the design in Fig. 24, the sole electrode requires special potential, but if it is improved into the one in Fig. 25, this sole potential becomes needless, too. Accordingly, the convergence characteristic is obtained with only one accelerating voltage.

The quality of the electron gun of M-type tubes can not be judged only by the relation between current and voltage, i.e. only by perveance. In other words, not only must it be considered whether the orbit is linear and rippleless but also the electronic efficiency must be taken into account.

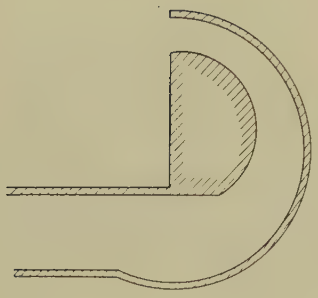

Fig. 25—Convergent gun design to eliminate sole voltage supply.

As to this electronic efficiency, the design in Fig. 25 is not very favorable, or rather inferior to the example in Fig. 26—into which the design in Fig. 24 has been transformed—whose interaction circuit is separated from the accelerating system to raise the circuit voltage.[4] In this case, however, the efficiency of the whole tube is also related to the beam coupling impedance of the interaction circuit, and so nothing definite can be said on the stage of electron guns.

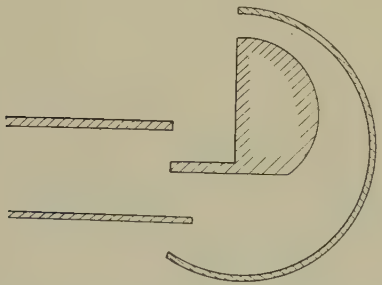

Fig. 26—Convergent gun design to improve electronic efficiency.

The design of the convergent gun in Fig. 24 is only an example. In this example, the focus point is designed to gather electrons at the center between parallel electrodes. Of course, this focus can be located at any arbitrary point by design. The electronic efficiency varies according to its height. If the focus is designed to come at a lower position, then the electronic efficiency can be raised theoretically without separating the circuit as shown in Fig. 26. Such design can freely be made by considering the potential distribution.

The longitudinal width of the cathode of such a convergent gun is determined by the ripple amplitude allowed the electron beam in the interaction space. That is, if the allowable ripple amplitude is determined, the limit of vertical velocity component at the focus position is determined through Eq. 18, and from this the maximum angle of the injection orbit is obtained. Subsequently, from the electron orbit obtained by calculation, the width of electron emitting surface is determined.

As already mentioned, one design can be widely used by the application of the scaling law.

9. Experiments

As a result of the theoretical consideration on M-type electron guns, new designs were obtained as above. On the basis of these, test tubes were made, and experiments were performed. The results will be shown in this section.[4][5]

9.1. Plane-Electrode Gun

The plane-electrode gun, which is very easy to make and needs no close adjustment, should come into use in future in place of the hyperbolic electrode gun.

The design of the test tube is illustrated in Fig. 27. As it was made only to test the electron gun, as shown in the figure only the plane is at the place where the microwave interaction circuit exists in the M-type tube commonly used. In this tube, a square section cathode sleeve 1.25 mm wide is used; the oxide coated part which emits electrons is limited to 10 mm in length. By dividing the collector electrode into three parts, the transverse divergence and the tilt to the axis of magnetic field can be checked. The electrodes are separated by narrow gaps so that the current flowing into them can be measured individually.

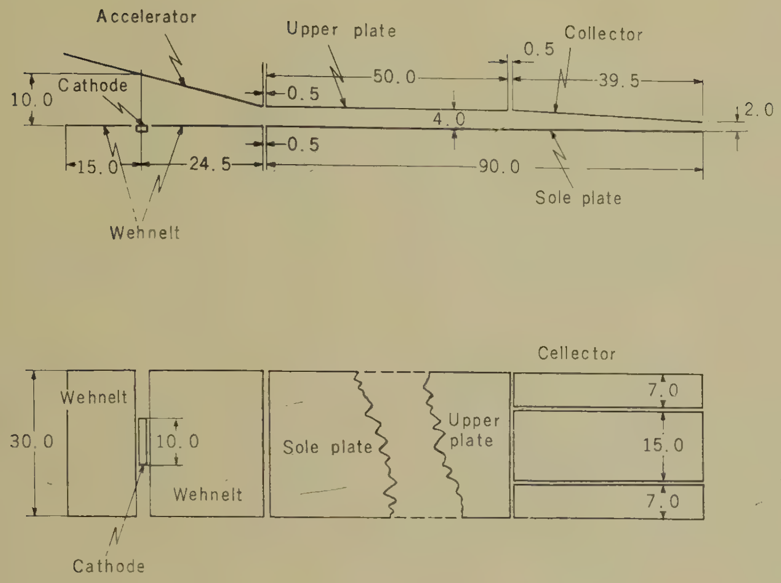

Fig. 27—Test tube design of plane electrode gun.

The characteristics of the electron orbit in this electron gun have already been dwelt upon. The ripple amplitude of the electron orbit in the accelerating system is calculated to be 1.086 mm with the accelerating electrode potential 1500 V and the magnetic field of 283 gauss for the electrode dimensions in Fig. 27. Compared with that of the hyperbolic electrode gun, with the same cathode height, its calculated ripple is larger by only 2 %.

When the potential difference is 1500 V and the magnetic field is 283 gauss, the beam of potential 500 V is expected to take a horizontal linear orbit at the lower 1/3 point of the parallel plane electrodes gap, i.e. the orbit is 1.33 mm above the sole plate.

In Fig. 28, is shown an example of electrode current curves obtained by measurement. In the measurement, the same potential was applied to the accelerator, the upper plate, the collector of the test tube; the current flowing into each electrode was measured. And a potential 0 was applied to the cathode, the wehnelt electrode, and the sole plate; each current was measured.

Fig. 28 shows the variation of the current of each high-potential electrode caused when the magnetic field strength was changed. As expected naturally from the scaling law, even when other voltages were used, identical current variation curves were obtained. From the above-shown design values of voltage and magnet field, i.e. 1,500 V and 283 gauss respectively, the corresponding magnetic field at 500 V was calculated by the scaling law, and the results are written in the figure. As seen from it, even when the voltage was changed, very good beam transmission, i.e, above 97 %, was obtained in any case at the designed megnetic field strength.

Perveance $P=I/V_0^{3/2}$, i.e. (total beam current)/(beam voltage)$^{3/2}$ is a factor which expresses the charactor of electron guns. The calculated values of perveance of this test tube are invariable even when the accelerating voltage varies, it is always 4.6×10^{-6}.

Little current flows through the sole plate or wehnelt electrodes. When negative voltage is applied to the wehnelt electrodes, the entire current decreases remarkably. But in the case of voltage which reduces current by half, i.e. a voltage below 10 V, no variation occurs in the beam current distribution.

When the magnetic field strength is high and is about the design value shown in Fig. 28, each of electrode currents is out of the range of sudden change, i.e., in the stable

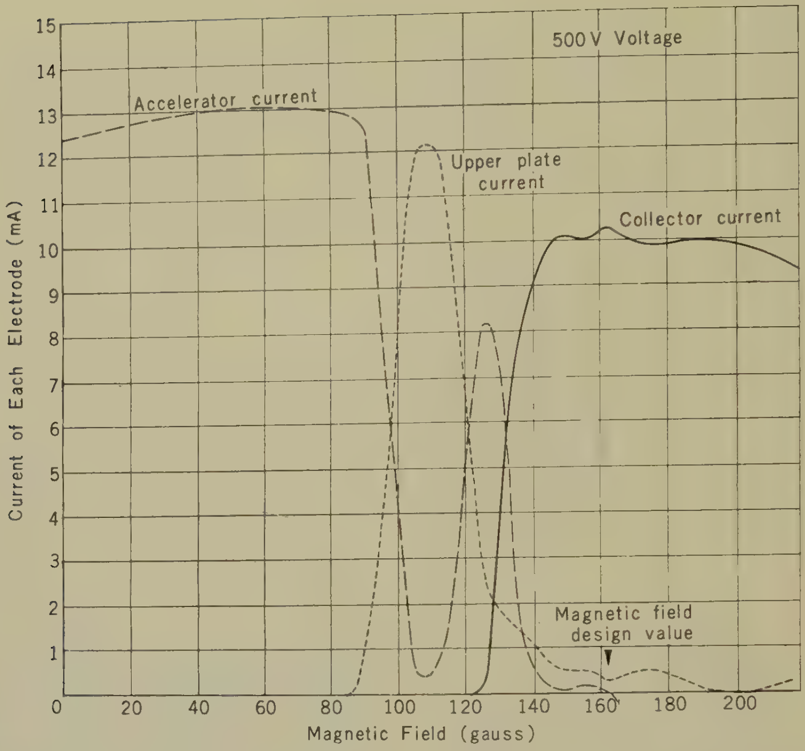

Fig. 28—Electrode currents in plane electrode gun v.s. magnetic field.

range, and the collector current does not vary much even when the magnetic field changes. Thus the electron gun using this plane accelerating electrode has been found to serve well in practical use in place of the hyperbolic electrode gun.

9.2 Cylindrical Electron Gun

The design of a test tube for the use of experiments on the cylindrical electrode gun is shown in Fig. 29. Except for the accelerating electrode, this test tube has nearly the same structure as the plane electrode gun test tube. The shape of the electron orbit obtained by calculation when the accelerating electrode voltage was 1,500 V and the magnetic field was 283 gauss is shown in Fig. 12. In this figure, the orbit has the accelerating electrode radius $A=15$ mm.

Fig. 30 shows the measured electrode currents for to the various magnetic field strengths. Each electrode current was measured with the same potential on the accelerator, the upper plate, and the collectors. In the figure, the magnetic field strengths into which the design values 1,500 V and 283 gauss were changed by the scaling law against for voltage are written. For this magnetic field, the beam transmission amounts to about 100 %.

For the cylindrical electrode gun used in this experiment, the cathode is so far from the accelerating electrode, and the accelerating field on the cathode surface is so weak, that the current is small. The perveance $P=I/V^{3/2}$ is as small as 0.7×10^{-6}. If the accelerating electrode radius of electron guns having this structure is reduced, the electric field stength has much smaller influence at the cathode surface. For this reason, the perveance decreases so much that this electron gun without further inprovement is not very good for practical use.

Therefore as already mentioned, it is neces-

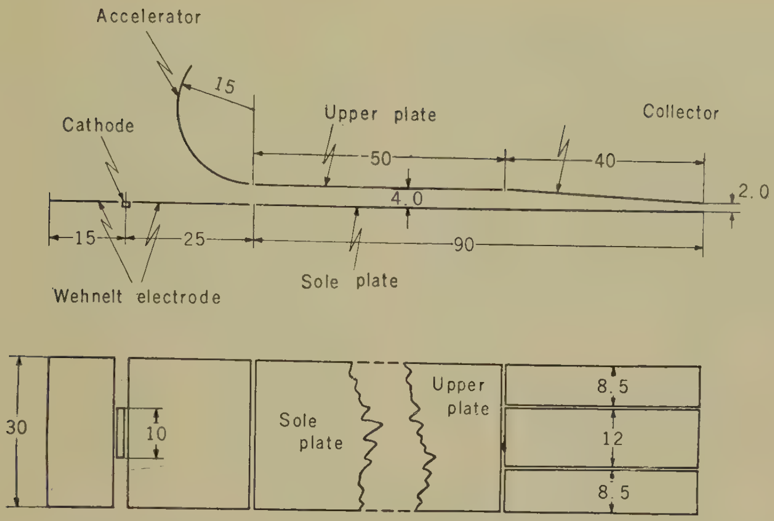

Fig. 29—Test tube design of cylindrical electrode gun.

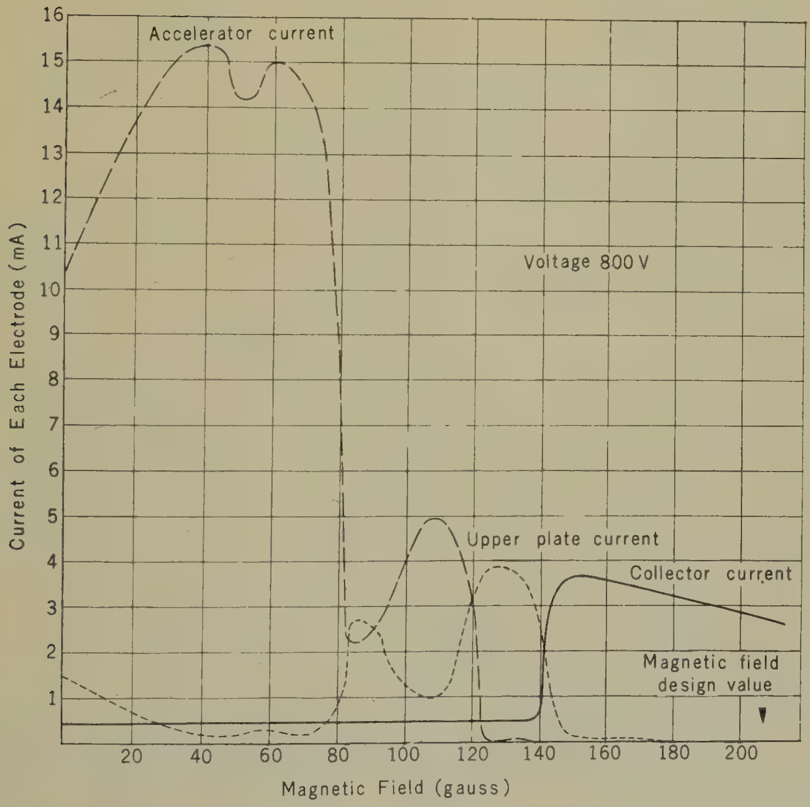

Fig. 30—Electrode currents in cylindrical electrode gun v.s. magnetic field.

sary to increase the emitted current by putting a positive accelerating electrode near the cathode. In spite of the defect mentioned above, the current transmission amounts nearly to 100% near the voltage and magnetic field design values. As expected from the orbit obtained by theoretical calculation, therefore, the rippleless injection is always realized. When a linear electron beam is necessary, this type of electron gun should be the most ideal.

9.3 Convergent Gun

Test tubes using the convergent gun treated in the preceding section were made; one on the basis of the design of separated accelerator type shown in Fig. 22 and another on the basis of the equipotential accelerator type design shown in Fig. 24. Then whether the electron beam can be converged as expected and a good beam transmission can be obtained, and also how much current is obtainable were

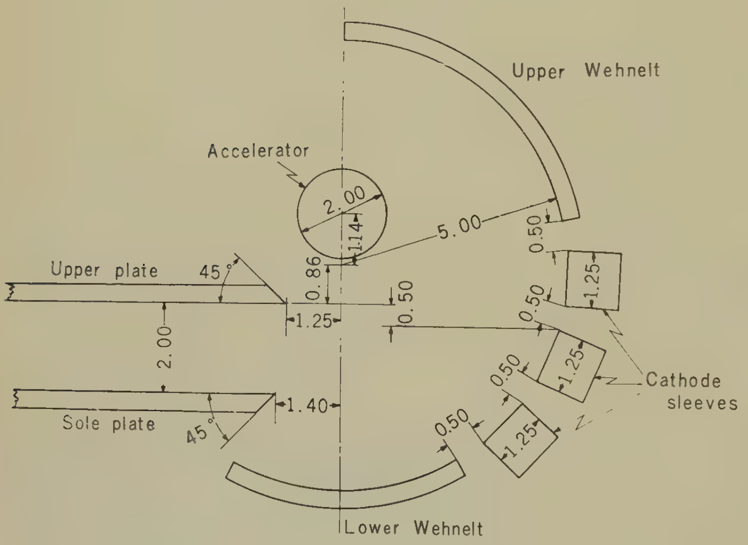

Fig. 31—Test tube convergent gun design (Separated accelerator type).

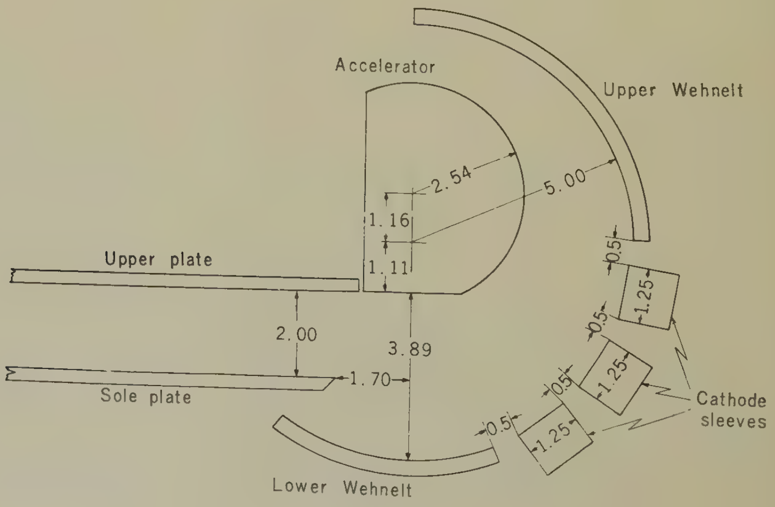

Fig. 32—Test tube convergent gun design (Equipotential accelerator type).

experimentally investigated. In the actual design of the gun, the curved cathode was replaced by an arrangement of square cross section sleeves due to its simpler preparation. Thus, the accelerating systems were constructed as shown in Figs. 31 and 32. Both of the structures of the whole systems of test tubes are shown in Fig. 33. The oxide-coated part of the cathode is 10 mm wide, and the collector is separated into three parts so that the transverse spread of the beam can be confirmed. The design voltage and magnetic field strength are as shown in Figs. 22 and 24. But when measurement was actually performed, the scaling law was applied to the several combinations of lower voltages.

9.3.1. Separated Accelerator Type

First, experimental results of the separated accelerator type convergent gun will be described. In the case of this structure, high voltage must be applied to the separated accelerator electrode; therefore this type of tube is not preferable for practical use. For practical usage, the improved equipotential acceler-

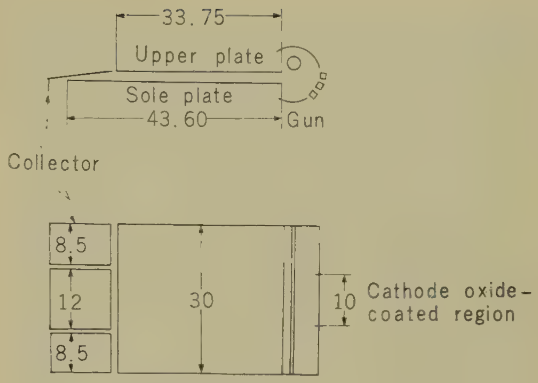

Fig. 33—Test tube design.

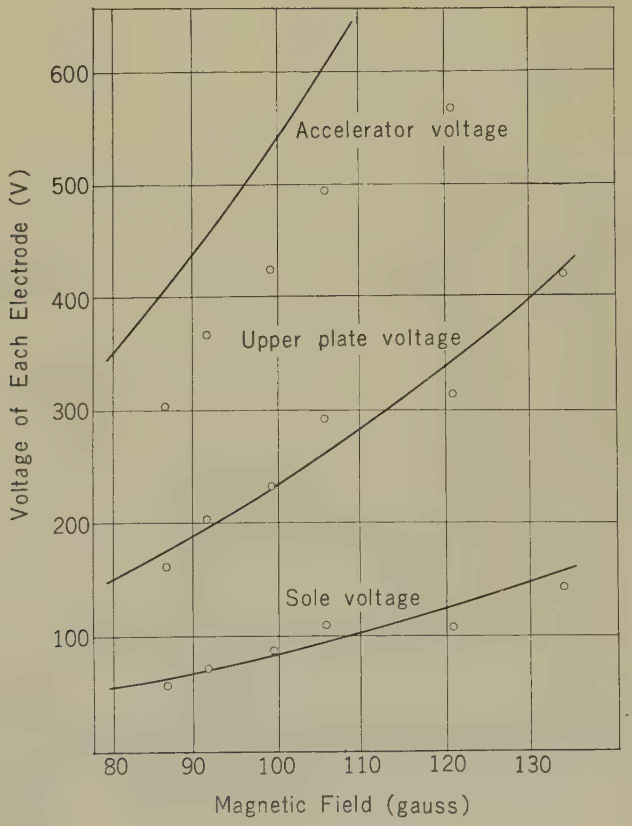

Fig. 34—Test tube electrode voltages v.s. magnetic field. Solid lines show theoretical values. (Separated accelerator gun)

ator type is better, but for the purpose of examining the results of theoretical calculations, this accelerator type is more suitable, because its electric field can be finely abjusted in by changing the electrode voltages.

In Fig. 34 is shown the results of measurements which were made at each magnetic field strength by finely adjusting each electrode voltage so that the best beam transmission might be obtained. A stable perveance of approx. 7×10^{-6} was obtained at every point. As shown in the figure, the theoretical design values of the sole voltage and the upper plate voltage correspond well with the experimental values.

The experimental values of accelerator voltage are somewhat lower than its theoretical values, but the slope of the change agree quite well. It is probably because the voltage of this electrode is so high and gradient of electric potential is so large that even a small mechanical error has a great effect on the experimental values of voltage.

In Fig. 35 is shown an example of the variation of each electrode current caused by the change of the magnetic field when the electrode voltage was fixed after being adjusted to give the maximum beam transmission at a certain magnetic field strength. As shown in this figure, when the magnetic field strength becomes approximately the design value, the collector current rapidly increases. This measurement was carried out several times changing the voltage setting, and all the measured values have proved to correspond well to the properly scaled design values when the beam transmission is optimum. But in the case of large current, it has been found that out of the range of good beam transmission, the state of beam distribution becomes unstable and the variation tends to be irreversible. This phenomenon seems

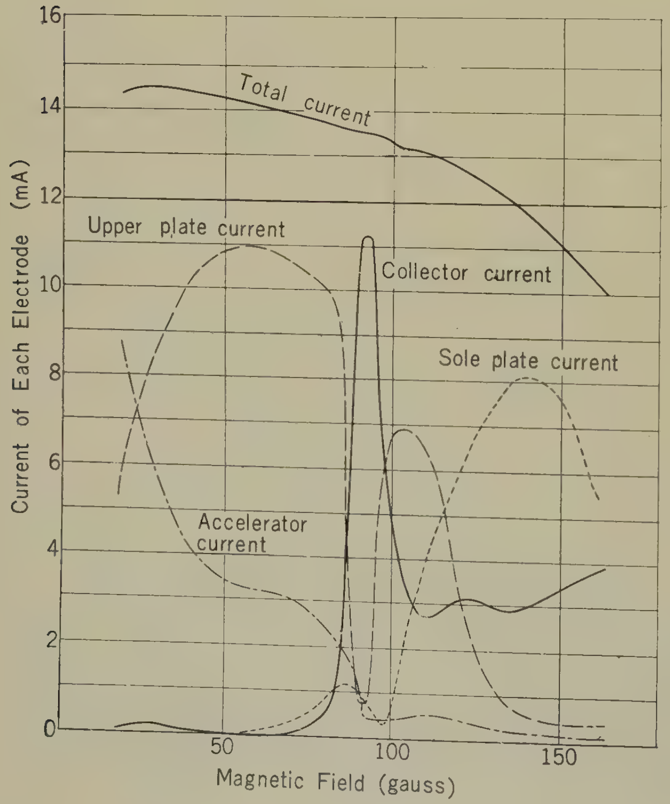

		Design	Exp.
Static conditions	V_A	452	360
	V_u	195	197
	V_S	71	70
	V_W	—	−4.1
	Mag.	91.5	91.8 gausses

Max. beam transmission 83 % at 91.8 gausses.

Fig. 35—Electrode currents v.s. magnetic field (Separated accelerator convergent gun).

to be due to secondary emission, but at the same time it shows some relationship to the instablity caused when the space charge itself has high density.

The wehnelt electrode voltage not only controls the total beam current but also influences the beam transmission as shown in Fig. 36. In this figure, the beam transmission becomes maximum at a certain value of wehnelt voltage. This can be explained as follows.

For the theoretical electron orbit on which the design is based, space charge effect is ignored. But in actual tubes, the effect of space charge can never be neglected. So by giving negative potential to the wehnelt electrode, the beam transmission is improved to neutralize the space charge effect and prevent the low-speed electrons near the cathode from diverging.

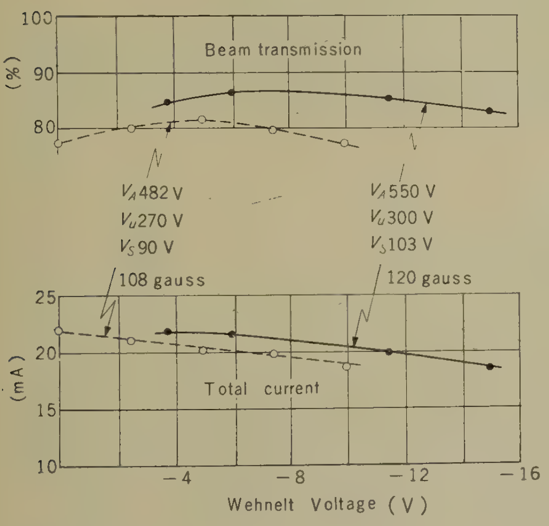

Fig. 36—Wehnelt voltage v.s. beam transmission and total current (Separated accelerator convergent gun).

Finally, it was examined how far the voltages of each electrode can be changed from the design values without decrease of beam transmission, keeping the magnetic field at the same value. That is, at first the magnetic field was fixed; the sole voltage was gradually changed; and the upper plate voltage, the accelerator voltage, and the wehnelt voltage were adjusted so that the collector current would attain its maximum value. The results are shown in Fig. 37. As

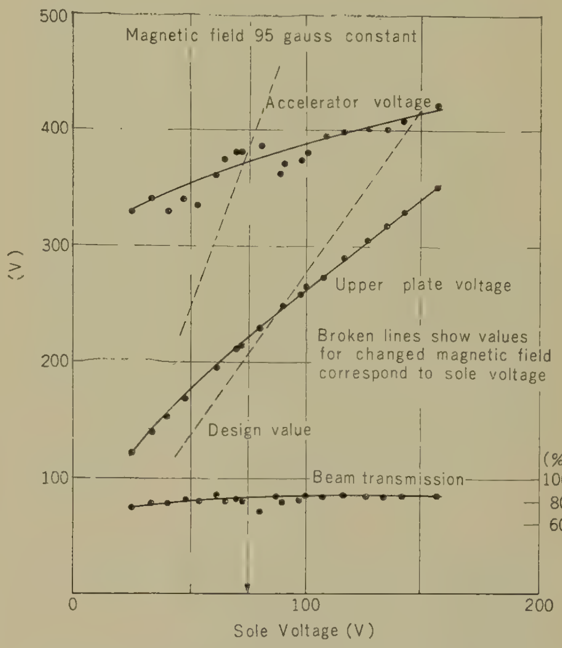

Fig. 37—Electrode voltage relations to give maximum beam transmission at fixed magnetic field. Beam-transmission is also shown. (Separated accelerator convergent gun)

shown, even when the sole voltage was changed upward or downward from the design value, good transmission, i.e., around 80 %, could be maintained by adjusting upper plate voltage and accelerator voltage. The collector current in the range shown in the figure, was increased from 7.5 mA to 15 mA, while the wehnelt voltage was changed from −5 V to −10 V. In the figure are drawn also the theoretical values of upper plate voltage and accelerator voltage which should be applied when the sole voltage, the magnetic field is intensified enough to the theoretical values which give maximum beam transmission. As a result of comparison between the two voltages, it was clarified that when the voltage is changed with a fixed magnetic field, good beam transmission can be maintained if only the upper plate voltage and accelerator voltage are adjusted against the variation of sole voltage in order to minimize the change of the electric potential distribution in the accelerating space. In Fig. 37, the full lines showing the experimental values of voltage have slopes gentler than the broken lines showing the theoretical values obtained when the magnetic field is also changed. But this experiment is not enough to examine the linearity of the beam, i.e., the ripple amplitude, at the part were the voltage is very different from the design value. The purpose of this experiment was to find whether it is possible or not to make the small adjustment of beam velocity required in actual traveling wave tubes. As shown above, the possibility has been confirmed.

9.3.2. Equipotential Accelerator Type

Subsequently will be treated the experimental result of the equipotential accelerator type of tube designed as shown in Fig. 32. This type is thought valuable for practical use, because its accelerator needs no special high voltage. The accelerator and the interaction electrode (i.e. upper plate) may be connected with each other, but in the test tube, they were insulated electrically for the purpose of measuring various characteristics such as beam current distribution. All the parts excepting the accelerator were constructed just like the preceding one. In this structure, the electric field on the cathode surface is quite strong, and even when the wehnelt voltage is made negative, enough current can be obtained and the beam transmission does not drop. In this type, therefore, higher wehnelt negative voltage is applied than for the preceding type.

Fig. 38 shows some current characteristics of each electrode against the magnetic field strength. Even improved designs whose ac-

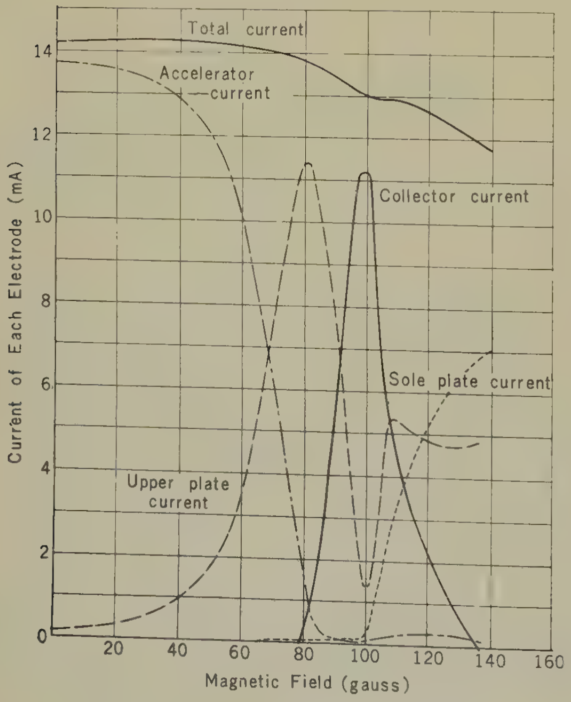

		Design	Exp.
Static conditions	V_A	200	200
	V_u		
	V_S	65	50
	V_W	—	−50
	Mag.	96	100 gausses

Maximum beam transmission 87 % at 100 gausses.

Fig. 38—Electrode currents v.s. magnetic field (Equipotential accelerator convergent gun).

Magnetic field	Wehnelt voltage	Accelerator voltage	Upper plate voltage	Sole plate voltage	Cathode current	Collector current	Beam transmission	Perveance
135 gauss	−70 V	365 V	300 V	61.5 V	35.8 mA	24.8 mA	70 %	10.2×6^{-6}

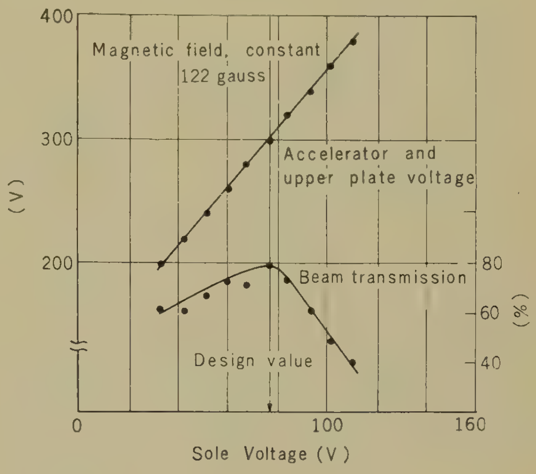

Fig. 39—Electrode voltage relation to give maximum beam transmission at fixed magnetic field. Beam-transmission is also shown. (Equipotential accelerator convergent gun)

celerator and upper plate electrode have equal potentials give results identical to those obtained for the separated acclerator type. In this case, the beam transmission rises to about 85 %, and the perveance becomes 8×10^{-6}. Even when the measurement was made at different voltages, similar characteristics corresponding well to the scaling law were obtained. Therefore, it has been ascertained that the improved equipotential accelerator type operates just as expected.

In addition, another test was made to determine how much the perveance can be improved by fine adjustment of the electrode voltage. Perveances as high as 10×10^{-6} were obtained by raising the accelerator voltage about 20 % higher than the upper plate voltage.

This experiment was not for improving the characteristics of guns by using two groups of high voltages, but for examining the possibility of further improvement of this equipotential accelerator type by reforming the electrode position.

Next, as in the case of the preceding test tube, it was examined how much the voltage can be changed without decreasing beam transmission when the magnetic field is kept a constant. Unlike the preceding type, this type has only one high potential electrode that affects the potential distribution of the accelerating space. Accordingly, the range of voltage variation without fall of beam transmission is smaller than for the preceding one. That is, as shown in Fig. 39, when the accelerator voltage and other voltages are changed, keeping the magnetic field constant, a variation of only 10 % causes a beam transmission fall of 10 %. As compared with the preceding tube in Fig. 37 whose voltage can be changed as much as 50 % with little variation of beam transmission, this type has much smaller allowable variation range. But this beam voltage adjustment range is considered large enough for the fine adjustment of beam velocity required in amplifier tubes. In this structure, the magnetic field must be changed when the electron velocity must be changed much as in the case of the M-type backward oscillator.

As a result of experiment on these two types of convergent gun test tubes, the following has been clarified.

The variation of potential distribution caused by connecting a parallel plane electrode after the focus of the eccentric cylinder converging system tends to make the electron beam orbit more horizontal. According to further inquiry, it has come to light that the electron orbit can be corrected by increasing the negative voltage applied to the wehnelt electrode, so that the convergent injection become possible over a fairly wide range of accelerating voltage. Though, on the injection into interaction space, no direct study by the computer has been made. However, by these experiments, it is confirmed that the beam convergence has not been lost, but rather promoted by this injection.

The experiments mentioned above have proved that the M-type convergent electron gun, which was designed on the basis of the electron orbit theoretically obtained, has good characteristics for practical use. That is, the immersed M-type electron gun has proved to be realizable experimentally as well as theoretically.

For studying the characteristics of electron guns, or for use at a fixed magnetic field, but with voltage varied over wide range, the separated accelerator type (Figs. 22 and 31) is the most suitable, because of its widely variable electrode voltage. But for application to tubes in practical use, the equipotential accelerator type (Figs. 24 and 32), which requires no special high voltage, is superior.

In each type, even in the test tubes, a perveance 8×10^{-6} or so was obtained with ease, and perveances as high as 10×10^{-6} could be obtained by careful adjustment. Raising the accuracy of construction should result in further improvement. Thus, they will become suitable electron guns of great utility for high-power M-type tubes.

10. Conclusion

As a result of researches on electron orbits with the help of electronic computer, the new designs described above have been obtained.

To begin with, the electron orbits of the M-type tube electron gun with a plane electrode or cylindrical electrode were calculaed, and this type of gun has proved to be not inferior to the hyperbolic electrode gun usually used. Therefore, difficult to make hyperbolic electrode has become unneccessary, because electron guns constructed with a plane electrode or the easy to fabricate cylindrical electrode is not inferior.

In the case of plane electrode system, too, the ripple amplitude has been obtained as a result of calculation of the orbit, and this makes its design easier. Thus, the plane electrode gun can be designed with ease.

As a developed cylindrical electrode gun, an electron accelerating system with two cylindrical electrodes was studied. It has been clarified that an immersed convergent electron gun is obtainable if two cylinders, one large and one small, are eccentrically arranged.

In this new design, it is noteworthy from the view-point of its practical use that the effective converging characteristic can be realized by using a simple, easy to fabricate cylindrical surface without using any special curve.

On the basis of these researches, test tubes were made—some including a plane electrode gun, some including a cylindrical electrode gun, and the others including a convergent gun—and experiments were carried out on them. Each new type of electron gun has proved to give satisfactory operation as theoretically expected.

These new M-type electron guns are expected to be applied effectively to M-type electron tubes which will be developed in future.

The auther owes much to the MUSASINO-1 parametron electronic computer used in making this study. Many thanks are due to the members of the Electronic Computer Section for their kind and cordial cooperation in making programs and carrying out calculations.

He is grateful also to the members of the electron tube factory in the Electrical Communication Laboratory who helped him make the test tubes.

References

(1) P. Guénard & H. Huber: Étude Experimentale de l'Interaction par Ondes de Charge d'Espace au sein d'un Faisceau Électronique se Déplacant dans des Champs Électrique et Magnétique Croisés, *Ann. Radioelect.*, vol. **7**,

p. 252–278, Oct., 1952.
(2) T. Unotoro: New Types of Crossed-field gun, *Technical Group on Microwave Tubes, the Institute of Electrical Communication Engineers of Japan*, June 15, 1959.
(3) T. Unotoro: Crossed-field Convergent Gun, *Tech. Group on Microwave Tubes, the Inst. of Elect. Comm. Eng. of Japan*, Nov. 9, 1959.
(4) T. Unotoro: Improved Designs and Experimental Results of Crossed-field Convergent Gun, *Tech. Group on Microwave Tubes, the Inst. of Elect. Comm. Eng. of Japan*, March 18, 1960.
(5) T. Unotoro: A Study of M-type Electron Gun, *Electrical Communication Laboratory Technical Journal*, Tokyo, p. 731–770, Vol. 10, No. 5, 1961.
(6) J. R. Pierce: Theory and Design of Electron Beams, Van Nostrand Co., 1949.

* * * *

REVIEW OF THE ELECTRICAL COMMUNICATION LABORATORY
VOLUME 9, NUMBERS 7-8, JULY-AUGUST, 1961

U.D.C. 621. 372. 823. 001. 2

Inclusive Telegraphist's Equations for Waveguides*

***Shin-ichi IIGUCHI*†**

First, Maxwell's equations expressed in orthogonal curvilinear coordinates are converted into convenient forms for the calculation of waveguide problems. The transverse fields in the cross section of nonuniform and curved waveguide are expanded into a series of normal mode functions of a uniform and straight waveguide whose cross section is the same as that of the waveguide to be analyzed. After multiplying the Maxwell's equations by the normal mode function, the equations are integrated over the cross section; and changing forms by boundary conditions on the wall surface, and substituting the above-mentioned series into the equations, telegraphist's equations for the waveguide are obtained.

These results contain almost all the telegraphist's equations for waveguides which have been reported up to date.

Introduction

Since the publication of Schelkunoff's generalized telegraphist's equations for waveguides in 1952, several papers which extended Schelkunoff's idea have been published.

They described the problems of curved circular waveguide, curved circular waveguide containing an inhomogeneous dielectric, nonuniform waveguide, tapered waveguide, and curved helix waveguide.

In these papers, telegraphist's equations have been derived individually from Maxwell's equations. In the present paper, the author derives the inclusive telegraphist's equations for curved and nonuniform waveguide containing a slightly inhomogeneous and anisotropic medium. These results should be applicable to many cases.

Glossary of Symbols:

$\boldsymbol{E}_t, \boldsymbol{H}_t$: Electric and magnetic fields on a cross section of waveguide (two dimensional vector)
$\boldsymbol{E}_z, \boldsymbol{H}_z$: Electric and magnetic fields perpendicular to a cross section of waveguide (one dimensional vector)
$\boldsymbol{n}$: Unit vector perpendicular to the periphery of a cross section
$\boldsymbol{\sigma}$: Unit vector tangential to the periphery of a cross section
$\boldsymbol{k}$: Unit vector perpendicular to a cross section
x, y, z: Orthogonal curvilinear coordinate system as shown in Fig. 1 (not cartesian coordinates)
$e_3=1+h_3=1-\dfrac{x}{R(z)}$: Metrical coefficient of z
∇ : gradient operator tranverse to z axis
$\boldsymbol{e}_n, \boldsymbol{h}_n$: electric and magnetic mode functions, respectively
$(n), [n]$: subscripts of TM and TE modes, respectively

---

* MS in English received by the Electrical Communication Laboratory, March 7, 1961. Originally published in the *J. Inst. Electr. Commun. Eng. Jap.* Vol. 44, No. 6, pp. 955–963, 1961.

† Hyper-frequency Research Section.

V_n, I_n: amplitudes of transverse electric and magnetic fields of the n-mode
Z_σ : wall surface impedance in circumferential direction
Z_g : wall surface impedance in generating line direction
$\epsilon=\epsilon_h+\varepsilon$: electric permittivity
ϵ_h……constant scalar
ε……variable in x and y

1. Coordinate System and Maxwell's Equations

In the orthogonal curvilinear coordinate, x, y, z which are shown in Fig. 1, Maxwell's equations for a field with time dependence $e^{j\omega t}$ may be written in the following form:

$$\left.\begin{aligned} \frac{1}{e_3}\left\{\frac{\partial}{\partial y}(e_3E_z)-\frac{\partial}{\partial z}(E_y)\right\}&=-j\omega B_x \\ \frac{1}{e_3}\left\{\frac{\partial}{\partial z}(E_x)-\frac{\partial}{\partial x}(e_3E_z)\right\}&=-j\omega B_y \\ \left\{\frac{\partial}{\partial x}(E_y)-\frac{\partial}{\partial y}(E_x)\right\}&=-j\omega B_z \end{aligned}\right\} \tag{1}$$

$$\left.\begin{aligned} \frac{1}{e_3}\left\{\frac{\partial}{\partial y}(e_3H_z)-\frac{\partial}{\partial z}(H_y)\right\}&=j\omega D_x \\ \frac{1}{e_3}\left\{\frac{\partial}{\partial z}(H_x)-\frac{\partial}{\partial x}(e_3H_z)\right\}&=j\omega D_y \\ \left\{\frac{\partial}{\partial x}(H_y)-\frac{\partial}{\partial y}(H_x)\right\}&=j\omega D_z \end{aligned}\right\} . \tag{2}$$

From (1) the following formulas can be obtained:

$$\nabla\times\boldsymbol{E}_t+\frac{1}{e_3}\nabla\times(e_3\boldsymbol{E}_z)+\frac{1}{e_3}\boldsymbol{k}\times\frac{\partial\boldsymbol{E}_t}{\partial z}=-j\omega\boldsymbol{B} \tag{3}$$

$$e_3\nabla\times\boldsymbol{E}_t+\nabla\times(e_3\boldsymbol{E}_z)+\boldsymbol{k}\times\frac{\partial\boldsymbol{E}_t}{\partial z}=-j\omega e_3\boldsymbol{B}. \tag{4}$$

From (2) the following formulas can be obtained:

$$\nabla\times\boldsymbol{H}_t+\frac{1}{e_3}\nabla\times(e_3\boldsymbol{H}_z)+\frac{1}{e_3}\boldsymbol{k}\times\frac{\partial\boldsymbol{H}_t}{\partial z}=j\omega\boldsymbol{D} \tag{5}$$

$$e_3\nabla\times\boldsymbol{H}_t+\nabla\times(e_3\boldsymbol{H}_z)+\boldsymbol{k}\times\frac{\partial\boldsymbol{H}_t}{\partial z}=j\omega e_3\boldsymbol{D}. \tag{6}$$

The two-dimentional vector fields $\boldsymbol{E}_t$ and $\boldsymbol{H}_t$ on the transverse cross sections of the waveguide shown in Fig. 1 may be expanded in the mean into the following forms by the use of the complete sets of normal mode functions, $\boldsymbol{e}_n$ and $\boldsymbol{h}_n$, respectively:

$$\boldsymbol{E}_t=\sum_{(n)}V_{(n)}\boldsymbol{e}_{(n)}+\sum_{[n]}V_{[n]}\boldsymbol{e}_{[n]}=\sum_n V_n\boldsymbol{e}_n \tag{7}$$

$$\boldsymbol{H}_t=\sum_{(n)}I_{(n)}\boldsymbol{h}_{(n)}+\sum_{[n]}I_{[n]}\boldsymbol{h}_{[n]}=\sum_n I_n\boldsymbol{h}_n. \tag{8}$$

And, the one dimensional scalar fields E_z and H_z in the z direction in the guide shown in Fig. 1 may be expanded in the mean into the following forms by the use of the complete sets $T_{(n)}$ and $T_{[n]}$, respectively:

$$E_z=\sum_{(n)}F_{(n)}T_{(n)} \tag{9}$$

$$H_z=\sum_{(n)}G_{[n]}T_{[n]} \tag{10}$$

$$\left.\begin{aligned} \nabla^2T_{(n)}+\chi_{(n)}{}^2T_{(n)}&=0 \\ T_{(n)}|_\sigma&=0 \end{aligned}\right\} \tag{11}$$

$$\left.\begin{aligned} \nabla^2T_{[n]}+\chi_{[n]}{}^2T_{[n]}&=0 \\ \partial T_{[n]}/\partial n|_\sigma&=0 \end{aligned}\right\} \tag{12}$$

$$\left.\begin{aligned} \boldsymbol{e}_{(n)}&=\text{grad }T_{(n)} \\ \boldsymbol{h}_{(n)}&=-\text{flux }T_{(n)} \end{aligned}\right\} \tag{13}$$

$$\left.\begin{aligned} \boldsymbol{e}_{[n]}&=\text{flux }T_{[n]} \\ \boldsymbol{h}_{[n]}&=\text{grad }T_{[n]} \end{aligned}\right\} \tag{14}$$

$$\left.\begin{aligned} \boldsymbol{k}\times\boldsymbol{e}_n&=\boldsymbol{h}_n \\ \boldsymbol{h}_n\times\boldsymbol{k}&=\boldsymbol{e}_n. \end{aligned}\right\} \tag{15}$$

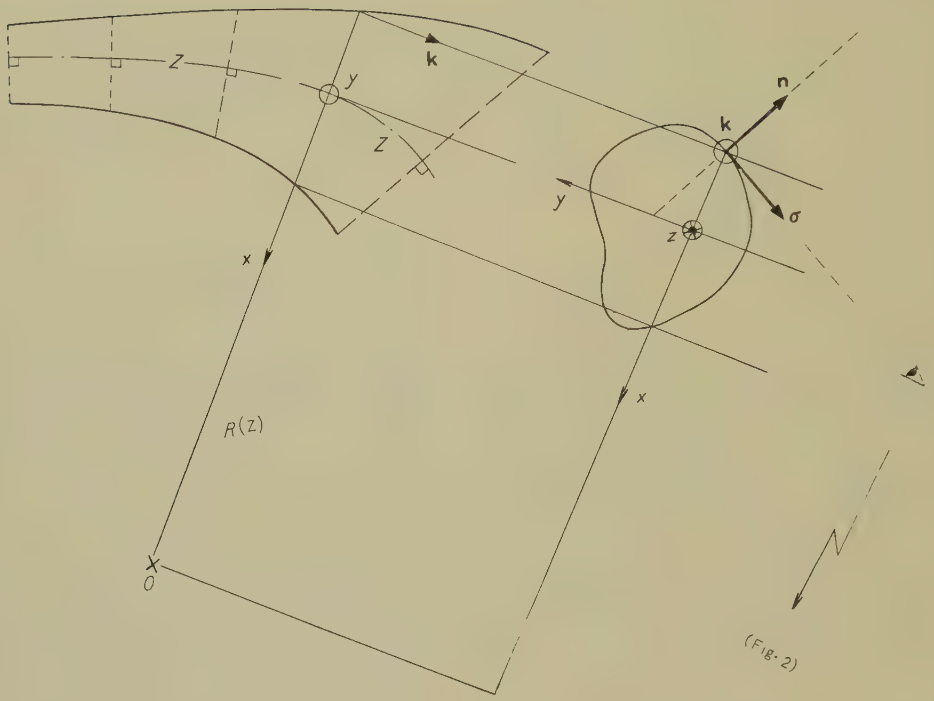

Fig. 1—Orthogonal curvilinear coordinate system.

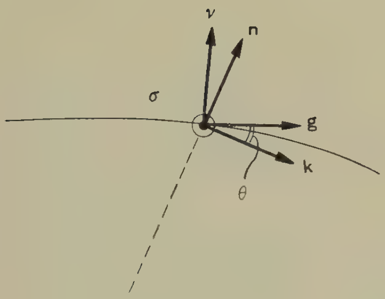

Fig. 2—Unit vectors on wall surface.

2. Derivation of the Telegraphist's Equation

2.1. Derivation of $dV_{(m)}/dz$

Multiplying (4) by $\boldsymbol{h}_{(m)}$ and integrating over the cross section, we obtain:

$$\iint \boldsymbol{h}_{(m)} \cdot \nabla \times (e_3 \boldsymbol{E}_z) dS + \iint \boldsymbol{h}_{(m)} \cdot \boldsymbol{k} \times \frac{\partial \boldsymbol{E}_t}{\partial z} \, dS$$

$$= -j\omega \iint e_3 \boldsymbol{B} \boldsymbol{h}_{(m)} dS.$$

The first term of the left-hand side of the above equation is

$$\iint \nabla [e_3 \boldsymbol{E}_z \times \boldsymbol{h}_{(m)}] dS + \iint e_3 \boldsymbol{E}_z \cdot \nabla \times \boldsymbol{h}_{(m)} dS$$

$$= \int_\sigma [e_3 \boldsymbol{E}_z \times \boldsymbol{h}_{(m)}] \boldsymbol{n} d\sigma$$

$$+ \iint e_3 \boldsymbol{E}_z (-\boldsymbol{k} \chi_{(m)}{}^2 T_{(m)}) dS$$

$$= \int_\sigma e_3 \boldsymbol{h}_{(m)} \cdot [\boldsymbol{n} \times \boldsymbol{E}_z] d\sigma - \chi_{(m)}{}^2 \iint e_3 E_z T_{(m)} dS$$

$$= \sum_n V_n \int_\sigma e_3 \tan \vartheta \boldsymbol{e}_n \boldsymbol{e}_{(m)} d\sigma$$

$$+\sum_n I_n\int_\sigma e_3 \sec \vartheta Z_g \boldsymbol{h}_n \boldsymbol{h}_{(m)} d\sigma - F_{(m)}$$

$$-\chi_{(m)}{}^2 \sum_{(n)} F_{(n)} \iint h_3 T_{(n)} T_{(m)} dS.$$

(See Appendix (A-7))

The second term of the left-hand side of the above equation is

$$\iint \boldsymbol{k}\times\boldsymbol{e}_{(m)}\cdot\boldsymbol{k}\times\frac{\partial \boldsymbol{E}_t}{\partial z}dS$$

$$=\iint \frac{\partial \boldsymbol{E}_t}{\partial z}\boldsymbol{e}_{(m)}dS$$

$$=\frac{dV_{(m)}}{dz}+\sum_n V_n\iint\frac{\partial \boldsymbol{e}_n}{\partial z}\boldsymbol{e}_{(m)}dS.$$

From these results, we can obtain:

$$\left.\begin{aligned}
&\frac{dV_{(m)}}{dz}+\sum_n V_n\iint\frac{\partial \boldsymbol{e}_n}{\partial z}\boldsymbol{e}_{(m)}dS\\
&+\sum_n V_n\int_\sigma e_3 \tan\vartheta\, \boldsymbol{e}_n\boldsymbol{e}_{(m)}d\sigma\\
&+\sum_n I_n\int_\sigma e_3 \sec\vartheta Z_g\boldsymbol{h}_n\boldsymbol{h}_{(m)}d\sigma\\
&-F_{(m)}-\chi_{(m)}{}^2\sum_{(n)}F_{(n)}\iint h_3 T_{(n)}T_{(m)}dS\\
&=-j\omega\iint e_3\boldsymbol{B}_t\boldsymbol{h}_{(m)}dS \qquad \text{(general)}\\
&=-j\omega\sum_n I_n\iint \mu e_3\boldsymbol{h}_n\boldsymbol{h}_{(m)}dS \quad \text{(isotropic)}\\
&=-j\omega\mu I_{(m)}-j\omega\mu\sum_n I_n\iint h_3\boldsymbol{h}_n\boldsymbol{h}_{(m)}dS.\\
&\qquad\qquad \text{(isotropic \& homogeneous)}
\end{aligned}\right\} \qquad (16)$$

2.2. Derivation of $dI_{(m)}/dz$

Multiplying (6) by $\boldsymbol{e}_{(m)}$ and integrating over the cross section, we obtain:

$$\iint\boldsymbol{e}_{(m)}\cdot\nabla\times(e_3\boldsymbol{H}_z)dS+\iint\boldsymbol{e}_{(m)}\cdot\boldsymbol{k}\times\frac{\partial\boldsymbol{H}_t}{\partial z}dS$$

$$=j\omega\iint e_3\boldsymbol{D}_t\boldsymbol{e}_{(m)}dS$$

The first term of the left-hand side of the above equation is

$$\iint\nabla(e_3\boldsymbol{H}_z\times\boldsymbol{e}_{(m)})dS+\iint e_3\boldsymbol{H}_z\cdot\nabla\times\boldsymbol{e}_{(m)}dS$$

$$=\int[e_3\boldsymbol{H}_z\times\boldsymbol{e}_{(m)}]\cdot\boldsymbol{n}d\sigma$$

$$=\int e_3\boldsymbol{H}_z[\boldsymbol{e}_{(m)}\times\boldsymbol{n}]d\sigma=0.$$

The second term of the left-hand side of the above equation is

$$\iint\frac{\partial\boldsymbol{H}_t}{\partial z}\cdot[\boldsymbol{e}_{(m)}\times\boldsymbol{k}]dS$$

$$=-\iint\frac{\partial\boldsymbol{H}_t}{\partial z}\boldsymbol{h}_{(m)}dS$$

$$=-\frac{dI_{(m)}}{dz}-\sum I_n\iint\frac{\partial\boldsymbol{h}_n}{\partial z}\boldsymbol{h}_{(m)}dS.$$

From these results, we can obtain:

$$\left.\begin{aligned}
&-\frac{dI_{(m)}}{dz}-\sum_n I_n\iint\frac{\partial\boldsymbol{h}_n}{\partial z}\boldsymbol{h}_{(m)}dS\\
&=j\omega\iint e_3\boldsymbol{D}_t\boldsymbol{e}_{(m)}dS \qquad \text{(general)}\\
&=j\omega\sum_n V_n\iint e_3\epsilon\boldsymbol{e}_n\boldsymbol{e}_{(m)}dS \quad \text{(isotropic)}\\
&=j\omega\epsilon V_{(m)}+j\omega\epsilon\sum V_n\iint h_3\boldsymbol{e}_n\boldsymbol{e}_{(m)}dS.\\
&\qquad\qquad \text{(iso. \& homo.)}
\end{aligned}\right\} \qquad (17)$$

2.3. Derivation of the Equation Containing $I_{(m)}$ and $F_{(m)}$

Multiplying (5) by $\boldsymbol{k}T_{(m)}$ and integrating over the cross section, we obtain:

$$\iint \boldsymbol{k}T_{(m)}\cdot\nabla\times\boldsymbol{H}_t = j\omega\iint D_z T_{(m)}dS.$$

The left-hand side of the above equation is

$$\iint\nabla[\boldsymbol{H}_t\times\boldsymbol{k}T_{(m)}]dS + \iint\boldsymbol{H}_t\cdot\nabla\times\boldsymbol{k}T_{(m)}dS$$

$$= \int_\sigma \boldsymbol{H}_t[\boldsymbol{k}T_{(m)}\times\boldsymbol{n}]d\sigma - \iint\boldsymbol{H}_t\cdot\boldsymbol{h}_{(m)}dS$$

$$= \int_\sigma \boldsymbol{H}_t[\boldsymbol{\sigma}T_{(m)}]d\sigma - I_{(m)} = -I_{(m)}.$$

From these results, we obtain:

$$\left.\begin{aligned} -I_{(m)} &= j\omega\iint D_z T_{(m)}dS && \text{(general)}\\ &= j\omega\sum_{(n)} F_{(n)}\iint\epsilon T_{(n)}T_{(m)}dS && \text{(isotropic)}\\ &= \frac{j\omega\epsilon}{\chi^2_{(m)}}F_{(m)}. && \text{(iso. \& homo.)}\end{aligned}\right\} \tag{18}$$

2.4. Derivation of $dV_{[m]}/dz$

Multiplying (4) by $\boldsymbol{h}_{[m]}$ and integrating over the cross section, we obtain:

$$\iint\boldsymbol{h}_{[m]}\cdot\nabla\times(e_3\boldsymbol{E}_z)dS + \iint\boldsymbol{h}_{[m]}\cdot\boldsymbol{k}\times\frac{\partial\boldsymbol{E}_t}{\partial z}dS$$

$$= -j\omega\iint e_3\boldsymbol{B}_t\cdot\boldsymbol{h}_{[m]}dS.$$

The first term of the left-hand side of the above equation is

$$\iint\nabla\cdot[e_3\boldsymbol{E}_z\times\boldsymbol{h}_{[m]}]\cdot dS + \iint e_3\boldsymbol{E}_z\cdot\nabla\times\boldsymbol{h}_{[m]}dS$$

$$= \int_\sigma[e_3\boldsymbol{E}_z\times\boldsymbol{h}_{[m]}]\cdot\boldsymbol{n}d\sigma + 0$$

$$= \int_\sigma e_3\boldsymbol{h}_{[m]}\cdot\boldsymbol{n}\times\boldsymbol{E}_z d\sigma$$

$$= \sum_n V_n\int_\sigma e_3\tan\vartheta\boldsymbol{e}_n\cdot\boldsymbol{e}_{[m]}d\sigma$$

$$+ \sum_n I_n\int_\sigma e_3\sec\vartheta Z_g\boldsymbol{h}_n\boldsymbol{h}_{[m]}d\sigma.$$

(See Appendix (A-7))

The second term of the left-hand side of the above equation is

$$\iint\boldsymbol{k}\times\boldsymbol{e}_{[m]}\cdot\boldsymbol{k}\times\frac{\partial\boldsymbol{E}_t}{\partial z}dS$$

$$= \iint\frac{\partial\boldsymbol{E}_t}{\partial z}\boldsymbol{e}_{[m]}dS$$

$$= \frac{dV_{[m]}}{dz} + \sum_n V_n\frac{\partial\boldsymbol{e}_n}{\partial z}\boldsymbol{e}_{[m]}dS.$$

From these results, we can obtain:

$$\left.\begin{aligned} &\frac{dV_{[m]}}{dz} + \sum_n V_n\iint\frac{\partial\boldsymbol{e}_n}{\partial z}\boldsymbol{e}_{[m]}dS\\ &+ \sum_n V_n\int_\sigma e_3\tan\vartheta\boldsymbol{e}_n\cdot\boldsymbol{e}_{[m]}d\sigma\\ &+ \sum_n I_n\int_\sigma e_3\sec\vartheta Z_g\boldsymbol{h}_n\boldsymbol{h}_{[m]}d\sigma\\ &= -j\omega\iint e_3\boldsymbol{B}_t\cdot\boldsymbol{h}_{[m]}dS \qquad \text{(general)}\\ &= -j\omega\sum_n I_n\iint\mu e_3\boldsymbol{h}_n\boldsymbol{h}_{[m]}dS \quad \text{(isotropic)}\\ &= -j\omega\mu I_{[m]} - j\omega\mu\sum_n I_n\iint h_3\boldsymbol{h}_n\boldsymbol{h}_{[m]}dS.\\ &\qquad\qquad \text{(iso. \& homo.)}\end{aligned}\right\} \tag{19}$$

2.5. Derivation of $d\boldsymbol{I}_{[m]}/dz$

Multiplying (6) by $\boldsymbol{e}_{[m]}$ and integrating over the cross section, we obtain:

$$\iint\boldsymbol{e}_{[m]}\cdot\nabla\times(e_3\boldsymbol{H}_z)dS + \iint\boldsymbol{e}_{[m]}\cdot\boldsymbol{k}\times\frac{\partial\boldsymbol{H}_t}{\partial z}$$

$$= j\omega\iint e_3\boldsymbol{D}_t\cdot\boldsymbol{e}_{[m]}dS.$$

The first term of the left-hand side of the above equation is

$$\iint \nabla\cdot[e_3\boldsymbol{H}_z\times\boldsymbol{e}_{[m]}]dS+\iint e_3\boldsymbol{H}_z\cdot\nabla\times\boldsymbol{e}_{[m]}dS$$

$$=\int_\sigma[e_3\boldsymbol{H}_z\times\boldsymbol{e}_{[m]}]\cdot\boldsymbol{n}d\sigma+\iint e_3\boldsymbol{H}_z\cdot\boldsymbol{k}\chi_{[m]}{}^2T_{[m]}dS$$

$$=\int_\sigma e_3\boldsymbol{H}_z\cdot[\boldsymbol{e}_{[m]}\times\boldsymbol{n}]d\sigma+\chi^2{}_{[m]}\iint e_3H_zT_{[m]}dS$$

$$=0+G_{[m]}+\chi_{[m]}{}^2\sum_n G_{[n]}\iint h_3T_{[n]}T_{[m]}dS.$$

The second term of the left-hand side of the above equation is

$$\iint\frac{\partial\boldsymbol{H}_t}{\partial z}\cdot[\boldsymbol{e}_{[m]}\times\boldsymbol{k}]dS$$

$$=-\iint\frac{\partial\boldsymbol{H}_t}{\partial z}\boldsymbol{h}_{[m]}dS$$

$$=-\frac{dI_{[m]}}{dz}-\sum I_n\iint\frac{\partial\boldsymbol{h}_n}{\partial z}\boldsymbol{h}_{[m]}dS.$$

From these results, we obtain:

$$\left.\begin{aligned}
&-\frac{dI_{[m]}}{dz}-\sum_n I_n\iint\frac{\partial\boldsymbol{h}_n}{\partial z}\boldsymbol{h}_{[m]}dS\\
&+G_{[m]}+\chi_{[m]}{}^2\sum_{[n]}G_{[n]}\iint h_3T_{[n]}T_{[m]}dS\\
&=j\omega\iint e_3\boldsymbol{D}_t\cdot\boldsymbol{e}_{[m]}dS \qquad \text{(general)}\\
&=j\omega\sum_n V_n\iint\epsilon e_3\boldsymbol{e}_n\boldsymbol{e}_{[m]}dS \qquad \text{(isotropic)}\\
&=j\omega\epsilon V_{[m]}+j\omega\epsilon\sum_n V_n\iint h_3\boldsymbol{e}_n\boldsymbol{e}_{[m]}dS.\\
&\qquad\qquad \text{(iso. \& homo.)}
\end{aligned}\right\}\qquad(20)$$

2.6. Derivation of the Equation Containing $V_{[m]}$ and $G_{[m]}$

Muitiplying (3) by $\boldsymbol{k}T_{[m]}$ and integrating over the cross section, we obtain:

$$\iint\boldsymbol{k}T_{[m]}\cdot\nabla\times\boldsymbol{E}_tdS=-j\omega\iint\boldsymbol{B}_z\cdot\boldsymbol{k}T_{[m]}dS.$$

The left-hand side of above equation is

$$\iint\nabla\cdot[\boldsymbol{E}_t\times\boldsymbol{k}T_{[m]}]dS+\iint\boldsymbol{E}_t\cdot\nabla\times\boldsymbol{k}T_{[m]}dS$$

$$=\int_\sigma[\boldsymbol{E}_t\times\boldsymbol{k}T_{[m]}]\cdot\boldsymbol{n}d\sigma+\iint\boldsymbol{E}_t\cdot\text{flux }\ T_{[m]}dS$$

$$=\int_\sigma\boldsymbol{k}T_{[m]}\cdot[\boldsymbol{n}\times\boldsymbol{E}_t]d\sigma+\iint\boldsymbol{E}_t\cdot\boldsymbol{e}_{[m]}dS$$

$$=\sum_n G_{[n]}\int_\sigma\sec\vartheta\,Z_\sigma T_{[n]}T_{[m]}d\sigma+V_{[m]}.$$

(See Appendix (A-11, 12))

From this result, we obtain:

$$\left.\begin{aligned}
&V_{[m]}+\sum_{[n]}G_{[n]}\int_\sigma\sec\vartheta\,Z_\sigma T_{[n]}T_{[m]}d\sigma\\
&=-j\omega\iint B_zT_{[m]}dS \qquad \text{(general)}\\
&=-j\omega\sum_{[n]}G_{[n]}\iint\mu T_{[n]}T_{[m]}dS \qquad \text{(isotropic)}\\
&=\frac{-j\omega\mu}{\chi_{[m]}{}^2}G_{[m]}. \qquad \text{(iso. \& homo.)}
\end{aligned}\right\}\qquad(21)$$

3. Arrangement of the Telegraphist's Equations

We shall now derive the first order approximations to the generalized telegraphist's equations from (16)∼(21), under the following assumptions

μ = constant scalar,
ϵ = slightly variable scalar $=\epsilon_h+\varepsilon$

where ϵ_h is constant and ε is variable in x and y.

$$\left.\begin{aligned}
\frac{dV_{(m)}}{dz} &= -\sum_{(n)} Z_{(m)(n)} I_{(n)} - \sum_{[n]} Z_{(m)[n]} I_{[n]} - \sum_{(n)} {}^{V}T_{(m)(n)} V_{(n)} - \sum_{[n]} {}^{V}T_{(m)[n]} V_{[n]} \\
\frac{dI_{(m)}}{dz} &= -\sum_{(n)} Y_{(m)(n)} V_{(n)} - \sum_{[n]} Y_{(m)[n]} V_{[n]} - \sum_{(n)} {}^{I}T_{(m)(n)} I_{(n)} - \sum_{[n]} {}^{I}T_{(m)[n]} I_{[n]} \\
\frac{dV_{[m]}}{dz} &= -\sum_{[n]} Z_{[m][n]} I_{[n]} - \sum_{(n)} Z_{[m](n)} I_{(n)} - \sum_{[n]} {}^{V}T_{[m][n]} V_{[n]} - \sum_{(n)} {}^{V}T_{[m](n)} V_{(n)} \\
\frac{dI_{[m]}}{dz} &= -\sum_{[n]} Y_{[m][n]} V_{[n]} - \sum_{(n)} Y_{[m](n)} V_{(n)} - \sum_{[n]} {}^{I}T_{[m][n]} I_{[n]} - \sum_{(n)} {}^{I}T_{[m](n)} I_{(n)}
\end{aligned}\right\} \tag{22}$$

where

$$\left.\begin{aligned}
Z_{(m)(n)} &= -\frac{\beta_{(m)}{}^2}{j\omega\epsilon_h}\delta_{(m)(n)} + \chi_{(m)}{}^2 \frac{\chi_{(n)}{}^2}{j\omega\epsilon_h}\iint h_3 T_{(n)} T_{(m)} dS - \frac{\chi_{(m)}{}^2}{\epsilon_h}\,\frac{\chi_{(n)}{}^2}{j\omega\epsilon_h}\iint \varepsilon T_{(n)} T_{(m)} dS \\
&\quad + j\omega\mu\iint h_3 \boldsymbol{h}_{(n)} \boldsymbol{h}_{(m)} dS + \int_\sigma e_3 \sec\vartheta Z_g \boldsymbol{h}_{(n)} \boldsymbol{h}_{(m)} d\sigma \\
Z_{(m)[n]} &= j\omega\mu\iint h_3 \boldsymbol{h}_{[n]} \boldsymbol{h}_{(m)} dS + \int_\sigma e_3 \sec\vartheta Z_g \boldsymbol{h}_{[n]} \boldsymbol{h}_{(m)} d\sigma \\
{}^{V}T_{(m)(n)} &= \iint \frac{\partial \boldsymbol{e}_{(n)}}{\partial z} \boldsymbol{e}_{(m)} dS + \int_\sigma e_3 \tan\vartheta \boldsymbol{e}_{(n)} \boldsymbol{e}_{(m)} d\sigma \\
{}^{V}T_{(m)[n]} &= \iint \frac{\partial \boldsymbol{e}_{[n]}}{\partial z} \boldsymbol{e}_{(m)} dS + \int_\sigma e_3 \tan\vartheta \boldsymbol{e}_{[n]} \boldsymbol{e}_{(m)} d\sigma
\end{aligned}\right\} \tag{23}$$

$$\left.\begin{aligned}
Y_{(m)(n)} &= j\omega\epsilon_h\delta_{(m)(n)} + j\omega\epsilon_h\iint h_3 \boldsymbol{e}_{(n)} \boldsymbol{e}_{(m)} dS + j\omega\iint \varepsilon \boldsymbol{e}_{(n)} \boldsymbol{e}_{(m)} dS \\
Y_{(m)[n]} &= \qquad\qquad\quad j\omega\epsilon_h\iint h_3 \boldsymbol{e}_{[n]} \boldsymbol{e}_{(m)} dS + j\omega\iint \varepsilon \boldsymbol{e}_{[n]} \boldsymbol{e}_{(m)} dS \\
{}^{I}T_{(m)(n)} &= \iint \frac{\partial \boldsymbol{h}_{(n)}}{\partial z} \boldsymbol{h}_{(m)} dS, \qquad {}^{I}T_{(m)[n]} = \iint \frac{\partial \boldsymbol{h}_{[n]}}{\partial z} \boldsymbol{h}_{(m)} dS.
\end{aligned}\right\} \tag{24}$$

$$\left.\begin{aligned}
Z_{[m][n]} &= j\omega\mu\delta_{[m][n]} + j\omega\mu\iint h_3 \boldsymbol{h}_{[n]} \boldsymbol{h}_{[m]} dS + \int_\sigma e_3 \sec\vartheta Z_g \boldsymbol{h}_{[n]} \boldsymbol{h}_{[m]} d\sigma \\
Z_{[m](n)} &= \qquad\qquad\quad j\omega\mu\iint h_3 \boldsymbol{h}_{(n)} \boldsymbol{h}_{[m]} dS + \int_\sigma e_3 \sec\vartheta Z_g \boldsymbol{h}_{(n)} \boldsymbol{h}_{[m]} d\sigma \\
{}^{V}T_{[m][n]} &= \iint \frac{\partial \boldsymbol{e}_{[n]}}{\partial z} \boldsymbol{e}_{[m]} dS + \int_\sigma e_3 \tan\vartheta \boldsymbol{e}_{[n]} \boldsymbol{e}_{[m]} d\sigma \\
{}^{V}T_{[m](n)} &= \iint \frac{\partial \boldsymbol{e}_{(n)}}{\partial z} \boldsymbol{e}_{[m]} dS + \int_\sigma e_3 \tan\vartheta \boldsymbol{e}_{(n)} \boldsymbol{e}_{[m]} d\sigma
\end{aligned}\right\} \tag{25}$$

$$\left.\begin{aligned}
Y_{[m][n]} &= -\frac{\beta_{[m]}{}^2}{j\omega\mu}\delta_{[m][n]} - \frac{\chi_{[m]}{}^2}{j\omega\mu}\frac{\chi_{[n]}{}^2}{j\omega\mu}\int_\sigma \sec\vartheta\, Z_\sigma T_{[n]} T_{[m]} d\sigma + \chi_{[m]}{}^2 \frac{\chi_{[n]}{}^2}{j\omega\mu}\iint h_3 T_{[n]} T_{[m]} dS \\
&\quad + j\omega\epsilon_h \iint h_3 \boldsymbol{e}_{[n]}\boldsymbol{e}_{[m]} dS + j\omega \iint \varepsilon \boldsymbol{e}_{[n]}\boldsymbol{e}_{[m]} dS \\
Y_{[m](n)} &= j\omega\epsilon_h \iint h_3 \boldsymbol{e}_{(n)}\boldsymbol{e}_{[m]} dS + j\omega \iint \varepsilon \boldsymbol{e}_{(n)}\boldsymbol{e}_{[m]} dS \\
{}^{I}T_{[m][n]} &= \iint \frac{\partial \boldsymbol{h}_{[n]}}{\partial z}\boldsymbol{h}_{[m]} dS, \qquad {}^{I}T_{[m](n)} = \iint \frac{\partial \boldsymbol{h}_{(n)}}{\partial z}\boldsymbol{h}_{[m]} dS.
\end{aligned}\right\} \quad (26)$$

where

$$\beta_{(m)}{}^2 = \omega^2\mu\epsilon_h - \chi_{(m)}{}^2, \quad \beta_{[m]}{}^2 = \omega^2\mu\epsilon_h - \chi_{[m]}{}^2.$$

(i) Eq. (21) can be realized, even though ϑ is large, when both Z_σ and Z_g are small; and (21) can be realized, even though Z_g is large, when both ϑ and Z_σ are small.

(ii) Eq. (22)~(26) can be realized only if all the terms containing ε^2, εh_3, $Z_\sigma{}^2$, and $Z_\sigma h_3$ are small. Therefore both ε and Z_σ must be small at first. When both ε and Z_σ are very small, h_3 may be large.

(iii) From the descriptions (i) and (ii), we can state that ϑ and h_3 may be large when all Z_σ, Z_g, and ε are small enough.

4. Practical Examples

Many telegraphist's equations of practical value can be derived from (22)~(26) {or (16)~(21)}. In this section, several practical examples will be shown in tabular form.

The telegraphist's equations shown in examples of Ⅰ~Ⅳ following can be obtained very easily from (22) {or (16)~(21)} by substituting the indicated values of the various symbols in Table 1 for the corresponding symbols in (23)~(26) {or (16)~(21)}:

Ⅰ. Curved waveguide with perfectly conducting wall
Ⅰ.1. Curved waveguide containing an inhomogeneous dielectric.
Ⅰ.2. Curved waveguide containing a homogeneous dielectric.

Ⅱ.
Ⅱ.1. Nonuniform (but straight) guide with perfectly conducting wall.
Ⅱ.2. Circular TE_{0n} waveguide taper.

Ⅲ. Waveguide with imperfectly conducting wall
Ⅲ.1. Curved helix waveguide
Ⅲ.2. Straight waveguide with imperfectly conducting wall.

Ⅳ. Straight waveguide containing anisotropic or inhomogeneous medium (perfectly conducting wall)

Table Ⅰ.

	h_3	ε	ϑ	Z_g	$Z\sigma$	$\iint \frac{\partial \mathbf{e}_n}{\partial z}\mathbf{e}_m ds$	References Page
Ⅰ.1			0	0	0	0	(3), p. 1218
Ⅰ.2⁽¹⁾		0	0	0	0	0	(2), p. 180
Ⅱ.1	0	0		0	0		(4), p. 55
Ⅱ.2⁽²⁾	0	0		0	0		(5), p. 911
Ⅲ.1		0	0	Z	0	0	(6), p. 1606
Ⅲ.2	0	0	0			0	
Ⅳ	0		0	0	0	0	(1), p. 790

Ⅰ.1~Ⅲ.2 can be obtained from (22)~(26), and Ⅳ from (16)~(21).

(1) Ⅰ.2 is included in Ⅰ.1.
(2) Ⅱ.2 is included in Ⅱ.1.

Conclusion

The author derived the general telegraphist's equations which may be inclusively applied to curved and nonuniform waveguides containing slightly inhomogeneous and anisotropic mediums. These results are applicable to many waveguide problems.

Acknowledgement

The author is indebted to Mr. T. Miwa, Dr. B. Oguchi, and Miss M. Kato of the Laboratory for their helpful suggestions to this work.

Appendix

Boundary Conditions on the Waveguide Wall

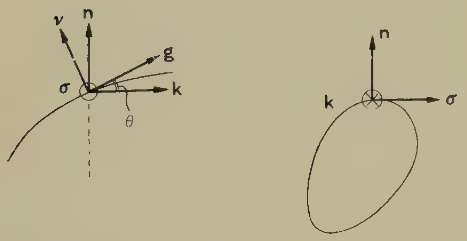

Fig. 3—Waveguide cross section and unit vectors on wall surface.

§1. Boundary condition due to impedance Z_g in the generating line direction ($\boldsymbol{g}$-direction) on wall surface

$$Z_g = \frac{E_g}{-H_\sigma} \qquad \text{(A-1)}$$

$$\left.\begin{aligned} E_g &= E_z \cos\vartheta + E_{tn} \sin\vartheta \\ H_\sigma &= H_{t\sigma}. \end{aligned}\right\} \qquad \text{(A-2)}$$

where $E_{tn} = \boldsymbol{n}\boldsymbol{E}_t$, $H_{t\sigma} = \boldsymbol{\sigma}\boldsymbol{H}_t$.

Substituting (A-2) into (A-1), we obtain

$$E_z = -\tan\vartheta \cdot E_{tn} - \sec\vartheta Z_g H_{t\sigma} \qquad \text{(A-3)}$$

$$\boldsymbol{n}\times\boldsymbol{E}_z = \boldsymbol{n}\times(\boldsymbol{k}E_z) = -\boldsymbol{\sigma}E_z. \qquad \text{(A-4)}$$

From (A-3, 4), we obtain

$$\boldsymbol{n}\times\boldsymbol{E}_z = \boldsymbol{n}\times\boldsymbol{k}(-\tan\vartheta \cdot E_{tn}) + \boldsymbol{\sigma}\sec\vartheta Z_g H_{t\sigma} \qquad \text{(A-5)}$$

And from (A-5), we obtain

$$\int_\sigma e_3\boldsymbol{h}_m \cdot [\boldsymbol{n}\times\boldsymbol{E}_z]d\sigma$$

$$= -\int_\sigma e_3\boldsymbol{h}_m \cdot [\boldsymbol{n}\times\boldsymbol{k}(\tan\vartheta \cdot E_{tn})]d\sigma$$

$$+ \int_\sigma e_3\boldsymbol{h}_m \cdot \boldsymbol{\sigma}\sec\vartheta Z_g H_{t\sigma} d\sigma. \qquad \text{(A-6)}$$

The first term of the above formula is

$$-\int_\sigma e_3[\boldsymbol{k}\times\boldsymbol{e}_m] \cdot [\boldsymbol{n}\times\boldsymbol{k}(\tan\vartheta \cdot E_{tn})]d\sigma$$

$$= \int_\sigma e_3 [\tan\vartheta \cdot E_{tn}(\boldsymbol{n}\cdot\boldsymbol{e}_m)]d\sigma$$

$$= \int_\sigma e_3 \tan\vartheta \cdot \boldsymbol{E}_t \cdot \boldsymbol{e}_m d\sigma$$

$$= \sum_n V_n \int_\sigma e_3 \tan\vartheta \cdot \boldsymbol{e}_n \cdot \boldsymbol{e}_m d\sigma.$$

The second term of the above formula is

$$\int_\sigma e_3 \sec\vartheta Z_g \boldsymbol{H}_t \cdot \boldsymbol{h}_m d\sigma$$

$$= \sum_n I_n \int_\sigma e_3 \sec\vartheta Z_g \boldsymbol{h}_n \cdot \boldsymbol{h}_m d\sigma.$$

Therefore

$$\int_\sigma e_3\boldsymbol{h}_m \cdot [\boldsymbol{n}\times\boldsymbol{E}_z]d\sigma$$

$$= \sum_n V_n \int_\sigma e_3 \tan\vartheta \boldsymbol{e}_n \cdot \boldsymbol{e}_m d\sigma$$

$$+ \sum_n I_n \int_\sigma e_3 \sec\vartheta Z_g \boldsymbol{h}_n \cdot \boldsymbol{h}_m d\sigma. \qquad \text{(A-7)}$$

§2. Boundary condition due to impedance Z_σ in the circumferential direction (**σ**-direction) on the wall surface:

$$\left.\begin{aligned} Z_\sigma &= \frac{E_\sigma}{H_g} \\ E_\sigma &= E_{t\sigma} \\ H_g &= H_z \cos\vartheta + H_{tn}\sin\vartheta \end{aligned}\right\} \qquad \text{(A-8)}$$

(i) The case in which both Z_σ and Z_g are small:

$$H_g = H_z \cos\vartheta + H_z \tan\vartheta \cdot \sin\vartheta = H_z \sec\vartheta. \qquad \text{(A-9)}$$

Here we use the relation $H_{tn} = H_z \tan\vartheta$ which is the boundary condition on the perfectly conducting surface. We may use this relation when the surface impedance is small.

From (A-8; 9), we obtain

$$E_{t\sigma} = \sec\vartheta Z_\sigma H_z. \qquad \text{(A-10)}$$

Therefore

$$\begin{aligned} &\int_\sigma \boldsymbol{k} T_{[m]} \cdot [\boldsymbol{n} \times \boldsymbol{E}_t] d\sigma \\ &= \int_\sigma \boldsymbol{k} T_{[m]} \cdot \boldsymbol{k} E_{t\sigma} d\sigma \\ &= \int_\sigma E_{t\sigma} T_{[m]} d\sigma \\ &= \int_\sigma \sec\vartheta Z_\sigma H_z T_{[m]} d\sigma \qquad \text{[Use(A-10)]} \\ &= \sum_{[n]} G_{[n]} \int_\sigma \sec\vartheta Z_\sigma T_{[n]} T_{[m]} d\sigma. \qquad \text{(A-11)} \end{aligned}$$

(ii) The case in which both ϑ and Z_σ are small (Z_g may be large):

$$\begin{aligned} E_{t\sigma} &= Z_\sigma H_g = Z_\sigma(H_z \cos\vartheta + H_{tn}\sin\vartheta) \\ &= Z_\sigma H_z\left(1 - \frac{\vartheta^2}{2} + \cdots\cdots\right) \\ &\quad + Z_\sigma H_{tn}\left(\vartheta - \frac{\vartheta^3}{6} + \cdots\cdots\right). \end{aligned}$$

Neglecting second order quantities of Z_σ and ϑ, we obtain

$$E_{t\sigma} \doteqdot Z_\sigma H_z.$$

Therefore

$$\int_\sigma \boldsymbol{k} T_{[m]} \cdot [\boldsymbol{n} \times \boldsymbol{E}_t] d\sigma = \sum_{[n]} G_{[n]} \int_\sigma Z_\sigma T_{[n]} T_{[m]} d\sigma. \qquad \text{(A-12)}$$

(A-11) differs from (A-12) by $\sec\vartheta$. When ϑ is small, $\sec\vartheta \doteqdot 1$. Therefore, let us describe $\int_\sigma \sec\vartheta Z_\sigma T_{[n]} T_{[m]} d\sigma$ for the integrals in both (A-11) and (A-12).

References

(1) S. A. Schelkunoff, "Generalized Telegraphist's Equation for Waveguides," *B.S.T.J.*, **31**, (4), p. 784, 1952-07.

(2) Y. Shimizu, "Theory of Transmitting Circular Electric Wave Around Bends," Onde électr. (International congress ultra-high-frequency circuits and antennas), Vol. I, p. 179, 1957.

(3) S. P. Morgan, "Theory of Curved Circular Waveguide Containing an Inhomogeneous Dielectric," *B.S.T.J.*, **36**, (5), p. 1209, 1957-09.

(4) G. Reiter, "Generalized Telegraphist's Equation for Waveguides of Varying Cross-Section," *Proc. I.E.E.*, (Convention on Long-Distance Transmission by Waveguide) **106**, Part B, Supple, No. 13, p. 54, 1959.

(5) H. G. Unger, "Circular Waveguide Taper of Improved Design," *B.S.T.J.*, **37**, (4), p. 899, 1958-07.

(6) H. G. Unger, "Helix Waveguide Theory and Application," *B.S.T.J.*, **37**, (6), p. 1599, 1958-11.

* * * *

Papers Contributed to Scientific and Technical Journals by the Members of the Laboratory

Papers Published in Other Publications of the Electrical Communication Laboratory

U.D.C. 537.311.3 : 546.48′24 : 548.5 : 621.382.2

Study of Cadmium Telluride Single Crystals
Kiichiro MIZUMA, *Osamu MIKAMI*, *Yukio KAMIYA* and *Kazumasa ONO*
Kenkyû Zituyôka Hôkoku (Electr. Comm. Labor. Techn. Journ.), NTT, **10**, 5, pp. 895–924, May, 1961

Single-crystal CdTe produced by the zone refining method is discussed. The methods of production, electrical and optical experiments, and the characteristics of diodes are described.

U.D.C. 537.533.3 : 621.385.65.001.2

A Study of M-type Electron Guns
Tomoyuki UNOTORO
Kenkyû Zituyôka Hôkoku (Electr. Comm. Labor. Techn. Journ.), NTT, **10**, 5, pp. 731–770, May, 1961

Electron orbits in M-type tube guns have been investigated. New types of simple designs with good characteristics, including an immersed-type convergent gun, have been obtained. Experiment has proved the utility of these new designs.

U.D.C. 541.124 : 546.36′86 : 533.15 : 546.6

Logarithmic Growth of Films of Cesium Antimonide on Antimony
Kiyosi MIYAKE
Kenkyû Zituyôka Hôkoku (Electr. Comm. Labor. Techn. Journ.), NTT, **10**, 6, pp. 1225–1232, June, 1961

Growth of films of cesium antimonide on antimony was studied. It is shown that the relation between the thickness of the layer x, and time t, is given by $x=k \log (t/c+1)$ x.

U.D.C. 541.124 : 546.36′86 : 533.15 : 546.6

Partial Pressure of Cesium over Cesium Antimonides
Kiyosi MIYAKE
Kenkyû Zituyôka Hôkoku (Electr. Comm. Labor. Techn. Journ.), NTT, **10**, 6, pp. 1225–1232, June, 1961

The partial pressure of cesium over cesium antimonides was measured at various temperatures ranging from room temperature to 180° C. The pressure can be represented by the equation, $\log p=A-B/T$.

Translations of many of these papers will appear in a future addition of the Review of Electrical Communication Laboratory.

Please address request for copies of these papers, which are in Japanese, directly to the authors to whom credited at: The Electrical Communication Laboratory, 1551 Kitizyôzi, Musasino-si, Tôkyô.

U.D.C. 546.824.36′431:537.226

Dielectric Properties of Single Crystal $BaTiO_3$ at Microwave Frequencies.
Ken'ichi SAWAMOTO, Masako YATANI
Kenkyû Zituyôka Hôkoku (Electr. Comm. Labor. Techn. Journ.), NTT, **10**, 6, pp. 1207–1216, June, 1961

Dielectric properties of $BaTiO_3$ single crystals were studied experimentally by the perturbation method. The dependencies of dielectric constants on temperature, dc bias microwave field strength, and microwave power were investigated.

U.D.C. 547.298 : 546.824.36′431 : 537.226

Ferroelectric Polarization Reversal by Linear Field
Hiroyuki SHIBATA, *Hiroo TOYODA*, and *Shigeru WAKU*
Kenkyû Zituyôka Hôkoku (Electr. Comm. Labor. Techn. Journ.), NTT, **10**, 6, pp. 1197–1205, June, 1961

Ferroelectric polarization reversal of triglycine sulfate and barium titanate was studied by the application of a linear field. The coercive field depends on dE/dt of the field. Phenomenological considerations on the polarization reversal are presented.

U.D.C. 548.5′547.298:537.226

Growth and Electrical Properties of Ferroelectric Glycine Sulfate Single Crystals
Hiroo TOYODA, *Yôichi TANAKA*, and *Wataru SHIOKAWA*
Kenkyû Zituyôka Hôkoku (Electr. Comm. Labor. Techn. Journ.), NTT, **10**, 6, pp. 1181–1195, June, 1961

Crystal habit, electrical conductivity, and dielectric constant of ferroelectric glycine sulfate, particularly in connection with crystal imperfections, are investigated.

U.D.C. 620.18 : 546.28 : 548.55

Residual Strain in Germanium and Silicon Single Crystals
Kazumasa ONO, *Osamu MIKAMI*, and *Joiti SUZUKI*
Kenkyû Zituyôka Hôkoku (Electr. Comm. Labor. Techn. Journ.), NTT, **10**, 5, pp. 925–942, May, 1961

The distribution of residual strain generated in germanium and silicon single crystals by cutting and grinding was determined by the electron diffraction method.

U.D.C. 621.315.66:624.97:519.2

Inclination of Pole with Constant Horizontal Load.
Nobuo MURAI
Kenkyû Zituyôka Hôkoku (Electr. Comm. Labor. Techn. Journ.), NTT, **10**, 6, pp. 1139–1147, June, 1961

The relationship between time and angle of inclination of a pole with a constant horizontal load is described.

U.D.C. 621.316.722-526:621.318.43.001.2:621.311.6

Optimum Design of Reactor Servo System
Shinichi SONODA
Kenkyû Zituyôka Hôkoku (Electr. Comm. Labor. Techn. Jour.), NTT, **10**, 6, pp 1111–1138, June, 1961

Problems of economical and quick response method for designing reactor-type voltage regulators are described.

U.D.C. 621.317.73:621.385.032.2:621.317.335

Input Admittance Meter for Electron Tubes
Takuya KOJIMA, Hirosi HARA
Kenkyû Zituyôka Hôkoku (Electr. Comm. Labor. Techn. Jour.), NTT, **10**, 5, pp. 969–979, May, 1961

An input admittance meter for electron tubes at 70 Mc was developed. In this meter a resonant circuit with a variable capacitor is used, and resonance is detected by the zero phase angle of the current.

U.D.C. 621.317.755:621.374.3:681.142:621.318.1

Display Device for Parametron Signals
Kôshirô HANAWA, Kikunobu KUSUNOKI
Kenkyû Zituyôka Hôkoku (Electr. Comm. Labor. Techn. Jour.), NTT, **10**, 5, pp. 959–968, May, 1961

All information in the core matrix can be simultaneously displayed on a cathode-ray tube in the same arrangement as in the matrix.

U.D.C. 621.318.57:621.382.2:621.314.63

Compound pnpnp Switches.
Kingo YAMAGISHI
Kenkyû Zituyôka Hôkoku (Electr. Comm. Labor. Techn. Jour.), NTT, **10**, 6, pp. 1173–1180, June, 1961

The fundamental characteristics of a compound pnpnp diode and its variations which are made by combination of one npn transistor and two pnp transistors are examined from the viewpoints of bidirectional and bistable electronic switches.

U.D.C. 621.382.333.33.029.6.002.2:546.289

Fabrication Techniques for a High-Frequency Diffused-Base Germanium Transistor
Minoru KOBAYASHI
Kenkyû Zituyôka Hôkoku (Electr. Comm. Labor. Techn. Jour.), NTT, **10**, 6, pp. 1043–1057, June, 1961

Techniques for fabricating a diffused-base transistor are described.

U.D.C. 621.382.333.33.029.6:546.289:621.317.616

Equivalent Circuits and Four Terminal Parameters of High-Frequency Transistors.
Seiichi KAWAGUCHI and *Minoru HIRAI*
Kenkyû Zituyôka Hôkoku (Electr. Comm. Labor. Techn. Jour.), NTT, **10**, 6, pp. 1015–1041, June, 1961

Equivalent circuits and 4-terminal parameters of high-frequency transistors, and measurement of these parameters, are described.

U.D.C. 621.382.333.33.029.6.002.2:546.289:532.72

Impurity diffusion in vacuum for a high-frequency diffused-base germanium transistor
Osamu MIKAMI
Kenkyû Zituyôka Hôkoku (Electr. Comm. Labor. Techn. Jour.), NTT, **10**, 6, pp. 1059–1078, June, 1961

Surface treatment of germanium with a newly developed etchant, CPD-2, and control of the surface concentration are described for the diffusion of antimony into germanium.

U.D.C. 621.382.333.33.029.6.001.2:546.289

The Design of a High-Frequency Diffused-Base Germanium Transistor
Makoto WATANABE
Kenkyû Zituyôka Hôkoku (Electr. Comm. Labor. Techn. Jour.), NTT, **10**, 6, pp. 999–1014, June, 1961

The design and characteristics of a diffused-base high-frequency germaniun transistor are described.

U.D.C. 621.383.2.032.217.2:537.312.5:535.215

Operation of Cs-Sb Phototubes at under High Light Levels
Kiyoshi MIYAKE
Kekyû Zituyôka Hôkoku (Electr. Comm. Labor. Techn. Jour.), NTT, **10**, 6, pp. 1217–1224, June, 1961

The fatigue phenomena of vacuum and gas-filled Cs-Sb photocathodes was studied. It was observed that photocathodes can be operated without fatigue at very high photocurrent densities.

U.D.C. 621.385.032.216:548.74:537.58

Study on Oxide Coated Cathodes by Electron Microscope
Shoichi HIROTA, Tetuji IMAI
Kenkyû Zituyôka Hôkoku (Electr. Comm. Labor. Techn. Jour.), NTT, **10**, 5, pp. 771–801, May, 1961

Electron Microscopic observations on oxide coated cathodes were made using the special replica method. Crystal growth during the decomposition process, relationship between crystal size and cathode emission, etc. were studied.

U.D.C. 621.391:621.394.1:621.391.883:621.395.5

Binary Data Transmission on Telephone Circuits
Tosi MINAMI, Hiroshi SUNAGAWA, and *Shun'itsu HAMAO*
Kenkyû Zituyôka Hôkoku (Electr. Comm. Labor. Techn. Jour.), NTT, **10**, 5, pp. 803–850, May, 1961

Theoretical and experimental research for high speed (1000∼2000 bauds) binary data transmission by use of the Amplitude Modulation Double Side Band System is described.

U.D.C. 621.394.1:621.391.883:621.317.799.087.6

Circuit Interruption and Circuit Interruption Measuring Set
Tosi MINAMI, Masamichi ONO
Kenkyû Zituyôka Hôkoku (Electr. Comm. Labor. Techn. Jour.), NTT, **10**, 5, pp. 851–865, May, 1961

Analysis of telephone circuit interruption in cable and radio systems measured by the newly developed interruption measuring set, which consists of a magnetic tape recorder and delay circuit, is described.

U.D.C. 621.395.36:621.395.123.621.395.34

Automatic Number Identification System in Step-by-Step Local Offices
Toshii KATO, Minoru AKIMOTO, Yoshiki ONISHI, and *Yoshio ARIIZUMI*
Kenkyû Zituyôka Hôkoku (Electr. Comm. Labor. Techn. Jour.). NTT, **10**, 5, pp. 943–958, May, 1961

An automatic number identification system in a step-by-step office is discussed. Also, fundamental data of transmission characteristics of identification signals, dial impulses, etc. tested in the laboratory and field by a newly developed apparatus are described.

U.D.C. 621.395.44:621.395.51:621.391.827.2

Additive Features of Crosstalk in Non-loaded Carrier-cable Systems

Akiyoshi TSUKAMOTO
Kenkyû Zituyôka Hôkoku (Electr. Comm. Labor. Techn. Jour.), NTT, **10**, 6, pp. 1079, June, 1961

The relationships between circuit length and signal-to-far-end crosstalk ratio, and between circuit length and far-end crosstalk noise are described.

U.D.C. 621.395.623.012.8:537.228:534.321.9

Equivalent Circuit of Piezoelectric Transducer

Kazuo HUSIMI, Keisuke KATAOKA
Kenkyû Zituyôka Hôkoku (Electr. Comm. Labor. Techn. Jour.), NTT, **10**, 6, pp. 1163–1171, June, 1961

A more formally well arranged the six-terminal impedance matrix and equivalent circuit than conventional one derived by Mason and Roth is proposed for the analysis of piezoelectric transducers.

U.D.C. 658.562:519.24

Dynamic Programming for Double Sampling Inspection

Gen-ichi TAGUCHI
Kenkyû Zituyôka Hôkoku (Electr. Comm. Labor. Techn. Jour.), NTT, **10**, 5, pp. 981–985, May, 1961

Dynamic programming theory for double sampling inspenction when the 2nd sample size is determined according to the results of the 1st sample is described.

U.D.C. 678.7.02:66.095.2.097:547.244

Vinyl-polymerization with Organoboron Catalysts

Nobuyuki ASHIKARI
Kenkyû Zituyôka Hôkoku (Electr. Comm. Labor. Techn Jour.), NTT, **10**, 5, pp. 867–894, May, 1961

Many organoboron compounds are effective initiators for various vinyl-polymerizations. The compounds act as free radical catalysts. Simple kinetic studies and stereoregular polymerizations on some monomers are described.

U.D.C. 681.177.7:621.374]:003.24

An Electronic Systems for Translating Japanese Braille

Zen'iti KIYASU, Sigeru SEKIGUTI
Kenkyû Zituyôka Hôkoku (Electr. Comm. Labor. Techn. Jour.), NTT, **10**, 6, pp. 1149–1161, June, 1961

Details of the experimental apparatus and translation process are described. This system uses a teleprinter with Roman letters, an electronic translator, and a new type of braille printer.

Papers Published in Publications of Scientific and Technical Societies

U.D.C. 537.311.33.537.222

Llewellyn-Peterson Equation in Semiconductor Space Charge Region
Hisanori YOSHIMURA
Jour. Inst. Electr. Engineers, Japan. **44,** 5, pp. 830–837, May, 1961

Motions of carriers in semiconductor space charge regions are discussed, and analogy between vacuum tubes is derived.

U.D.C. 537.311.4:539.379

Contact Resistance of Contacts having Surface Layer
Takuya TANII, Kozo TOMA
Jour. Inst. Electr. Engineers, Japan. **44,** 6, pp. 822–830, May, 1961

The influences of surface layer to contact resistance of contacts have been investigated theoretically and experimentally.

U.D.C. 621.318.56:534.1

Contact Chatter of Relay-Springs
Giiti ITO, Masao TAKAMURA, Yuiti SIMIZU, and *Yuji OTUKA*
Jour. Inst Electr. Engineers, Japan. **44,** 6, pp. 973–979, June, 1961

The design of chatterless relays and methods of improving of contact spring of chatterless relays are described.

U.D.C. 621.372.81

On the Action of Dipole in Waveguide Circuits.
Shoji TSUCHIYA
Jour. Inst. Electr. Engineers, Japan. **44,** 6, pp. 963–973, June, 1961

The new principle on waveguide networks, called "Actions of phase rotation and phase constancy", and the two novel devices, called a reflection type phase shifter and a phase directional coupler are discussed.

U.D.C. 621.372.81.09

New Generalized Telegraphist's Equations for Waveguides.
Shinichi IIGUCHI
Jour. Inst Electr. Engineers, Japan. **44,** 6, pp. 955–963, June, 1961

The author derives the inclusive telegraphist's equations for the curved and nonuniform waveguide containing a slight inhomogeneous and anisotropic medium. These results contain almost all the telegraphist's equations for waveguides which have been reported up to date.

U.D.C. 621.382.233

Three Terminal Esaki-Diodes (Control Method of Esaki-Diodes)
Toshiya HAYASHI, Yoshio SUNOHARA
Jour. Inst. Electr. Engineers, Japan. **44,** 5, pp. 806–810, May, 1961

New control methods of Esaki-Diodes having three terminals are proposed and their applications in a bistable switching are described.

U.D.C. 621.383.323:621.3.011.22

The Field Effect Transistor as a Negative Resistance Device.
Tatsuya NIIMI, Toshiya HAYASHI, and *Yoshio SUNOHARA*
Jour. Inst. Electr. Engineers, Japan. **44,** 5, pp. 811–815, May, 1961

The structure, principle, design methods, fabrication procedures, static characteristics, and the application areas concerning the field effect transistor as a negative resistance device are studied.

U.D.C. 621.39:621.376.5

Theory of Digital Communication System
Yukio HOSHIKO
Jour. Inst. Electr. Engineers, Japan. **44,** 5, pp. 631–649, May, 1961

Fundamental problems of digital communication systems, especially for data processing, information source channel characteristics, encoding, modulation and pulse transmission are discussed.

U.D.C. 621.3.002.62:658.516

Coding Economics of Electrical Communication Parts.
Hideo KUBOKOYA
Jour. Inst. Electr. Engineers, Japan. **44,** 5, pp. 798–805, May, 1961

Coding economics and lot frequency for minimization of manufacturing costs of parts and correction of coding due to periodic variation of demand are described.

U.D.C. 621.391.832:534.78:530.132.2

On the Transmission Quality Estimated from the Point of View of Fluctuation Characteristics of Speech Sound.
Shuzo SAITO, Ryoichi MATSUDA
Jour. Inst. Electr. Engineers, Japan. **44,** 5, pp. 816–822, May, 1961

This paper describes the effects of fluctuating characteristics of speech sounds on the tonal differential linear in the typical frequency response system having single peak in transmission band.

U.D.C. 621.396.41.029.631.64:621.396.677

Equipments of Microwave Relay System. (B)-Antenna System
Keigo ÔHASI
Jour. Inst. Electr. Engineers, Japan. **44,** 5, pp. 730–735, May, 1961

Recent development of antenna systems for the broadband radio relay systems are described.

* * * *

Vol. 9, Nos. 7-8 JULY-AUGUST, 1961

CONTENTS

Radioactivation Analysis of Oxygen and Boron in Transistor-Grade Silicon 403
Tadashi NOZAKI, and *Junichi SHIMADA*

Observations of Uniaxial Anisotropy in Ferromagnetic Thin Films by Means of Bitter Technique 408
Yuzo ODANI, and *Yuzi GOMI*

A 48 Gc Center-Excited Type Channel Branching Filter for Circular Electric Waves 421
Shin-ichi IIGUCHI, Bun-ichi OGUCHI, and *Kazuo YAMAGUCHI*

The Design of Germanium Diodes used for Junction Capacitance Parametrons 429
Yasuhiro HIYAMA

Binary Data Transmission on Private Telephone Line 437
Toshi MINAMI, Hiroshi SUNAGAWA, and *Shun'itsu HAMAO*

Growth and Electrical Properties of Ferroelectric Glycine Sulfate Single Crystals .. 485
Hiroo TOYODA, Yoichi TANAKA, and *Wataru SHIOKAWA*

A Study of M-type Tube Electron Guns 497
Tomoyuki UNOTORO

Inclusive Telegraphist's Equations for Waveguides 526
Shin-ichi IIGUCHI

Papers Contributed to Scientific and Technical Journals by the Members of the Laboratory 536

Copyright 1961 by the Electrical Communication Laboratory, NTT